THE UNIVERSITY *of* EDINBURGH

High Pressure Studies of Hydrogen-Chalcogen Systems

Edward J. Pace

Doctor of Philosophy
The University of Edinburgh
October 22, 2018

Abstract

Binary element-hydride systems have become a pertinent topic for high pressure research, following the measurement of record high temperature superconductivity in the dense hydrogen-sulfur system. The experimental study followed predictions of superconductivity with high transition temperature (T_c) in $(H_2S)_2H_2$ at high pressures, leading to the current consensus that the high T_c phase is H_3S, produced from the decomposition and recombination of H_2S at high pressures. However, conjecture over the behaviour of hydrogen sulfide upon compression, and experimental limitations, cast significant ambiguity over interpretations of the structure and mechanism of the superconducting phase. Nonetheless, theory also predicts high T_c superconductivity in the dense hydrogen selenide and telenide systems; both experimentally uncharted at high pressures prior to this study. This thesis explores and maps the phase diagrams of hydrogen-chalcogen (S, Se, Te) systems using a combination of high pressure Raman spectroscopy and x-ray diffraction techniques. Gaining a comprehensive understanding of the behaviour of these systems under pressure is crucial to the eventual elucidation of the true nature of high T_c superconductivity.

Hydrogen sulfide (H_2S) and hydrogen selenide (H_2Se) are appreciably toxic. A simple in situ synthesis technique is reported for producing hydrogen-chalcogenides directly from their constituent elements within diamond anvil cells, circumventing the need to condense toxic gases. This technique is also utilised to provide excess hydrogen, in order to produce the hydrogen-rich cocrystals thought to be vital to the formation of the high T_c phase.

The hydrogen-sulfur system is most thoroughly investigated, and first presented. High quality Raman spectroscopic data provides an experimental review of pure H_2S. Studies of $(H_2S)_2H_2$ evaluate the current known ambient temperature phases and reveal three novel low temperature phases. Phase II′ is identified on cooling of

phase I to 173 K (10 GPa), via splitting of both the single S-H stretching mode and low-frequency H_2 vibron; sharp stretching modes indicate a significant reduction in orientational disorder. Successive splitting of the low-frequency H_2 vibrons indicates two additional phase changes at 29 GPa (phase III′) and 53 GPa (phase-IV′) respectively, at 80 K. Phase IV′ is associated with an overall increase in symmetry. Evidence is also presented for a tentative fourth novel low temperature phase at ∼160 GPa (20 K) and for the formation of an exceptionally stable hydrogen-sulfur compound with potentially novel stoichiometry. The behaviour of the H_2S and $(H_2S)_2H_2$ mixed molecular system is also reported; demonstrating that the coexistence of $(H_2S)_2H_2$ and H_2S can influence the hydrogen-bonding within both systems at high pressures.

The first high pressure studies of the hydrogen-selenium system at ambient temperature are reported. The high pressure phase sequence of H_2Se (I – I′ - IV) is identified by Raman spectroscopy, mirroring that of H_2S. The isothermal boundaries for phases I′ and IV are found at 7 and 12 GPa respectively, at 300 K. Phase IV may have higher symmetry than phase IV H_2S. X-ray diffraction and Raman spectroscopy demonstrate that the H_2Se:H_2 mixtures form cocrystals of $(H_2Se)_2H_2$ from 4.2 GPa, with tetragonal space group $I4/mcm$, analogous to $(H_2S)_2H_2$. Both H_2Se and $(H_2Se)_2H_2$ are shown to decompose into their constituent elements above 24 GPa.

Attempts to synthesise the elusive H_2Te directly from hydrogen and tellurium are reported. No reaction occurs upon heating Te in H_2 at 0.2 GPa to 573 K. No visible reaction occurs between H_2 and the high-pressure phases of Te, upon laser-heating. No photoreaction occurs upon exposure of tellurium in hydrogen to intense laser light (532 nm) at 0.2 GPa and 300 K, but formation may be stabilised at lower temperatures.

Lay Summary

High pressure science is a fascinating field of research. It enables us to recreate the conditions of physically inaccessible places which we cannot directly measure, such as the centres of planets. It may not seem immediately applicable to everyday life but understanding what state matter is in at extreme conditions helps us to build a comprehensive picture of our universe.

The arrangement, or structure, of atoms and molecules in a material can change quite drastically when subjected to high pressures. A great deal of high pressure science revolves around determining the specific arrangement of atoms in compressed materials, which in turn elucidates any other properties which might emerge. In fact, some astounding phenomena have been observed in matter under extreme pressures which would not have been otherwise observed.

For example, below certain temperatures some materials exhibit a property known as superconductivity, where electrical resistance drops completely to zero. This effect is utilised for technology such as magnetic resonance imaging and high-speed magnetic levitation trains. But at ambient pressures, these materials must be made extremely cold before superconducting; most must be cooled far below the temperature of the coldest planet in our solar system. This has resulted in an ongoing search to find a material which can superconduct at room temperature. In 2014 it was discovered that hydrogen sulfide, when compressed to 1.5 million atmospheres, exhibits superconductivity up to -70 ℃; breaking the previous record by more than 60 degrees.

However, generating high pressures in a material requires a special device, called a diamond anvil cell (DAC), which unfortunately limits the quality of data that can be obtained from a compressed material. As a result, presently it is unclear whether the superconductivity arises from hydrogen sulfide (H_2S)

or a compound with a different arrangement, such as H_3S, or an even more complicated structure such as $(H_2S)_2H_2$. Theoretical studies have now predicted similar superconducting behaviour at high pressures in other members of same the molecular family as hydrogen sulfide, known as the hydrogen-chalcogenides, which had not been studied under pressure prior to this project. Understanding what happens to these materials when they are compressed is a small step down a long road, which may eventually lead to harnessing room temperature superconductors at more manageable pressures.

In this thesis, hydrogen sulfide (H_2S), hydrogen selenide (H_2Se) and hydrogen telluride (H_2Te) are studied at high pressures, and various temperatures, to better understand their behaviour upon compression. As they are normally toxic and flammable gases, it is safer and easier to synthesise them directly from their less hazardous constituent elements, within the diamond anvil cells themselves; i.e. creating H_2S from S and H_2. This also facilitates the study of more complicated arrangements such as $(H_2S)_2H_2$, which is also reported.

Declaration

I declare that this thesis was composed by myself, that the work contained herein is my own except where explicitly stated otherwise in the text, and that this work has not been submitted for any other degree or professional qualification except as specified.

Parts of the work presented in Chapter 8 have been published in [1, 2].

(*Edward J. Pace, October 22, 2018*)

Acknowledgements

I extend my deepest gratitude and appreciation to everyone who has helped me in some way over the last three years, and made this thesis possible. Many of whom are not named below, to keep this from becoming a tenth chapter.

First and foremost Prof. Eugene Gregoryanz. Thank you for the inspiration, knowledge and opportunities; all the stories, trips to Hefei, 肉棒, 拉面, 啤酒 and 硒.

I'm extremely grateful to Prof. J. Paul Attfield for taking me on as a PhD student, providing constant support, fruitful discussions and for always sharing biscuits with the group.

My first publication and a large portion of this thesis would not have been possible without the guidance and teachings of Dr. Ross Howie, and the other members of *Howie and the Anvils*: Drs. Phil Dalladay-Simpson, Jack Binns and Mary-Ellen Donnelly. Thank you so much for all that you've taught me, your companionship, and making me so welcome in Shanghai. I'd also like to sincerely thank Xiaodi, 刘晓迪, for her enthusiasm and hospitality, without whom none of the low temperature experiments would have been possible, 谢谢.

Everyone in the physics workshop for their outstanding engineering and patience.

All those in CSEC who've taught me, and whose friendship has been invaluable. In particular Drs. Amy Coleman, Graham McNally, Miriam Peña-Alvarez, Robin Turnbull, Ángel Arévalo-López and Mungo Frost; soon-to-be-Drs. Paul Sarte, Alex Browne, Jacky (Ka) Hong, and everyone else in the Attfield group.

My good friends Adam Czajka and Joe Matthews, for council throughout the years. Ian Waters for never saying no, to anything. Andrei Dobrescu for the chess games, and Gaz, Ali, Oli and Jon for the jams. ◯

I express warmest thanks to my whole family for their constant love and support. Moja kochanie, Ala, for always being by my side and believing in me.

Finally, my main docs Mum, Dad and Ellie, to whom this thesis is dedicated.

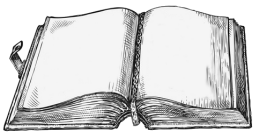

"..meddle first, understand later. You had to meddle a bit before you had anything to try to understand."

Terry Pratchett
Interesting Times

Contents

List of Figures

Chapter 1

Introduction

Exploring extreme states of matter is crucial to understanding the inner workings of our universe. Much like visualising the vast distances of deep space, it is challenging to truly comprehend the magnitude of pressures attainable with modern devices. For instance, the deepest accessible point on earth experiences a crushing one-thousand atmospheres of pressure, exerted by eleven kilometres of ocean; yet several million atmospheres are routinely contained within contemporary diamond anvil cells, which can fit in your pocket. Strange and exotic states of matter are found at such conditions, many of which are only poorly understood; whilst more mysterious properties are predicted at pressures beyond our current capabilities. The science of condensed matter is still in its infancy compared to what is yet to be discovered.

1.1 A Brief Review of High Pressure Science

The field of high pressure is easily traced to Percy Bridgman. His vast scientific achievements stemmed from designing a simple pressure seal in 1905, opening the door to the gigapascal (GPa) regime [3]. He promptly developed the multi-anvil press, pushing the boundary by an order of magnitude, and planting the seeds for unprecedented novel research. By simply applying great force to the small area between hard tungsten-carbide anvils, Bridgman was able to explore unusual aspects of many material systems under pressure, such as resistivity changes in compressed metals [4]. His legacy leaves numerous prolific fields of

scientific research in its wake, from geological studies of planetary interiors [5, 6] to investigations into the nature of dense hydrogen [7, 8].

Although modern high pressure technology has not shifted drastically from Bridgman's opposed tungsten-carbide anvils, the Cambrian explosion of scientific endeavours in condensed matter can be traced to a few key innovations and discoveries. The use of diamond over tungsten-carbide was a major breakthrough. Diamond not only has a high bulk modulus ($\sim$440 GPa), allowing greater load transfer before mechanical failure, but is transparent to most of the electromagnetic (EM) spectrum. This allows samples to be probed *in situ*, using techniques such as Raman spectroscopy and x-ray diffraction. in 1958, in a classic story of scientific serendipity, early pioneer Van Valkenburg prepared a high pressure experiment using diamonds as anvils, to pass an infra-red beam through his sample [9, 10]. After experiencing difficulties transmitting the beam, he placed the two anvils under a microscope to check they were parallel and realised he could actually see a pressure gradient across the sample. The importance of viewing a sample is often overlooked in the modern era, but EM radiation based analytical techniques all find their roots in visual observation. The idea of precise culet alignment was revolutionary in itself, not to mention the ability to witness properties such as phase boundaries, phase transitions, colour changes and recrystallisation rates.

Van Valkenburg also went on to develop the gasket which allowed fluids to be compressed within the diamond anvil cell (DAC), and enabling materials to be compressed hydrostatically [11]. Another great leap was made in 1972 when Forman developed a quick and reliable pressure calibration using ruby fluorescence [12]; prior to this, pressure was calculated from applied load or from the equation of state (EoS) of a material. Shortly thereafter the field began to flourish, and the Mao-Bell cell was introduced as the first piston-cylinder DAC design, which facilitated the first megabar (Mbar) on compression of ruby [13]. Modifications to the classic Merrill-Bassett design were made to better accommodate the collection of x-ray diffraction (XRD) data which lead to an important milestone in the determination of the crystal structure of solid hydrogen at 5 GPa [7]. Despite considerable advances in analytical techniques, the near ubiquitous use of these cell designs, and the ruby scale, in contemporary high pressure DAC studies speaks to their efficacy. All were essential tools for the experiments reported in the contributing work.

1.2 The Role of Hydrogen

The study of dense hydrogen has long been an attractive area of the field, following the prediction of metallisation at pressures of 25 GPa [14]. Later theoretical work forecast metallic hydrogen the exhibit superconducting properties at ambient temperature: arguably the holy grail of modern physics [15]. Modern pressure estimates for hydrogen metallisation are approaching 500 GPa, exceeding current experimental limitations [16]. Despite the ongoing hydrogen campaign, it has been proposed that ambient temperature superconductivity can be achieved at more readily accessible pressures by pre-compressing H_2 as an alloy or hydride with other materials [17]. Currently this is rationalised from the Bardeen-Cooper-Schrieffer (BCS) theory of conventional superconductivity; it is thought that hydrogen can provide a combination of high-frequency phonons from strong electron-phonon coupling and a high density of states, favourable for high superconducting at higher temperatures [18]. Indeed, theoretical studies predict ever higher superconducting transition temperatures (T_c) in compressed binary hydrides [19–25]. Making such measurements practically can be challenging, hence experimental studies of high T_c superconductivity are limited. The most significant progress towards achieving room temperature superconductivity has been found in the sulfur-hydrogen[†] system [28].

1.2.1 Superconductivity in the Sulfur-Hydrogen System

A transition temperature (T_c) of 203 K was measured in hydrogen sulfide (H_2S) at 155 GPa, after following a peculiar pressure-temperature phase path [28]. H_2S, compressed at low temperatures, began to superconduct above ∼100 GPa ($T_c <$ 100 K). On further compression to 150 GPa, the T_c steadily increased, exceeding 150 K. The sample was then warmed above 250 K and cooled once more, now superconducting with a T_c of 203 K. Drozdov *et al.* propose that H_2S decomposes into S and H_2 on warming, reforming H_3S as the high T_c phase.

The potential of H_2S was realised following a theoretical study, where a T_c of 204 K was found in $(H_2S)_2H_2$ at 200 GPa [23]. The molecular H_2 units within $(H_2S)_2H_2$ were projected to break at 111 GPa, and form an intercalated lattice

[†]Very recent experimental studies report higher T_c measurements of 215 K [26] and 260 K [27] in compressed lanthanum hydrides, which await peer-review.

of body centred cubic (bcc) sulfur and hydrogen atoms, composed of molecular H_3S units. A successive theoretical study proposed that the bcc structure is composed of Perovskite-like (SH^-) and (H_3S^+) units [29], whilst another described the formation mechanism as symmetrised hydrogen bonds (H-bonds) between H_3S units [30]. Although these theories advocate that the high T_c phase has $Im\bar{3}m$ cubic symmetry, alternative structures have also been put forward. For example an alloyed H_2S/H_3S Magnéli phase was proposed, which is suggested to explain the strange pressure dependence of the observed T_c [31]. However, despite extensive modelling of the high T_c phase, the mechanism is still largely unclear. Whilst experimental XRD measurements have since confirmed a bcc S lattice with a high T_c, the true nature and position of H atoms remains speculative [32]. Furthermore, the direct measurement of superconductivity at $\sim$200 K has yet to be confirmed or even investigated with an independently prepared sample [33–35].

T_c measurements and theories aside, the behaviour and structures of H_2S (D_2S) at high pressures are also not definitively characterised. In particular, there are several conflicting experimental and theoretical interpretations as to the nature of H_2S above $\sim$50 GPa [22, 36–41]; here all features of the Raman spectra disappear, whilst the weak scattering nature of hydrogen prevents the positions of H atoms from being established by XRD. Analogous hydrogen-chalcogenide systems of selenium and tellurium have also been found potential high T_c superconductors [42–45], yet the elementary systems on compression remain experimentally unexplored. The apparent significance of H_3X stoichiometry (X = S, Se, Te) makes $(H_2X)_2H_2$ systems in particular attractive candidates for study. But despite the prescience of predictions in the $(H_2S)_2H_2$ system [23], direct experimental studies are limited [46, 47], and results from exploration near high T_c conditions are in direct conflict [48, 49]. Thus the high pressure hydrogen-chalcogen systems present ample scope for novel and significant scientific research.

1.3 Thesis Outline

The ambiguity over the nature of high T_c superconductivity in sulfur-hydrogen is preceded by deficient characterisation of the precursor and related systems. This thesis aims to explore and characterise the nature of the fundamental H_2X and $(H_2X)_2H_2$ systems (X = S, Se, Te) at high pressures, with the intent of establishing a better foundation to interpret the high T_c phenomenon. As the nature of bonding and the behaviour of H atoms is clearly important, Raman spectroscopy was the primary diagnostic used in this endeavour, supported by XRD studies.

This thesis is composed of nine chapters. This introductory chapter has provided an overview of the requisite for an in depth investigation of the hydrogen-chalcogen systems at high pressure, and has set the study into the broader context of the field of condensed matter. The following chapters are composed as follows:

Chapter 2 concerns the background theory relevant to the contributing studies. The fundamental aspects of Raman spectroscopy are given from both classical and quantum mechanical standpoints, before covering the principles of diffraction and crystallography.

Chapter 3 gives an overview of the experimental techniques pertinent to the preparation and performance of high pressure experiments. A technical review of DAC preparation and sample loading is given, followed by methods of measuring and controlling pressure and temperature. The practical aspects of performing Raman spectroscopy and x-ray diffraction at high pressures are discussed.

Chapter 4 provides an experimental review of high pressure H_2S at ambient and low temperatures. High quality Raman spectroscopy data of the most relevant phases is presented and discussed, with comparison to literature data, providing a comprehensive overview of the system. Prevalent inconsistencies in known work are illuminated and expanded upon via the contributing studies and a detailed analysis of the current literature is given.

Chapter 5 is dedicated to novel synthesis techniques developed to overcome inherent issues with loading hydrogen-chalcogenides directly, and for reliably producing $(H_2X)_2H_2$ systems within DACs. The first section concerns the direct synthesis of H_2S from sulfur and hydrogen, and highlights some interesting peripheral results which arose as a consequence of varying synthesis conditions. The second section details the direct synthesis of H_2Se from selenium and hydrogen, and the final section briefly describes various attempts to synthesise the elusive H_2Te.

Chapter 6 presents results from the study of $(H_2S)_2H_2$. The currently known ambient temperature phases are investigated in depth with high quality Raman data, and a brief XRD study; the data are examined in the context of different theoretical models from previous studies, and possible alternatives. Raman studies conducted between 15 and 80 K provide confirmation of at least three novel low temperature phases, followed by a speculative fourth which could be the high T_c phase. The chapter closes with a short section providing evidence of a remarkably stable sulfur-hydrogen compound, with potentially novel stoichiometry.

Chapter 7 investigates the effects of coexistence and mixing of different sulfur-hydrogen systems. The chapter begins with the formation of $(H_2S)_2H_2$ clathrates from direct synthesis of fluid H_2S at low pressures. This is followed by a complementary study of H_2S trapped in a fluid state within fluid H_2, above the solidification pressure of H_2S. The next section presents Raman studies of H_2S and $(H_2S)_2H_2$ mixtures, exhibiting marginally distorted properties compared to the individual systems. The chapter concludes with the formation of $(H_2S)_2H_2$ directly from pure H_2S as a consequence of laser-induced decomposition.

Chapter 8 examines the H_2Se and $(H_2Se)_2H_2$ systems on compression. High quality Raman data, supported by XRD studies, characterises both systems for the first time (prior to this study) at high pressure and ambient temperature. H_2Se is found to follow the same phase sequence as H_2S, with subtle differences to the lowest symmetry phase. $(H_2Se)_2H_2$ is found to have a single phase analogous to phase I of $(H_2S)_2H_2$. The data from this chapter are also published in [1, 2].

Chapter 9 summarises and draws together the main conclusions from the contributing studies and presents ideas for future work, before discussing the significance of the results in the wider context of the field.

Chapter 2

Theory

This chapter describes some of the fundamental theories underpinning the diagnostic techniques employed in this study. Raman spectroscopy and x-ray diffraction are discussed, before touching upon the subject of crystallography and structure analysis. A detailed commentary on these topics within the context of practical high pressure experiments can be found in Chapter 3

2.1 Raman Spectroscopy

2.1.1 Introduction

Optical spectroscopies facilitate direct measurements of internal energies within atomic and molecular systems via exposure to EM radiation. They are particularly pertinent for probing condensed matter *in situ* within DACs. Optical spectroscopies can be loosely divided into emission, absorption and Raman techniques.

Emission techniques measure photons of distinct energies, produced from the excitation and relaxation of electronic states within a material. The characteristic colours produced from burning different elements is a primitive example of emission. A range of excitations can be probed through absorption techniques, which analyse the absent energies from a continuous spectrum of light, passed through a material. Some incident photons will excite transitions of comparable energy within the material, and become absorbed (See Figure 2.1). Higher

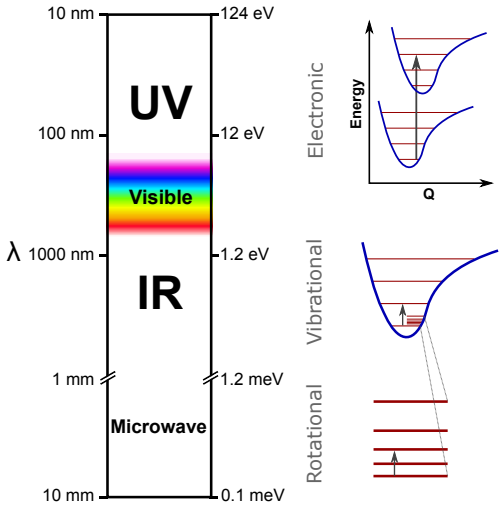

Figure 2.1 Left: Electromagnetic spectrum indicating the approximate relative energy ranges for electronic (highest energy), vibrational and rotational (lowest energy) transitions within molecules. Right: Typical graphic representations of relevant energy transitions in a diatomic molecule.

energies in the ultra-violet (UV) and visible region typically correspond to electronic transitions. Molecular vibrations are characterised by lower energies, absorbing infra-red photons, whilst molecular rotations will couple to microwave radiation of an even lower frequency range.

Raman spectroscopy is decidedly different, based on measuring the frequencies of scattered photons, after monochromatic incident radiation. Following the emergence of quantum mechanics, it was theorised by Smekal that a system of quantised energy states would inelastically scatter incident radiation with shifted frequency [50]. This was then observed congruently by two independent research groups; Landsberg and Mandelstam witnessed the scattering in crystalline materials [51], whilst Raman and Krishnan observed the effect in liquid samples [52]. Since these early experiments, where filtered sunlight was used as a monochromatic radiation source, light sources and detection methods have been significantly refined.

The modern Raman spectrometer makes use of powerful, finely-tuned lasers and sensitive charge-coupled devices (CCD) for high resolution measurements. Raman spectra of measured intensity as a function of energy can provide a myriad of useful information, such as the electronic, vibrational, magnetic and elastic properties of a material. Since these physical properties are greatly influenced by pressure, Raman spectroscopy is a key diagnostic tool for high-pressure scientists.

2.1.2 Theory of Raman Scattering

Consider a material illuminated with a beam of monochromatic radiation of frequency ν_0. A small component of the incident radiation is scattered, whilst the majority is transmitted unaffected [53]. The bulk of this scattered light is of the same frequency as the incident radiation (Rayleigh scattering, ν_0) whilst the remainder comprises components of discretely shifted frequency (Raman shift, ν_M). The resultant spectrum of intensity as a function of frequency is composed of a central Rayleigh band, with symmetrically distributed Raman bands on either side, described by:

$$\nu_S = \nu_0 \pm \nu_M \tag{2.1}$$

where frequency ν_M relates to an internal rotational, vibrational or electronic transition within the excited material. Raman excitations at frequencies lower than the Rayleigh band are referred to as Stokes lines ($\nu_0 - \nu_M$), and the symmetrical higher frequency excitations are anti-Stokes lines ($\nu_0 + \nu_M$). Raman spectra are plotted in units of reciprocal centimetres, relative to the energy of the incident radiation (rel cm^{-1}). The relevant information is contained within the energy difference between the inelastically scattered photons and the incident radiation; the relative frequencies of the Stokes and anti-Stokes lines can be considered independent of the incident photon energy. The relative intensities of Stokes and anti-Stokes scattering differ, and are described by Boltzmann distributions (Equation 2.9). The nature of Raman spectroscopy can be elucidated effectively by both quantum and classical mechanics. Beginning with classical derivations allows us to understand Raman excitations in terms of polarisability.

Classical Theory

Raman spectroscopy and Infra-red (IR) spectroscopy are complementary techniques, due to the difference in selection rules which allow for excitations to occur. Consider a homonuclear diatomic molecule such as H_2, which exhibits a single vibrational mode under ambient conditions. The electrons can be considered equally distributed at any point in time during the oscillation of its molecular vibration; there is no permanent dipole or change in dipole moment, hence the ν_1

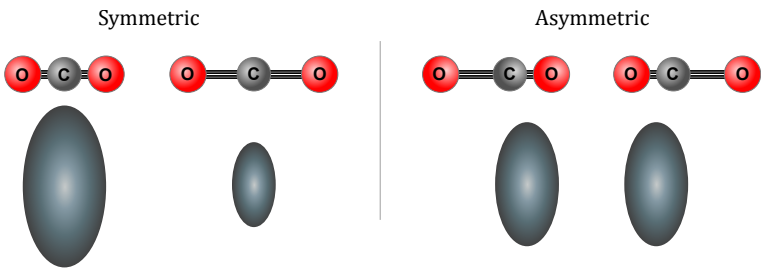

Figure 2.2 Representative polarisability clouds at vibrational maxima for the symmetric (left) and asymmetric (right) stretching modes of CO_2. A larger cloud indicates greater polarisability: electrons are more dispersed and hence their position more easily influenced by an external electric field. Therefore the magnitude of polarisability for the symmetric stretching mode varies with time, and is Raman-active. The asymmetric stretching mode is thus Raman inactive.

vibrational mode of H_2 is classically IR-inactive [54]. However, when subjected to an external electronic field, a dipole can be induced. The magnitude of the dipole moment, μ_{ind}, is proportional to the intensity of the applied electric field, $\mathbf{E}$ and the *polarisability* of the molecule:

$$\mu_{ind} = \alpha \mathbf{E} \tag{2.2}$$

The polarisability of any molecule (α) can be considered the degree to which electron density within the molecule can be influenced by an external electric field. In any non-spherical molecule the polarisability is described by a tensor as it depends on the atomic coordinates, but in this case α is considered as a scalar. The polarisability of a molecule therefore depends on the electronic distribution. Figure 2.2 shows how polarisability changes throughout the oscillation of different stretching modes within a molecule of CO_2. In order to be Raman active, a molecular vibration must exhibit a change in magnitude of polarisability with respect to time.

Consider again the H_2 molecule within an electric field. The incident field now acts on the electrons within the molecule, and induces an oscillating dipole. The intensity of any radiation scattered by the interaction with this dipole moment is proportional to the square of the magnitude of the dipole moment. The intensity of the dipole moment itself is affected by the intensity of the electric field, which can be expressed as a function of time:

$$\mathbf{E} = \mathbf{E}_0 \cos(\omega_0 t) \tag{2.3}$$

where ω_0 articulates the angular frequency of the induced dipole oscillation. The induced dipole moment with respect to time is thus expressed by substituting 2.3 into 2.2:

$$\mu_{ind}(t) = \alpha \mathbf{E}_0 \cos(\omega_0 t) \tag{2.4}$$

The polarisability term, α, can also be expanded for time dependence, accounting for perturbations due to the internal molecular motion (ω_M):

$$\alpha = \alpha_0 + \alpha_1 \cos(\omega_M t) \tag{2.5}$$

Expanding 2.4 by substituting 2.5 then gives an expression for the magnitude of the time dependent induced dipole moment μ_{ind}, when an electromagnetic wave of angular frequency ω_0 acts upon a molecule vibrating with angular frequency ω_M:

$$\mu_{ind}(t) = \alpha_0 \mathbf{E}_0 \cos(\omega_0 t) + \alpha_1 \mathbf{E}_0 \cos(\omega_0 t) \cos(\omega_M t) \tag{2.6}$$

$$cos(A)cos(B) = \frac{1}{2}\big[cos(A+B) + cos(A-B)\big] \tag{2.7}$$

Applying the trigonometric identity (2.7) and reducing angular frequencies ω_0 and ω_M to ν_0 and ν_M respectively, shows classically how the scattered radiation is composed of an elastically scattered Rayleigh component, ν_0, and inelastic Stokes ($\nu_0 - \nu_M$) and anti-Stokes ($\nu_0 + \nu_M$) components:

$$\mu_{ind}(t) = \alpha_0 \mathbf{E}_0 \cos(2\pi\nu_0 t) + \frac{1}{2}\alpha_1 \mathbf{E}_0 \big[\cos\big(2\pi[\nu_0 - \nu_M]\big) - \cos\big(2\pi[\nu_0 + \nu_M]t\big)\big] \tag{2.8}$$

Quantum Theory

Quantum mechanics illuminates some aspects of Raman spectroscopy which classical mechanics fails to predict, such as intensities of scattered photons and the origin of the selection rules [53]. Raman scattering can be considered a two-

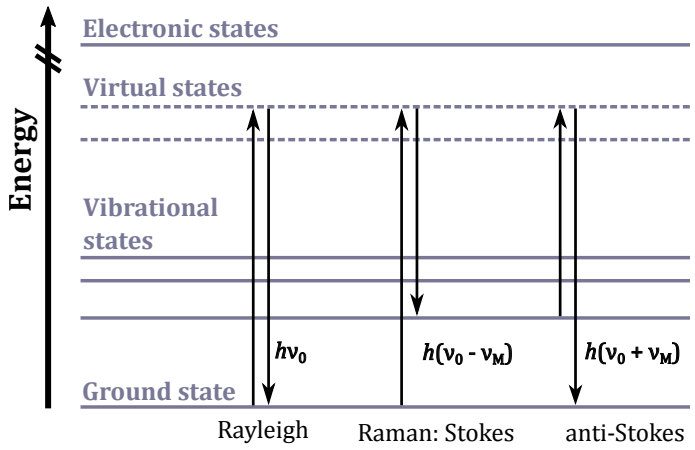

Figure 2.3 Energy diagram detailing transitions for Rayleigh, Stokes and anti-Stokes scattering. These *virtual* transitions are higher in energy than vibrational transitions, but lower energy than electronic transitions.

photon process. Illustrated in Figure 2.3 are the differences between Rayleigh, Stokes and anti-Stokes scattering, in terms of excitations. When an incident photon does not have sufficient energy to excite a full electronic transition, it is still absorbed and excites a *virtual state*. Returning from a virtual state occurs in one of three ways:

- **Rayleigh scattering:** The excited photon returns to its original state, emitting or elastically scattering a photon of the same energy as the incident photon: (ν_0)
- **Stokes scattering:** The excited photon returns to a state of higher energy than the initial state, for example to a vibrational state from the ground state. The emitted photon possesses less energy than the incident photon $(\nu_0 - \nu_M)$ appearing below Rayleigh band in the resultant spectrum.
- **anti-Stokes scattering:** The excited photon returns to a state of lower energy than the state from which excitation occurred, for example to the ground state from a vibrational state. The emitted photon possess more energy than the incident photon $(\nu_0 + \nu_M)$ appearing above the Rayleigh band in the resultant spectrum.

The measured Raman spectrum for any given molecular system will be composed of a Rayleigh band, dependent on the frequency of the incident laser beam, and Stokes and anti-stokes components for each Raman-active transition within the system. The relative intensities of the Stokes and anti-Stokes bands relate to the relative populations of the initial states from which the respective transitions

occur, which is given by a Boltzmann distribution [53, 54]. Anti-Stokes intensities become negligible at higher frequencies as fewer initial excited states exist. At ambient temperature the ground state is predominantly occupied, so usually in practice only the Stokes bands are measured. An intensity ratio for Stokes and anti-Stokes scattering can be expressed as:

$$\frac{I_{aSt}}{I_{St}} = \frac{(\nu_0 + \nu_M)^4}{(\nu_0 - \nu_M)^4} e^{\frac{-h\nu_M}{k_B T}} \tag{2.9}$$

where ν_0 and ν_M refer to the frequency of the incident photon and the molecular vibration respectively. k_B is the Boltzmann constant, T is absolute temperature of the molecule and h is the Planck constant.

2.2 X-ray Diffraction & Crystallography

2.2.1 Introduction

In material systems, variations in internal pressure are always accompanied by a change in volume. Solid materials at high pressures will often undergo phase changes characterised by a distinct shift in the spatial relationship of atomic positions, such that a new overall structure is adopted. The ability to determine where atoms lie with respect to each other is important in understanding new phases, and provides other useful information about the properties of a material. Solids frequently exhibit a crystalline atomic arrangement, where the structure possesses long range order and translational symmetry within three spatial dimensions. Such crystals are typically expressed as a composition of infinitely repeating smaller units, known as the unit cell, situated upon an infinite array of discrete points within an abstract lattice. Characterising the size and symmetry of the smallest possible repeating unit is the most efficient way of describing the entire crystal structure of a material.

There are a number of different methods of obtaining structural information for a solid material; this study primarily employed powder x-ray diffraction from synchrotron radiation. X-rays are useful because their wavelength is comparable to the interplanar distances within the atomic arrays of most solids. Typical x-rays used for these diffraction studies possess wavelengths of 0.3 -

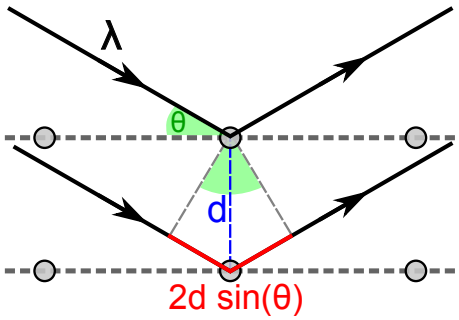

Figure 2.4 A two-dimensional representation of scattering conditions for x-ray diffraction (The Bragg condition). X-rays of wavelength λ are incident at angle θ (green), on a periodic atomic array, with planes separated by distance, d (blue). Constructive interference occurs when reflected waves travel with a path difference of $2d\sin(\theta) = n\lambda$ (red).

0.5 Å. When an x-ray interacts with the electron-density surrounding an atom within a periodic array, it becomes elastically scattered (Thompson scattering). Multiple interactions produce measureable interference patterns. The angles and intensities of the diffracted x-rays are extracted from these patterns, which in turn are used to produce a three-dimensional map of electron density, and thus the average atomic positions within the unit cell of the analyte material. The observation of diffraction of x-rays by crystals was first observed by M. Von. Laue in 1912, earning him the Nobel prize in physics [55].

2.2.2 Diffraction conditions

Consider a monochromatic[†] beam of x-ray radiation (wavelength λ) incident at an angle (θ) on a series of planes composed of ordered arrays of atoms, separated by a distance (d). A percentage of the incident radiation on each plane is reflected with a path difference, calculated from the interplanar distance and incident angle ($2d\sin(\theta)$), shown in Figure 2.4. Wherever this path difference is an integer number (n) of wavelengths (λ) the reflected waves are in-phase and their superposition creates a region of measurable intensity. This is known as the Bragg condition, for which the Nobel Prize in physics was awarded jointly to W. L. Bragg and his father W. H. Bragg in 1915 [56]:

$$2d_{hkl}\sin\theta = n\lambda \tag{2.10}$$

[†]Laue diffraction can also be performed, where the wavelength of incident x-rays is varied whilst the sample orientation is fixed.

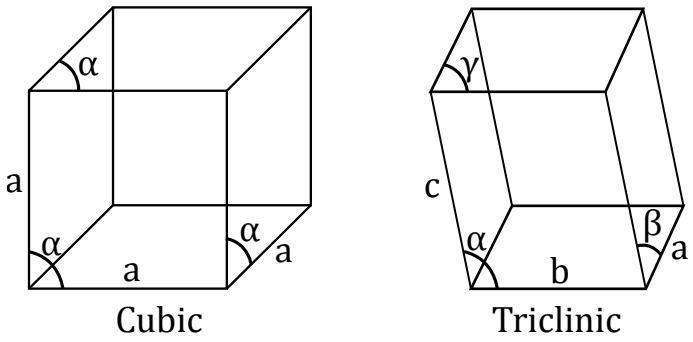

Figure 2.5 Diagrams of two of the seven lattice systems, described by the lengths (a, b, c) and angles (α, β, γ) of the unit cell volumes. (a) cubic unit cell: $a = b = c$ and $\alpha = \beta = \gamma = 109.5°$(b) triclinic unit cell: $a \neq b \neq c$ and $\alpha \neq \beta \neq \gamma \neq 90°$.

Reflected waves not meeting the Bragg condition essentially have no measurable intensity. Therefore, measuring the reflected intensity (at a fixed distance) as a function of incidence angle generates a pattern, unique to the orientation and spacing of planes of atoms within the analyte crystal.

2.2.3 Crystallography

Geometry

Several different constraints apply when describing the unit cell of a crystal structure. As previously mentioned, the unit cell is the smallest possible volume of a crystal, which can be repeated infinitely in three dimensions to give the overall arrangement of atoms in a crystal. One can start by defining the lattice parameters; the lengths of the principle axes (a, b, c) and the angles between them (α, β, γ) give the size, shape and volume of the unit cell. There are seven *lattice systems* which can be described by different relationships of these factors. For example, the most simple and symmetric crystal structures possess a cubic unit cell, where $a = b = c$ and $\alpha = \beta = \gamma$ (Figure 2.5a). The lattice system with the lowest symmetry is the triclinic unit cell, where $a \neq b \neq c$ and $\alpha \neq \beta \neq \gamma \neq 90°$ (Figure 2.5b).

Sets of common planes are produced when repeating any arbitrary unit cell on a three-dimensional lattice. The notation for a set or family of lattice planes is known as its Miller Index [54, 57]. The spacing between a set of planes, d, will satisfy the Bragg Condition (2.10) at an appropriate incident angle or Bragg angle. The Miller indices for a plane are given by three integers, h, k and l. The

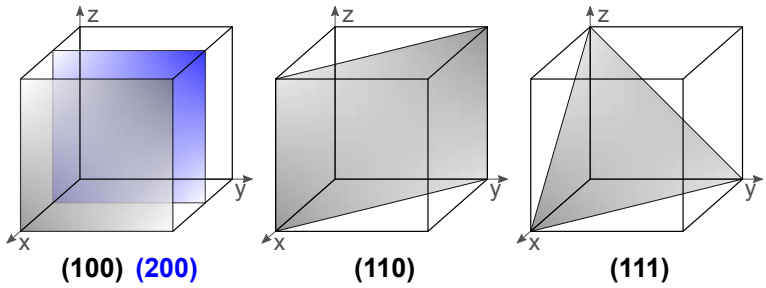

Figure 2.6 Examples of Miller indices for simple planes. The plane (200) is indicated in blue; $h = 2$ which intercepts the a axis at the position $\frac{1}{2}$. The values for k and l are both 0 indicating they do not intercept b and c respectively. (200) describes a set of planes parallel to (100).

indices are orthogonal vectors proportional to the inverse intercept of the axes a, b, c. For example a value of 1 for h indicates an intercept of $\frac{1}{1} = 1$ along the a axis. Similarly an index value of 0 indicates the vector does not intercept the relative axis. An index of $\bar{1}$ indicates an intercept at -1.

The atomic positions, x_i, y_i, z_i, describe where atoms reside within the unit cell. These are usually given as a fractional coordinate of the length of the relative side of the unit cell. The repeating patterns of these atomic positions in three-dimensions is given by the space group. The space group describes symmetry operations (e.g. rotation, reflection, translation) which can be applied to any point on an infinite lattice to produce a new position indistinguishable from the original. In other words, when applied to an atom within a unit cell, the space group reproduces its exact relative position within a different unit cell at another place in the crystal structure. There are 230 distinct space groups which are listed in the *International Tables for Crystallography* [58].

2.2.4 Powder Diffraction

Regions of scattered intensity are referred to as reflections. Reflections from planes within a single crystal are observed by the detector as discrete points of intensity (Figure 2.7a). The relative positions of the individual reflections determines the unit cell geometry, whereas the specific intensities correlate to the type and position of the individual atoms. Therefore in the absence of a perfect single crystal sample, information can still be extracted from a powder (polycrystalline) sample. A powder is considered a collection of randomly oriented crystallites. In a hypothetically perfect powder, every plane within the individual crystal is present in every possible orientation [59]. Therefore an x-ray beam

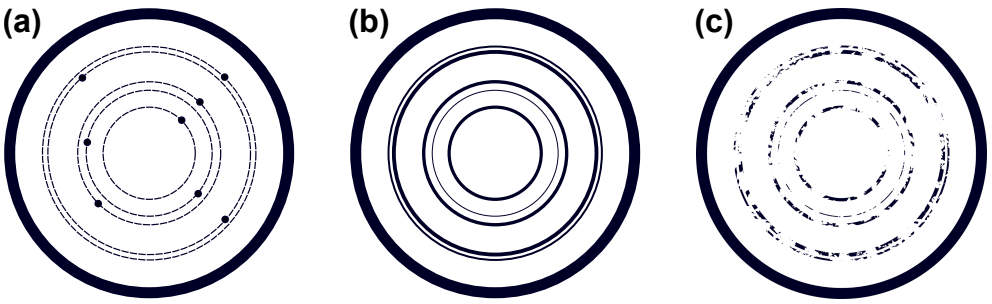

Figure 2.7 Representative characteristic area detector diffraction patterns. (a) Shows diffraction from a single crystal sample, where dashed lines indicate the d-spacing of each reflection. (b) Debye-Scherrer rings generated from a powdered sample. The rings can be considered the sum of many individual reflections from randomly oriented crystals. (c) A representation of incomplete and irregular Debye-Scherrer rings, from a poor-quality powder.

at any angle of incidence should satisfy the Bragg condition for every plane simultaneously. A single beam of incident x-rays generates a series of cones emanating from the sample, rather than discrete reflections, at angles where 2.10 is satisfied. These cones are observed upon a two-dimensional detector as a series of concentric rings, known as Debye-Scherrer rings (Figure 2.7b). Practically, the pattern is generated from a finite number of crystals; by exposing a larger volume of a powder sample to the incident radiation (for example, by rotating it) the statistical relevance of the measurement can be increased. However, planes with different Miller indices within the individual crystal may possess similar d-spacing making it difficult to distinguish which plane is contributing to a single reflection. Rietveld refinement (see section 2.2.5) is required to resolve the intensities from individual reflections. Although crystal structures can be completely solved from powder diffraction, its primary advantages lie in its efficiency as an analysis technique. Single crystal diffraction is considerably more powerful but requires samples of much higher quality.

Powder diffraction was primarily used for structure confirmation during these studies. Containing samples at high pressures makes it difficult to dictate the quality and type of sample produced; i.e. growing perfect single crystals or producing high quality powder samples. Additionally, DACs limit the sample volume and the range of incidence angle, hence it is not always possible to satisfy the Bragg condition for every orientation of planes (see section 3.2). Partial coverage of an irregular powder will produce a grainy pattern with uneven, broken rings (Figure 2.7c), which limits the amount of information which can be extracted from a structural refinement.

2.2.5 Structure Refinement

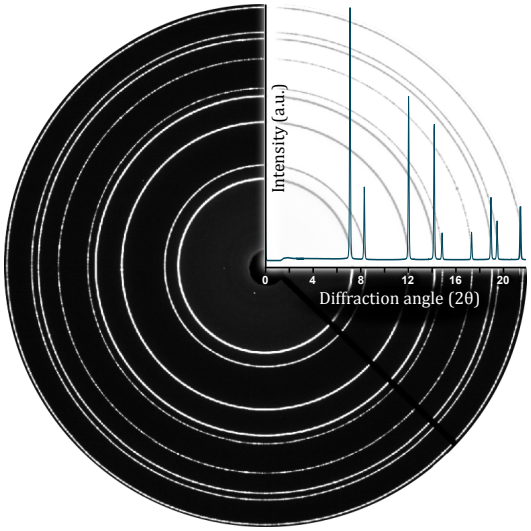

Figure 2.8 Typical raw powder diffraction data, and the subsequent integrated pattern (overlaid) as a plot of diffraction angle 2θ versus intensity.

Diffraction data is most commonly analysed and presented as an integration of the diffraction pattern (Figure 2.8). In x-ray diffraction, this becomes a plot of 2θ versus relative intensity, which is easily converted into d (interplanar distance between Miller indices) versus relative intensity. As discussed, the peak intensity is pertinent to the atomic positions within the unit cell. In single crystal diffraction, mathematical checks can be performed to match the individual reflections to other symmetry equivalent reflections to determine the space group. In powder diffraction a degree of dimensionality is lost as symmetry equivalent reflections possess the same d-spacing. Because of this, powder diffraction analysis usually begins with some assumptions about the structure of the analyte material, and a mathematical function is generated to fit the data as closely as possible. Iterations are performed by a computer whilst varying particular parameters within the overall function, until the difference between the data and the function is minimised. The final values of the refined parameters give a more statically relevant evaluation of the unit cell dimensions and geometry than the initial assumption.

The *Rietveld* method and the *Le Bail* method are two key techniques for structure refinement, which rely on a least squares difference approach. A Rietveld refinement is used to extract structural information from good quality powder data (i.e. consistent rings, Fig 2.7b) [60]. The observed pattern is compared directly to a calculated pattern. The peak positions and intensities are calculated

from the space group, approximated lattice parameters and atomic positions. Experimental parameters such as the x-ray wavelength and distance from sample to detector are also taken into account. By refining the values of the given structural parameters, the sum of the squares of the residual differences between the observed and calculated patterns, S_y, is minimised for every component of the overall function making up the calculated pattern:

$$S_y = \Sigma_i \frac{1}{y_i}(y_i - y_{ci})^2 \tag{2.11}$$

Where y_i and y_{ci} are the observed and calculated intensities respectively at point i (either diffraction angle, 2θ or interplanar distance, d). The Rietveld refinement gives an assessment of the overall crystal structure based on the accuracy of many parameters such as positions and occupancies of atoms within the unit cell, phase fractions and preferred orientation of crystallites.

The Le Bail method is a primitive form of the Rietveld method [61], and only refines parameters relating to peak positions and shapes; the peak intensities are fitted as independent variables rather than being calculated from the atomic positions within the structural model. The Rietveld method is considerably more powerful, as it allows overlapping reflections to contribute to the calculated intensity y_{ci}. The Le Bail method hence does not refine atomic positions within the unit cell, but is limited instead to the unit cell parameters, peak width and shape parameters, and systematic instrument error. Peak shapes are described mathematically by a series of functions, accounting for deviation from a standard Gaussian profile. The Caglioti equation gives a value for H_G, the full-width-at-half-maximum (FWHM) for a Gaussian profile, where U, V and W are refineable parameters:

$${H_G}^2 = U \tan^2\theta + V \tan\theta + W \tag{2.12}$$

The addition of a Lorentzian component, H_L to the FWHM calculation allows for the shape of the peak to diverge from a Gaussian distribution, where X and Y are the refineable parameters accounting for strain and particle size respectively:

$$H_L = \frac{X}{\cos\theta} + Y \tan\theta \tag{2.13}$$

The sum of the calculated and refined peak parameters is compared to the observed pattern. For both Rietveld and Le Bail methods the quality of the refinement is expressed by a mathematical value, χ^2, which is known as the 'goodness of fit':

$$\chi^2 = \frac{\Sigma_{i=1}^{n} \frac{1}{y_i}[y_i - y_{ci}]^2}{n - p} \tag{2.14}$$

Where p is the number of parameters in the refinement, and n is the number of observations. Lower numbers express a better 'fit' to the data. Typically, refined XRD data is presented as the observed pattern overlaid with the calculated pattern, with a difference plot underneath. (e.g. Figure 4.3).

Collecting quality XRD data with DACs can be challenging, requiring the use of special cells and synchrotron x-ray radiation which is discussed in section 3.4. The samples analysed in the contributing studies gave poor powder data or incomplete single crystal data, which limited refinement to the Le Bail method. Consequently XRD was used for clarification of symmetry and establishing the unit cell dimensions, rather than solving the structures.

Chapter 3

Experimental Methods

3.1 Introduction

This chapter describes the practical aspects of the high pressure experiments undertaken in the contributing studies. The first section describes the diamond anvil cell (DAC, Figure 3.1) in a technical context: From the underlying principles, to the basics of assembly and sample loading required to prepare a high pressure experiment. This section also details methods used to generate and measure high pressures, and equipment used to access low temperatures. The second section discusses how the experimental Raman spectroscopy set-up interfaces with the DAC, while the third section concerns the practice of XRD using synchrotron radiation, for DAC samples at high pressures.

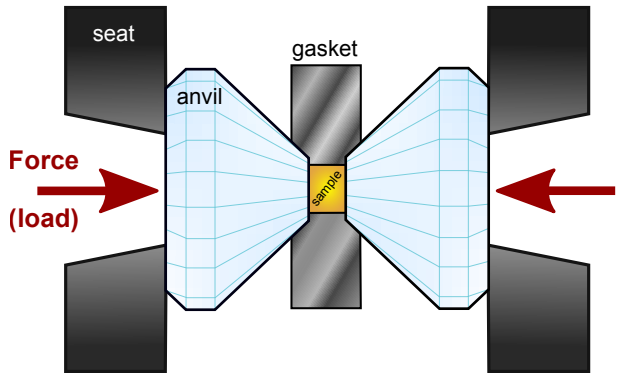

Figure 3.1 Schematic showing the transfer of load in a diamond anvil cell.

3.2 Diamond Anvil Cells

The modern DAC operates on very basic principles; Figure 3.1 shows how uniaxial force is transferred to a sample through two opposed flat diamond tips (culets). As pressure is inversely proportional to the area over which force is applied, the transfer of moderate load to very small culets facilitates routine access to pressures on the scale of planetary cores. A brief review of key developments to DAC design is given in section 1.1. A metallic gasket confines the available sample volume to a circular chamber between the two anvils (Figure 3.1). The sample chamber volume reduces when the load exerted on the anvils exceeds the yield strength of the metal, causing the gasket to 'flow' in towards the centre. The gasket thins as the anvils are brought together, until the metal has work hardened and ductile flow ceases. Further load continues to reduce the volume of the sample chamber through the length of the central axis of the anvils.

3.2.1 Preparation

Diamonds and Seating

The sequential preparation of a DAC for sample loading begins with the selection of diamonds and cell type, which essentially depends on the desired diagnostic and target pressure. For example, large culets are useful for studying systems where the changes occur over a small range at relatively low pressures; one might use ∼1000 μm culets to study a clathrate system in small pressure steps, up to a few GPa with neutron diffraction. Whereas the use of smaller culets allows generation of higher pressures before mechanical failure, but at the expense of sample volume. Higher pressures can be attained by the addition of double or

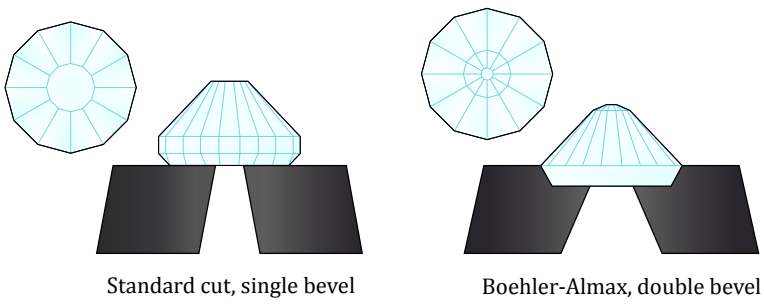

Figure 3.2 Representations of single and double bevelled diamonds, fixed to a standard seat (left) and a *Boehler-Almax* seat (right) with wider openings.

even triple bevels, as localised stresses are distributed more evenly throughout the diamond, and anvil cupping is reduced [62] (Figure 3.2). Pressures of ∼180 GPa were attained in this study using 50 μm double bevelled culets, but most experiments were performed up to ∼50 GPa using 200 μm single bevelled culets. A pair of culets should be of comparable size but they can differ up to ∼20 μm if necessary.

If diffraction is to be performed, the opening angle from the back side of the diamond (table) through the supporting seat must be maximised. A specific diamond geometry has been developed by *Boehler-Almax* (BA) involving a smooth conical base allowing the diamond to sit beneath the surface of special BA seats (Figure 3.2), maximising the available scattering angle (see section 2.2) [63]. If Raman spectroscopy is required, then the diamond fluorescence must also be considered along with size and geometry. Fluorescence amplifies the background noise in a spectrum, and tends to increase with pressure. Consequently special low-fluorescence diamonds must be used where possible for high pressure Raman experiments. Once selected, diamonds are carefully affixed to the appropriate seats using a thermally conducting *Stycast* epoxy; seats are usually made of hard materials such as tungsten-carbide or boron-nitride.

Cell Selection

A plethora of variant DAC designs are available for many specific experiments; for the scope of this project standard piston-cylinders and GG-symmetrical cell designs were employed for Raman spectroscopy and XRD experiments respectively (Figure 3.3). For Raman experiments, a piston-cylinder design is desirable as the tight fitting piston gives highly reproducible diamond alignment, generally allowing higher pressures to be accessed. Piston-cylinders were required to fit the lever-arms necessary to increase pressure (section 3.7) in cells within the cryostat for low temperature Raman experiments (section 3.2.4). However, the range of scattering angles available to piston-cylinders is poor. GG-type symmetrical cells were used for XRD experiments, offering wide openings allowing the cell to be rotated further without cutting the incident x-ray beam. GG cells employ four guide posts with a looser fit than the piston-cylinder design, which presents a higher risk of misalignment under load.

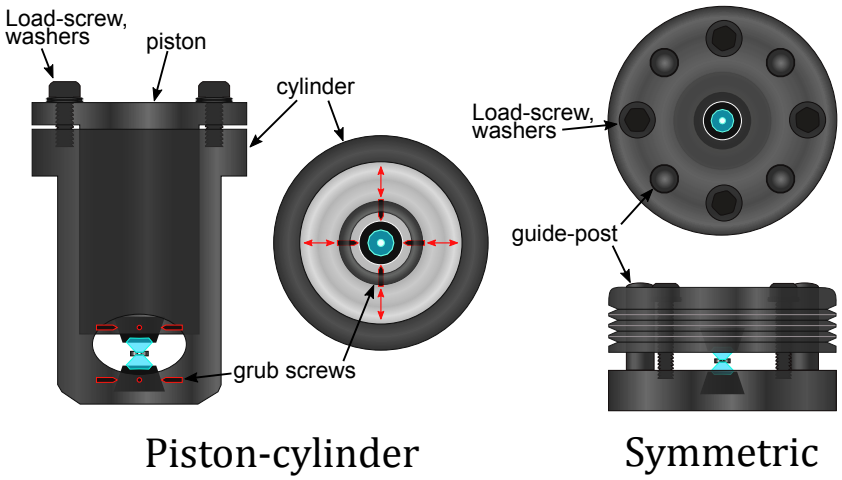

Figure 3.3 Schematics of piston-cylinder (left) and GG-symmetric cell designs (right), with top down views adjacent respectively.

Culet Alignment

Precise alignment of diamond culets is crucial for achieving high pressures without breaking the diamonds or losing the sample through movement or rupture of the gasket chamber. Care must be taken to ensure the diamond culet is completely parallel to the base of the seat when glueing. The seat-and-diamonds are then fixed in place by four sharpened grub screws; the points deform when tightened and bite into the seat, limiting movement. Alignment is achieved by first fixing one seat in place, making the screws as tight as possible. The other is fitted loose, but tight enough that it will not fall if inverted. Then the parallel culets are brought within a few μm of each other under a microscope. Ring-cracks can occur if the culets touch which compromise the integrity of the diamond. Hence, the distance is very carefully controlled by adjusting the tension between the load-screws and a set-screw. Once sufficiently close, both culets can be viewed simultaneously down the central axis of the cell. The position of the loose diamond can then be adjusted, aligned and tightened.

Gasket Preparation

Sheet rhenium (Re) 200 – 300 μm thick was used for gaskets, offering ductility with a high bulk modulus. A small square ($\sim$5x5 mm) is placed between the aligned culets, with some ruby powder. Pressure is increased to $\sim$25 GPa,

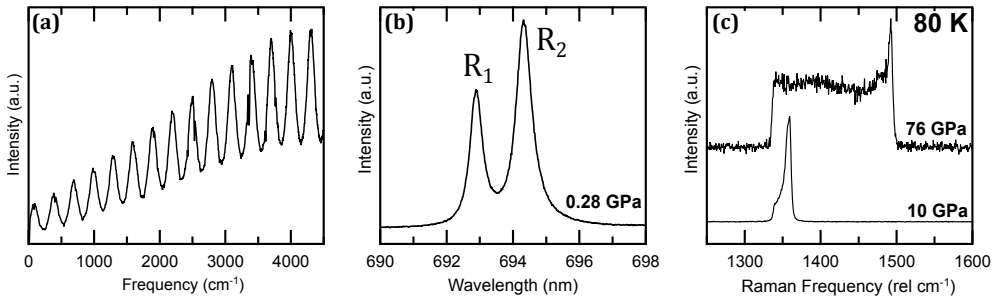

Figure 3.4 (a) Interference pattern obtained from a thick gasket (∼30 μm), used to determine the depth of the sample chamber. (b) R_1 and R_2 fluorescence lines from ruby at 0.28 GPa (c) Example Raman diamond edge spectra obtained from the same DAC at 10 and 76 GPa respectively.

indenting and work hardening the metal. A hole is drilled in the centre of the indent using a pulsed IR laser, ∼75% of the culet diameter. With the cell closed, the sample chamber depth is measured by passing white light through the diamonds, which partially reflect and act as a Fabry-Pérot interferometer [64]. An interference pattern is generated with maxima (minima) wherever an integer (half-integer) number of wavelengths (λ) fit within one length of the cavity (d). The pattern is plotted in wavenumbers (ν) as a function of intensity (Figure 3.4a), where the periodicity of the fringes is expressed by:

$$\Delta\nu\,(cm^{-1}) = (2d\,n)^{-1} \tag{3.1}$$

Where n is the refractive index of the cavity; the interference pattern can then be used to calculate the optical path length (d) and hence the thickness of the sample chamber. Gaskets are thinned to 5 – 15% of the culet diameter, depending on the experiment. For example, a highly compressible material such as H_2 requires a thicker gasket, for more initial ductile flow and reduction of sample chamber volume, to reach the highest pressures.

3.2.2 Pressure Control and Calibration

The most basic method to increase pressure is to simply tighten the load screws. Load screws must be used in pairs of opposing threads (right and left) and tightened either in unison, or small equal increments. Greater manual control is afforded by using more washers. The second method employed in this study was the use of a lever arm with piston-cylinder cells (Figure 3.7a). A loaded piston-cylinder is fitted (sideways) cylinder first into a housing-bracket, and

a push-plate is fitted on the back of the piston. A mechanism is assembled which transfers uniaxial load applied to a single plate on top of the device into perpendicular uniaxial force applied evenly to the push-plate, driving the piston into the cylinder, shown by red arrows in Fig. 3.7a. The (horizontal) distance moved by the push plate is less than the (downward) distance moved by the lever-arm load screw, generally affording finer control than would be achieved by simply using the DAC load-screws. Washers can also be used to further reduce sensitivity. Evenly applied force reduces the risk of misalignment at high pressures. The lever arm assembly can be affixed to an XYZ stage for Raman experiments, allowing load to be increased without removing the cell from the beam path. Lever arms also allow pressure to be increased during low-temperature experiments, through a set of very long hex screws which are accessed from the top of the cryostat (Figure 3.7).

Ruby Scale

The discovery and impact of pressure dependent ruby fluorescence on the field of high pressure science is described in section 1.1 [12]. Ruby (Al_2O_3) doped with Cr^{3+} will fluoresce upon illumination with focussed laser light, producing a doublet of emissions; at ambient pressure R_1 and R_2 are observed at 692.7 and 694.2 nm respectively (Figure 3.4b). As ruby is generally chemically inert, the fluorescence can be measured from a small sphere or chip included inside the sample chamber, using a standard high pressure Raman spectroscopy set up. The extensively calibrated ruby scale is now arguably the most prolific metric for determining pressure up to 100 GPa (at ambient temperature). The R_1 shift is reported linear up to ∼20 GPa ($\frac{d\lambda_{R1}}{dP}$ = 2.746 nm GPa^{-1}) [65]. The non-linear deviation above 29 GPa was calibrated and revised by Mao *et al.* up to 80 GPa [66], who proposed the equation:

$$P = 380.8\left[\left(\frac{\delta\lambda_{R1}}{694.2}\right)^5 - 1\right] \tag{3.2}$$

Where P is non-hydrostatic pressure (GPa) and λ_{R1} is the measured wavelength (nm). The R_1 emission line broadens with pressure (and temperature) and intensity drops at ∼100 GPa, above which the ruby scale becomes unreliable and other metrics must be utilised. This equation was used for measuring pressure from ruby fluorescence in all room temperature experiments up to ∼50 GPa.

Diamond Edge Scale

The second pressure calibration used depends on the Raman frequency shift (rel cm^{-1}) of the optical phonon from the stressed $\langle 1\,0\,0 \rangle$ face of the diamond culet. At ambient pressure the first-order diamond phonon is observed at a frequency of 1332 rel cm^{-1}, which increases on compression. Diamond anvils under load experience a pressure differential from the stressed culet, which confines and imposes pressure on the sample, to the unstressed table on the exterior of the cell. As the first-order diamond excitation is so intense, a laser focused onto a sample through the central axis of the diamond will produce a Raman spectrum containing peaks from both the unstressed table and the stressed culet. At high pressures this appears as a single broad contribution connecting two sharper peaks; Figure 3.4c shows the difference between measured spectra at 10 and 76 GPa. The frequency difference between the unstressed and stressed edge has been calibrated extensively up the multi-megabar regime. The frequency dependence is initially linear [67] but deviates at higher pressures [68–70]. The pressure dependence up to ∼200 GPa is given as:

$$P = A\frac{\delta\omega}{\omega_0}\left[1 + \frac{(B-1)}{2}\frac{\delta\omega}{\omega_0}\right] \tag{3.3}$$

Where P is pressure (GPa), ω_0 and ω are the unstressed (∼1332 cm^{-1}) and stressed frequencies respectively. A is a constant with a value of 547, and B is a constant with a value of 3.7 GPa. This equation was used to calculate pressures for low temperature experiments up to ∼180 GPa, as the diamond edge frequency has only a weak temperature dependence above 300 K [71]. The obvious advantage is that no additional pressure calibrant, such as Ruby or a chip of noble metal, needs to be included in the sample chamber. However, the diamond edge scale is considered less reliable < 25 GPa, and pressures obtained from diamond edge are generally not as precise as the ruby scale. This arises from the non-linear stress profile experienced by a given diamond anvil, along with effects of spatial filtering from the Raman set-up which can make it difficult to consistently determine the frequency of the stressed and unstressed edges.

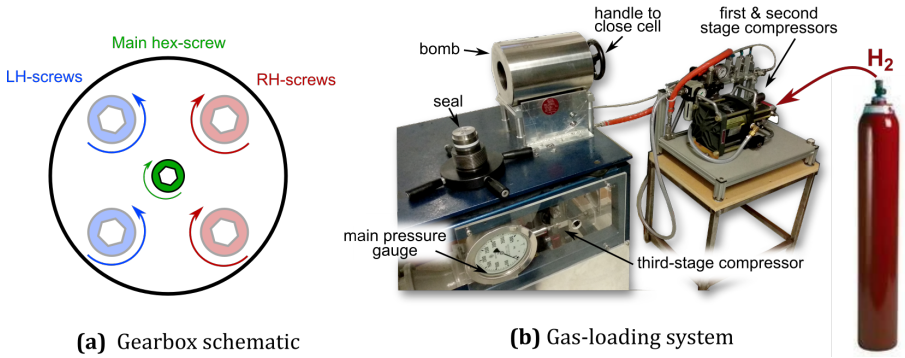

(a) Gearbox schematic **(b)** Gas-loading system

Figure 3.5 (a) Top down schematic looking through a gearbox. The main screw (green, top-side) is used to activate all four left (blue) and right (red) screws on the bottom-side of the gearbox which attaches to the DAC. (b) schematic photograph of the gas-loading system.

3.2.3 Sample Loading

Gas Loading

H_2 was loaded as a gas at 0.2 GPa (2 kbar) into cells already containing solid chalcogen (S, Se or Te). The precise number of screw turns required to close and open the cell must be calibrated using a gear-box prior to gas-loading. Figure 3.5a shows how the gearbox transfers the clockwise rotation of a single exterior screw (green) to four screws of a DAC: two clockwise (right-handed, red) and two anticlockwise (left-handed, blue) screws. The gearbox and DAC assembly is inserted into a large thick-walled stainless steel pressure vessel, known as a bomb (Figure 3.5b). The bomb is securely sealed and H_2 gas is pumped in from the gas bottle via three-stages of compressors, with the open cell inside. Once the loading pressure of 0.2 GPa is reached, the handle outside the bomb rotates the single gearbox screw inside, and thus the load-screws of the DAC, closing the cell and trapping H_2 at 0.2 GPa within the sample chamber. The excess H_2 is released via a valve and the loaded cell can be removed.

Cryogenic Loading

Cryogenic loading (cryo-loading) was used to load condensed H_2S gas into piston-cylinder DACs. It is imperative that full-face respirators are used when working with gaseous H_2S as it is extremely toxic; the entire operation must be performed within a fume hood. As with gas-loading the cell must be precisely calibrated to determine the number of screw turns required to completely seal the gasket,

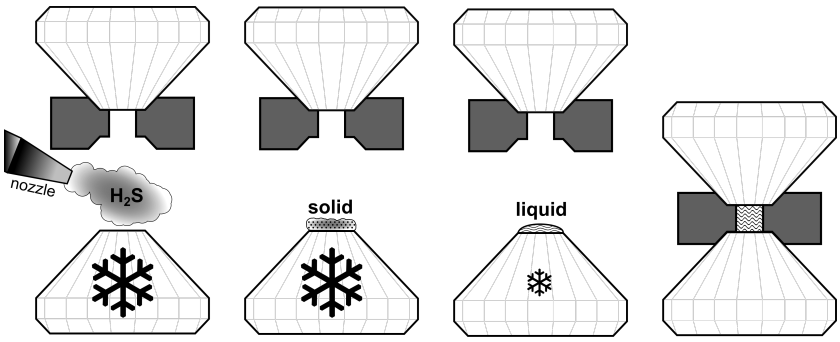

Figure 3.6 Sequential schematic of cryoloading H_2S: first condensing the gas as a solid powder onto the cold culet, and allowing it to melt before closing the cell.

from open. The entire cryo-loading process occurs within a sealed glove-bag which enables the user to interact with the contained environment. The open cell is first mounted on its side, within a polystyrene tray inside the bag, and a thermostat secured to the cylinder via the grub screw threads. The H_2S gas-cylinder is connected to a hose and nozzle via a corrosion resistant regulator, and fed through the glove-bag wall. A nitrogen (N_2) gas line is also fed into the bag. A jug of liquid N_2 is placed inside and the bag is sealed with clips. The bag is flushed with N_2 gas several times to ensure an inert atmosphere, and no moisture condenses on the cell once it is cooled. Then the tray is filled with liquid N_2 until level with the lowest edge of the diamond seats. The cell temperature is monitored until it drops below the H_2S melting point (191 K). The H_2S nozzle is angled in between the open diamonds, and the regulator opened very briefly so that a small quantity of gas escapes and condenses on the cold diamonds (Figure 3.6). The cell is then up-righted and temperature allowed to increase above the H_2S melting point (191 - 213 K). Before the gas evaporates, the cell is closed to the calibrated number of screws turns, using an Allen key. If the cell is closed when H_2S is solid, the expansion on warming can be significant enough to rupture the ductile gasket; additionally the low friction between the diamonds and the solid H_2S coated gasket can make the gasket unstable on compression. The closed cell is warmed slowly to room temperature, although an increase in pressure is usually unavoidable. Once loaded, H_2S seemed to visually form a powder.

3.2.4 Low Temperature

A continuous flow cryostat with a modified core was used to access low temperatures. Liquid N_2 and He cryogens were used to access temperatures down to 77 and 15 K respectively. The sample was mounted in a lever arm

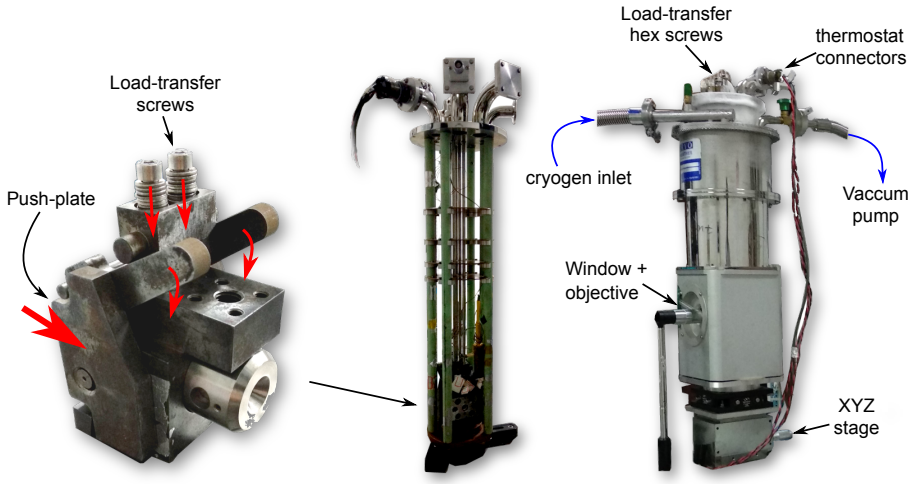

Figure 3.7 (a) DAC in a lever-arm. Red arrows indicate transfer of vertical to horizontal load. (b) Lever-arm mounted in the cryostat core (c) Fully assembled cryostat.

(Figure 3.7a) and attached to the cryostat core (3.7b). The modified core allows access to the load-screws from outside the sealed cryostat via long Allen keys. Positive pressure from the Dewar forces cryogen inside the main cryostat body, containing the cell, whilst a vacuum is pumped on a second insulating layer between the main body and the exterior. The rate of cryogen flow determines the rate of cooling. The core also carries wires from two thermostat-heaters to a dual proportional-integral-derivative controller (PID). One PID thermostat-heater is fixed close to the sample, and the other is fixed near the cryogen inlet. A desired temperature is set on the PID controller, and the heaters activate accordingly in a continuous feedback loop, based on the difference between the set point and measured temperature. This works against the cooling cryogen to maintain a stable temperature. Once sufficiently cold the cryogen flow rate can be reduced to a gentle positive pressure.

The cryostat presents some experimental issues for Raman spectroscopy. When cooled the entire assembly slowly contracts, moving the sample position out of the beam path. Stabilising the temperature requires a careful balance between cryogen flow-rate and heater sensitivity. Consequently the temperature can take some time to completely stabilise, hence obtaining high quality spectra from long exposures on cooling is not practical. In lieu, shorter exposures were acquired on coarse Raman gratings whilst constantly monitoring the temperature and sample position, at the expense of resolution. Furthermore, some signal intensity is lost upon passing through the double windows.

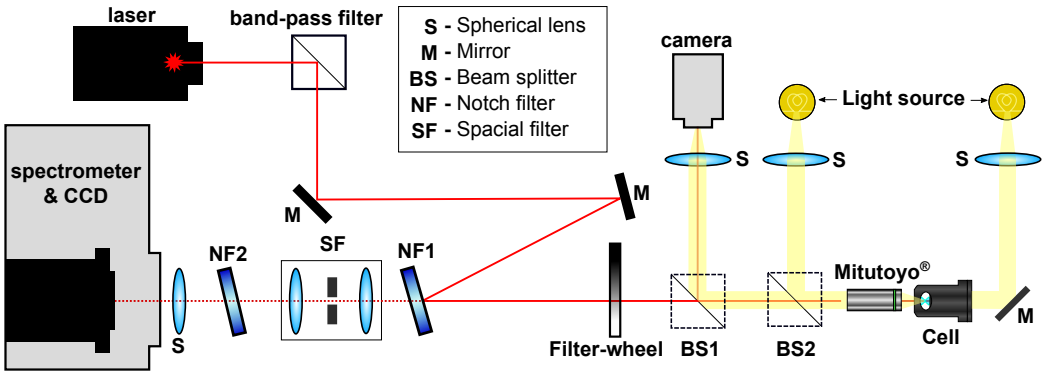

Figure 3.8 Schematic for a typical high pressure Raman spectroscopy set-up with 180° backscattering geometry.

3.3 High Pressure Raman Spectroscopy

This section serves to describe the experimental Raman spectroscopy set-up used for interface with DACs. An overview of Raman spectroscopy theory is given in 2.1. The optical components will be described in context, sequentially following path of the laser from emission to detection. The general schematic operates from a 180° backscatter geometry as shown in Figure 3.8.

Argon-ion (514 nm), krypton-ion (647 nm) and solid-state (532 nm) lasers were used with different Raman systems set up in the same fashion. Laser emissions are first filtered using a holographic Band-Pass Filter, which acts as a mirror reflecting only the desired wavelength at an angle of 90°, with ∼98 % efficiency. The filtered beam is reflected in a 'Z' configuration by two mirrors which can manipulate the angle and direction. After hitting the second mirror the beam is incident on a holographic notch filter (NF1), which acts as another Band-Pass Filter. The laser line is reflected at a sharp angle, necessitating the two prior mirrors, and all other light passes straight through.

A filter wheel enables the beam power to be quickly reduced if desired (for example when measuring ruby fluorescence) but is not essential. The two Beam-Splitter cubes (BS1 and BS2) are only necessary to view and focus light onto the sample respectively. BS1, BS2 are removed and both front and back lights switched off during data collection.

The monochromatic beam is focussed onto the sample using a *Mitutoyo* objective lens, with magnification from x5 to x50. These lenses have long working distances (13 - 16 mm) essential for integrating Raman spectroscopy with DACs, in

particular for low temperature experiments where the outer layer of the cryostat separates the objective and sample. The light interacts with the sample and is scattered at 180° back towards NF1. Again, the laser-line is scattered at an obtuse angle and the remaining light containing the information passes directly through towards the spectrometer. The angle of NF1 determines the width of the frequency band (centred on the laser line) which is filtered out, and hence the lowest frequencies of Stokes and anti-Stokes scattering which can be measured; the minimum Stokes frequencies observable with notch filters used in this work varied from $\sim$50 – 200 rel cm^{-1}.

The scattered light is then passed through a spatial filter which is essential for interfacing DACs with conventional micro-focussed Raman spectroscopy [72]. The spatial filter comprises two optical lenses directed at a central focal point, where a pinhole is located. The spatial filter focusses the scattered light, such that only the photons scattered from the sample chamber are passed through. This is important when dealing with small samples as spurious signals are cleaned from the scattered light, and for example reducing the signal from the anvils which is generally much more intense than the sample signal (see section 3.2.2). The positions of all three components are individually adjusted to optimise the ratio of signal to background noise.

Finally the light passes through a Super Notch Filter (NF2) to attenuate the more of the laser line before a final lens focusses the signal containing all the valuable information onto a diffraction grating which disperses the signal onto the CCD. *Coherent* Innova 70-C Ar^+ and Innova 300-C Kr^+ ion lasers were used with *Princeton Instruments* Acton SpectraPro 2500i spectrometers in tandem with *Princeton Instruments* 7500-0003 CCDs, outputting to computers using *WinSpec* software. *Coherent* 532 nm Verdi solid-state lasers were used with *Princeton Instruments* Iso-Plane SCT-320 spectrometers in tandem with *Princeton Instruments* PyLoN CCDs, connected to computers running *Princeton Instruments* Light-Field. Data were analysed with *IGOR Pro* (WaveMetrics Inc.) and *Fityk* [73] software packages.

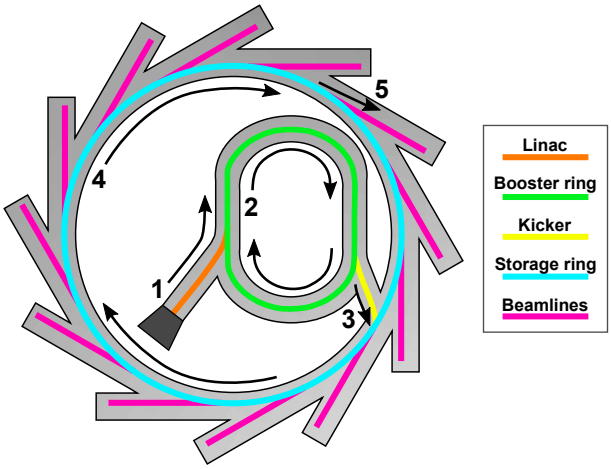

Figure 3.9 Simplified schematic showing the sequential path of electrons from generation to the storage ring in a standard synchrotron. The resultant x-rays pass down the beamlines to where the experiments are performed.

3.4 High Pressure X-ray Diffraction

This section describes the practical requirements for performing XRD on samples contained within DACs. The theory of diffraction and crystallography is discussed in section 2.2 and the appropriate selection of cell, diamond and seat type for XRD experiments has been described in section 3.2.1. To briefly reiterate, the first factor affecting XRD for DACs is essentially the limited range of angles, through which an unbroken straight line can pass. A further consideration is the limited amount of sample which can be measured, and the fact that the Re gasket scatters x-rays with considerably greater intensity than the light element samples used in these studies. In order to overcome both of these issues the incident x-ray beam must be very intense and tightly focussed. As such, third generation synchrotron sources are necessary for XRD with DACs. Synchrotrons at the Advanced Photon Source (APS), SPring-8 and Diamond Light Source* were visited to gather the XRD data used in this work.

The process of generating intense x-ray synchrotron radiation relies on the principle that an accelerating charged particle emits electromagnetic radiation. This is achieved by first generating bunches electrons and accelerating them with a linear accelerator (Linac, Figure 3.9) before injecting them into a small synchrotron known as a booster ring. The path of the electrons is influenced by strong electromagnets which further accelerate them around the ring to near relativistic speeds, until they attain the operating energy of the synchrotron

*US, Japan and UK respectively

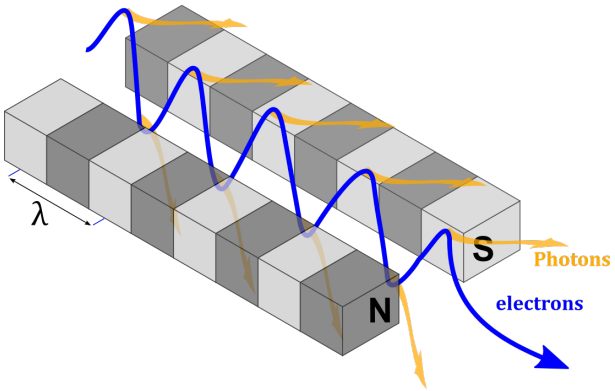

Figure 3.10 Representation of the oscillating path of electrons through an undulator and subsequent emission of photons.

source and are ready to be injected into the main storage ring: APS operates at 7 GeV, SPring-8 at 8 GeV and Diamond Light Source at 3 GeV.

Although apparently circular, the storage ring comprises alternating straight and bent sections. Powerful bending magnets curve the path of the electrons, which emit a wide spectrum of electromagnetic radiation. The straight sections contain insertion devices which generate intense collimated x-ray beams, and connect the storage ring to the beamlines. Basic insertion devices are known as undulators, comprising two arrays of magnets of alternating polarities which the electrons pass through, forcing them to oscillate at a specific wavelength and emit cones of intense radiation (Figure 3.10). Insertion devices are evaluated by the *strength parameter*, K, which describes the nature of electron motion:

$$K = \frac{eB\lambda_u}{2\pi m_e c} \tag{3.4}$$

where B is the magnetic field strength and λ_u the periodic spacing of the magnets; e and m_e are the electron charge and mass respectively and c is the speed of light. For an undulator, $K \ll 1$, and the magnets are spaced far apart with a small oscillation amplitude; radiation is emitted in tight energy bands. Insertion devices with $K \gg 1$ are known as wigglers; they have a more complex magnetic array and produce a broad spectrum of radiation. The beamlines then tightly focus the radiation, which is passed through a monochromater to produce intense x-ray radiation of a single wavelength, which is used for angle dispersive XRD experiments.

The DAC is mounted onto a goniometer which allows the angle and position of the sample to be manipulated externally. All synchrotrons operate differently, but the general process involves first aligning the centre of the sample relative the beam path before moving to the desired sample position. For powder diffraction, the cell can be rotated during an exposure in a process known as 'rocking', to maximise the number of crystallites satisfying the Bragg condition. The rocking range is limited by the geometry of the cell and diamonds, and the seat aperture.

A diffraction pattern is also obtained of a well-studied calibration standard (e.g. LaB_6 or CeO_2), which is coupled with key experiment parameters such as the incident wavelength and distance from sample to detector, to accurately integrate the experimental data. A final consideration is the appearance of diamond reflections. Fortunately carbon is a light scatterer and the diamonds themselves are large single crystals, with cubic symmetry. Consequently the diamond reflections are easily identifiable and can be masked out of the diffraction pattern prior to integration. Analysis and integration was performed using *Dioptas* [74], and structure refinement was performed with *FullProf* and *JANA* [75, 76]. Equation-of-state (EoS) functions were calculated using *EosFit7-GUI* [77].

Angle dispersive XRD data collected at the Advanced Photon Source (APS) at beamline 16-IDB (HPCAT) were recorded on a Pilatus 1M-F image-plate detector with micro-focused synchrotron radiation (∼3x6 μm) of 30 keV (0.4066 Å). Data collected at APS Beamline 13-IDD (GSECARS) were recorded on a MAR165 image-plate detector with micro-focussed synchrotron radiation (∼5x5 μm) of 40 keV (0.3344 Å). Data collected at Diamond Light Source beamline I15 were recorded on a MAR345 image-plate detector with focused synchrotron radiation (∼70x70 μm) of 40 keV (0.4246 Å). Data collected at SPring-8, beamline BL10XU were recorded on a *Rigaku* R-AXIS IV^{++} image-plate detector with a microfocussed synchrotron radiation (∼ 5x15 μm) of 30 keV (0.4136 Å).

Chapter 4

Hydrogen Sulfide

4.1 Introduction

This chapter documents high resolution Raman studies of pure H_2S up to 50 GPa (300 K) and 120 GPa (80 K). It seemed prudent to begin studying a mixed molecular system, i.e. $(H_2S)_2H_2$, by first assessing the individual components. H_2 is well documented at the pertinent conditions, whereas the behaviour of H_2S at high pressures is not as clear. As previously discussed, the difficulty in determining the H atomic positions experimentally has resulted in conjecture over the precise structural arrangement in the higher pressure H_2S solid phases. This chapter provides an in-depth experimental review of H_2S at high pressures, up to dissociation, and attempts to illuminate some discrepancies in the literature. Results and discussions for phases I-IV are confluent, whereas phase V (and above) warranted separate sections; a thorough commentary and analysis of the results in the context of the literature is given.

H_2S gas (*BOC*, 99.5 % purity) was directly cryo-loaded via the methods outlined in section 3.2.3. Raman spectra were obtained using 532 nm solid state excitation wavelengths. XRD data for phase I was obtained at Diamond Light Source - beamline I15, using a diffraction wavelength 0.4246 Å. Pressure was measured using a combination of Ruby fluorescence [66, 78] and stressed diamond edge frequency [70], calibrated to universal standards.

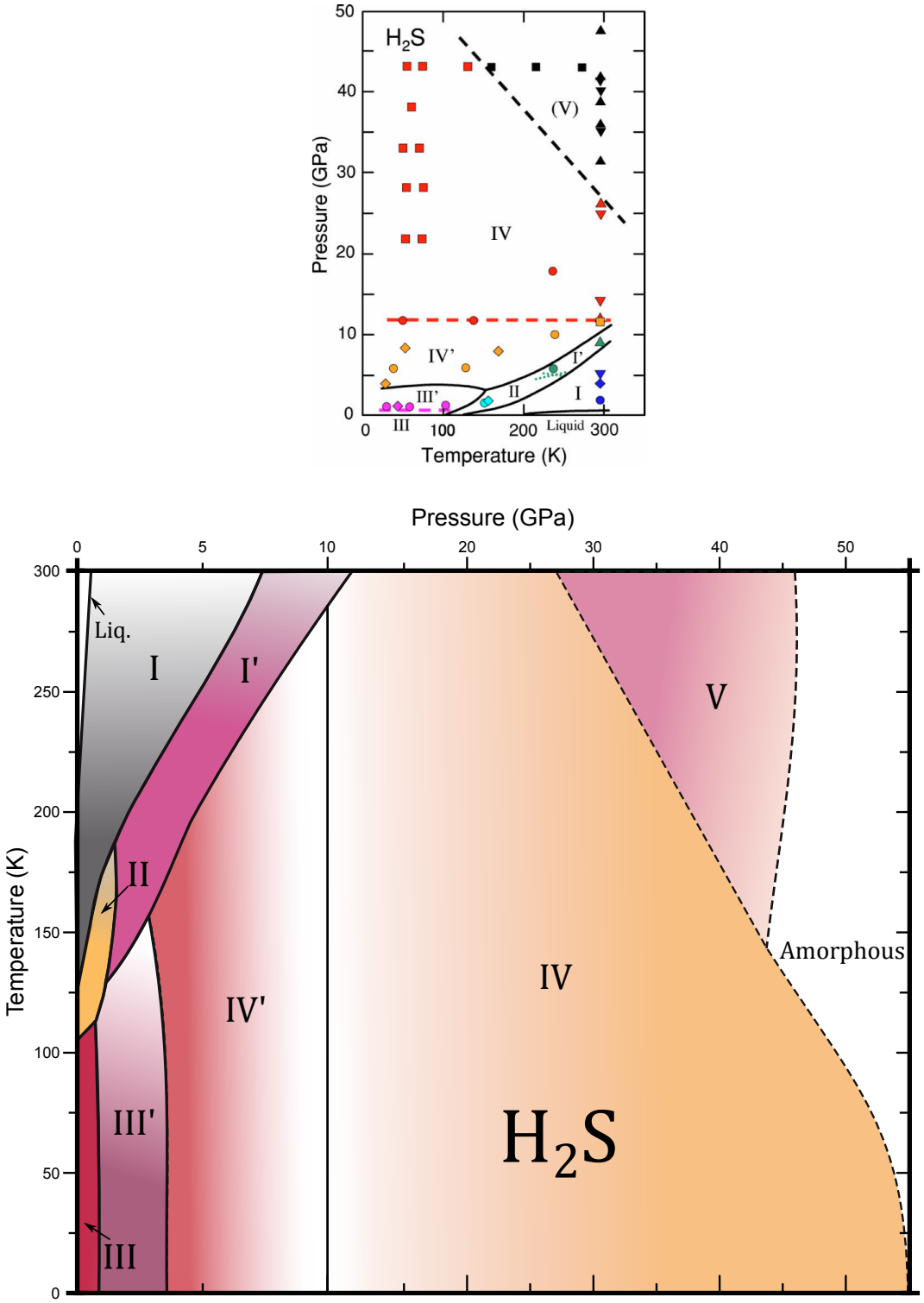

Figure 4.1 (above) Formerly most recent phase diagram of H_2S, from Fujihisa *et al.* (2004) [38] (below) An up-to-date approximate thermodynamic/kinetic phase diagram of H_2S, amalgamated from data obtained in this study and references [38, 79, 80]. Solid lines indicate phase boundaries; dashed lines indicate kinetic boundaries, irreversibly crossed on compression.

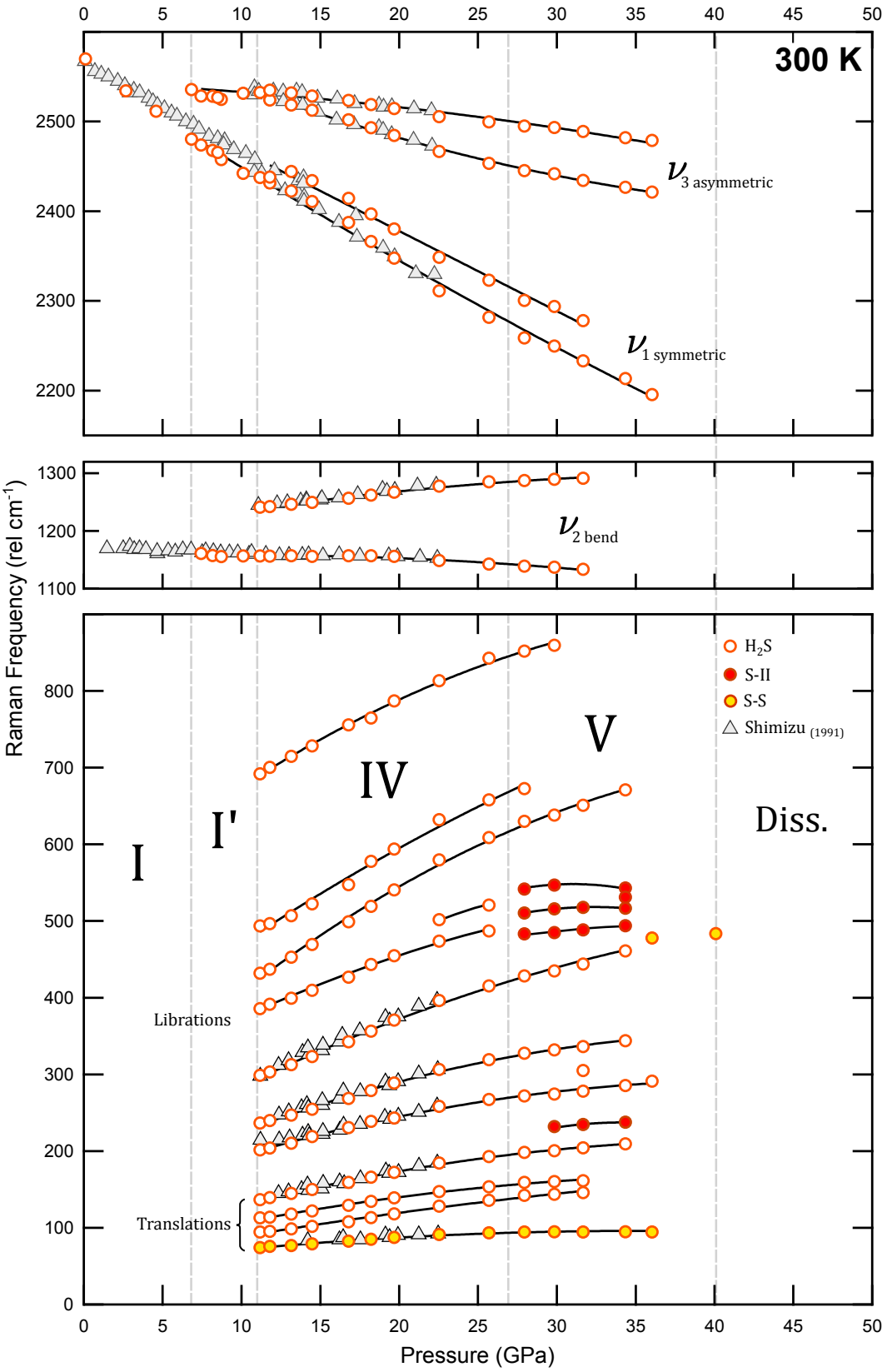

Figure 4.2 Observed Raman excitation frequencies of pure H_2S plotted as a function of pressure, at 300 K. Orange circles are data obtained in this study, filled circles refer to excitations corresponding to sulfur-II (red) and S-S bonds (yellow). Filled grey triangles are replotted from reference [81]. Black lines are intended as guides for the eye.

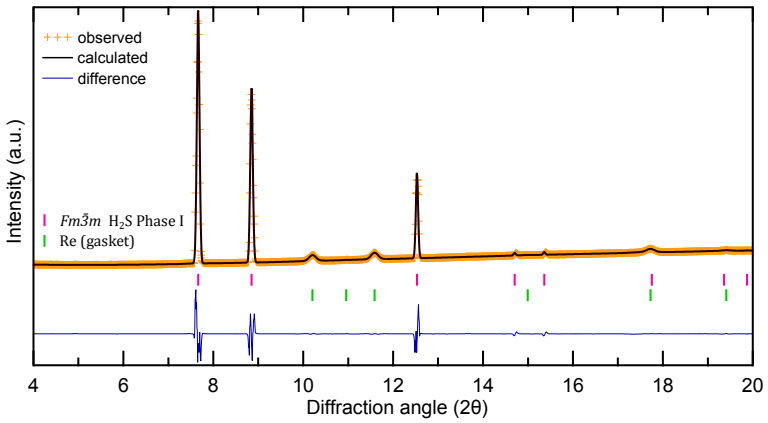

Figure 4.3 Observed diffraction pattern (orange +), Le Bail fit (black) and difference plot (blue) for a single crystal of phase I H_2S (1.1 GPa, 300 K) fitted with $Fm\bar{3}m$ symmetry, a = 5.5025(6) Å.

4.2 Ambient Temperature

4.2.1 Fluid - Phase I

The S-H stretching mode of fluid H_2S at 0.11 GPa was observed at 2569 rel cm^{-1} in agreement with literature data [81, 82]. Fluid H_2S froze between 0.4 and 1.1 GPa, forming phase I. At 1.1 GPa Phase I exhibited a single stretching mode at 2540 rel cm^{-1}, comprising convoluted ν_1 symmetric and ν_3 asymmetric stretches, which softened at a rate of -9.9 cm^{-1}/GPa upon compression. XRD data collected at 1.1 GPa from a synthesised sample of H_2S indexed readily to $Fm\bar{3}m$ (a = 5.5025(6) Å) in agreement with previous studies (Figure 4.3) [83, 84].

Phase I of H_2S is cubic, composed of face-centred cubic (fcc) S atoms, with rotationally disordered S-H bonds. Hydrogen bonding (H-bonding) between neighbouring H_2S molecules limits the S-H bond rotational disorder to 12 equally probable, evenly distributed orientations. The average H-S-H bond angle of 92.2° is maintained whilst the H atoms perpetually reorient themselves. A previous study demonstrated with Brillouin spectroscopy that rotational-translational coupling occurs in phase I [85]. Upon compression of phase I, the degree of rotational-translational coupling was shown to decrease as the strength of H-bonding increases, confirming the orientational disorder is limited rather than completely disordered. Stronger H-bonding is also evident from the softening of the $\nu_{1,3}$ stretching modes. Despite the contraction of the unit cell, each S-H bond lengthens to reflect an increase in charge transfer to neighbouring S lone pairs.

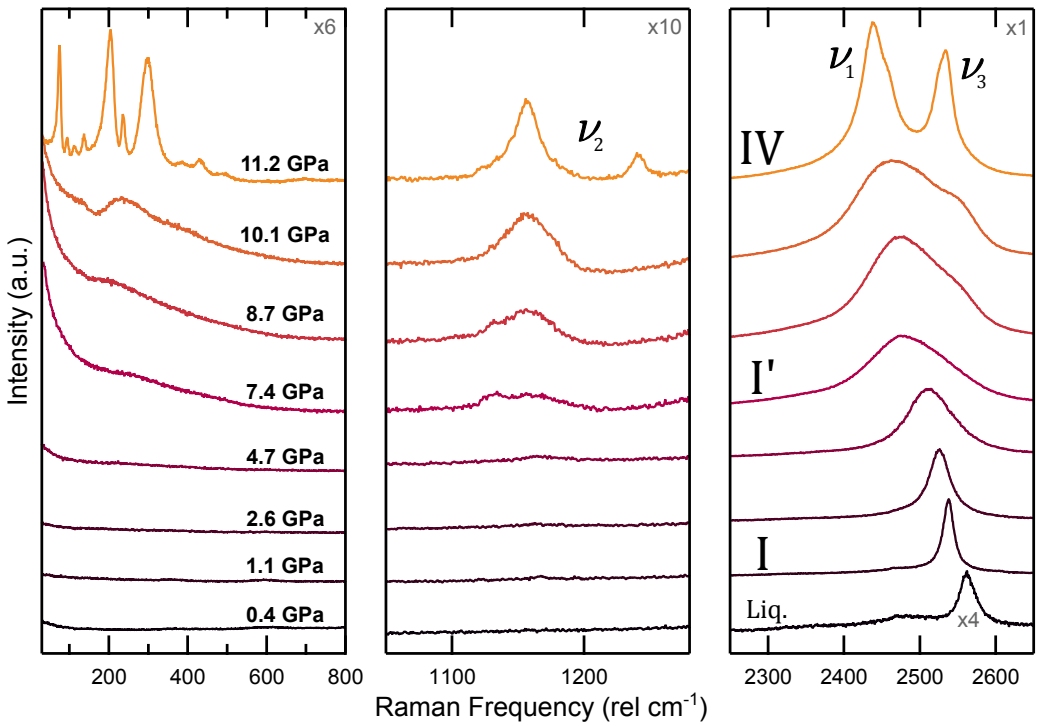

Figure 4.4 Representative Raman spectra of pure H_2S (phases I - I′ - IV) as a function of pressure, at 300 K. Relative scales of each panel are indicated top right.

4.2.2 Phase I′

Phase I′ was identified from 7.44 GPa, slightly below the literature transition pressure of 8 GPa [84, 86]. The phase change was recognised when the convoluted stretching excitation became asymmetric; ν_1 and ν_3 become non-degenerate, with ν_1 exhibiting a higher intensity (Figure 4.4) congruent with previous studies [79, 81]. The Raman spectrum of phase I′ is essentially identical to phase II. Both phases possess hindered rotational disorder, but phase I′ adopts a primitive S lattice ($P2_13$) whereas phase II remains face-centred ($Pa\bar{3}$) [83, 84, 86, 87]. The transition to phase I′ is characterised by a reduction from 12 to 6-fold orientational disorder, about the $\langle 1\,1\,1\rangle$ axes [86, 88]. The H-bonds consolidate further, driving the structural change from face-centred → primitive cubic, reducing the number of nearest neighbours and limiting the possible orientations of each S-H bond.

At 7.44 GPa, a weak ν_2 bending mode emerged at 1161 cm^{-1}, in contrast to the data presented by Shimizu *et al.* who detect ν_2 from 1.5 GPa (Figure 4.2). Additionally the low frequency region developed broad contours indicative of librational motion of the S-H bonds, which arises as a consequence of the increased H-bond strength [88, 89]. The rotations becomes more hindered with

lower interatomic distances, and charge transfer between an H-bonded (H---:S) pair becomes greater. This increases the time that each S-H bond spends in a given orientation, and the lifetime of the librational excitation becomes longer allowing it to be detected above the background noise.

Upon compression the convoluted stretching modes continue to soften, as H-bonding increases (ν_1 = -11.5, ν_3 = -5.7 cm^{-1}/GPa respectively). The assignment of stretching symmetry is based on the disparity in these $\frac{d\nu}{dP}$ values; A C_2v asymmetric stretch is less influenced by H-bonding than its symmetrical counterpart which is reflected by the reduced softening on compression [81, 89]. The frequency of the ν_2 mode remains close to constant, as the bending motion is perpendicular to the direction of the H-bonds and thus unaffected. The librational mode around 200 cm^{-1} continues to strengthen and gains intensity up to the transition to phase IV at 11 GPa.

4.2.3 Phase IV

Phase IV was detected from 11.2 GPa in excellent agreement with literature data [81, 84]. The abrupt transition exhibits a distinct splitting of the ν_1 and ν_3 modes into two separated, convoluted pairs around 2435 and 2530 cm^{-1} respectively (Figure 4.4. The ν_2 bend becomes sharp and splits to 1157 and 1241 cm^{-1} respectively. A number of strong lattice modes appear below 400 rel cm^{-1} at the transition, ostensibly translational and librational modes.

It is widely accepted that the transition to phase IV is also driven by strengthening H-bonds. However, there are several different interpretations of the phase IV model. The two experimentally determined structures are an orientationally ordered orthorhombic lattice ($I4_1/acd$, Figure 4.5) [86], where S-S bonds form spiral chains along the c-axis, and an orientationally disordered monoclinic lattice (Pc) where S-S bonds are arranged in branched chains [91]. Both structures embody S lattices marginally dislocated from fcc, like phase I′. Theoretical studies have advocated both orientationally ordered ($Ibca$ [41], $Pbca$ [92]) and disordered models ($I4/mmm$, [93]).

The Raman data suggest that the rotational disorder observed in phases I and I′ ceases in phase IV [79, 81]. Limiting molecular orientation explains the distinct splitting of ν_1 and ν_3, and the sudden appearance of sharp translational

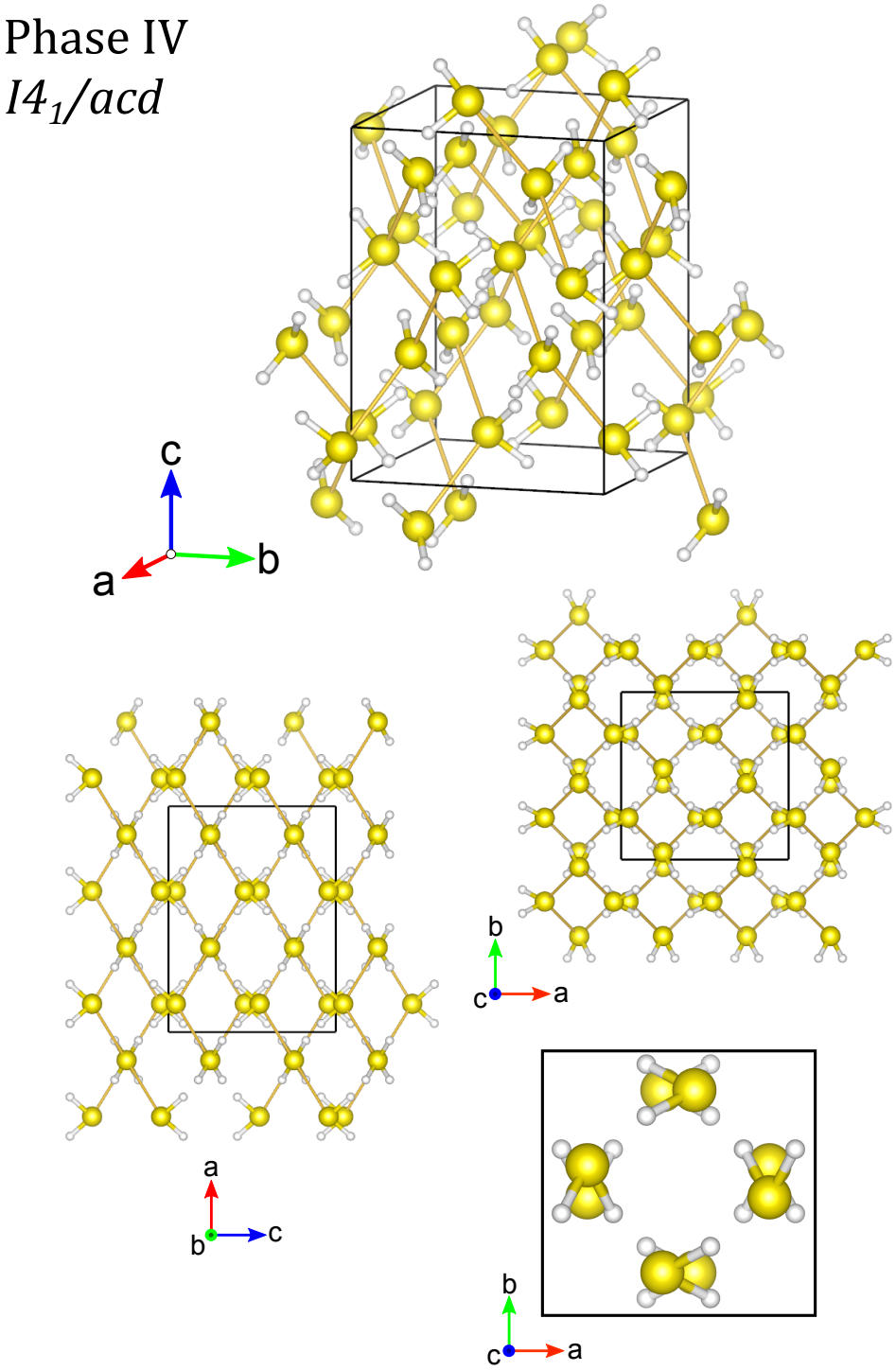

Figure 4.5 Representation of the structure of H_2S phase IV; modelled using VESTA [90] with $I4_1/acd$ symmetry at 14 GPa, adapted from reference [86]: Large yellow spheres (S), small white spheres (H). Thin yellow bonds (S-S). S-S bonds develop upon compression of phase IV, resulting in spiral S-S chains along the *c*-axis, joined by hydrogen bonds

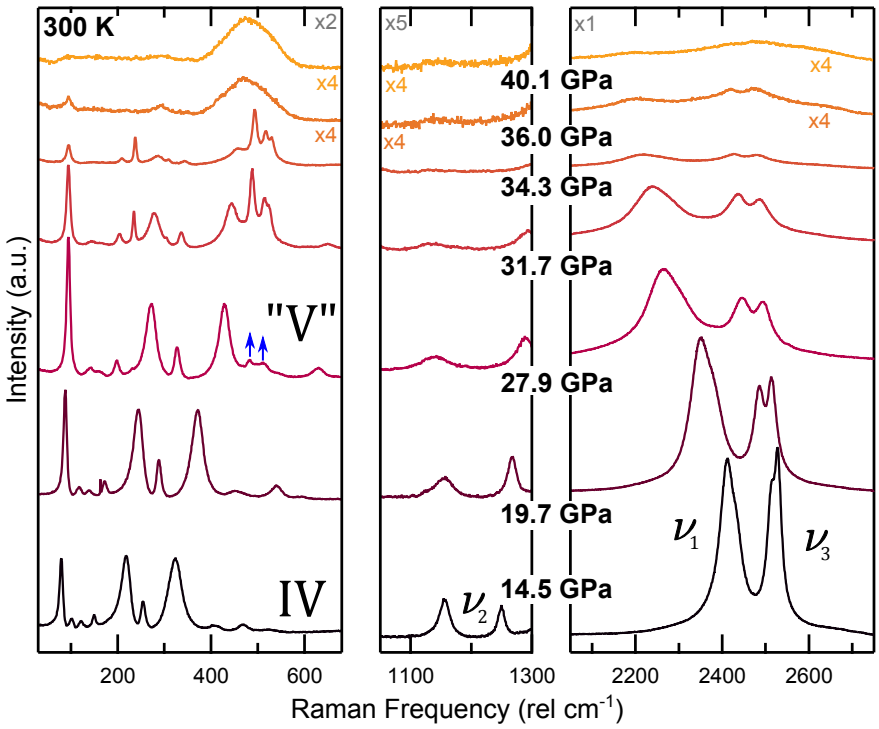

Figure 4.6 Representative Raman spectra of pure H_2S (phases IV - V - Amorphisation) as a function of pressure, at 300 K. Blue arrows indicate elemental S-II peaks which signify crossing the kinetic boundary to "phase V", where H_2S partially decomposes. Relative scales of each panel are indicated top right; individually scaled spectra are labelled.

lattice modes. It is difficult to precisely assign lattice modes to a particular motion, but the narrow bandwidth of the lowest frequency excitation suggests it is a translational mode from an orientationally ordered structure. The sharp peak profile, low frequency and low $\frac{d\nu}{dP}$ distinguish this mode from the others (Figures 4.2 and 4.6). Given this, the translational vibration of spiral S-S chains along a single axis would be a valid assignation. A comparison of the peak profiles, frequencies and $\frac{d\nu}{dP}$ of the remaining low frequency excitations allows the next three lowest frequencies to be assigned to additional translations, and the remainder as librations.

Both ν_1 and ν_3 pairs continue to separate upon compression. The splitting of the ν_3 pair was more distinct than the splitting of the ν_1 pair. For the ν_1 pair the lower frequency component was the most intense, whilst the opposite is true for the ν_3 pair. The splitting of the stretching modes into pairs is explained well by the experimental and theoretical models exhibiting orientational order [41, 86]. The experimental model for $I4_1/acd$ is shown in Figure 4.5: alternating rows of two orthogonal H_2S environments are seen when viewed down any axis.

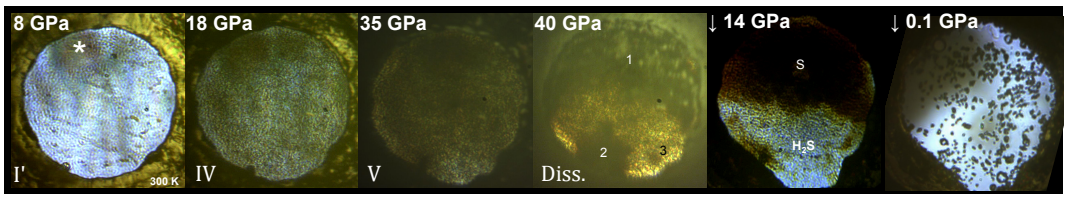

Figure 4.7 Photomicrographs of pure H_2S upon compression and decompression. Region 1: sample was exposed to prolonged high intensity laser exposure (200 mW). Region 2: 10 s exposure (5 mW). Region 3: two successive 1 s exposures (5mW) (Spectra 1 and 2 respectively in Figure 4.8). * indicates dirt on the back of the diamond, not darkening of the sample.

It can be concluded that the model proposed by Fujihisa *et al.* shown in Figure 4.5 is most representative of the experimental data obtained in this study [86]. Despite disagreements regarding dynamic behaviour, the theoretical literature largely finds the formation of S-S bonds favourable in phase IV [40, 41, 92–94].

4.2.4 Phase V – Amorphisation & Decomposition

Results

For consistency, herein *amorphisation* refers to the adoption of an amorphous state, which could also involve breaking and reforming bonds, *dissociation* refers specifically to molecular dissociation, (i.e. no covalent bonds are broken but intermolecular order diminishes), *decomposition* refers only to the breaking of covalent bonds. As the 532 nm green laser is appreciably energetic, it should be noted that amorphisation pressures are slightly lower than the literature.

The transition to phase V occurred by 27.9 GPa, signified by the appearance of excitations corresponding to elemental sulfur-II (Figure 4.2), in accordance with previous studies [95, 96]. The S-II peaks gained intensity upon compression, whilst all other spectral features diminished rapidly indicating partial decomposition and dissociation respectively. Above 35 GPa the S-II peaks also suddenly weakened. By 40 GPa the spectra was composed of a single broad excitation around 475 rel cm^{-1}.[†] A comparable broad feature at 475 rel cm^{-1} was observed upon compression of D_2S in previous studies [37, 39], therefore it is assumed to arise from the formation of an S-S bond and the adoption of an amorphous state. It is not strictly linked to decomposition as some S-H bonds may be retained.

[†]300 μm diamond culets limited the highest pressure in this particular study to 40 GPa. In order to obtain decompression data, further compression was not risked.

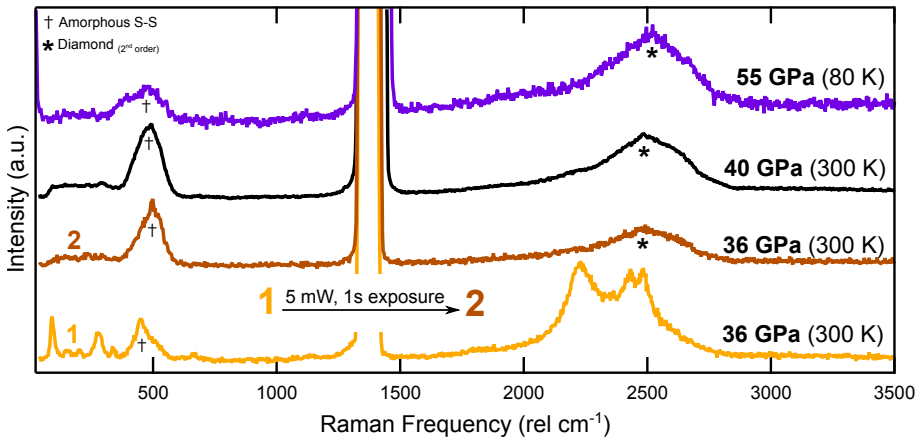

Figure 4.8 Raman spectra of dissociated samples of H_2S at different pressures and temperatures. Spectra 1 was obtained after 1s of exposure in an untouched region (region 3, Figure 4.7). Spectra 2 was obtained in the same position, immediately after the first 1 s exposure, demonstrating the rapid dissociation and formation of amorphous sulfur. * indicates the second order diamond phonon, not to be confused with an S-H bond.

The sample became photosensitive above 35 GPa; the sample darkened after a few seconds of laser exposure and spectra resembled the largely featureless plots shown in Figure 4.8. Spectra 1 in Figure 4.8 demonstrates that structurally ordered H_2S was still present at 35 GPa – obtained after focussing on a lighter, untouched part of the sample, with reduced laser power (20 $\rightarrow$ 5 mW) and exposure time (10 $\rightarrow$ 1 s). Spectra 2 was obtained after a subsequent 1s exposure in the same (now darkened) position, which only exhibited the broad S-S excitation around 475 rel cm^{-1}. At 40 GPa, 1s exposures in untouched regions of the sample produced the third spectra shown in Figure 4.8. Figure 4.6 shows the relative mode intensities before and after amorphisation. A previous combined IR and Raman study of H_2S found evidence of H-bonding and the presence of S-H stretching modes up to 46 GPa [36], so it is assumed that the higher energy green laser accelerated the amorphisation. It is interesting that at 80 K, S-II was not observed at all, but the spectra above 50 GPa showed the same broad S-S feature (Figure 4.8). Low temperatures may stabilise H_2S against decomposition but not amorphisation.

On decompression, the spectra of the dark regions showed the broad S-S feature which partially transformed to S-II and S-I. H_2 was only detected in areas which had been exposed to substantial laser power, in the form of $(H_2S)_2H_2$, which is discussed in section 7.5, on mixtures of H_2S and $(H_2S)_2H_2$. The broad excitation at 475 rel cm^{-1} is therefore assigned to amorphous sulfur, or an amorphous sulfur-hydrogen compound which decomposes on decompression. Similar observations were made in previous studies [37, 38]. Pure sulfur was

detected upon decompression of every single experimental run of both pure H_2S and $(H_2S)_2H_2$ that exceeded ∼40 GPa, showing that some decomposition occurs on decompression even when using lower energy red excitation wavelengths. The final picture shown in Figure 4.7 shows pure S-I crystals suspended in H_2S at 0.1 GPa. Interestingly, molecular H_2 was only detected faintly after intense irradiation (200 mW). H_2 has only been reported to form from H_2S after laser-heating at similar conditions [97]. An earlier study reports no evidence of the H_2 vibron after an hour accumulation at 48 GPa (1 mW, Ar^+ laser) [38]. It is clear that pressure induces dissociation and the adoption of an amorphous state, and promotes formation of S-S bonds but it cannot be said with certainty that the S-H bonds are decomposed by pressure alone. H_2 only seems to be observed when samples are subjected to significant laser power.

Discussion

The structural nature of phase V is still widely disputed in the literature, although it is clear that H_2S becomes increasingly unstable upon compression above 27 GPa, and partially decomposes to S-II. Stronger H-bonding is associated with a progressive lengthening and weakening of the S-H bond. The formation of S-S bonds in phase IV are likely to aid molecular dissociation and decomposition; indeed pure S forms spiral chains at these pressures. The first experimental evidence reported for phase V was a change in colour from yellow to black above 27 GPa, and the appearance of new diffraction peaks [95]. The colour change was associated with bandgap closure of phase V, but a theoretical study suggested the change in colour arises from S, which has been confirmed by the observations made in this study. H_2S has also been shown to turn metallic at 96 GPa, which is very close to the metallisation pressure of pure S [36].

Although the structure of phase V has never been resolved experimentally there have been several theoretical propositions: Rousseau *et al.* posit an orthorhombic lattice ($Pmn2_1$) where protons dynamically fluctuate between charged species SH_3^+ and SH^-; they also find an orthorhombic phase (VI) above 65 GPa, composed of sheets of S atoms with $Cmc2_1$ symmetry. Wang *et al.* describe phase V with a hexagonal lattice of $P63/mmc$ symmetry, where H atoms are labile and S-H bonds rotationally disordered [41], whereas simulations performed by Duan *et al.* find a monoclinic lattice above 27 GPa with Pc symmetry [98]. There are merits and flaws with all of the aforementioned studies, but there is little to be

said conclusively about the structure of phase V in relation to experimental data, despite the additional diffraction peaks observed by Endo *et al.*. Based on the data it seems phase V is not structurally distinct from phase IV. The less defined lattice modes could indicate an increase in orientational disorder which would distinguish it from phase IV, however the "transition pressure" may simply be the point where the H_2S molecules in phase IV begin to dissociate or partially decompose. Additionally the partial decomposition into S-II is apparently not reversible, therefore Phase V should not strictly be called a phase as the boundary is kinetic (Figure 4.1).

A more interesting discussion regards the nature of H_2S above 40 GPa. It seems that amorphous S is obtained above 40 GPa regardless of laser power and exposure, although it is worth mentioning that the sample only seems to turn completely black where it has been irradiated (See Figure 4.7). It is also curious that H_2 was only observed after intense laser exposure whereas amorphous sulfur was ostensibly observed after any low power irradiation. Several potential theories arise from these observations:

- H_2S decomposes straight into amorphous S + molecular H_2 upon compression. Most of the H_2 either forms a hydride with the gasket material, or it has also been proposed that H_2 could become included in either the diamond or S lattices [38]. Intense laser exposure produces a sufficient excess of H_2, which can then be detected.
- The black compound is an amorphous S-H compound, which then decomposes to S + H_2 after intense irradiation. This is related to a proposition that S forms an atomic lattice, which fosters H atoms within the interstices, as this would likely produce a similar Raman spectra [36].
- H_2S remains structurally coherent above 40 GPa, explaining why it does not turn black upon compression alone, but it becomes so delicate and sensitive that any exposure instantly causes dissociation or decomposition (including exposure to synchrotron radiation). It would be difficult to clarify experimentally if EM probing actually causes the change. To the authors knowledge no experiments have been performed where H_2S has been compressed above 50 GPa without any exposure to laser or x-ray photons; this experiment may be worth performing if resources were more expendable. Although, H_2S certainly becomes black on compression near the metallisation pressure.

More recently, the formation of alternative H_xS_y stoichiometries have been proposed; although it is important to considers these theories within a slightly wider context, which is worth discussion. The experimental measurement of high T_c superconductivity in the hydrogen-sulfur system (T_c = 203 K at 155 GPa) [28] was preceded by two theoretical studies: Li *et al.* found that H_2S formed units of H_3S-SH_3 above 80 GPa, (T_c = 80 K, 160 GPa) [22], then Duan *et al.* studied the $(H_2S)_2H_2$ system (stoichiometrically H_3S) and found another superconducting H_3S phase (T_c = 204 K, 200 GPa). Immediately after Drozdov *et al.* published the experimental study, papers came out from both Li (Y. Ma group) and Duan (T. Cui group) advocating the stability of many alternative stoichiometries above 25 GPa (e.g. H_3S, H_2S_3, H_3S_2, HS_2, H_4S_3), which all form as a consequence of the pressure driven decomposition of H_2 into S and H_2 [98, 99]. H_3S_5 and H_5S_8 have also been experimentally proposed but XRD data was low quality and inconclusive [97]. Whilst the formation of alternative stoichiometries explains the lack of H_2, one would expect to see some variation in Raman activity between compounds, yet all Raman studies from this thesis and the literature exhibit the same featureless spectrum above ∼50 GPa. Although the behaviour of H_2S at high pressures is clearly complex, currently there is not sufficient experimental evidence to advocate the formation of many (albeit-metastable) molecularly distinct stoichiometries; more likely is the formation of amorphous sulfur-hydrogen compounds which would have widely varying local stoichiometry.

Despite the exhaustive list of potential structures and mechanisms, there are ultimately few firm conclusions to draw. It can be said that dissociation to an amorphous state is an inevitable consequence of compression, which is accelerated by intense laser irradiation, and probably also synchrotron radiation. The following mechanism is proposed, based on all previous observations: on compression of phase IV, S-S bonds progressively form spiral axial S-S chains along the *c*-axis of the H_2S lattice. Upon reaching 27 GPa (Phase V) the H-bonds are elongated such that the H atom is almost midway between the two S atoms involved, resulting in much weaker orthogonal bonding between the chains. Given that theory finds large fluctuations in atomic positions,[40, 93] it is plausible to imagine that two S:---H---:S configurations could come into sufficient proximity that the two weakly bonded H atoms could spontaneously combine to from an H_2 molecule, and an S-S bond is forged between the two previously H-bonded S atoms. This would likely not occur in an ordered manner and could result in an

amorphous S lattice potentially trapping molecular H_2 (or even H atoms) within the interstices. Some S-H bonds may also be retained resulting in an amorphous sulfur-hydrogen compound. Then perhaps the S atoms are forced into an ordered metallic array upon compression to very high pressures. On decompression, some of the amorphous S adopts the S-II and S-I configurations, whilst the rest remains amorphous which could still contain interstitial H atoms.

4.3 Low Temperature

At ambient pressures H_2S exhibits three low temperature phases: rotationally disordered cubic phase I condenses below 188 K ($Fm\bar{3}m$); phase II is formed at 126 K, also cubic and disordered ($Pa\bar{3}$); phase III finally forms below 104 K, and is tetragonal and completely ordered ($Pbcm$). [82, 83, 87, 100–104]. These temperature driven transitions are akin to the pressure driven phase transitions, where strengthening H-bonds causes a sequential lowering of rotational disorder and symmetry. Phase III′ is reported on compression of phase III above 1 GPa ($<$ 100 K) [38], purportedly forming chains of S atoms along the c-axis, as in phase IV. Pressures of 4-10 GPa yield a very similar structure known as phase IV′ [38, 89]. An approximated phase diagram is presented in Figure 4.1, compiled from the literature and data obtained in this study.

4.3.1 Phase IV′

One low temperature run was performed with pure H_2S. H_2 was cooled from 300 $\rightarrow$ 80 K at 6.4 GPa, with a modest pressure increase to 7.0 GPa. This was found to follow the isotherm covering phases I – I′ – IV′. It is unfortunate that data was not obtained for phases II, III and III′, but cryoloading to low pressures can be challenging, as pressure tends to increase upon warming. The transition from phase I – I′ occurred between 260 and 230 K at $\sim$6.5 GPa, and phase IV′ was adopted between 160 and 180 K, both as expected. The spectra of phases II and III′ upon cooling are appended in Figure A.1. The transition from phase IV′ to phase IV occurred between 8 and 15 GPa, also in accordance with previous studies [38].

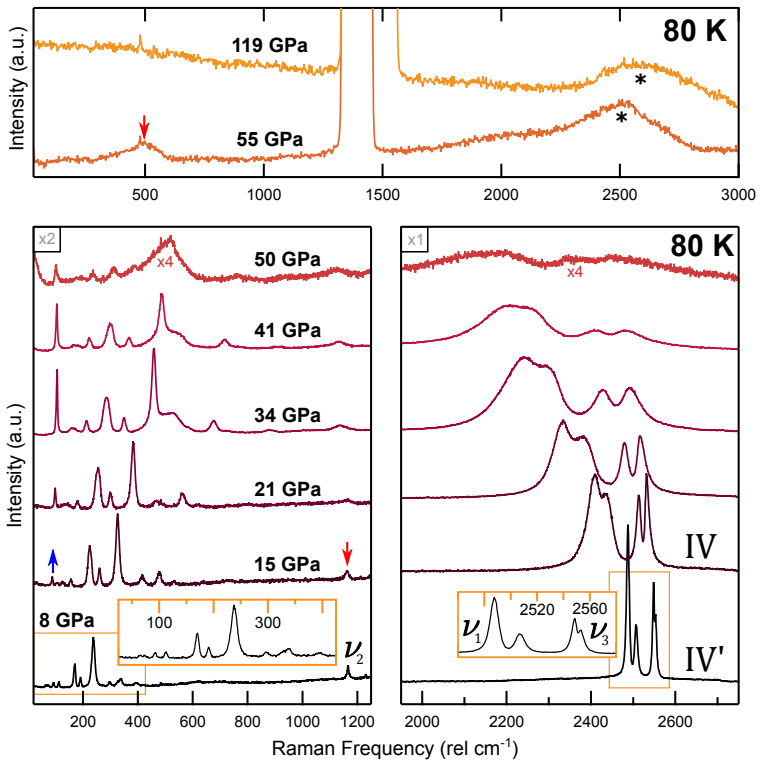

Figure 4.9 Raman spectra of pure H_2S (phases IV′ - IV) as a function of pressure, at 80 K. Relative scales of each panel are indicated in the top left. The blue arrow indicates emerging excitation from S-S chains. * indicates 2^{nd} order diamond phonon.

The splitting between of two ν_1 stretches is more pronounced in phase IV′ than in Phase IV, whilst the opposite is true for the ν_3 stretches (Figure 4.9). The bending mode in phase IV′ is far sharper suggesting less intermolecular interaction, which is plausible given the lower density. The lattice modes are also very similar; although an additional narrow, sharp mode emerges on entering phase IV, at a lower frequency than all other lattice modes (indicated on Figure 4.9). This was concluded to be a translational lattice mode arising from the formation of axial spiral S-S chains in phase IV at 300 K. This phase IV peak at 80 K exhibits the same behaviour upon compression; the frequency does not change drastically and the peak remains sharp. Given the similarities in the spectra and reported structures of phases IV′ and IV [38, 86], the difference between them could simply be the formation of the S-S chains. Fujihisa *et al.* report the formation of S-S chains in both phases III′ and IV′, but base their assumption on interatomic distances. In their previous study they posit that S-S bonds form in phase IV when the S-S interatomic distance becomes smaller than the constant energy radius of sulfur (2.92 Å [105]), but from their own structural data the S-S interatomic distances for phases III′ (3.65 Å) and IV′ (3.41 Å) respectively are above this value. Theoretical studies of the phase III – III′ transition also find the

formation of S-S bonds unfavourable at these conditions [94]. Spectroscopy data from this study suggests that the chains only form upon entering phase IV. This is conceivable, given that the chains seem to form gradually upon compression of phase IV at ambient temperature, and do not appear to develop immediately.

4.3.2 Amorphisation

Phase IV behaved exactly as at ambient temperature upon compression, except that the peaks pertaining to S-II (and phase V) are not observed. The stretching modes redshifted while the lattice modes blueshifted on compression; amorphisation occurred from 50 GPa, where the intensity of all peaks diminished. As no crystalline S was observed it cannot be certain that decomposition took place. The broad peak around 475 rel cm^{-1} corresponding to amorphous sulfur (or amorphous sulfur-hydrogen) was the only observable feature of the spectrum around 55 GPa, bar a very broad and weak peak around 2000 rel cm^{-1} suggesting that some S-H covalent bonds partially remain. This feature and the intensity of the amorphous peak suddenly dropped between 61 and 68 GPa, and no evidence of either peak was detected above 87 GPa. The sample became visibly light and reflective above 90 GPa, which increased the background noise of the Raman spectra. Although the S-S peak could have become smothered by background noise, it is well established that S (and H_2S) metallises above 90 GPa, which would also result in the peak disappearing [36, 106, 107]. No other changes to the spectra occurred up to 120 GPa. No changes to the spectra occurred during the following temperature cycles: 80 ↑ 300 ↓ 80 ↑ 300 K.

It is interesting that the amorphisation of S occurs with pressure at 80 K, despite the lack of direct decomposition. The formation of crystalline S would be expected to give sharp modes in all non-metallic phases [108]. Therefore the amorphisation is described only in the context of dissociation. The drop in intensity of the amorphous mode above 61 GPa could correspond to the sample starting to become metallic. Phase VI of H_2S has been proposed in a theoretical study to form above 50 GPa, composed of sheets of S atoms with H trapped in between, which is another consideration [40]. As with the ambient temperature behaviour of H_2S above 46 GPa, little can be said with any conviction other than the fact that a similar amorphous phase seems to be adopted above 55 GPa at 80 K.

4.4 Conclusions

Phase I – IV transitions are driven by H-bonding, resulting in a progressive lowering of rotational disorder and symmetry. Given a thorough literature review and data obtained in this study, the $I4_1/acd$ model of phase IV is selected as the best structural candidate [86]. The sharp lattice mode appearing at 74 rel cm^{-1} at 11.2 GPa (300 K) is thought to arise from the translational movement of spiral S-S chains as they form along the *c*-axis. These S-S chains are found not to form in low temperature phases III' and IV', as previously suggested [38]. Ambient temperature Phase V is not a distinct phase in its own right as previously thought, and simply where phase IV begins to dissociate. It is clear that partial decomposition always occurs at 27 GPa (the phase V transition pressure in the literature [95]) so the boundary is considered kinetic, on compression. This partial decomposition is not observed at low temperature, where phase IV H_2S appears to simply dissociate to an amorphous state on compression. The mechanism for dissociation and amorphisation is suggested to arise from the progressive pressure driven H-bonding between the S-S chains. This elongates the S-H bonds and eventually results in spontaneous formation of H_2 from two weakly bonded H atoms, joining the S-S chains at different points along their length resulting in an amorphous structure. This process appears to be accelerated by interaction with the excitation laser. Whether this would occur purely from compression remains to be seen; a desired future study would involve low intensity transmission measurements at ambient and low temperatures, to determine exactly where transmission ceases.

Chapter 5

Direct Synthesis of Hydrogen Chalcogenides at High Pressure

5.1 Introduction

Hydrogen chalcogenides can be synthesised at ambient pressure by heating elemental solid X (where X = S or Se) in the presence of H_2 [109, 110]. This method is one of several used for large scale production of H_2X gases. Here the direct synthesis of H_2X has been achieved within pressure cells by sequentially loading solid X (where X = S or Se) then gas-loading H_2, before heating the reactants to produce H_2X (and excess H_2). *In situ* syntheses of H_2X compounds within DACs are beneficial for several reasons. Firstly, it is far safer and simpler than cryo-loading the toxic gases directly, although this method was used to study pure H_2S (Chapter 4). Additionally, starting from X and H_2 facilitates rudimentary control over the resultant ratio of H_2X:H_2. This is advantageous for producing cocrystals of $(H_2X)_2H_2$, a primary focus of this thesis. The alternative preparation of $(H_2X)_2H_2$ requires sequentially cryo-loading H_2X then gas-loading of H_2 [46], offering a low success rate with little-to-no control over stoichiometry. Furthermore *in situ* syntheses generally produced single crystals of H_2S and H_2Se, whereas cryo-loaded H_2S tends to be a poor powder.

This chapter details the synthesis of H_2S, H_2Se and the attempts at synthesis of the elusive H_2Te. Aside from being practical, several interesting observations and discoveries arose during the development of the *in situ* method. The first section

is the most comprehensive and concerns *in situ* synthesis of H_2S. A reaction mechanism is proposed, and techniques for influencing the nature of the sample discussed. The next section details the correspondent syntheses of H_2Se samples. Finally, unsuccessful attempts to synthesis H_2Te are described with potential alternatives for future work.

All loading techniques are described in full in section 3.2. Solid reagents were obtained from *Alfa Aesar*: crystalline sulfur (99.998%), grey selenium powder (-100 mesh, 99.99 %) and tellurium powder (-200 mesh, 99.999%), were used with purity determined on trace metals basis. High purity research grade H_2 gas was obtained from *BOC* (99.99999 %). Heating for synthesis was performed using a *Heidolph* MR magnetic stirrer-hotplate with a digital readout. Temperature measurements on cooling were made using a *UKAS* calibrated thermocouple held in contact with the diamonds, whilst visually observing the sample through a microscope. Raman experiments referred to in this chapter were performed using Ar^+ ion (514 nm) and Kr^+ ion (647 nm) excitation wavelengths. For brevity, experimental Raman data is confined to chapters 6, 7 and 8. XRD and laser-heating experiments were performed at SPring-8, beamline BL10XU with a monochromatic beam of 0.4136 Å. Pressures were measured using Ruby fluorescence calibrated to universal standards [66, 78].

5.2 Synthesis of Hydrogen Sulfide

5.2.1 Reaction

The reaction between H_2 and S was found to occur spontaneously at 0.2 - 0.4 GPa and 300 K, although very slowly. At 0.2 GPa and 300 K, S suspended in fluid H_2 visibly reduced in size after 11 days, whilst pressure drifted up to 0.4 GPa (Photomicrographs appended in Figure A.2a). The rounding of the solid edges are reminiscent of dissolution, however, no S stretching modes were detected within the H_2 media by Raman spectroscopy. Although no H_2S was detected in the Raman spectra either, the fluid H_2S stretching mode is sufficiently weak and could be masked by the second-order diamond phonon. The multiple stretching modes of α-S are very intense and would likely be detected if S had simply dissolved; solid α-S comprises stacked 8-membered rings, which would retain their cyclic molecular structures upon dissolution [111]. Therefore it was assumed that H_2S

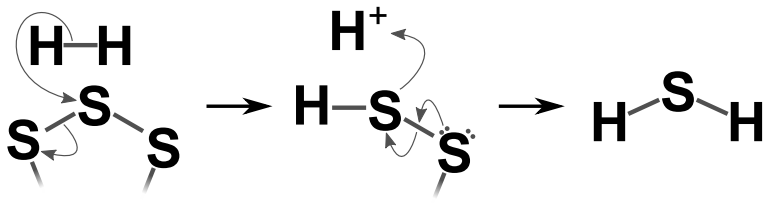

Figure 5.1 A proposed 'curly arrow' synthesis mechanism for the reaction between αS rings and H_2, where arrows indicate the movement of electrons (or rather electron density) as atomic bonds are broken and formed. Double dots represent electron lone pairs.

forms spontaneously, and the reaction is thermodynamically favourable at room temperature from 0.2 - 0.4 GPa.

Heating to 333 K at 0.2 GPa for 12 h significantly improved the reaction rate, confirmed by the fluid H_2S stretching mode in the Raman spectrum around 2600 rel cm^{-1} (Spectra is shown in Figure 7.1), but did not promote a complete reaction between S and H_2. Approaching the melting point of S[†] significantly improved the rate of reaction. 373 K was established as the minimum optimal temperature for promoting complete reaction between S and H_2 below 2 GPa, within a practical timeframe ($<$ 2 h), even when using substantial quantities of S (Figure A.2b). Raman analysis shows the transparent samples at 373 K to be a fluid mixture of H_2 and H_2S. The mixture is homogenous and transparent, as shown in Figure 5.2a. Direct synthesis of H_2S at ambient pressure requires temperatures of 723 K [110], indicating greater efficacy under pressure. However, heating S at pressures where H_2 remains fluid was found optimal. At 8 GPa, only partial reaction between S and H_2 was observed upon heating to 453 K for approximately 3 h. These conditions are above the melt curve of H_2 [113] but far below for S, similar to 333 K and 0.2 GPa. Thus, approaching the melting point of S (whilst H_2 is fluid) seems significant to the reaction mechanism. Therefore it is postulated that the reaction is kinetically mediated: the rate at which individual cyclic α-S molecules are liberated from the bulk solid S into the fluid H_2 media is greatly increased upon approaching the melting point of S, substantially increasing the rate of reaction from classic collision theory. Figure 5.1 gives a proposed reaction mechanism, from a chemistry perspective; this is merely a representation of a concerted mechanism as the first two stages would likely occur simultaneously.

[†]At ambient pressure the melting point of α-S is 388 K, which increases sharply with pressure; approximately 620 K by 2 GPa [112].

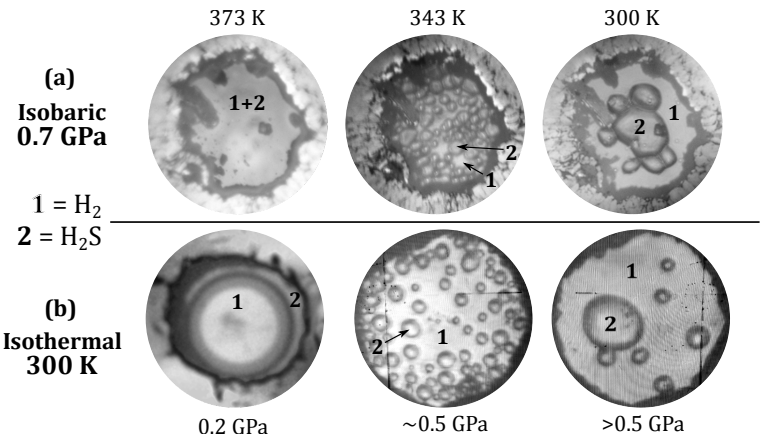

Figure 5.2 (a) Sequential photomicrographs showing isobaric (0.7 GPa) phase separation of H_2S and H_2 upon cooling from 373 to 300 K, above the solidification pressure of H_2S. (b) Photomicrographs showing isothermal (300 K) phase separation of H_2S and H_2 upon compression from 0.2 to 0.5 GPa; the images at 0.5 GPa were taken in quick succession, compression was halted at 0.5 GPa but the pressure continues to gently drift up, and H_2S crystals coalesced.

5.2.2 Phase separation

H_2S solidifies in phase I at 0.47 GPa, at 300 K [81]. Cooling down a hot solution of H_2S and H_2 below 0.5 GPa results in distinct segregation of the fluid phases, as shown in figure 5.2b. Fluid/fluid (H_2S/H_2) samples appear as a bubble of H_2 surrounded by H_2S (< 0.47 GPa, 300 K). Solid/fluid (H_2S/H_2) samples appear as a crystal of H_2S surrounded by fluid H_2 (> 0.47 GPa, 300 K). Phase separation occurred at ~323 K, on cooling a synthesised sample at 0.2 GPa. Above 0.47 GPa, phase separation occurred at higher temperatures, in agreement with the H_2S phase diagram [79, 80]. For example at 0.7 GPa, sudden phase separation was observed at ~343 K. Figure 5.2a shows how many small domains of H_2S suddenly appear as the sample cools, coalescing upon approaching room temperature. Solidifying H_2S isobarically (i.e. 373 $\rightarrow$ 300 K at 0.7 GPa) looks visually very similar to crossing the phase boundary isothermally (i.e. 0.2 $\rightarrow$ 0.5 GPa at 300 K). In the isothermal instance, the H_2 domain seems to disappear as multiple small H_2S domains simultaneously form, before coalescing into larger single crystals (Figure 5.2b). XRD data confirming phase I H_2S ($Fm\bar{3}m$) is presented in Figure 4.3, and spectra of synthesised H_2S phase I are shown in Figures 6.5 and 7.4.

Quenching

After heating, the physical nature of the samples was affected by the rate at which the hot reaction mixture was cooled. Two basic cooling techniques were employed, herein referred to as quenching (< 15 min) and slow-cooling (60-90 min). Often, phase separation was not entirely complete, and a weak H_2S signal could be detected in the Raman analysis of the H_2 region and vice versa. Generally, the rate of cooling offered some control over the extent to which this phase mixing occurred, in the synthesis of both fluid/fluid and solid/fluid samples.

Quenching was achieved simply by removing the hot DAC from the hotplate and standing it on a large block of aluminium with another block on top, to act as a heat sinks; samples reached room temperature within approximately 15 minutes, generally with little pressure increase. Cooling faster than this was deemed unnecessary, and risked unwarranted increases in pressure. Quenching was found to minimise the degree of phase mixing between fluid and solid H_2S and H_2 phases, based on relative signal intensities. A fluid/fluid sample quenched at 0.2 GPa, with minor phase mixing, showed complete separation of H_2 and H_2S phases after one week at 300 K, from Raman signals of their respective ν_1 stretching modes. This demonstrates that a fluid mixture of H_2 and H_2S is thermodynamically unstable at 300 K (0.2 GPa).

Quenching above 0.47 GPa generally produced smaller individual H_2S crystals, in greater numbers (Figure 5.2a). Quenching at 1.5 GPa caused such rapid solidification that many irregular crystals of H_2S and pockets of H_2 could be produced, such as the sample shown in Figure 5.3c. Usually if H_2S is compressed above 3.5 GPa in the presence of sufficient excess H_2 will completely form $(H_2S)_2H_2$ cocystals [46]. However, compression of irregularly crystallised samples resulted in solid mixtures of H_2S, $(H_2S)_2H_2$ and H_2. The behaviour of these mixtures at high pressures was found to deviate from that of the respective constituent systems, and the results are discussed at length in section 7.4.

Slow-cooling

Slow-cooling was simply achieved by switching off the hotplate, leaving the cell upon it and allowing it to cool to ambient temperature, which generally took 60-90 min depending on the size of the cell. Contrary to quenching, slow-cooled

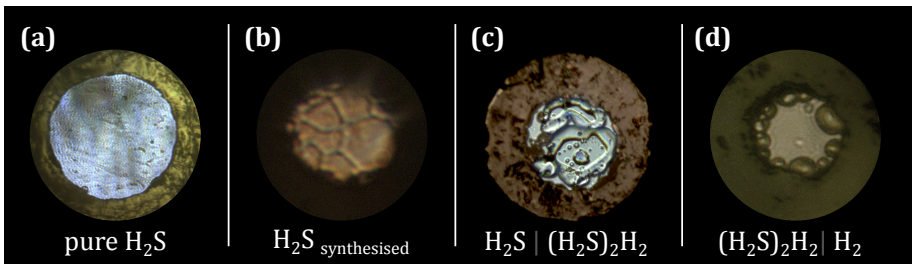

Figure 5.3 Photomicrographs of different sulfur-hydrogen sample compositions. (a) pure H_2S (b) H_2S dominant mixture ($1 < H_2$:S < 1.5) (c) H_2S:$(H_2S)_2H_2$ mixture synthesised by quenching > 1.5 GPa (d) $(H_2S)_2H_2$ (H_2:S $\gg 1.5$). All samples are shown < 2 GPa.

samples seemed to exhibit a greater degree of phase mixing, and rarely resulted in any increase in pressure. Cooling slowly above 0.47 GPa unsurprisingly tended to produce a smaller quantity of larger H_2S crystals.

Nonetheless, slow cooling also serendipitously produced intriguing results. Twice, in samples slow cooled at 0.2 GPa, a low-frequency H_2 vibron at 4140 rel cm^{-1}, characteristic of $(H_2S)_2H_2$, was observed in the fluid H_2S phase. The observation is consistent with the formation of an $(H_2S)_2H_2$ clathrate; the results are presented and discussed at length in section 7.2. A second, contrary observation was made in one of the same samples where phase mixing was significant, and a fairly strong H_2S vibron was detected in the fluid H_2 phase. The H_2S ν_1 vibron had higher frequency compared to that of the bulk H_2S fluid. Remarkably it remained within the fluid H_2 phase, and blueshifted on compression to 5 GPa, in stark contrast to the bulk H_2S. The results indicate that H_2S was somehow 'trapped' in a fluid state within the fluid H_2, above the solidification pressure of H_2S. These results are presented and discussed in section 7.3.

5.2.3 Stoichiometry Control

Stoichiometry control was qualitative and approximate, depending on the amount of S used relative to the volume of the sample chamber. The molar ratio of H_2:S can be roughly estimated from the mass of the S piece used (from size and density), the volume of the sample chamber, and the density of H_2 at the gas-loading pressure of 0.2 GPa. However, with experience a visual assessment was sufficient to produce the desired ratio of H_2:S, which have the following results:

- **(H_2:S) $\gg$ 1.5**: Most samples were prepared in this stoichiometry range, producing samples such as shown in Figures 5.2 and 5.3d. This is ideal for producing systems of pure $(H_2S)_2H_2$ on compression, surrounded by H_2.
- **1 < (H_2:S) < 1.5**: This stoichiometry range was achieved by using significantly large pieces of S (exemplified in Figure A.2b), generally producing a heavily H_2S dominant mixture of H_2S and $(H_2S)_2H_2$ (Figure 5.3b). This method was used to study "pure" H_2S, prior to the availability of cryo-loading H_2S directly, and before the effects of sample mixing were realised (see section 7.4). However, trial and error was often necessary to attain an appropriate stoichiometry, and eventually the quench method proved more effective for producing the mixtures.
- **(H_2:S) < 1**: This ratio was never prepared as S has a relatively low density, but could probably be achieved by packing the sample chamber with S before gas loading H_2.

Figure 5.3 shows the variation in sample textures between different compositions at low pressure. (a) shows 100% H_2S (powder), (b) is an H_2S dominant mixture from 1 < (H_2:S) < 1.5 (single crystals) (c) shows quenched, irregular H_2S crystals in H_2, very favourable for forming H_2S:$(H_2S)_2H_2$ mixtures (multiple single crystals), (d) H_2S with high H_2 content, (H_2:S) $\gg$ 1.5, very favourable for forming pure $(H_2S)_2H_2$ on compression above 4.77 GPa (single crystals).

5.2.4 Laser-Induced Synthesis

The spontaneous reaction between S and H_2 at 300 K can be accelerated by exposure of S to light of sufficient energy, but relatively low power. However, inducing reaction via laser exposure was far less effective as a synthesis method than heating as reaction only occurs in the region of the laser spot, and still takes some time. It could be argued that this localisation can be advantageous as it does not heat the DAC itself, whereas drastic global temperature changes from heating the entire cell can induce fluctuations in sample pressure, as the metal expands and contracts. Despite this, pressure increase on heating is usually negligible and is minimised by slow cooling.

The reactivity was dependent on the incident energy of the laser. No reaction was observed in a sample of S suspended in fluid H_2 at 0.2 GPa when exposed

to a red Kr^+ ion laser (647 nm) at 70 mW for 16 h (300 K). Visible reaction was observed upon exposure to a green Ar^+ ion laser (514 nm) at 70 mW for 30 min (300 K). The crystal growth rate appeared accelerated upon increasing the pressure to 1 GPa . Although this evidence is anecdotal, it demonstrates the increased photosensitivity of S on compression [114].

A study by Duwal *et al.* investigates the photochemical reactions of S and H_2, and find $(H_2S)_2H_2$ forms from 3 GPa upon exposure to 514 nm Ar^+ wavelengths [47], which is lower than the usual formation pressure (3.5 GPa in [46] and 4.7 GPa in Chapter 6). Although this could be seen as an advantage, promoting complete reaction between S and H_2 via laser exposure would be very time consuming. Therefore all synthesised H_2S samples used for experiments in this study were prepared using the direct heating method, offering much higher sample quality within a shorter time frame.

5.3 Synthesis of Hydrogen Selenide

5.3.1 Reaction

The reaction between Se and H_2 was not spontaneous at room temperature. Samples left between 0.2 - 3 GPa for one month showed no visible or spectral changes [1]. Reaction was promoted within 2 hours at 0.4 GPa, after heating to a minimum temperature of 473 K, ∼20 K below the melting point of Se at ambient pressure [115]. This mirrors the behaviour of S where temperatures approaching the melting point were required for reaction within a practical timeframe. The reaction between Se and H_2 at ambient pressure purportedly occurs above 573 K, 150 K lower than S at ambient pressure, although the scale of production may be a factor in these values [109, 110]. It is interesting that H_2S requires harsher conditions than H_2Se to form from constituent elements at ambient pressure, but milder temperatures are required when compressed. Nonetheless the efficacy of heating the chalcogen within fluid H_2 is proved further. Consequently the same reaction mechanism proposed in Figure 5.1 is likely also true for Se, which is not surprising giving the comparable electronic configurations of S and Se. Slightly higher synthesis pressures of 0.4 GPa were used to avoid H_2 leaking during heating, but it is suspected that heating close to the melting point of Se would still be most favourable at 0.2 GPa. Raman spectra and XRD patterns of

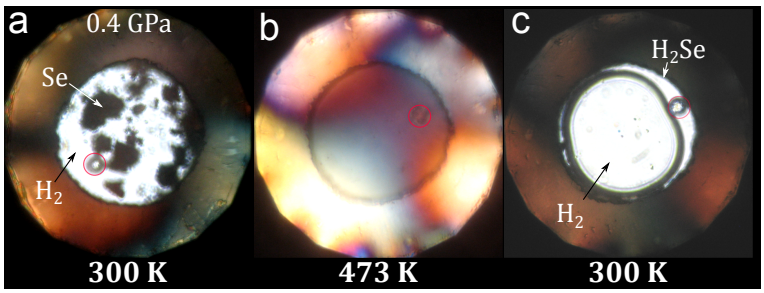

Figure 5.4 Photomicrographs showing the synthesis of H_2Se from Se and H_2 at 0.4 GPa: a) solid Se and fluid H_2 at 0.4 GPa and 300 K, prior to heating. b) hot fluid mixture of H_2Se and H_2 at 473 K. c) phase separation of fluid H_2 and H_2Se upon cooling to ambient temperature. Ruby sphere is outlined in red.

phase I H_2Se are shown in Figures 8.3 and 8.4.

5.3.2 Phase Separation

At 0.4 GPa, phase separation of H_2Se and H_2 occurred around 323 K, upon cooling the hot mixture from 473 K. Although it is likely that temperature readings have some associated error, the temperature where H_2Se and H_2 became immiscible was comparable to H_2S:H_2 fluids, but at a higher pressure (versus 323 K at 0.2 GPa). Although the difference in pressure is small, H_2S at 0.4 GPa separated at a higher temperature. This is probably due to the slightly reduced attraction between H_2Se molecules, as Se is larger and less electronegative than S. The H_2Se syntheses were explored far less thoroughly than H_2S and were only performed close to 0.4 GPa, but it is likely that higher pressures would still cause phase separation at higher temperatures, from the increased H-bonding strength in H_2Se upon compression (See Chapter 8).

Laser-Induced Synthesis

Prolonged laser exposure was also found to promote synthesis of H_2Se from H_2 and Se, with similar results to H_2S. Red wavelengths (647 nm) were also insufficient to instigate reaction between Se and H_2 whereas green wavelengths (514 nm) promoted reaction very quickly at 0.4 GPa. This method was also employed by Zhang *et al.* to synthesise H_2Se [116].

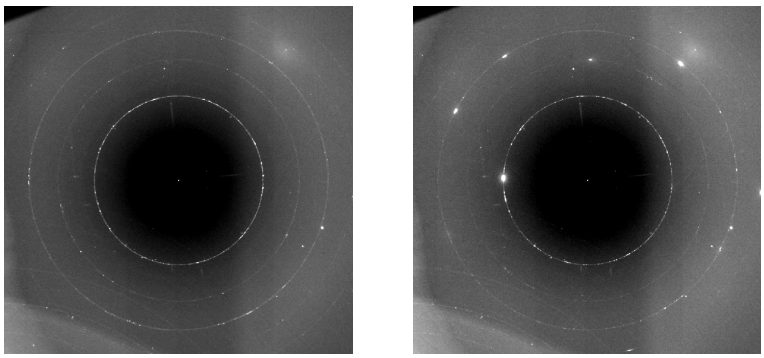

Figure 5.5 XRD detector plate images for Te-V in H_2 at 35.3 GPa; prior (left) and after (right) laser-heating at 1500 - 3500 K. The right hand image shows conversion of Te-V powder to single crystals from the heating, but with no structural changes.

5.4 Synthesis of Hydrogen Telluride

Hydrogen telluride exhibits significantly weaker covalent bonding than H_2S and H_2Se. It is purportedly only stable below 271 K and will also degrade upon exposure to visible light and air [115, 117, 118]. Despite this, H_2Te can be prepared from electrolysis and hydrolysis (e.g. $Al_2Te_3 + H_2O \rightarrow 2\ Al(OH)_3 + 3\ H_2Te$ [119]) Unlike H_2S and H_2Se, the direct synthesis of H_2Te at ambient pressure is not known, and there are no known attempts at synthesis within pressure cells. Nevertheless, the *in situ* synthesis was investigated as H_2Te (H_3Te) has also been predicted to possess high temperature superconducting properties at high pressures [44, 45].

5.4.1 Heating attempts

Although success was not expected, an attempt at synthesis via heating was made. Te suspended in H_2 (0.2 GPa) was heated to a maximum temperature of $\sim$600 K, by a hotplate combined with a standard resistive heating jacket for a piston-cylinder DAC. No change was observed in the Raman spectra after heating, and the cell received minor damage from the process.

As temperatures never quite approached the melting point of Te ($\sim$722 K at 0 GPa [115]), laser-heating was also attempted to transiently synthesise and simultaneously measure the formation of H_2Te with XRD, expecting it to decompose on exposure. A sample of Te suspended in H_2 was laser-heated at the BL10XU beamline (SPring-8) using a double-sided near-infrared (IR) fibre laser heating system, to temperatures estimated from 1500 - 3500 K. Samples were

visually observed with online optics during laser-heating, and XRD was performed *in situ*. In order to be thorough, Te was laser-heated at the following pressures to see if any of the high pressure phases would react with H_2: 0.5 GPa (Te-I), 4.3 GPa (Te-II), 13.0, 16.9, 22.7 GPa (Te-IV), 28.1, 32.7, 35.3 GPa (Te-V). No changes were observed at any pressure, other than the generation of single crystals from powder samples (Figure 5.5). Wherever heated, the dark Te solid would usually move away from the laser and did not appear to even 'dissolve'. Although the stable pressure range for Te-III was accidentally skipped, it seems unlikely that Te-III would have reacted either. In hindsight, laser-heating may have been too extreme given the reported instability of H_2Te at room temperature.

5.4.2 Potential Low-Temperature Laser-Induced Synthesis

The reaction of Te with H_2 is potentially viable via prolonged laser-exposure, if the sample can be kept at sufficiently low temperatures. No reaction was observed between Te and H_2 upon exposure to 514 nm wavelengths (70 mW, 1 h) at 300 K. The effect of temperature on the laser-promoted reactivity of even S and Se is unknown, but a good starting point would be below the Te boiling point of 271 K. Ideally the experiment would be performed in a cryostat, the sample could be cooled to 250 K whilst Te is exposed to a green laser of a reasonable power ($>$ 40 mW). It is plausible that a small piece of Te could react with the surrounding H_2 and any crystals of H_2Te would probably grow around the beam rather than in it, hopefully remaining cold and stable. The next issue would be analysing the sample without causing decomposition. If any crystals visibly formed around the Te, then the sample could be cooled down to 80 K and exposed for a short time with a very low laser power. The ν_1 vibrational mode would be expected to be lower still than that of H_2Se, perhaps around 2000 rel cm^{-1}. Given the behaviour of H_2Se, H_2Te would probably exhibit a featureless spectra upon compression to $\sim$10 GPa, even at low temperatures. These experiments have yet to be attempted but present the best possibility for experimental study of H_2Te.

5.5 Conclusions

H_2 and S react spontaneously at 300 K and 0.2 - 0.4 GPa, but very slowly. Formation of H_2S was achieved in under 2 hours by heating the reactants to 373 K ($<$ 2 GPa). Reacting at pressure significantly lowers the synthesis temperature compared to the ambient pressure syntheses. The rate of cooling from 373 K can be utilised, with pressure, to influence the nature of the sample: for example, quenching to room temperature within 15 minutes above 1.5 GPa reliably produced solid mixtures of H_2S and $(H_2S)_2H_2$ (and H_2), which exhibit different behaviour on compression than the individual constituent systems. The reaction was also promoted by exposing S in H_2 to 70 mW 514 nm laser radiation for 30 minutes; laser-induced reaction is less favourable than simple heating because of the time required to move the beam onto different parts of the sample. H_2 and Se will not react spontaneously at 300 K from 0.2 - 3 GPa, but will react to form H_2Se upon heating to 473 K for 2 hours. Reaction also occurred after exposing Se in H_2 to 70 mW 514 nm laser radiation, in a shorter time than S and H_2, but was still deemed impractical. The direct synthesis of H_2Te from Te and H_2 was unsuccessful on heating to $\sim$600 K, and laser-heating most high pressure phases of Te in H_2. The results are unsurprising, but a potential avenue to produce H_2Te may be found in laser-induced synthesis at low temperatures.

Chapter 6

$(H_2S)_2H_2$

6.1 Introduction

The compression of H_2S and H_2 above 3.5 GPa results in the formation of $(H_2S)_2H_2$ cocrystals [46]. A structure of alternating H_2S and H_2 layers is assembled by weak H-bonding (phase I), which transforms at 17 GPa to produce two unique 'guest' H_2 sites (phase II). Simulations of $(H_2S)_2H_2$ up to 200 GPa find a third phase above 40 GPa, and a transformation to molecular H_3S with superconducting properties and a high T_c of 204 K at 200 GPa [23]. Although similar results were achieved experimentally through compression of H_2S, the nature of H_3S has yet to be precisely confirmed and $(H_2S)_2H_2$ still presents the most promising precursor for a dense molecular H_3S system. A valuable opportunity for study is found in the relatively unexplored, intermediary high pressure phases of $(H_2S)_2H_2$, at low temperatures in particular.

A comprehensive Raman study of $(H_2S)_2H_2$ is presented at ambient and low temperatures, up to 50 and 180 GPa respectively. High quality data are compared with current structural candidates of phases I - III attempting to highlight inconsistencies between the two models of phase II. Evidence is provided for at least three novel low-temperature phases, II′ III′ and IV′. Buttressed by two brief XRD studies, this chapter aims to properly characterise the $(H_2S)_2H_2$ phase diagram, infer the nature of bonding and identify structural features of the various phases, with reference to previous experimental and theoretical studies.

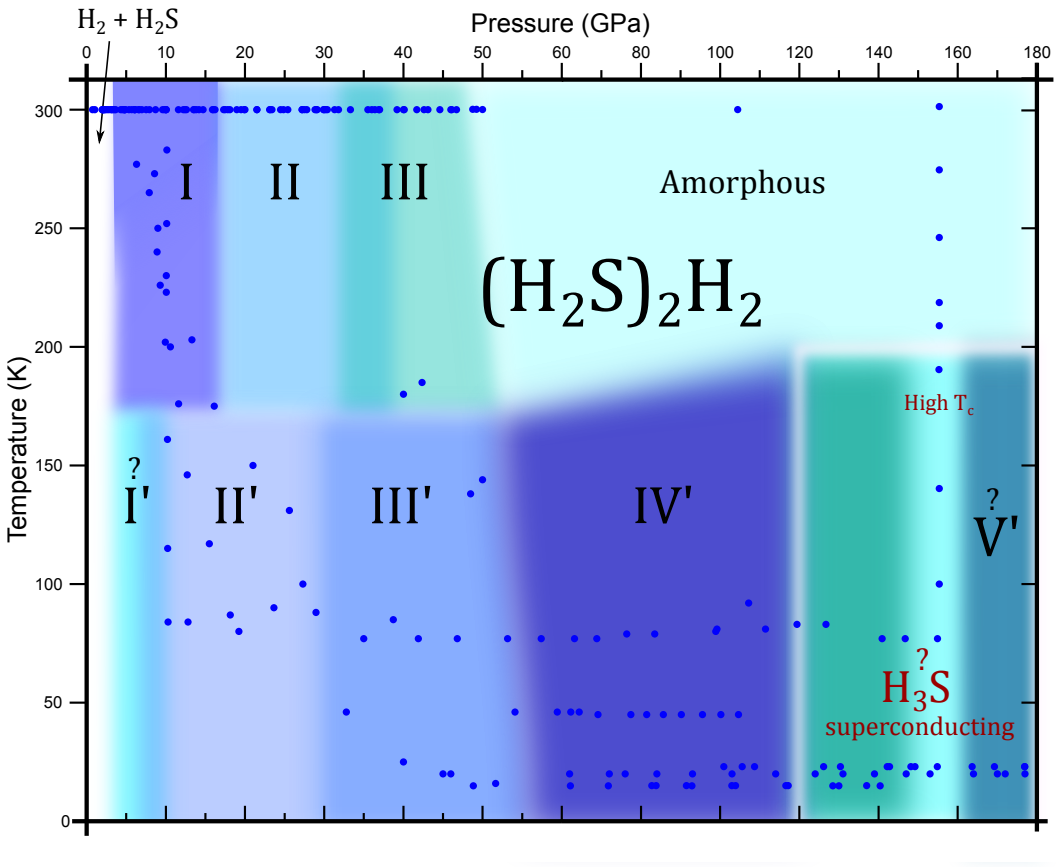

Figure 6.1 Approximate up-to-date thermodynamic/kinetic phase diagram of $(H_2S)_2H_2$, extrapolated from data obtained in this chapter (blue data points) and references [23, 46]. Phases II′, III′ and IV′ are novel; speculative phases are indicated by a question mark. Red text indicates the superconducting phases with boundaries adapted from references [28, 32]. The amorphous state is separated by a kinetic boundary.

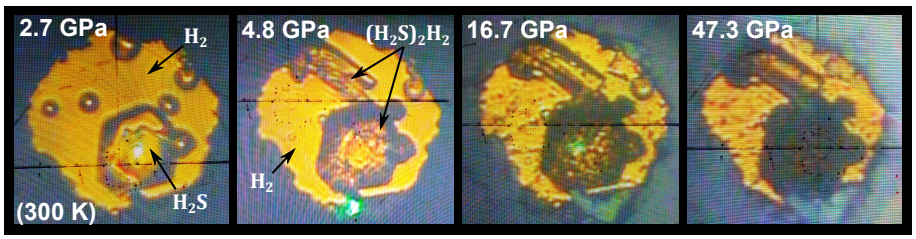

Figure 6.2 Sequential photomicrographs of a typical $(H_2S)_2H_2$ sample upon compression at 300 K. The elongated crystal appearing at 4.8 GPa is characteristic of $(H_2X)_2H_2$ compounds (X = S or Se).

Without high quality XRD data it was not possible to determine if the 3:1 stoichiometry of H:S changes in the higher pressure phases, but this has been considered. However, all phases are described as $(H_2S)_2H_2$ for consistency. $(H_2S)_2H_2$ exhibits a plethora of excitations which are often broad and convoluted, particularly in the S-H stretching region from 1500 - 3000 rel cm^{-1}. Spectra were fitted with the minimum number of peaks (pseudo-Voigt) required to best describe a particular excitation region, from which the frequencies were extracted; examples of peak fitting are appended in Figures A.4, A.5 and A.6. S-H and H-H stretching modes arising from $(H_2S)_2H_2$ are labelled alphabetically in order of appearance. ν_1H_2 refers to pure H_2, and ν_{1-3} refer to pure H_2S.

6.2 Ambient Temperature

All samples were synthesised directly from S and H_2 using the methodologies outlined in 3.2.3 and 5.2. Raman spectra were obtained using 514 nm Ar^+ ion excitation wavelengths. XRD data was obtained at Diamond Light Source beamline I-15, using a monochromatic wavelength of 0.4246 Å. Pressure was measured using Ruby fluorescence [66, 78] and stressed diamond edge frequency [70], calibrated to universal standards.

At ambient temperature (300 K), H_2 vibrons from $(H_2S)_2H_2$ are labelled $\nu_1H_2(a-f)$. Note that ν_1H_2c is only observed in phase II in the mixed $(H_2S)_2H_2$:H_2S system (See section 7.4). S-H stretching modes in phase II and above are simply labelled $\nu(g-l)$ (see Figure 6.3). The assignments of vibrational mode symmetries are suggested in the relevant discussion sections. The label for a given vibrational mode is also used to refer to the molecule itself, i.e. ν_1H_2a arises from H_2a.

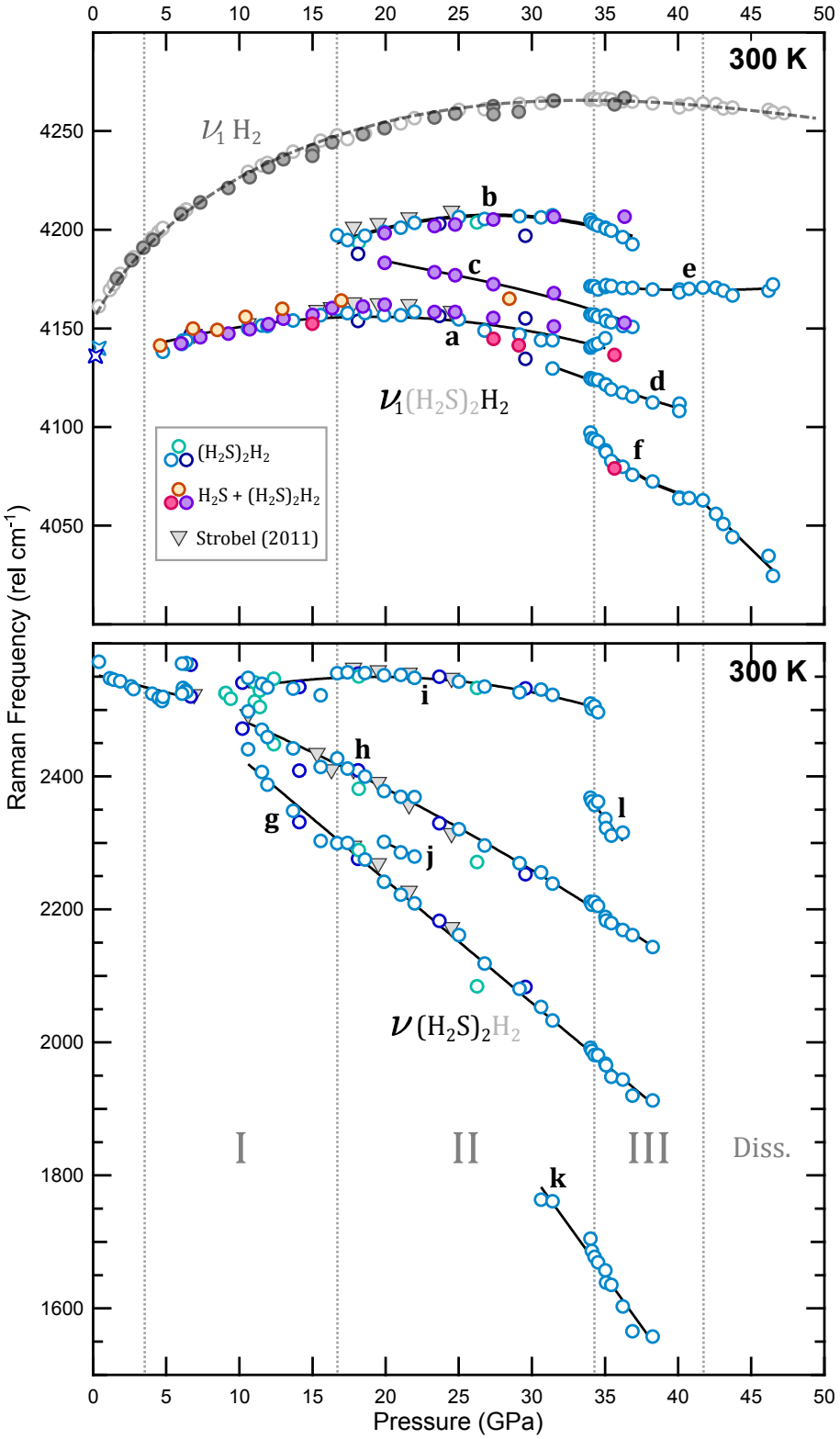

Figure 6.3 Observed Raman excitation frequencies between 1500 - 4300 rel cm^{-1} of $(H_2S)_2H_2$ plotted as a function of pressure, at 300 K. Open circles are data from $(H_2S)_2H_2$ samples, filled circles are from mixed $(H_2S)_2H_2/H_2S$ samples, grey points refer to molecular H_2, grey dotted line is data from pure H_2 for comparison. Open stars indicate fluid phase $(H_2S)_2H_2$ clathrate. Filled grey triangles are replotted from reference [46]. Black lines are intended as guides for the eye. The splitting at 6 GPa is not a phase transition, but is the point where both $\nu_{1,3}$ stretching modes are fitted to a single convoluted peak.

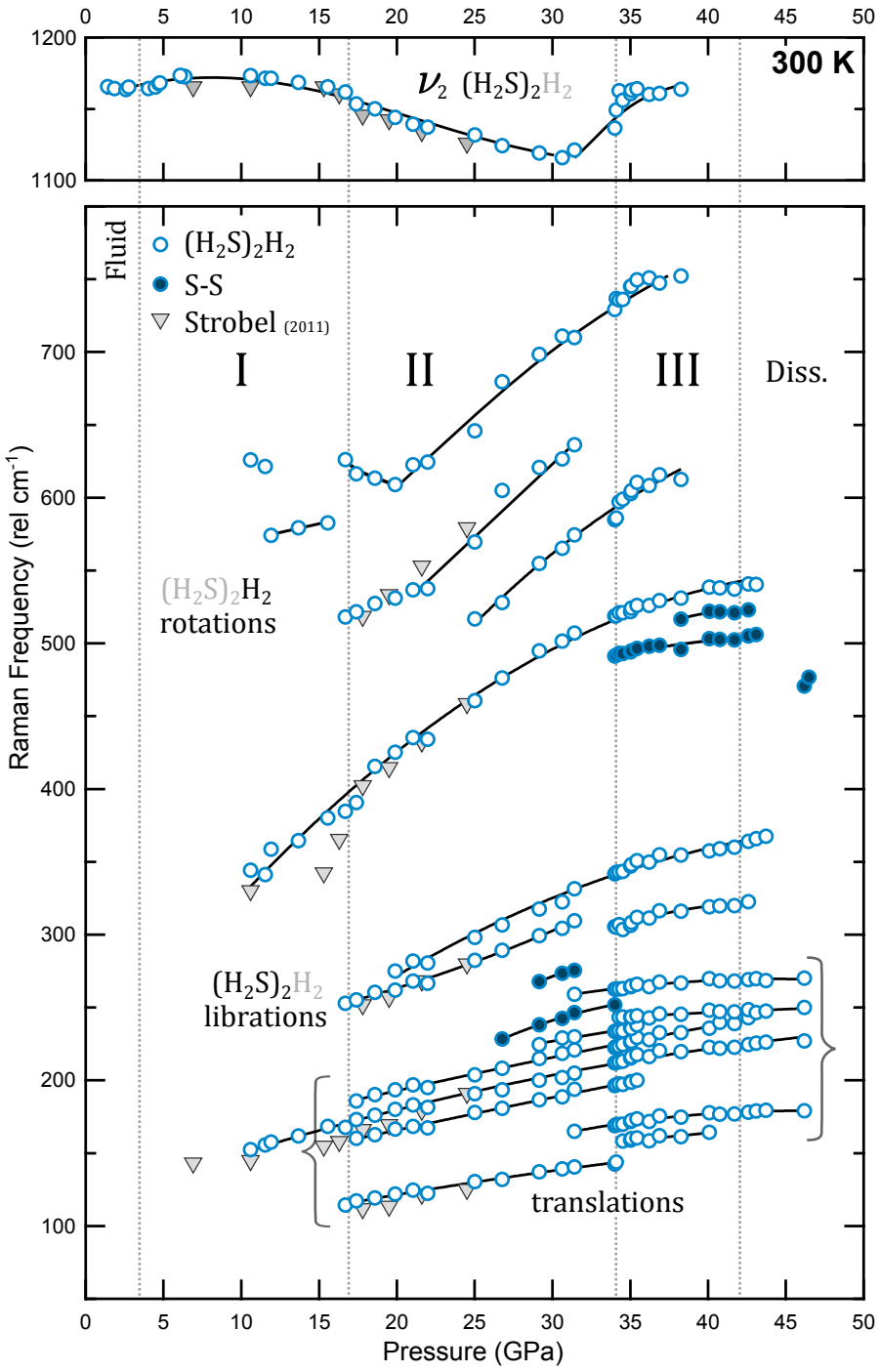

Figure 6.4 Observed Raman excitation frequencies between 0 - 1200 rel cm^{-1} of $(H_2S)_2H_2$ plotted as a function of pressure, at 300 K. Open circles are are data from $(H_2S)_2H_2$, filled blue circles are from elemental sulfur (II, III and amorphous). Filled grey triangles are replotted from [46]. Black lines are intended as guides for the eye.

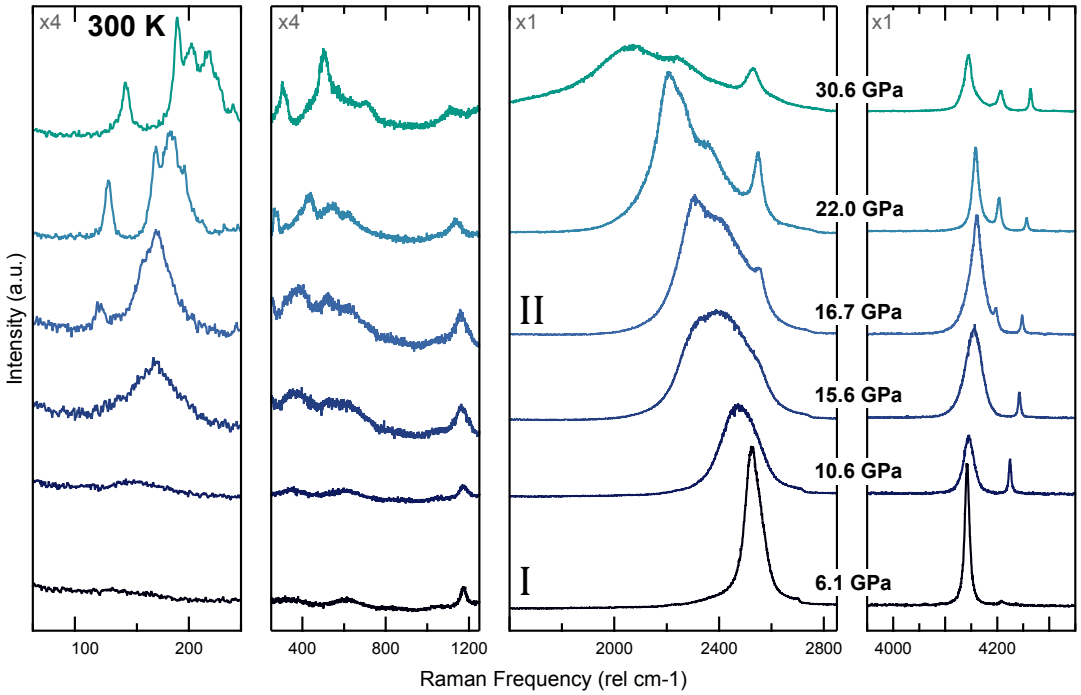

Figure 6.5 Representative Raman spectra of $(H_2S)_2H_2$ (phases I - II) as a function of pressure, at 300 K. Relative scales of each panel are indicated top left.

6.2.1 Phase I - Phase II

Phase I: Results

Figure 6.5 shows Raman spectra of phases I and II, and Figures 6.3 and 6.4 are referred to for frequencies plotted as a function of pressure. Figure 6.8 is a representation of the $I4/mcm$ structure describing phase I, and Figures 6.9 and 6.10 are representations of two proposed structures for phase II derived from references [23, 46]. Full-width-half-maxima (FWHM) for key vibrational modes are plotted as functions of pressure in Figure A.3.

Phase I was not observed below 4.77 GPa, whereas Strobel *et al.* report 3.5 GPa. Upon formation the characteristic 'guest' H_2 vibron (ν_1H_2a) appeared at 4138 rel cm^{-1}, 60 cm^{-1} lower in frequency than ν_1H_2 at the same pressure. ν_1 and ν_3 stretching modes were convoluted into a single intense band at 2520 rel cm^{-1}, shifted 10 cm^{-1} higher than in pure H_2S, both in good agreement with the previous study [46]. The ν_2 bending mode was sharp, and shifted 12 cm^{-1} higher than previous studies of pure H_2S [81] (Figure 6.5). The ν_2 vibron was not observed until ~7 GPa for pure H_2S data obtained in this study (section

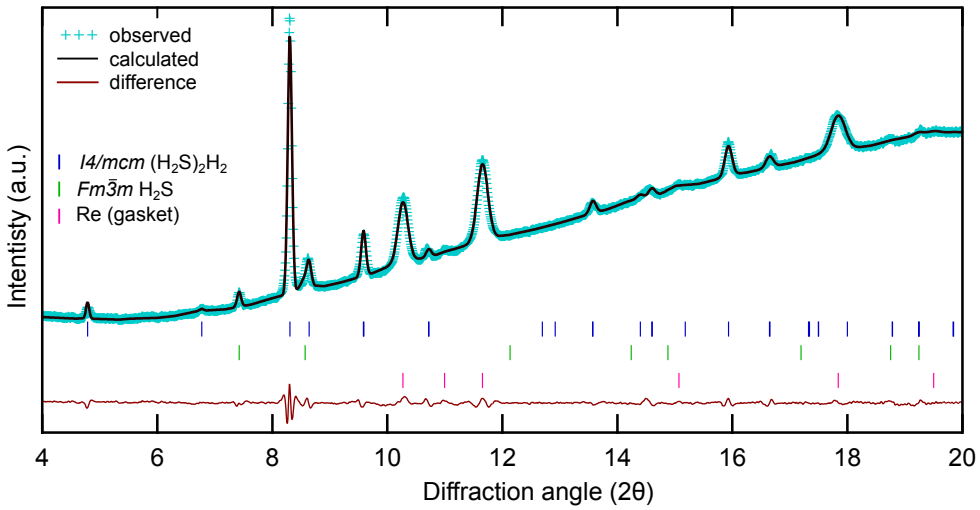

Figure 6.6 Observed diffraction pattern (+), Le Bail fit (black) and difference plot (red) for phase I $(H_2S)_2H_2$ (6.8 GPa, 300 K) fitted with $I4/mcm$ symmetry, a = 7.19(2) Å, c = 5.864(5) Å, direct cell volume = 302.8(9) Å^3 (χ^2 = 1.17). The sample also contained phase I H_2S, $Fm\bar{3}m$ symmetry, a = 5.68(6) Å.

4.2.2). Very little Raman activity was observed below 1000 rel cm^{-1} indicative of orientational disorder, similar to pure H_2S phases I - I′. XRD data collected at 6.8 GPa was fitted with tetragonal $I4/mcm$ symmetry (Figure 6.6); the Le Bail refinement produced unit cell parameters of a = 7.19(2) Å, c = 5.864(5) Å and a direct cell volume of 302.89 Å^3 which returned a pressure of 6.72 GPa from the EoS [46].

Visually, the sample did not change much upon initially entering phase I, but in several experiments an additional elongated crystal of $(H_2S)_2H_2$ would grow parallel to the diamond culet (Figure 6.2). This is also observed in other studies of $(H_2S)_2H_2$ and $(H_2Se)_2H_2$ [46, 47, 116]. Upon compression all crystals became grainy and progressively darkened, and the H_2 region became textured.

On compression of phase I, up to the phase II transition pressure (16.7 GPa), $\nu_1 H_2 a$ hardened by 1.6 cm^{-1}/GPa and broadened (FWHM) by 5.3 cm^{-1}/GPa. The S-H stretching modes softened at a rate of -9.1 cm^{-1}/GPa and the bandwidth increased substantially by 31.5 cm^{-1}/GPa. Softening is indicative of an increase in H-bonding between adjacent H_2S molecules, as the S-H bond lengthens from an increase in charge-transfer [81, 88, 89]. The increase in bandwidth is linked to H-bonded (O-H---:O) solids, where broadening of the symmetric O-H stretch is observed when it couples to the lattice via the H-bond [120–122]. As the H_2S lattice is strengthened by H-bonds the layers surrounding H_2a contract, inducing a slight repulsion effect and gentle increase in frequency. The frequency of ν_2 did

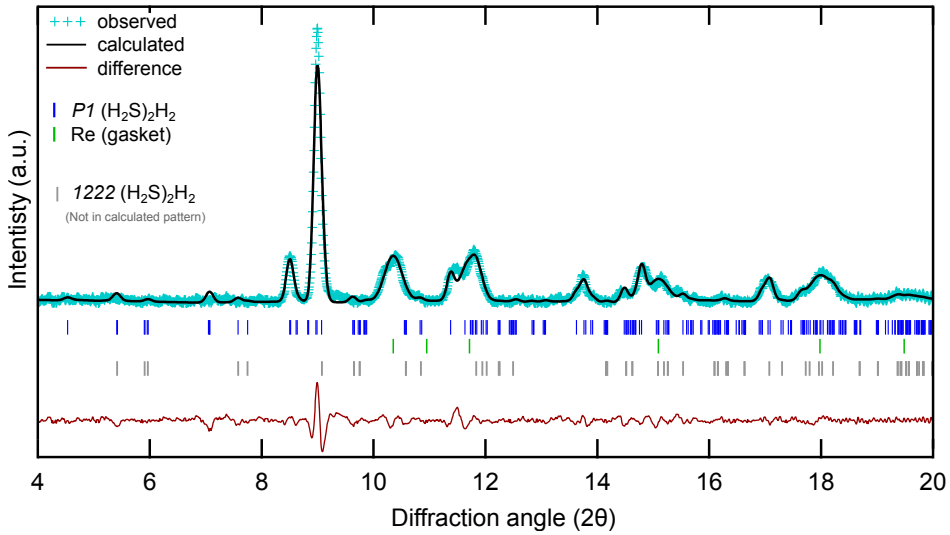

Figure 6.7 Observed diffraction pattern (+), Le Bail fit (black) and difference plot (red) for phase II $(H_2S)_2H_2$ (20.3 GPa, 300 K) fitted with $P1$ symmetry, a = 6.29(1), b = 6.43(1), c = 5.36(1) Å, α = 90.12°, β = 89.85°, γ = 90.15° (χ^2 = 0.79). Tick marks for $I222$ symmetry with comparable unit cell dimensions are shown in grey.

not change substantially and remained sharp from 5 - 17 GPa, as its motion is perpendicular to the direction of H-bonding. From 6.1 GPa ν_1 and ν_3 became non-degenerate, identified at 2524 and 2570 cm^{-1} respectively; they remained convoluted, with ν_1 being the most intense, as in pure H_2S (phase I′). Broad weak modes were observed at 130, 347 and 616 cm^{-1} respectively, suggested to be librations of S-H bonds and H_2a. By 15.6 GPa the convoluted stretching modes split further, comprising νg, νh and νi at 2303, 2414 and 2522 rel cm^{-1} respectively. Here the low frequency excitation at 168 cm^{-1} suddenly gained intensity just before the transition to phase II occurred, proposed to be coupling of an S-H libration to the lattice.

Phase II: Results

The transition to phase II occurred at 16.7 GPa (17 GPa in [46]), heralded by the second low-frequency H_2 vibron (ν_1H_2b) which emerged at 4197 rel cm^{-1}, 37 cm^{-1} higher than ν_1H_2a and closer to the frequency of bulk molecular H_2, indicating the H_2b environment is less perturbed by interactions with H_2S than H_2a. At the transition the S-H stretching excitations became well defined: νg (symmetric) was the most intense with the lowest frequency, νh (symmetric) appeared in the centre and νi (asymmetric) was the least intense with the highest frequency, concurring with previous studies [39, 46].

XRD data collected at 20.3 GPa was better fitted with the lower symmetry triclinic $P1$ structure of Duan *et al.*, rather than the orthorhombic $I222$ structure of Strobel *et al.* (Figure 6.7). The Le Bail refinement produced unit cell parameters $a = 6.29(1)$, $b = 6.43(1)$, $c = 5.36(1)$, $\alpha = 90.12°$, $\beta = 89.85°$, $\gamma = 90.15°$, comparable to the predictions made in [23]. The lower symmetry $P1$ structure accounts for extra peaks observed in the diffraction pattern which $I222$ failed to predict. Nonetheless, the fit was not ideal and the merits of both structures are considered in the discussion. The S atom configurations are very similar across all models of $(H_2S)_2H_2$ phases, which is appended in Figure A.9 for reference.

At 16.7 GPa the translational lattice mode at 168 cm^{-1} gained intensity and split, gaining a low and high frequency shoulder at 114 and 249 cm^{-1} respectively (Figure 6.4). Further splitting into sharp contributions was observed from 22 GPa, indicating phase II is significantly less orientationally disordered than phase I. The stretching modes became more distinct at 22 GPa. $\nu 1H_2a$ narrowed, separating it from $\nu 1H_2b$. νg and νh softened monotonically herein at rates of -18.5 and -12.1 cm^{-1}/GPa respectively, whereas the frequency of νi did not vary significantly with pressure. This allows the assignment of νg and νh as symmetric stretches and νi as an asymmetric stretch, similar to the relative differences in $\frac{d\nu}{dP}$, and intensities of ν_1 and ν_3 in pure H_2S. $\nu_1 H_2a$ softened above 22 GPa, whereas the frequency of $\nu_1 H_2b$ remained fairly constant until ∼30 GPa. Excitations corresponding to S-II were detected from 27 GPa, concurrent with partial decomposition of H_2S at the same pressure (Figure 4.6) [38, 95, 96].

Discussion

The behaviour of $(H_2S)_2H_2$ upon compression is apparently similar to pure H_2S, with H-bond driven phase transitions. The initial lack of any lattice modes indicates orientational disorder of S-H bonds. The initial softening of the S-H bond in $(H_2S)_2H_2$ (-9.14 cm^{-1}/GPa) was a fraction less than in the pure species (-9.93 cm^{-1}/GPa). As the ν_1 frequency is also 10 cm^{-1} higher in $(H_2S)_2H_2$, this suggests that H-bonding is initially slightly weaker in the cocrystal. This is plausible considering the $I4/mcm$ model proposed by Strobel *et al.* as the distance between any H and S lone pair is greater than in phase I H_2S at the same pressure (Figure 6.8). The $I4/mcm$ model fits the XRD data well, and concords with the Raman spectra.

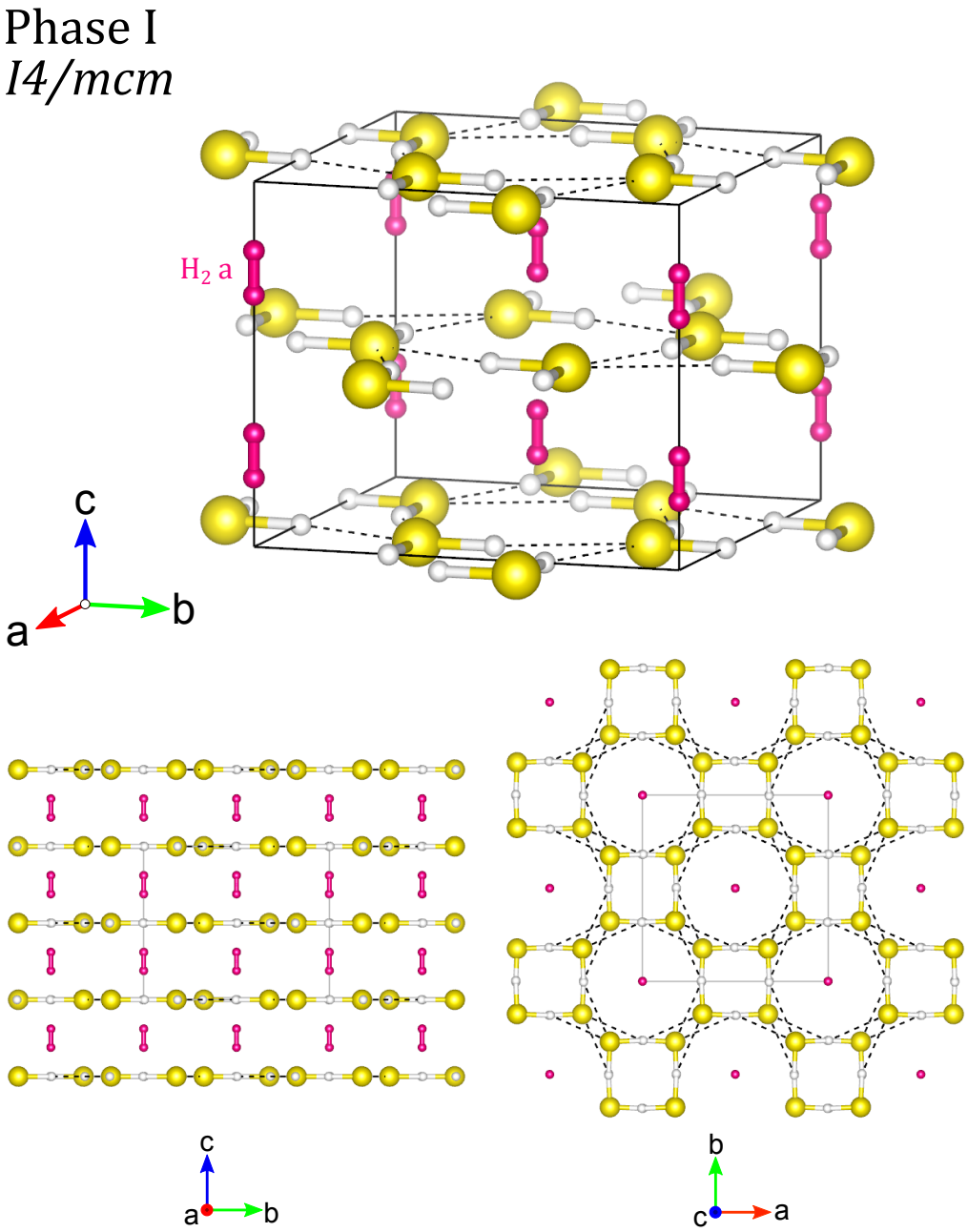

Figure 6.8 Representation of the structure of $(H_2S)_2H_2$ phase I; modelled using VESTA [90] with $I4/mcm$ symmetry at 5 GPa, adapted from Density Functional Theory (DFT) calculations from [46]. H_2S molecules are yellow (S) and white (H) spheres. H_2a is represented by pink spheres. Hydrogen bonds are indicated by black dashed lines.

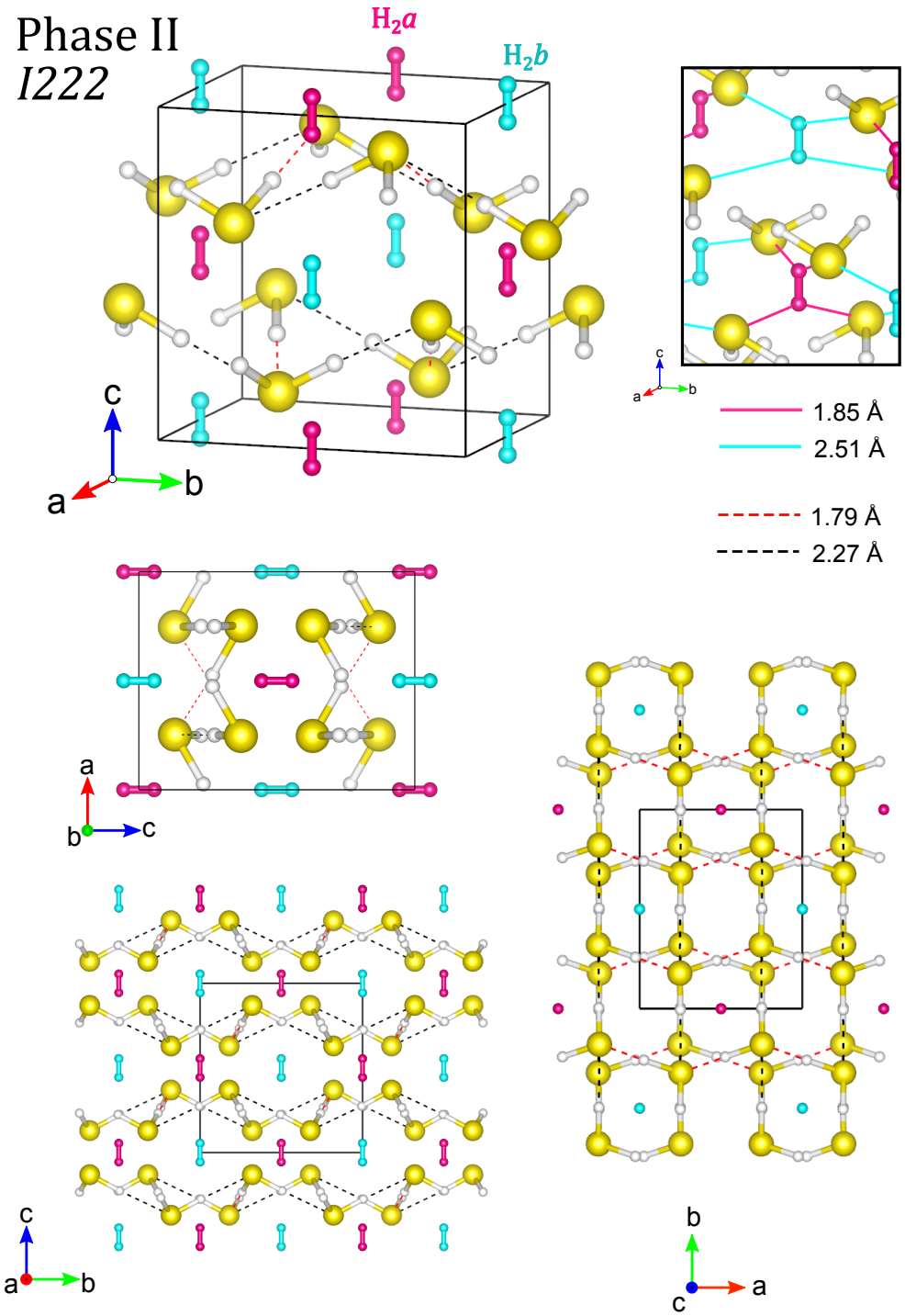

Figure 6.9 Representation of the structure of $(H_2S)_2H_2$ phase II; modelled using VESTA [90] with $I222$ symmetry at 19 GPa, adapted from DFT calculations from [46]. H_2S molecules are yellow (S) and white (H) spheres. Distances from H atoms to nearest S lone pairs for assigned environments H_2a (pink), and H_2b (turquoise) are shown in the inset bottom left. The two hydrogen bond types are indicated by red and black dashed lines.

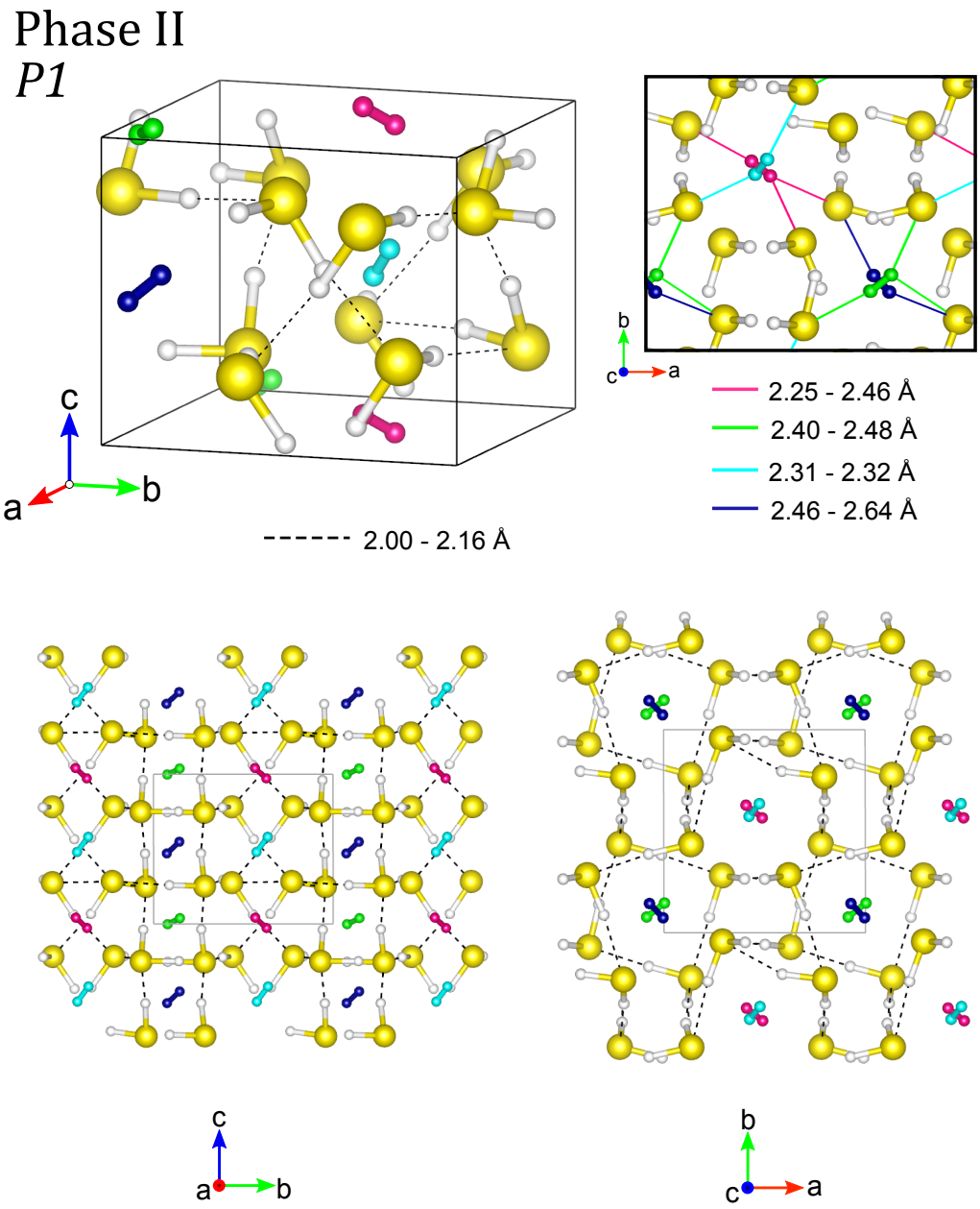

Figure 6.10 Representation of the structure of $(H_2S)_2H_2$ phase II; modelled using VESTA [90] with $P1$ symmetry at 20 GPa, adapted from DFT calculations from [23]. H_2S molecules are yellow (S) and white (H) spheres. Distances from H atoms to nearest S lone pairs for assigned environments H_2a (pink, green), and H_2b (turquoise, blue) are shown in the inset bottom right. Hydrogen bonds are indicated black dashed lines.

Compression and reduction of interatomic distance is likely to restrict the rotation of H_2a which is thought to be responsible for the broad modes around 350 and 600 rel cm^{-1}. At these conditions, the frequencies are more comparable to pure H_2 rotons than any low frequency H_2S modes. This also initially causes a repulsion effect in H_2a causing the frequency to increase on compression. The mode which emerges around 130 cm^{-1} is assigned to a libration of the S-H bond. The development of this libration is thought to be similar to the transition from phase I′ to IV in pure H_2S; the disordered S-H bonds begin to spend more time in a given orientation before switching position, which increases the lifetime of the libration and allows it to be detected. The transition to phase II in $(H_2S)_2H_2$ seems to reflect a reduction in the overall orientational disorder. The S-H libration around 130 cm^{-1} gains intensity and narrows at the transition pressure, associated with a gradual coupling to the lattice. This mode continues to develop upon compression of phase II, increasing intensity, narrowing and splitting. When compared to the abrupt phase IV transition, this indicates that some orientational disorder still exists in phase II, at least up to 22 GPa.

The two models which have been proposed for phase II in previous studies have $I222$ symmetry [46] and $P1$ symmetry [23]. Both were generated in *VESTA* [90] from the data provided from each respective study. Assessment of the quality of the calculations themselves is beyond the scope of this study, the models are simply judged in the context of experimental data. Although the EoS for individual unit cell dimensions (UCDs) were not provided in the literature, $P1$ and $I222$ were modelled at 20 and 19 GPa respectively, allowing a near direct comparison to be made. Their characteristics are surmised as follows, with reference to Figures 6.9 and 6.10:

- $I222$ exhibits almost direct alignment of S-H bonds with neighbouring lone pair S atoms. In the unit cell there are two different H-bond lengths: 1.79 Å (4 x red dashed) and 2.27 Å (8 x black dashed, parallel to the b,c plane).
- The alignment of S-H---:S bonds in $P1$ are slightly dislocated, ranging from 167°– 174° at 20 GPa. 9 x H-bonds were found in the unit cell, distributed in the range 2.00 – 2.16 Å (black dashed).

- $I222$ has two distinctly different H_2 environments. One is located within an interstice bordered by four S lone pairs (pink), the equilibrium position of each H is 1.84 Å from two lone pairs. The other resides in a larger interstice (turquoise). The equilibrium position of each H-(H) atom is 2.51 Å from two lone pairs and 1.99 Å from two **H**-(S) atoms.

- $P1$ has four H_2 environments of different symmetry. They can be loosely grouped into two groups of two, based on interatomic distances: pink and green are influenced by three lone pairs each respectively; turquoise and blue by two lone pairs each respectively. However, the interatomic distances varied from 2.25 – 2.64 Å so it is unlikely that any of the environments are completely degenerate.

H-bonding is initially slightly stronger in pure H_2S than in $(H_2S)_2H_2$, up to about 10 GPa. However, once the S-H stretches split, $\frac{d\nu}{dP}$ decreases far more rapidly for all modes demonstrating enhanced H-bonding throughout all ambient temperature phases of $(H_2S)_2H_2$. Both phase II models exhibit greater alignment of H-bonds than the $I4/mcm$ phase I model, but H-bonding would likely be stronger in $I222$ than in $P1$ given the shorter H-bond length and better alignment. $I222$ also offers two distinct H-bonds which describes the two S-H stretching frequencies νg and νh; the counter to this is that the S-H stretches are very broad which could be arise from a range of H-bond lengths, as expressed by the $P1$ model. The two distinct environments, H_2a and H_2b, are better described by $I222$ than $P1$: In Figure 6.9, H_2a (pink) experiences significantly more charge transfer from the surrounding lone pairs, resulting in more frequency attenuation, whereas H_2b (turquoise) exists in a larger interstice, experiences less electronic interaction and is therefore closer to the frequency of molecular H_2. Nonetheless, the lower symmetry of $P1$ does account for the observation of the extra S-H stretch νj which $I222$ does not, although there is no evidence of the two additional H_2 vibrons expected from $P1$. Neither model offers an explanation for the difference in intensities of $\nu_1 H_2a$ and $\nu_1 H_2b$.

To summarise: Phase II is characterised by the generation of at least one extra H_2 environment. The transition is associated with an increase in H-bonding and a reduction in orientational disorder, evident from softening of the S-H stretching modes, appearance of librational modes with subsequent coupling to the lattice, and transformation to translational modes. It is likely that some orientational disorder exists upon the initial adoption of phase II at 16.7 GPa but ceases

above 22.0 GPa. H-bond strength increases dramatically above the transition. Although $P1$ symmetry gave a slightly better fit to the XRD data, the S atoms are very similarly distributed, and $I222$ better represents most aspects of the Raman data. Given the quality of the XRD data, $I222$ is selected as the more favourable candidate for phase II $(H_2S)_2H_2$. In reality both models have shortcomings; phase II is expected to exhibit two distinctly different H_2 environments with a 2:1 ratio of a:b. Neutron diffraction and further theoretical studies of phases I and II of $(D_2S)_2D_2$ are therefore desirable.

6.2.2 Phase III

Results

The evolution of phase II with pressure is pertinent to the formation of phase III, which was observed from 32.6 GPa (Figure 6.11). Above 22 GPa, the S-H stretching modes softened monotonically, and continued to broaden indicating continued strengthening of H-bonds and closer proximity of H and :S. At 30.6 GPa an additional S-H stretch (νk) emerged from the convoluted cluster at 1763 cm^{-1}. Above 22 GPa the ν_2 bending mode softened and lost intensity, whilst all H_2 vibrons softened. The broad mode around 500 cm^{-1} prescribed to restricted H_2 rotation sharpened substantially from 26.8 – 32.6 GPa, as it coupled to the lattice.

Figure 6.11 shows the sluggish evolution of phase II to phase III from 32.6 GPa - 39.5 GPa. A distinct shift in the lattice modes occurred over the transition. Four of the translational modes gradually exchanged intensity to four higher frequencies, suggesting a progressive change in the structure. A marked change in the H_2 environment occurred during the transition where H_2a, b were progressively replaced by $H_2c - f$ (Figure 6.3). The $\nu_1 H_2 c, d$ vibrations were only observed during the transition, as was the S-H stretching mode νl at 2368 cm^{-1}. A blueshifted ν_2 bending emerged at 32.6 GPa, correlating with the new lattice modes; the ν_2 frequency remained constant throughout the transition. All new lattice modes and H-H stretches gained intensity upon compression. An excitation corresponding to S-III also emerged above 36.2 GPa around 525 cm^{-1}.

The transition was deemed complete at 39.5 GPa, when only $\nu_1 H_2 e$ and $\nu_1 H_2 f$ remained of the H_2 environments. Interestingly, Raman activity decreased

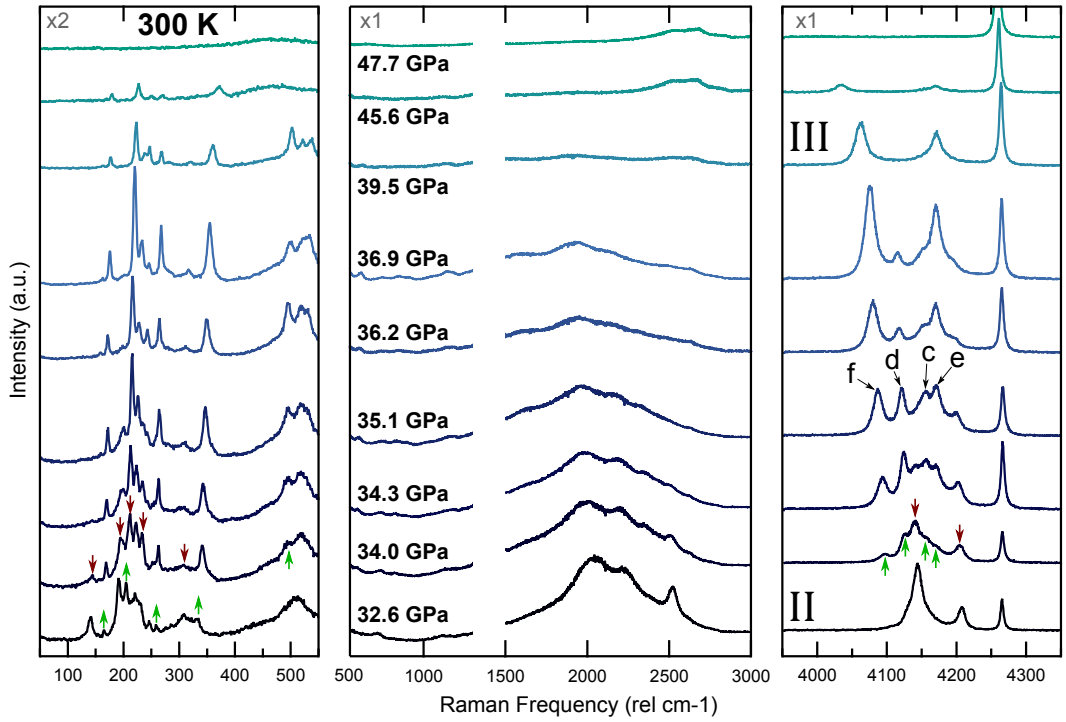

Figure 6.11 Representative Raman spectra of $(H_2S)_2H_2$ (phases II (red arrows) - III (green arrows)) as a function of pressure, at 300 K. Relative panel scales shown top left.

substantially upon compression of phase III. The lattice modes suddenly lost intensity, as did $\nu_1 H_2 e$ and $\nu_1 H_2 f$. Up to this point, the progressive reduction S-H stretching intensity correlated to the dramatic increase in bandwidth, but at 39.5 GPa a substantial drop in intensity was observed (Figure 6.11). All detectable activity, including the pure S modes, subsided upon reaching 47.7 GPa, bar a weak and broad excitation around 475 cm^{-1} identified as amorphous S-S bonds (See section 4.2.4). This is reminiscent of dissociation of pure H_2S above 40 GPa. Samples became visually very dark, but apparently this was not accelerated by laser exposure as in pure H_2S. (Figure 6.2).

XRD data collected at 36.2 GPa was fitted with *Cccm* structure (Figure 6.13). The Le Bail refinement produced unit cell parameters $a = 8.38(3)$ Å, $b = 8.59(1)$ Å, $c = 4.98(2)$, giving a direct cell volume of 356(2) $Å^3$. The EoS data presented in [23] at 36.2 GPa gives 21.97 $Å^3/H_3S$ unit; the *Cccm* fit gives a remarkably close value of 22.3(1) $Å^3/H_3S$ unit (for 16 H_3S "units" in the cell). Sue to the quality, it was not possible to fit both phase II and III to the XRD data, although the Raman data suggests that some phase II should be present at 36.2 GPa. Tick marks from a separate refinement with *I*222 structure are shown in Figure 6.13 for comparison.

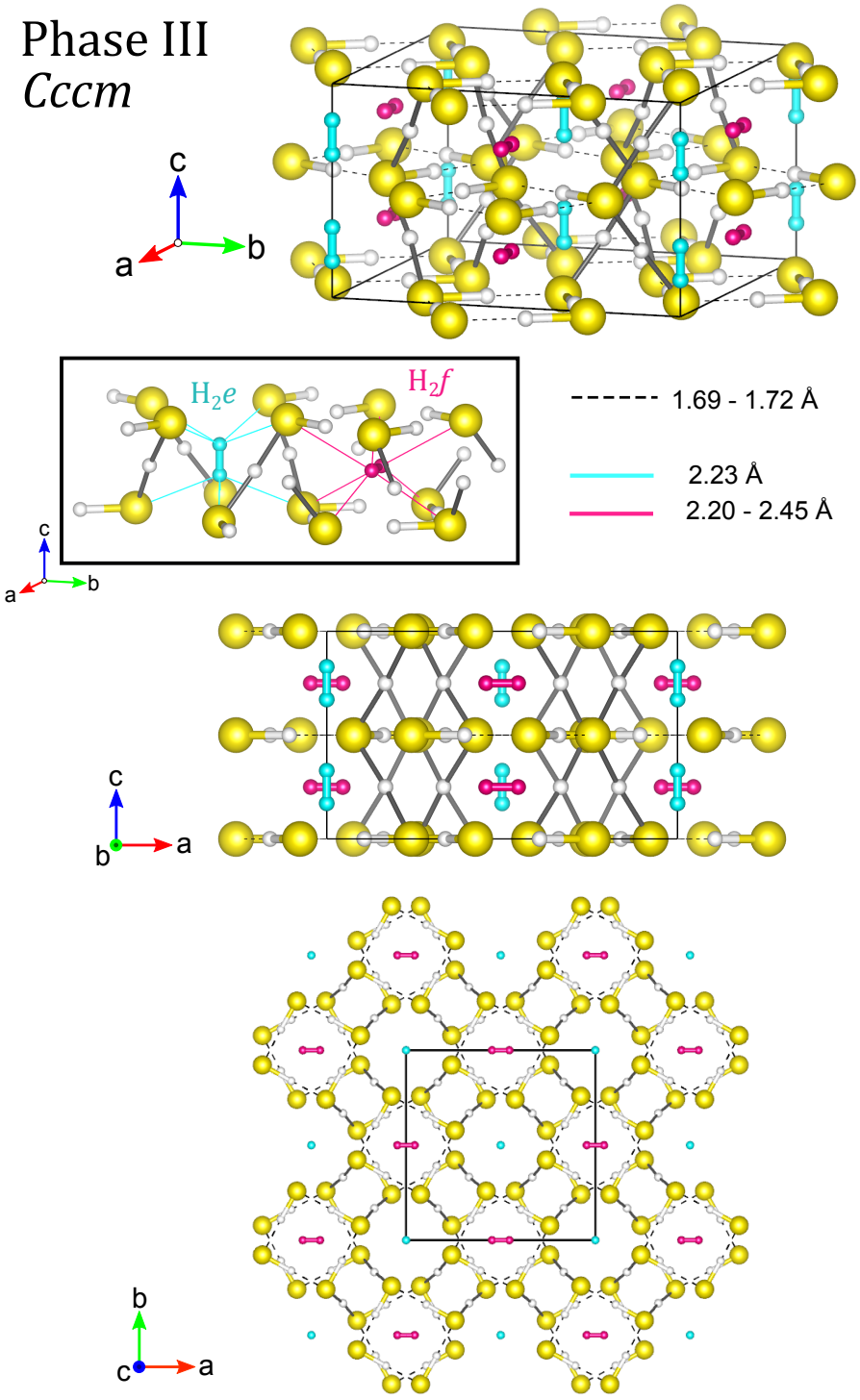

Figure 6.12 Representation of the structure of $(H_2S)_2H_2$ Phase III; modelled using VESTA [90] with *Cccm* symmetry at 60 GPa, adapted from DFT calculations from [23]. H_2S molecules are yellow (S) and white (H) spheres. Grey bonds represent fluctuating H-bonds (i.e. S-H---:S $\leftrightarrow$ S:---H-S). Distances from H atoms to nearest S lone pairs for environments H_2f (pink), and H_2e (turquoise) are shown in the inset bottom left. Hydrogen bonds are indicated by black dashed lines.

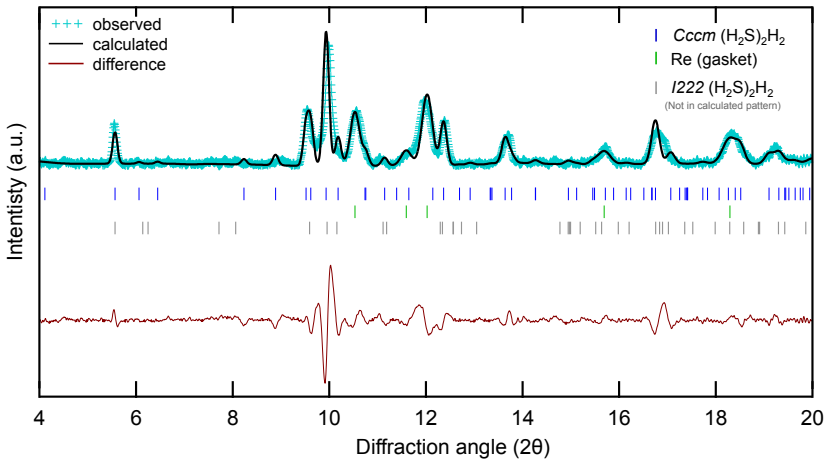

Figure 6.13 Observed diffraction pattern (+), Le Bail fit (black) and difference plot (red) for phase III $(H_2S)_2H_2$ (36.2 GPa, 300 K) fitted with $Cccm$ symmetry, $a = 8.38(3)$ Å, $b = 8.59(1)$ Å, $c = 4.98(2)$, direct cell volume = 358(2) Å^3 ($\chi^2 = 1.41$). Tick marks for $I222$ symmetry with comparable unit cell dimensions are shown below for comparison.

Discussion

The $Cccm$ structure (Figure 6.12) has -S-H-S-H- chains running down the c-axis (grey bonds), which can be thought of as dynamically alternating H-bonds (i.e. S-H$---$:S $\leftrightarrow$ S:$---$H-S), with orthogonal H-bonds connecting the chains in the a,b plane. This mechanism is also a plausible precursor to symmetrisation of H-bonds proposed in the high T_c phase [30]. This generates two channels and two distinct H_2 environments, with orthogonal equilibrium positions. The $Cccm$ structure describes the characteristics of phase III well, concurring with previous experimental studies [48, 49]. The transition was completed at 39.5 GPa, which harmonises well with Duan *et al.* who find the $Cccm$ structure to be stable above 40 GPa. However, it is evident that phase III is at least in part stable from 32.6 GPa. The sluggish exchange of the sharp translational modes to higher frequencies could arise from a gradual reordering of H-bonds from phase II to phase III. Presumably the strength of H-bonding in phase II prevents all molecules from immediately adopting the conformation for phase III. The similarities between the $P1$ and $Cccm$ structures are clear when viewed down their respective c-axes (The $I222$ structure can also be compared by viewing down the a-axis). However, a progressive change is better rationalised with an $I222 \rightarrow Cccm$ model. The $I222$ structure has two distinctly different H-bond strengths which would explain a differential in pressure driven reorganisation. The stronger H-bond in $I222$ (red dashed line Figure 6.9) also corresponds to the chains of alternating H-bonds running down the c-axis (equivalent to the b axis

in $I222$). The difference in $\frac{d\nu}{dP}$ between the phase II and phase III translational modes above 34 GPa suggests a reduction in cell volume which is supported by the transition to $Cccm$ symmetry, from a shortening of the distance between the layers in the a,b plane.

The $Cccm$ structure also describes the S-H stretching region well. An excitation from an alternating H-bond would likely be short-lived and appear very broad in the spectra. The disappearance of the νi asymmetric mode fits the model: if an H_2S molecule transitions from having two proper S-H bonds, to a single S-H bond (a,b plane) and a transient S-H bond (c axis), the possibility of normal harmonic motion is removed, but at least one constant stretching motion in the a,b plane remains. The νl mode appears as νi disappears, which could pertain to an asymmetric stretch between the a,b S-H bond and the transient c-axis S-H bonds (Figure 6.3). The νk mode is likely the symmetric stretch of the transient c-axis bonds which are ∼1.5 Å long, whereas the a,b S-H bonds are ∼1.4 Å (in the DFT model at 60 GPa [23]). The v_2 mode frequency remains constant in phase III but the intensity was weak, so it could be assigned to the motion between the a,b S-H and the transient c-axis S-H.

The H_2 environments in phase III are substantially different to those in phase II. the notable difference in $\frac{d\nu}{dP}$ allows H_2e and H_2f to be assigned to turquoise and pink respectively in Figure 6.12. Dotted lines show the nearest S atoms to each H-H environment. The frozen equilibrium position of each atom of H_2f (pink) is 2.21 Å away from four lone pairs, whereas H_2e (turquoise) is 2.23 Å away from four lone pairs. The difference is not vast, but it is clear that upon compression the channels and layers would likely contract around H_2f (pink), whereas H_2e (turquoise) would expected to be less affected, and hence $\frac{d\nu e}{dP} \approx 0$. This theory is reinforced from a comparison of $I4/mcm$ (phase I) and $Cccm$ (phase III) models, when viewed down their respective c-axes. The H_2f and H_2a environments are comparable in the models and on the frequency vs. pressure plots (Figure 6.3); the higher density in $Cccm$ accounts for the higher frequency observed in $\nu_1 H_2f$.

The disappearance of Raman activity and emergence of amorphous S-S stretch around 475 cm^{-1} agrees with the behaviour of pure H_2S. However, Duan *et al.* predict the $Cccm$ structure of $(H_2S)_2H_2$ to remain stable to decomposition up to 300 GPa at room temperature. The $Cccm$ structure has also been measured

between 50 and 160 GPa, as the product of laser-heated S and H_2 [48, 49] which does not agree with an amorphous model. Although such measurements pertain to the arrangement of S atoms and not the positions of H, the presence of H_2 must be intrinsic to the structural integrity of $(H_2S)_2H_2$, otherwise H_2S would adopt the same structure. Until high pressure neutron diffraction experiments are possible, the behaviour after the Raman signal is lost cannot be firmly concluded. It is clear the H_2 environments are no longer detected; if S exhibits a similar structural arrangement, but H_2 environments are no longer fostered, then it suggests an entirely different arrangement of S-H bonding is adopted. The formation of molecular H_3S may be responsible. The similarities between the measured Raman spectra of $(H_2S)_2H_2$ and H_2S at these pressures however requires reconciliation.

To conclude: On compression above 32.6 GPa, phase II gradually evolves to phase III; strong H-bonding in phase-II retards the transition. There is strong evidence from both Raman and XRD data that phase III has $Cccm$ structure. The slow transition is also well described by a $I222 \rightarrow Cccm$ model. Some decomposition is evident above 34 GPa from the appearance of sulfur-III, and an amorphous S-S excitation is all that remains in the spectra above 48 GPa. From previous experimental studies S purportedly retains the same structural arrangement, but the lack of H_2 environments suggests the formation of molecular H_3S may have occurred.

6.3 Low-Temperature

Raman spectra were obtained using a 532 nm wavelength, solid state excitation laser. Samples were cooled in a cryostat using methods described in 3.2.4. Pressure was measured using stressed diamond edge frequency [70]. XRD was performed at the Advanced Photon Source, beamline 13-IDD, using a wavelength of 0.3344 Å; low quality data were collected at ambient temperature from a sample pressurised in a piston cylinder at 80 K and recovered to 300 K.

The prime $'$ symbol is used to indicate low temperature phases and excitations. H_2 cocrystal vibrons are labelled alphabetically $\nu 1H_2(a'–i')$ and distinct S-H stretching modes are labelled $\nu(j'–o')$ (Figures 6.16 and 6.17). No low temperature phases are identified in the literature for $(H_2S)_2H_2$ at the time of writing, aside from studies of the high T_c phase in the Mbar regime [28, 32, 48, 49].

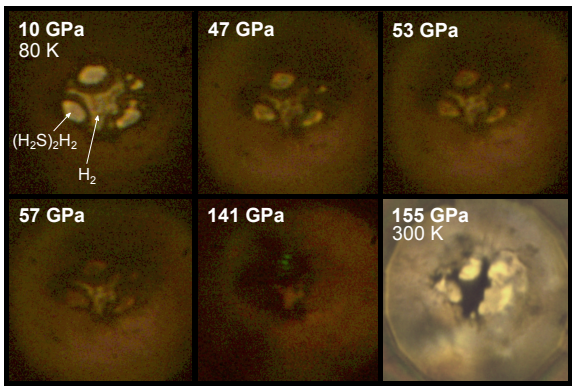

Figure 6.14 Photomicrographs of $(H_2S)_2H_2$ and H_2 compressed at 80 K (transmitted and reflected); final photomicrograph obtained after warming at 155 GPa (reflected).

6.3.1 Phase II'

Results

Phase II′ was adopted upon cooling of phase I $(H_2S)_2H_2$ at a fixed pressure of 10 GPa[‡]; the transition occurred between 184 and 173 K. Figure 6.15 shows Raman spectra obtained upon cooling. Exposure times were limited (10 s) as $\frac{dT}{dt}$ was continuous. A coarser diffraction grating was used to maximise Raman signal in the widest range of frequencies, at the expense of resolution (see section 3.2.4). The spectra of phase II′ are similar to ambient temperature phase II.

Upon cooling the S-H stretching region broadened and split into three excitations by 173 K (10.2 GPa), strongly resembling the phase II spectra at 16.7 GPa (300 K). Upon reaching 125 K the bandwidths reduced, revealing a two additional S-H stretching components. Although resolution was low, splitting of the H_2 vibron was also identified at 125 K. Longer exposures at higher resolution were obtained once the temperature stabilised at 80 K. Six peaks were conservatively fit to the S-H stretching region, although eight gave a perfect fit (Figure A.6). The three most intense modes, ($\nu o'$, $\nu m'$ and $\nu k'$), are reminiscent of Phase II stretches νg, νh and νi. Four distinct H_2 environments (a', b', c' and d') distinguish the Raman spectra of Phase II′ from any room temperature phase of $(H_2S)_2H_2$. Two broad and weak modes were observed around 300 and 600 rel cm^{-1}, which could be hindered rotational modes. A cluster of sharper peaks thought to be translational modes existed from 80 – 150 rel cm^{-1}.

[‡]usually, cooling causes significant pressure increases due to contraction of the metal cell body, here pressure remained between 10.1 and 10.6 GPa from 300 to 80 K.

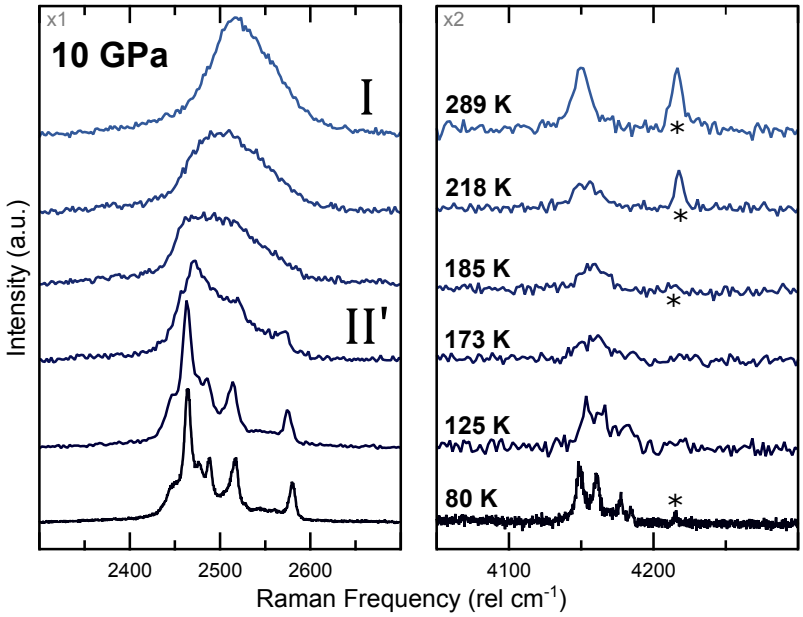

Figure 6.15 Representative Raman spectra of $(H_2S)_2H_2$ (phases I - II′) as a function of temperature, cooled at 10 GPa. * indicates pure H_2 vibron. Relative scales of each panel are indicated in the top left.

The behaviour of phase II′ upon compression is similar to that of phase II; the S-H stretching excitations broadened and softened substantially, while the ν_1H_2 vibrons all initially hardened, indicating similar H-bond driven structural changes seen in compression of phase II (Figure 6.17). The notable difference in overall S-H stretching profile between 10.3 – 12.8 GPa (Expanded in Figure 6.18 suggests that a simpler spectra may be observed below 10.3 GPa at 80 K, from another phase. This also raises the idea that the spectra obtained at 10.3 GPa could be part-way through a slow transformation like the phase II - III transition at 300 K, which would reconcile the number of stretching modes observed. Above 18 GPa the S-H stretching frequencies for phases II′ (80 K) and II (300 K) begin to converge, and become almost identical from 23 GPa, although the H_2 environments allow the phases to be distinguished. A direct comparison of phases II and II′ is shown for clarity in Figure A.7. From 18 GPa the translational modes gained intensity and split, whilst ν_1H_2d' and ν_1H_2c' began to converge into a single hump; ν_1H_2a' and ν_1H_2b' continued to gain intensity. An initially broad excitation emerged around 400 rel cm^{-1} and strengthened, whilst gaining frequency, up to the phase III′ transition at 29 GPa.

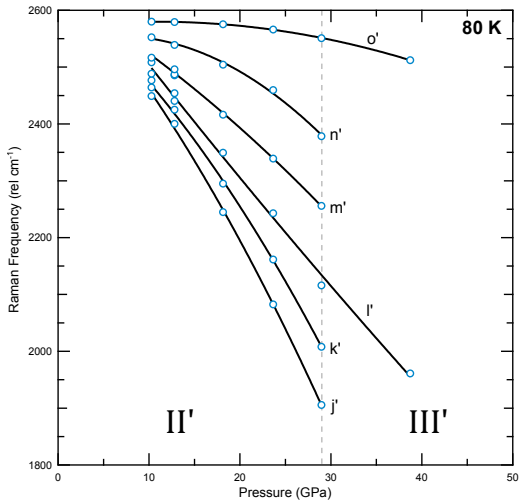

Figure 6.16 Observed Raman excitation frequencies between 1800 - 3600 rel cm^{-1} of $(H_2S)_2H_2$ plotted as functions of pressure, at 80 K. Black lines are guides for the eye.

Discussion

The S-H stretching region of phase II′ is apparently more complex that its ambient temperature counterparts, indicating significantly lower symmetry. The convergence of S-H stretches for II and II′ around 23 GPa suggests that phases II, II′ and III′ of $(H_2S)_2H_2$ could have a triple point around these conditions. But there is a clear relationship between phases II and II′, as the stretching modes bear a striking resemblance at higher pressures. However, like the phase I′ and II relationship of pure H_2S, phase II′ is structurally distinguished by having double the number of H_2 environments. Additionally, the sharpness of the stretching modes in phase II′ and the presence of lattice modes suggests complete orientational order, whereas some rotational disorder is thought to still exist in phase II at the transition pressure. In phase II′, the four H_2 environments a', b', c' and d' appear in two groups of two, which raises the notion that the $P1$ DFT optimisation of phase II could be a candidate for phase II′ (Figure 6.10). The formation of phase II′ also appears directed by H-bonding, as the ν_1 stretch softens on cooling to the transition at 125 K. Upon further cooling to 80 K the stretching frequencies hardly change. This could be interpreted as the adoption of a structure where the H-bonds are fully aligned (along the axis S-H---:S). The H-bonding seems to reach a soft-limit where an increase in pressure is then required to strengthen the bond. This however is better described by the arrangement in the $I222$ model, as H-bonds are slightly dislocated in $P1$.

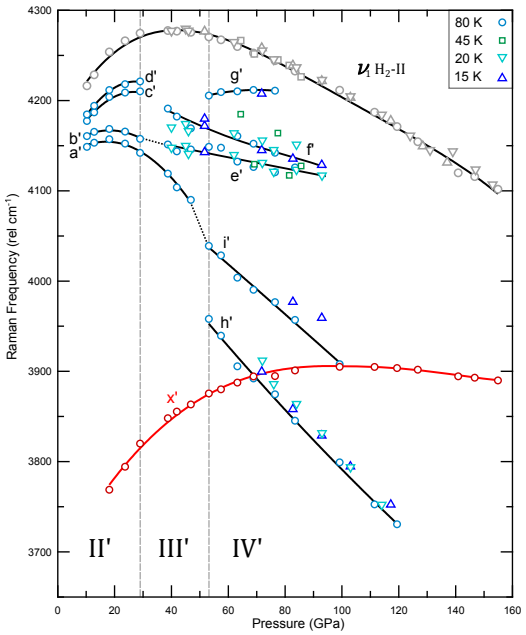

Figure 6.17 Observed Raman excitation frequencies between 3650 - 4300 rel cm^{-1} of $(H_2S)_2H_2$ plotted as functions of pressure, at various temperatures: circles (80 K), squares (45 K), down-triangles (20 K) and up-triangles (15 K). light blue, dark blue, green and turquoise points are from $(H_2S)_2H_2$, red open circles are from phase X′ (single sample), grey points are from normal molecular H_2. Black/red lines are guides for the eye.

The behaviour of the H_2 vibrons a', b', c' and d' upon compression allows them to be grouped into $a'b'$ and $c'd'$ (Figure 6.17). H_2a' and H_2b' appear to occupy two similar interstices, as do H_2c' and H_2d'. In contrast to the behaviour of phase II, all four vibrons harden with pressure indicating that they all initially experience repulsion interactions. The $\nu_1H_2a'b'$ pair frequencies follow a parabola, peaking around 18 GPa. $\nu_1H_2c'd'$ pair frequencies harden up the phase III′ transition. As the $\nu_1H_2a'b'$ frequency drops above 18 GPa, it is likely that lone pairs border their respective interstices which begin to interact with H_2a' and H_2b'. H_2c' and H_2d' appear to merely experience steric effects from their interstices. From this, the $a'b'$ sites are probably composed of S lone pairs facing into the interstice, whereas the $c'd'$ sites are potentially bordered by **H**-(S) atoms. Upon compression the $c'd'$ sites ostensibly squeezes H_2c' and H_2d' out, mostly into the $a'b'$ sites, (and a little to the new H_2f' site) resulting in the increase in intensity of ν_1H_2a' and ν_1H_2b' at 29 GPa. This indicates a rearrangement of S-H bonds, which is likely given the transition appears driven by the strengthening of H-bonds.

In conclusion: the isobaric transition, at 10 GPa, from phase I to phase II′ occurs at 173 K and is apparently also driven by establishment of H-bonds; phase II′ likely has much lower symmetry than phase II. Given the arrangement of S atoms is very similar across all ambient temperature phases of $(H_2S)_2H_2$, it is probable

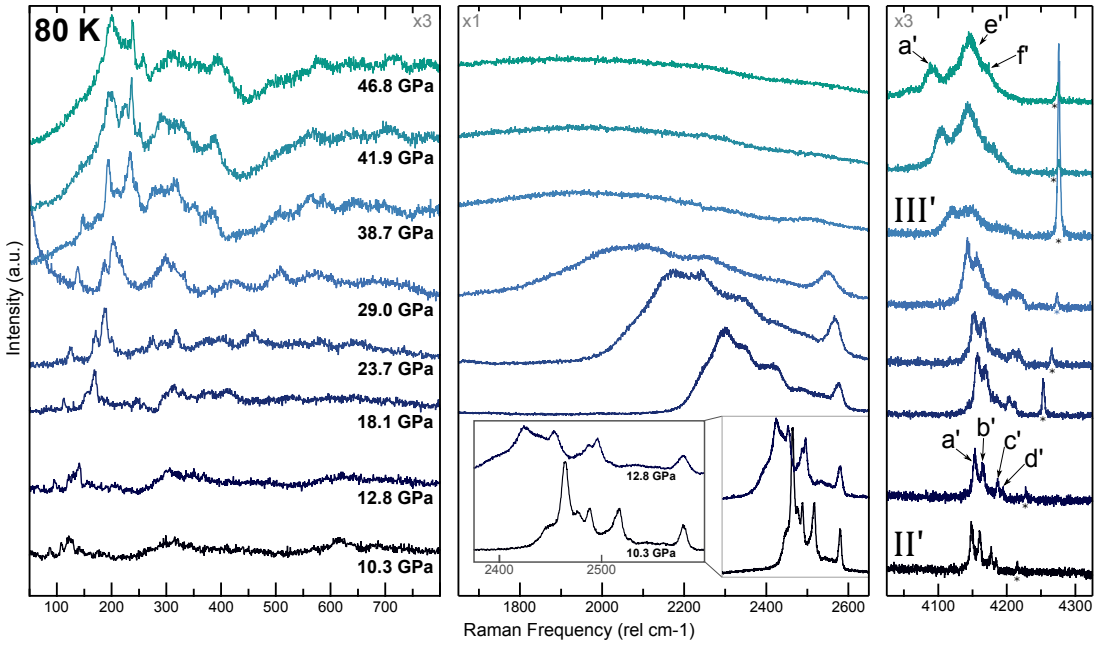

Figure 6.18 Representative Raman spectra of $(H_2S)_2H_2$ (phases II′ - III′) as a function of pressure, at 80 K. * indicates pure H_2 vibron. Relative scales of each panel are indicated at the top.

that a similar distribution exists for phase II′. Based on Raman alone, the $P1$ model proposed by Duan *et al.* is actually a better candidate for phase II′ than it is for phase II, although it still fails to account for the initial hardening of all H_2 environments, and the directly aligned H-bonds which are expected in phase II′. Neutron studies of $(D_2S)_2D_2$ are required to fully characterise phase II′. Low temperature studies below 10 GPa are also desirable to see if phase II′ is preceded by another low temperature phase.

6.3.2 Phase III'

Results

The first signs of a transition to phase III′ were seen from 29 GPa (Figure 6.18); new lattice modes emerged, previously weak translational modes gained intensity. The S-H stretching modes continued softening and broadening rapidly indicating the continued establishment of a tight H-bond network. As in other phases of $(H_2S)_2H_2$, phase III′ is characterised by a shift in the H_2 environment, namely the disappearance of ν_1H_2c' and ν_1H_2d'. H_2f' environment was faintly detected. The divergence of ν_1H_2a' and $\nu_1H_2b'(e')$ indicates a decrease in symmetry. There is a

notable dip in intensity of $\nu_1 H_2 b'$ at 38.7 GPa. After this dip $\frac{d\nu b'}{dP}$ approaches monotonic, interpreted as a structural shift in the interstice and hence $H_2 b'$ becomes $H_2 e'$ (Figure 6.17). Above 38.7 GPa $\nu_1 H_2 a'$ softens exponentially, leading to the notion that $H_2 a'$ and $H_2 b'$ resided in individual interstices in phase II′. 38.7 GPa is the highest pressure at which frequencies could be fitted to the S-H stretching region before peaks became too broad reflecting the behaviour of phase III (300 K). From the highest quality data (80 K), Phase III′ was fully established by 41.9 GPa, defined primarily by environments $H_2 a'$ and $H_2 e'$ with $H_2 f'$ as a high frequency shoulder. Evidence of Phase III′ was observed down to 15 K.

Discussion

Phase III′ is evidently more strongly H-bonded than phase II′ from the softening S-H stretches with strengthening of lattice modes. It would appear that much like phase III, charge transfer interactions between the H_2 environments and the H_2S lattice increase with pressure, causing $\nu_1 H_2 a$ to soften substantially in phase III′. The linear softening of $H_2 e'$ and $H_2 f'$ could be linked to the difference in $\frac{d\nu}{dP}$ of $\nu_1 H_2 e$ and $\nu_1 H_2 f$ in phase III (Figure 6.3). This would suggest a lower symmetry *Cccm* model for phase III′. The substantial broadening of S-H stretches also supports this notion; phase III′ possibly exhibits fluctuating H-bond chains (S-H−−−:S ↔ S:−−−H-S) along an axis. It is noteworthy that both phase III′ and III both appear to become fully established around 40 GPa. It is also very interesting that the H_2 environments continue to exist long after the S-H stretches become so broad they are almost undetectable, which offers an insight into the behaviour of $(H_2S)_2H_2$ at ambient temperature; perhaps the thermal motion is too high to foster H_2 environments above 50 GPa.

In conclusion: phase III′ likely has even lower symmetry than phase II′, evident from the behaviour of the H_2 environments above 29 GPa. Phase III′ appears to have several features in common with the *Cccm* model of phase III; the significantly broad S-H stretches could be explained by the formation of alternating H-bond chains (S-H−−−:S ↔ S:−−−H-S). It is likely that $H_2 a'$ experiences greater (equilibrium) alignment and charge transfer from S-H bonds than the $H_2 e'$ and $H_2 f'$ environments respectively. The structure of phase III′ is therefore suggested to be similar to the *Cccm* phase III model but with even lower symmetry, where $H_2 e'$ and $H_2 f'$ are different environments parallel to the axial H-bond chains, and $H_2 a'$ is orthogonal.

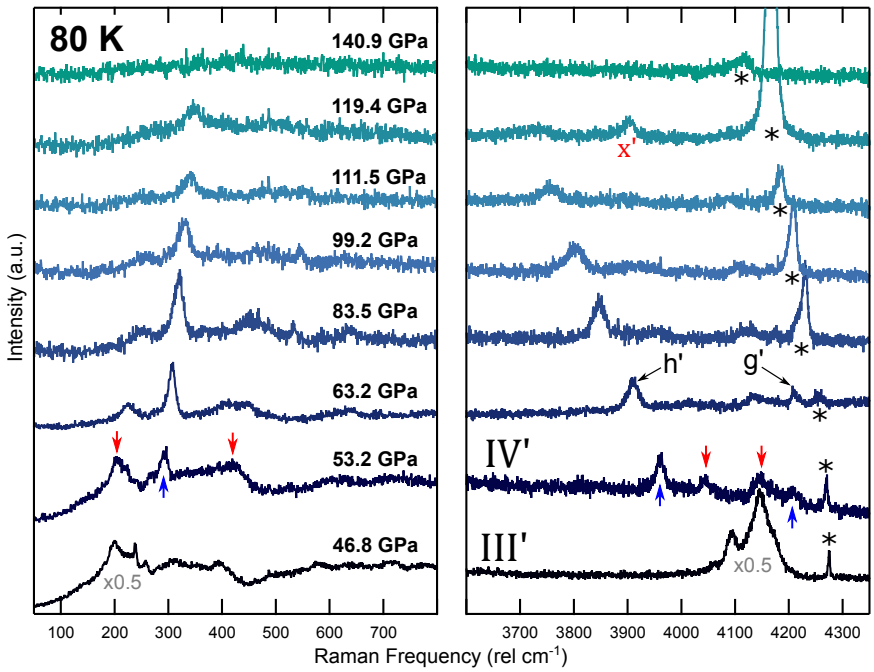

Figure 6.19 Representative Raman spectra of $(H_2S)_2H_2$ (phases III′ - IV′) as a function of pressure, at 80 K. Red arrows indicate fading phase III′ features. Blue arrows indicate emerging lattice mode and H_2 peaks from phase IV′. * indicates pure H_2 vibron.

6.3.3 Phase IV'

Results

The transition to phase IV′ was more abrupt than the previous low temperature transitions. At 53.2 GPa (80K) two new H_2 environments H_2h' and H_2g' appeared suddenly, at 3958 and 4206 rel cm^{-1} respectively; these environments exhibit the lowest and highest frequencies of all H_2 environments observed in $(H_2S)_2H_2$. At the transition pressure, H_2a' redshifted 50 cm^{-1}, becoming weaker and broader (H_2i'), whilst the intensities of ν_1H_2e' and ν_1H_2f' dropped; H_2i', H_2e' and H_2f' were all faintly detected up to ∼100 GPa. The Phase IV′ transition was also characterised by the emergence of a single sharp lattice mode around 300 rel cm^{-1} (Figure 6.19). A comparison of H_2h' vibron intensities, and low frequency regions at 53 GPa (15 and 80 K) suggests the transition pressure is slightly higher at 15 K than at 80 K, although further studies with low fluorescence diamonds are required. A comparison of the spectra at both temperatures is appended in Figure A.8. The reduction in the number of lattice modes indicates that phase IV′ has higher symmetry than phases II′ and III′.

The sample visibly darkened upon entering phase IV′ and became progressively more reflective on compression. The cryostat hinders an accurate assessment, but transmission only seemed to cease above 120 GPa, higher than was observed in pure H_2S at the same temperature. Photomicrographs obtained during the experiment at 80 K are shown in Figure 6.14.

At 80 K, the translational lattice mode at 300 cm^{-1} and the H_2h' vibron gained intensity up to 63 GPa. All features gradually weakened on further compression. The translational mode hardened while ν_1H_2h' and ν_1H_2i' softened monotonically. The frequency of ν_1H_2g' mode remained relatively constant until 80 GPa, where it was no longer detected. Upon reaching 120 GPa only pure H_2 was detected at high frequencies, although it is noted that background fluorescence and sample reflectivity could mask weak excitations.

Discussion

Phase IV′ does not have an equivalent ambient temperature counterpart for comparison. It is interesting that features are identifiable in the Raman spectra up to 120 GPa, compared to 50 GPa for pure H_2S at the same temperature. Although the S-H stretches are no longer observed, the presence of a lattice mode and H_2 environments is remarkable. The softening of H_2h' suggests it is either involved in significant charge transfer or the H-H bond is breaking. The latter proposition is suggested, given there is no evidence of H-bonding. The theoretical predictions made by Duan *et al.* state that *Cccm* $(H_2S)_2H_2$ becomes H_3S with trigonal *R*3*m* symmetry above 111 GPa [23]. This would also concur with an increase in symmetry,

In conclusion: phase IV′ has higher symmetry than phases II′ and III′, with only a single lattice mode. The environments H_2h' and H_2i' appear to rapidly dissociate upon compression which could be evidence of the formation of H_3S. This may suggest that $(H_2S)_2H_2$ is a preferable starting material for the production of H_3S than H_2S, as it appears to form from direct compression at low temperature, rather than requiring an obscure P/T path.

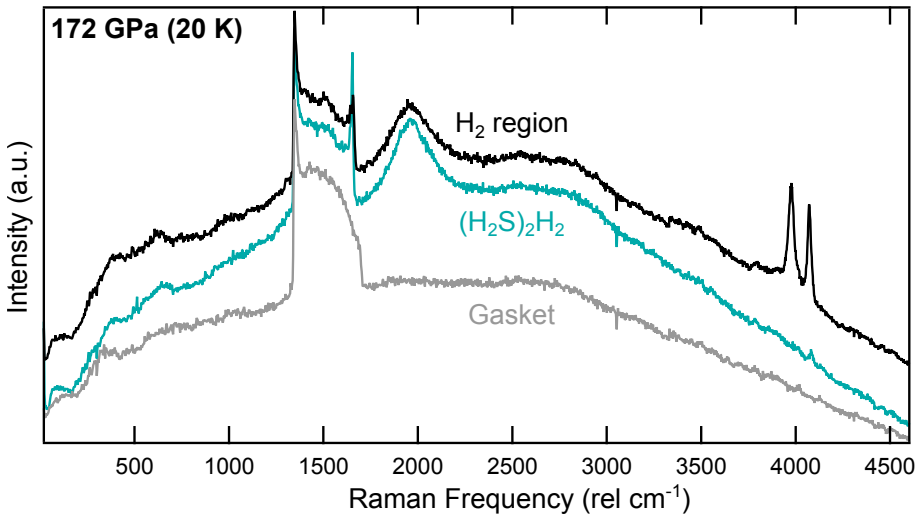

Figure 6.20 A comparison of Raman spectra from different sample regions: $(H_2S)_2H_2$, H_2 and gasket, at 172 GPa (20 K). The excitation at 1967 cm^{-1} is tentatively assigned to a new potential low temperature phase, V′, which could be the high T_c H_3S phase [28].

6.3.4 Tentative Phase V'

Results

Several intriguing results were obtained during the experimental runs performed at low temperature. At 20 K, a particular run exhibited evidence of phase III′ and phase IV′. The spectra lost all features by 120 GPa as expected. However, further compression to 172 GPa resulted in a sudden emergence of a broad excitation at 1967 cm^{-1} in both the $(H_2S)_2H_2$ and H_2 regions of the sample. The peak hardened on further compression and an additional high frequency shoulder was observed in the H_2 region of the sample.

Discussion

Figure 6.20 shows a comparison of the spectra to the gasket; although the background fluorescence is very high the excitation appears to be legitimate. Analysis of the H_2 region showed that the change occurred exactly where bulk pure H_2 transitioned from phase II to phase III. However, the pressure of 172 GPa obtained from the diamond edge is higher than the expected pressure for this transition in pure H_2. The author is tentative to assign a new phase as the result was never repeated. Nevertheless, this was an intriguing result as 1697 cm^{-1} is in the region where S-H stretching modes are usually observed.

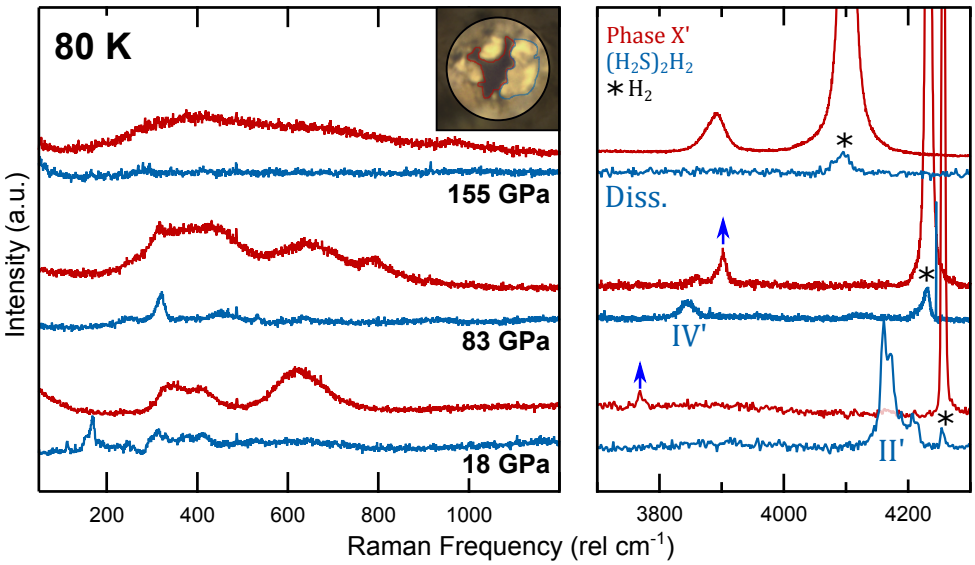

Figure 6.21 Representative Raman spectra as functions of pressure (80 K) of unidentified sulfur-hydrogen compound phase X′ (red) and $(H_2S)_2H_2$ (blue), obtained from sample regions indicated in inset (photomicrograph obtained at 155 GPa, 300 K).

If the pressure is corrected for the H_2 phase II - III transition pressure (∼155 GPa at 20 K) [123] then the potential phase V′ transition is much more comparable to the pressure of the high T_c superconducting phase of H_2S. It is possible that the excitation pertains to the symmetrisation of H-S-H bonds within the $Im\bar{3}m$ lattice predicted to be responsible for the superconducting phase [23, 28, 32]. These conclusions remain speculation until the result is repeated.

6.3.5 Phase X'

Results and Discussion

Another interesting result occurred during an experimental run performed at 80 K. This experiment produced the highest quality data for phases II′, III′ and IV′ using ultra-low-fluorescence diamonds. At 18 GPa, in the H_2 dominant region of the sample, a second H-H vibron appeared at 3769 cm^{-1} at 18 GPa ($\nu_1 H_2 x'$) (Figure 6.21). This indicates that a small quantity of H_2S was present in the H_2 dominant media after synthesis. This fact is not unusual, phase mixing was observed many times during synthesis, but the frequency of the H-H vibron was uncharacteristically low for $(H_2S)_2H_2$ at 18 GPa. Studying Figure 6.17 shows such low frequencies were only attained by H_2h' in phase IV′ above 110 GPa,

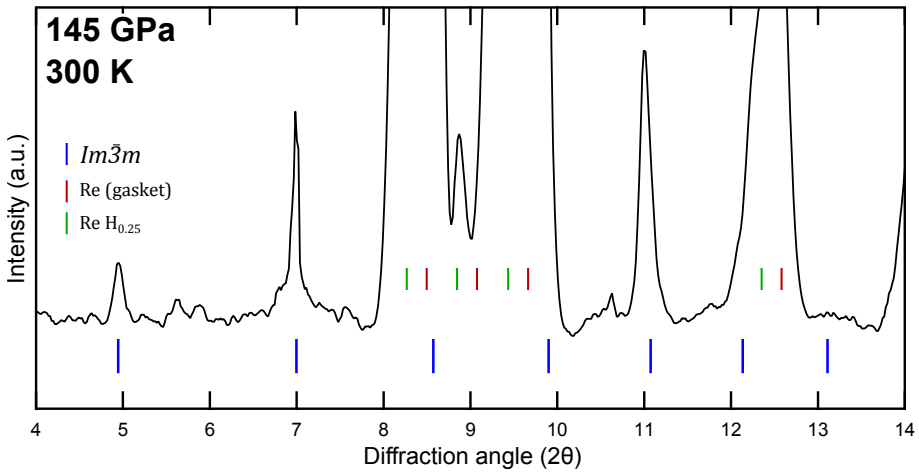

Figure 6.22 Observed diffraction pattern for phase X′. Tick marks indicate *bcc* ($Im\bar{3}m$) symmetry with unit cell $a = 5.48(2)$ Å. Although the data is poor, the unit cell indicates phase X′ has a higher H:S stoichiometry than 3:1.

which is thought to be a consequence of progressive weakening of the H-H bond. Upon compression the H_2x' sample region grew uniformly darker, confirming that it did not consist solely of pure H_2 (Figure 6.14). Although the behaviour appears substantially different to $(H_2S)_2H_2$, the nature of the compound remains unclear and it is therefore referred to as Phase X′ for brevity. A comparison of the complete data sets from both H_2 and $(H_2S)_2H_2$ regions of the sample is appended in Figures A.10 and A.11.

Figure 6.17 shows how the response to pressure was entirely different to $\nu_1H_2(a'-i')$; the excitation frequencies of H_2x' and H_2h' even became equivalent and crossed over at 69 GPa. H_2x' hardens substantially up to ∼80 GPa, after which the frequency becomes steady, interestingly almost mimicking the behaviour of pure H_2. Most astoundingly ν_1H_2x' continued to gain intensity and broaden up to 155 GPa, where Raman activity in the other areas of the sample had subsided. This suggests that the quantity increased with pressure, although it is unclear how this could occur. Phase X′ also survived two temperature cycles from 80 → 300 → 80 → 300 K, without any change in relative vibron intensity, demonstrating incredible stability.

XRD data collected at 300 K was indexed to bcc symmetry of S atoms, with $a = 5.48(2)$ Å (Figure 6.22); much larger than the unit cell length of 3.089 Å observed in H_3S at 150 GPa [32]. With the caveat that the data is rather poor, this suggests phase X′ could have a different stoichiometry to H_3S, with much higher hydrogen content, and containing molecular H_2. This would also be supported by the fact

that the H_2 environment is entirely different to the ones exhibited by phases II′ – IV′. XRD data was also collected on the $(H_2S)_2H_2$ section of the sample which fitted with bcc symmetry with a similar unit cell size; because the sample was a piston cylinder this data was discounted as it was likely also from phase X′ and not the $(H_2S)_2H_2$ region, which would have H_3S stoichiometry. Although the result is unusual and must be repeated the Raman data is clear and undeniable. There are two possible conclusions to draw:

- The first idea is that a sulfur-hydrogen compound of novel stoichiometry has formed within the H_2 media. The compound exhibits a single distinct molecular H_2 environment, which seems significantly different to the environments of $(H_2S)_2H_2$, as the frequency is remarkably low when first observed at 18 GPa. Additionally the $\nu_1 H_2 x'$ vibron does not split and appears to mimic the behaviour of pure H_2 on compression at low temperatures. The unit cell is significantly expanded in comparison to H_3S at similar pressures [32] which implies a much higher hydrogen content.

- The alternative proposal is that phase X′ is a form of $(H_2S)_2H_2$, but the surrounding excess H_2 has some effect on the behaviour and nature of bonding in the compound. This would justify the unit cell volume from the XRD data being comparable to the $(H_2S)_2H_2$ region of the sample. It would make sense that the components of phase X′ are H_2S and H_2, but it is difficult to justify how they would arrange any differently to the normal, well-defined phases of $(H_2S)_2H_2$ at low temperatures. Chapter 7 presents evidence that unusual behaviours are also observed in other sulfur-hydrogen mixtures, with H-bonding affected in particular. H-bonding is a key driving force in high pressure phases of $(H_2S)_2H_2$ and a distinct shift could instigate radically different behaviour on compression, particularly if stabilised by low temperatures. These results are included here rather than Chapter 7 for direct comparison to the low temperature behaviour of $(H_2S)_2H_2$.

At the very least, these results are evidential that sulfur-hydrogen compounds containing molecular H_2 are very stable around the superconducting pressure range. This could impact the theory of molecular H_3S being responsible for the high T_c phenomenon. It would be very interesting to see if bcc is adopted by S immediately from 18 GPa, or if phase X′ has various structural phases in its own right. Clearly the abundance of H_2 in the surrounding media, and the low temperatures, are pertinent to its formation and behaviour.

6.4 Conclusions

Phase I $(H_2S)_2H_2$ was only observed from 4.77 GPa, from many experiments, which is higher than the 3.5 GPa reported in previous studies [46]. Phase I is confirmed to have $I4/mcm$ symmetry. A thorough analysis of the data obtained in this study, compared to DFT models proposed in references [23, 46], finds orthorhombic $I222$ as the current best structural candidate for phase II, although it still fails to account for the expected 2:1 ratio of a:b H_2 environments. A previously unobserved slow phase transition between phases II and III (32.6 – 39.5 GPa) has been well documented by Raman spectroscopy. Phase III is thus shown to become stable from a lower pressure than previously anticipated (40 GPa), but is still very well described by the orthorhombic $Cccm$ symmetry as proposed by Duan *et al.* [23]. Evidence of sulfur-II and sulfur-III were identified upon compression of $(H_2S)_2H_2$ from 27 GPa, as is observed in pure H_2S. However, $(H_2S)_2H_2$ dissociates to amorphous sulfur above 48 GPa, demonstrating enhanced stability with respect to dissociation of pure H_2S (40 GPa) at the same temperature, with similar laser energy and power. The exact nature of the dissociated state of $(H_2S)_2H_2$ remains unclear.

A novel low temperature phase (II′) of $(H_2S)_2H_2$ was identified below 173 K at 10 GPa. Phase II′ ostensibly exhibits lower symmetry than $I4/mcm$ phase I and $I222$ phase II, and has four individual H_2 environments. $P1$ may be an appropriate structure candidate for phase II′ based on the Raman data. Upon compression at 80 K, a transition to another novel phase (III′) was identified at 38.5 GPa. Phase III′ would be well described by a lower symmetry version of the ambient temperature phase III $Cccm$ model. A third novel phase (IV′) was found stable above 53 GPa (80 K) which is associated with an increase in symmetry. Phase IV′ fosters two new H_2 environments (H_2h' and H_2g') which emerge at lower and higher frequencies (respectively) than all other phases of $(H_2S)_2H_2$. Phase III′ environments (H_2e' and H_2f') were observed up to 100 GPa (80 K). Phase IV′ was no longer detected above 120 GPa. 111 GPa is where $R3m$ H_3S is predicted to form, which aligns with the loss of H_2 detection above 120 GPa. A single study performed at 20 K up to 180 GPa yielded a measurement which could pertain to another low temperature phase (V′); evidence of phase V′ was found at the H_2 phase II – III transition, which is comparable to where the high T_c phase of H_3S is identified [28]. This could mean the broad vibron found in phase V′ relates to the predicted $Im\bar{3}m$ H_3S superconducting phase

[23, 32]. A strange sulfur-hydrogen compound containing molecular H_2 (dubbed phase X′) was observed in the H_2 rich media at low temperatures, identified from a low frequency shifted H_2 vibron. Although the nature of phase X′ is unclear it contains molecular H_2, and is suggested to have a higher H:S stoichiometry than 3:1. An alternative theory is that phase X′ is $(H_2S)_2H_2$ with distorted behaviour as a consequence of existing in low concentrations within an H_2 matrix.

These studies set up a plethora of future experiments. Neutron studies of the $(D_2S)_2D_2$ clathrate and phases I - III (and above the dissociation pressure, if it were possible) are essential to the complete elucidation of room temperature behaviour. Indeed, such studies may also be useful for the pure D_2S system. The S-H stretching region of phase II′ was complex and shifted rapidly upon compression, so it is likely that another low temperature phase exists below 10 GPa ($<$ 173 K); this could be investigated through the use of large diamond culets, limiting the maximum pressure but allowing a thorough exploration of the lower pressure regime, at low temperatures. The pressure boundaries of all low temperature phases could be refined by repeating the experiments at 80 K, and performing pressure runs at various temperatures to fully map out the phase diagram. The phase V′ and X′ results must be further investigated and repeated. XRD studies are also desirable for $(H_2S)_2H_2$ at low temperatures.

Chapter 7

Mixtures of Hydrogen-Sulfur Systems

7.1 Introduction

This chapter explores various mixtures of H_2S, $(H_2S)_2H_2$ and H_2. The development of techniques for direct synthesis of H_2S led to some interesting peripheral findings, providing further insight into the high pressure sulfur-hydrogen systems. The first section provides evidence that $(H_2S)_2H_2$ clathrates can form within the fluid H_2S phase at very low pressures. The second section shows that H_2S can be trapped in a fluid state above the usual solidification pressure, when mixed in low concentrations with fluid H_2. The third section presents a Raman study of coexisting H_2S and $(H_2S)_2H_2$ crystallites, and how the nature of H-bonding is influenced in both systems at high pressures; these results help explain the enhanced stability of $(H_2S)_2H_2$ over H_2S, with respect to pressure induced dissociation. The final section describes how $(H_2S)_2H_2$ mixtures can be formed directly via laser induced decomposition of pure H_2S.

Samples were either synthesised from S and H_2 (5.2) or prepared via cryo-loading pure H_2S (3.2.3). Raman spectra were obtained using both 514 nm Ar^+ ion, 647 nm Kr^+ ion and 532 nm solid state excitation wavelengths. XRD data was obtained at Diamond Light Source beamline I-15, using a monochromatic wavelength of 0.4246 Å. Pressure was measured using Ruby fluorescence [66, 78] and stressed diamond edge frequency [70], calibrated to universal standards.

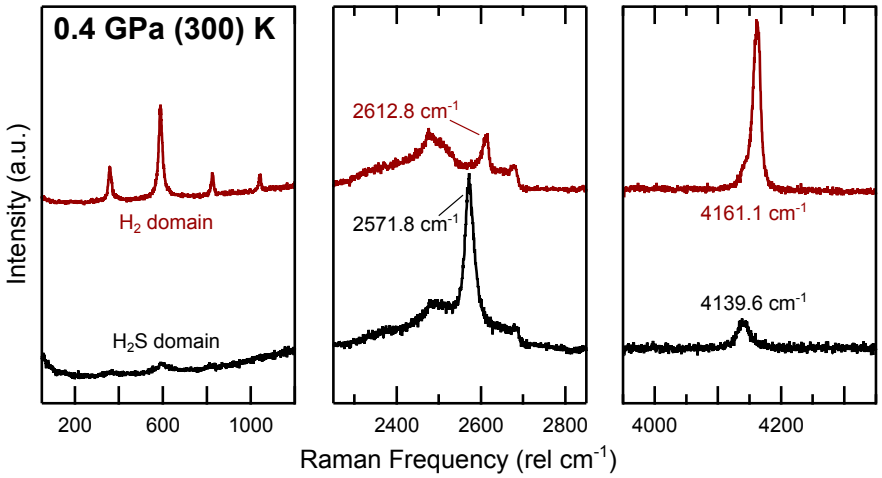

Figure 7.1 Representative Raman spectra of fluid H_2S (containing an $(H_2S)_2H_2$ clathrate) (black) and fluid H_2 (red) regions of a sample at 0.4 GPa and 300 K (Figure 5.2b for reference photomicrograph). $(H_2S)_2H_2$ is identified in the fluid H_2S phase from the redshifted H_2 vibron at 4139.6 cm^{-1}. The ν_1 H_2S vibron present in the H_2 phase is blueshifted closer to the frequency of gaseous H_2S.

7.2 Fluid Phase $(H_2S)_2H_2$ Clathrate

Results

$(H_2S)_2H_2$ was observed in the fluid H_2S phase at 300 K from 0.2 - 0.4 GPa, which has not been reported previously. Formation was identified from the Raman spectrum by a single hydrogen vibron (ν_1H_2a) at 4140 rel cm^{-1}, shifted 22 cm^{-1} lower in frequency than ν_1H_2, and ν_1 (S-H) shifted 9 cm^{-1} higher in frequency, which is also observed in solid $(H_2S)_2H_2$ (See Figure 7.1). Formation was observed below the solidification pressure for phase I (H_2S), reminiscent of the behaviour of clathrate hydrates, whereby the H_2S must be frozen by the interaction with H_2 [124–126]. The ν_1H_2a vibron was much weaker in the clathrate phase than in solid $(H_2S)_2H_2$ above 5 GPa, which could be due to limited mixing between the H_2 and H_2S domains. Formation of clathrates was only witnessed twice out of many syntheses, and was only observed when using the slow cooling technique described in 5.2.2. In both cases, solidification of H_2S resulted in the disappearance of ν_1H_2a and ν_1 shifted to a normal frequency for phase I (H_2S). Samples were visually identical to all other H_2/H_2S samples at the same conditions (Figure 5.2). Unfortunately, no structural data was obtained.

Discussion

The limited number of observations of $(H_2S)_2H_2$ clathrates indicate low stability. Mixed phase fluid/fluid samples (i.e. fluid H_2 containing a small H_2S component, and *vice versa*) where clathrate formation was *not* observed, would essentially separate over time to isolated H_2 and H_2S phases. This suggests that the slow-cooling synthesis technique is significant. The formation of a clathrate would imply the presence of very weak H-bonding. If true, this is the lowest pressure, at ambient temperature, where evidence of H-bonding has been observed in H_2S. Although the frequency of $\nu_1 H_2 a$ is only 2 cm^{-1} higher in the clathrate than in phase I $(H_2S)_2H_2$, the frequency of ν_1 is $\sim$50 cm^{-1} higher in the clathrate (Figure 6.3). This is likely due to increased H-bonding between the H_2S molecules upon solidification of $(H_2S)_2H_2$, and demonstrates there is little direct charge transfer to H_2a. It also implies that the clathrate likely exhibits a different molecular arrangement to solid phase I $(H_2S)_2H_2$. Nonetheless, ν_1 is blueshifted by $\sim$10 cm^{-1} in both the clathrate and in phase I with respect to pure H_2S at the same conditions, perhaps due to Van der Waals interactions with $\nu_1 H_2 a$ which would not be present in the pure species.

These results are consistent with the formation of a weakly H-bonded H_2S structure with a single H_2 environment resembling a clathrate hydrate [124–127]. Interactions are stronger between the neighbouring H_2S molecules than between H_2S and H_2a. The presence of H_2 must somehow drive the formation, although curiously $(H_2S)_2H_2$ did not always form when a small H_2 component was contained in the H_2S phase. This could explain why formation ostensibly requires slow-cooling; fast quenching may not give the clathrate enough time to form, or an increase in pressure upon fast quenching may destabilise the formation, consistent with hydrate behaviour [127]. It could also simply be due to the enhanced mixing effect observed from slow cooling. Above 0.5 GPa the fcc arrangement of phase I H_2S becomes favourable, excluding H_2 from the structure, until the formation of phase I $(H_2S)_2H_2$ occurs at 4.77 GPa. It was considered that the observed frequency shifts could also arise from phase mixing. This seems to occur in the H_2 dominant region, which is discussed below: Figure 7.1 shows that the small H_2S component mixed with the H_2 region is sharp and shifted to 2613 cm^{-1}, close to gaseous H_2S (2617 cm^{-1}). However, the excitation from the H_2 component within the H_2S dominant region is far broader than gaseous H_2, and much lower in frequency, more consistent with an ordered structure than fluid mixing.

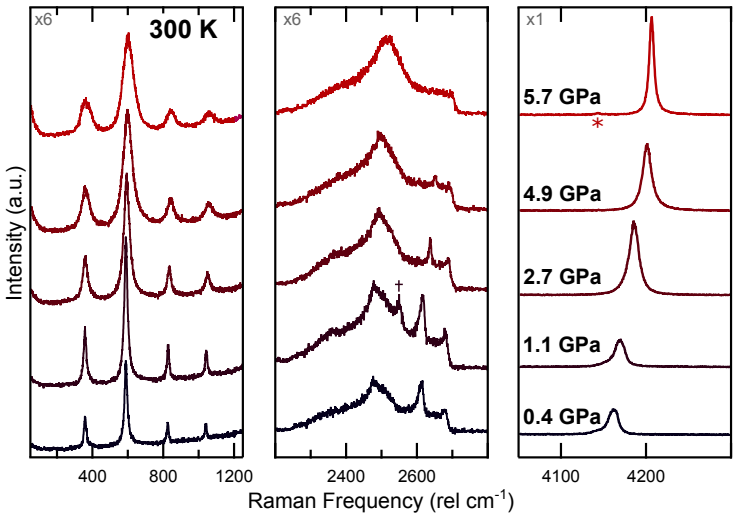

Figure 7.2 Representative Raman spectra on compression of fluid H_2S trapped within the bulk fluid H_2 region of a synthesised sample, at 300 K (reference photomicrograph: Figure 5.2b) † indicates ν_1 from phase I H_2S and * indicates $\nu_1 H_2 a$, both are assumed to be detected from the beam passing through the transparent sample. The relative scale of each panel is indicated top left.

7.3 Hydrogen Sulfide Dilution in Hydrogen

Results

When H_2S is mixed in low concentrations within the bulk H_2 phase of the sample, it exhibits a peak profile and frequency shift consistent with fluid H_2S at ambient pressure. When dissolved in the major H_2 phase at 0.4 GPa (300 K), the ν_1 fundamental stretch of H_2S was shifted about 55 cm^{-1} higher in frequency, to 2613 rel cm^{-1} (Figure 7.2). This is much more reflective of gaseous H_2S at ambient temperature and pressure (2617 cm^{-1}). The frequency of the H_2 stretch did not seem to shift from the norm. Contrary to the behaviour of pure H_2S the frequency of ν_1 increased while the bandwidth decreased upon compression. The intensity of the ν_1 H_2S mode progressively decreased and was no longer detected upon the solidifications of H_2 above 5 GPa.

Discussion

From these observations H_2S ostensibly acts as a gas within fluid H_2 media. In pure fluid H_2S, the ν_1 frequency softens upon compression due to the progressive establishment of intermolecular H-bonds. Here the hardening of the ν_1 vibration indicates that no H-bonding takes place between the H_2S molecules, and thus the

molecules must be individually isolated, suspended within the H_2 media. The H_2 phase is less dense than bulk H_2S at the same pressure, so the individual H_2S molecules experience a lower hydrostatic pressure and the frequency of molecular vibration is higher. When the density of the H_2 media increases the H_2S molecules experience repulsion interactions which raises the S-H stretching frequency. The bandwidth narrows because the Brownian motion of molecules is reduced at higher density, diminishing the number of collisions with neighbours. The intensity of ν_1 decreases as H_2S is squeezed out from the solidifying H_2 phase.

Similar frequency shifts have been observed in pressure induced supercritical fluid mixtures of CO_2 and CH_3OH [128], which is comparable to H_2 and H_2S in terms of being a non-polar/polar mixture. The influence of the solvent is thus steric rather than electrostatic. However, such studies of very low solute concentrations under pressure generally pertain to industrial applications and offer little insight into the mechanisms. A theoretical study of the directly comparable H_2O:H_2 system finds isotherms and molar fractions where a homogenous phase can exist [129]; coexistence at 300 K was only found at low H_2O mole fraction (< 0.05), and was significantly improved by compression up to 0.25 GPa. This is fairly congruent with these observations as the H_2S mole fraction was likely very low, although it could never be accurately determined. Other studies of dense mixtures related to polar solvents (e.g. H_2O:CH_3OH), but at higher molar fractions where H-bonding becomes more relevant [130–132]. Some interesting results might arise from a study where the molar fractions of H_2S:H_2 could be accurately controlled; it can be postulated that H-bonding would only become significant above a certain H_2S:H_2 molar ratio, which could be determined when $\frac{d\nu_1}{dP}$ (H_2S) shifts from positive to negative.

Although the solubility of fluid H_2S in H_2 appears to be thermodynamically unstable at 300 K, as the phases separate slowly over time (see section 5.2), the effects can be explored if a mixture is compressed soon after synthesis. Here H_2S has been dissolved in low concentrations, maintaining a fluid state within fluid H_2, $\sim$4.5 GPa above the usual solidification pressure of H_2S.

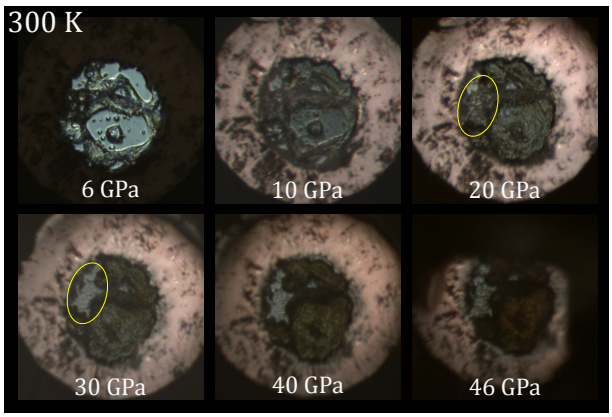

Figure 7.3 Photomicrographs (simultaneous transmission/reflection) of an $(H_2S)_2H_2$ and H_2S mixed sample at different pressures. A section (outlined in yellow) exhibited an interesting change of texture between 20 - 30 GPa. The sample takes on a yellowish appearance above 40 GPa from the emergence of elemental sulfur.

7.4 Mixtures from Synthesis

When experimenting with synthesis conditions it was found that mixtures of $(H_2S)_2H_2$ and H_2S could be reliably synthesised. The methodology is detailed in section 5.2.2, but can be summarised as forced non-uniform phase separation by quickly quenching a hot solution of H_2S and H_2 above the solidification pressure of H_2S. Samples produced in this manner have many interspersed pockets of H_2 and H_2S (Figure 7.3). As a result, $(H_2S)_2H_2$ would often only partially form on compression, and entirely separate crystallites of molecular H_2S, and H_2 could be simultaneously measured in the same Raman spectrum from one laser exposure. The coexistence of H_2S and $(H_2S)_2H_2$ seems to affect the detected frequencies of various Raman excitations, and the phase transition pressures. Although in reality these samples were composed of many individual clusters of H_2S and $(H_2S)_2H_2$ crystallites, the term mixture is used as it describes the overall macroscopic composition.

Results

The formation of phase I $(H_2S)_2H_2$ usually occurs at 4.8 GPa, but was delayed until 6.1 GPa in the mixture, identified by the appearance of $\nu_1 H_2 a$. molecular H_2 frequencies from mixtures are plotted alongside pure species in Figure 6.3; the mixture did not appear to affect the frequencies of H_2 vibrons from $(H_2S)_2H_2$, but an additional vibron was clearly identified from 19 - 32 GPa, as a high frequency

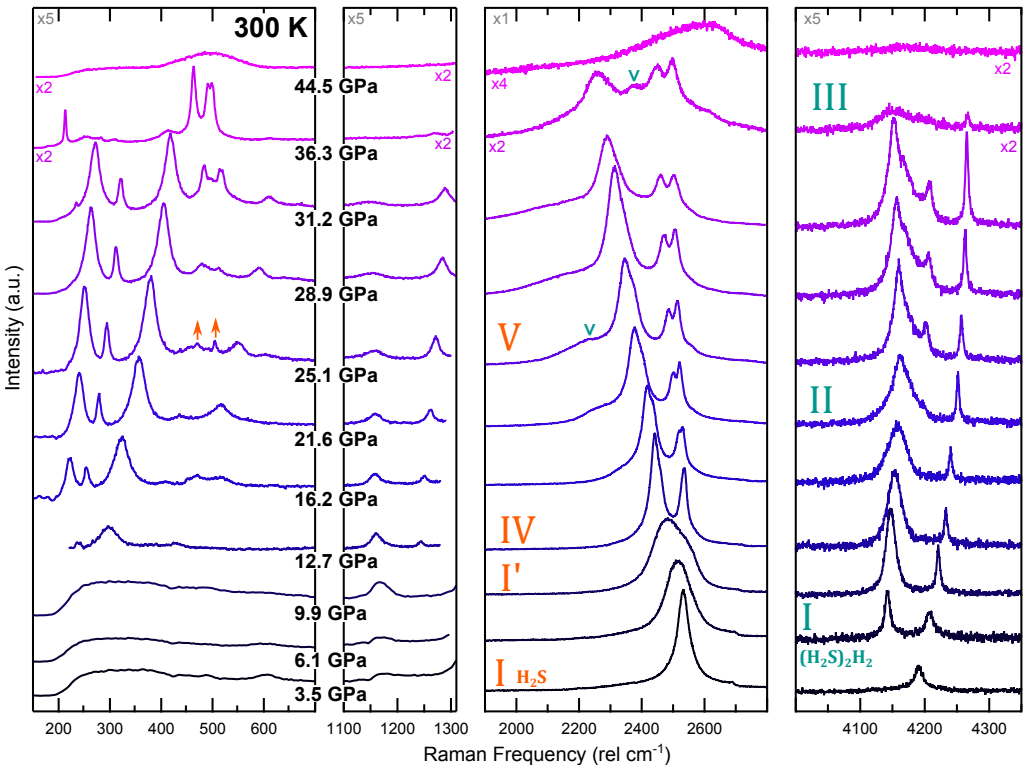

Figure 7.4 Representative Raman spectra of $(H_2S)_2H_2$, H_2S (and H_2) mixtures as a function of pressure, at 300 K, obtained from the same spatial point in the sample. Orange labels and arrows pertain to H_2S phase transitions; turquoise labels pertain to $(H_2S)_2H_2$. Relative scales of each panel are indicated top left.

shoulder on $\nu_1 H_2 a$ in the mixture. This vibron was identified as $\nu_1 H_2 c$ which curiously emerges at the phase III transition in pure $(H_2S)_2H_2$. The transition to phase II $(H_2S)_2H_2$ was also ostensibly delayed as $\nu_1 H_2 b$ was not identified until 21.6 GPa, usually observed from 16.7 GPa. The dissociation of $(H_2S)_2H_2$ seems accelerated, and the high frequency excitations suddenly lost intensity and clarity above 36 GPa, in both runs where mixtures were produced (Figures 7.5 and 7.4). In the pure species, the slow transition from phase II to III occurred from $\sim$ 32 GPa, and was completed by 39.5 GPa. The only evidence of phase III in mixtures were H_2 vibrons with frequencies corresponding to $\nu_1 H_2 a$ and $\nu_1 H_2 f$ detected in one run, and the frequencies of $\nu_1 H_2 b$ and $\nu_1 H_2 c$ in another run, all detected around 36 GPa. Phase I′ of H_2S was observed at 7.6 GPa, as would be expected for the pure species, but persisted over a slightly wider pressure range. Phase IV is usually adopted from 11 GPa, but the ν_1 and ν_3 peaks were still convoluted at 11.5 GPa; the characteristic phase IV splitting was not observed until 12.7 GPa. Although the phase IV H_2S transition also appears delayed, the margin is apparently less severe than transitions in $(H_2S)_2H_2$.

In both cases where mixtures were produced, the S-H stretching excitations from H_2S dominated those from $(H_2S)_2H_2$ (Figure 7.4). νg and νi (the lowest and highest frequency S-H stretches respectively from $(H_2S)_2H_2$ can be identified on either side of ν_1 and ν_3 (H_2S), but frequencies from fits were deemed too inaccurate due to the broadness and convolution of the bands. A peak which potentially corresponds to νl $(H_2S)_2H_2$ was definitively detected in both runs, but only after dissociation had reduced the intensity of the H_2S stretches (Figure 7.5). The softening of this peak with pressure was significantly reduced compared to pure $(H_2S)_2H_2$. on Figure 7.4, green 'v' labels indicate the S-H stretches on the spectra from $(H_2S)_2H_2$.

Above phase I′, the rate of softening for $\nu_{1,3}$ frequencies in the mixture was significantly reduced compared to pure H_2S suggesting the H-bonding was weakened. Figure 7.5 shows how these frequencies deviated further from the pure species upon increasing pressure. Interestingly the ν_2 H_2S frequency was entirely unaffected, congruent with an influence solely on H-bonding. The lattice modes from the mixture were also initially of comparable frequency to pure H_2S, but the rate of hardening upon compression was also reduced.

The frequencies of excitations corresponding to elemental sulfur were not shifted in the mixture. Peaks corresponding to S-II were observed in the mixtures at 25.1 GPa, indicating the onset of dissociation occurs 2 GPa lower than in the isolated H_2S and $(H_2S)_2H_2$ systems. When using higher energy excitation wavelengths (514 nm), dissociation was essentially complete by 39.1 GPa in the mixture, versus 47.7 GPa in $(H_2S)_2H_2$ and 40.1 in H_2S. One mixture run was measured with a lower energy excitation wavelength (647 nm), where complete dissociation occurred at 46 GPa. It would appear that dissociation of $(H_2S)_2H_2$ in particular is accelerated by the mixture.

Diffraction data obtained from a sample of H_2S:$(H_2S)_2H_2$ mixture has been presented in Figure 6.6 at 6.8 GPa. The unit cell volume obtained for phase I $(H_2S)_2H_2$ was 302.9 Å^3 which corresponded to 6.72 GPa from EoS data for $I4/mcm$ structure extracted from reference [46]. However, Phase I H_2S ($Fm\bar{3}m$) had an expanded unit cell dimension of $a = 5.68(6)$ Å compared to 5.5025(6) Å for the same sample at 1 GPa, when only containing phase I H_2S and H_2. Although the error is substantially large, the expanded unit cell reflects the weaker H-

bonding in the mixed system. The raw detector data at 6.8 GPa shows both substances exist as individual single crystals (Figure A.12). Visually the mixture samples darkened on compression as expected. However, Figure 7.3 highlights a curious observation where a darker patch, containing the mixed species, lightened and became more visually transparent after the onset of dissociation (above 25 GPa), where it was shown to contain mostly molecular H_2.

Discussion

The mixture is actually many small clusters of H_2S and $(H_2S)_2H_2$ crystallites residing in close proximity. A continuous uniform mixture is not consistent with the XRD data (Figure A.12). The composition and behaviour on compression can be compared to various systems. For example, regions of incomplete mixing in H_2O:CH_3OH mixtures result in segregated crystallites of both H_2O and CH_3OH; the softening of the O-H water stretch on compression (i.e. $\frac{d\nu}{dP}$) is reduced in the mixture, from shifts in the local H-bonding regimes [130, 133, 134]. Comparable effects are also observed in high pressure 'salty ices'where ionic inclusions partially break up the H-bonded H_2O network and reduce the overall strength of H-bonding [135]. Similarities can also be drawn between non-H-bonding mixtures, such as Xe-N_2 Van Der Waals compounds [136]. The mixture is not homogenous and no chemical bonds exist between Xe and N_2, yet the position of the N_2 vibron is shifted from a collective 'matrix effect'.

It is clear that H-bonding is weakened in both components, apparently as a consequence of their coexistence. The softening of S-H stretching frequencies in H_2S is attenuated, and the H-bond driven phase transitions are delayed. Ostensibly, the phase transitions in $(H_2S)_2H_2$ are more affected by H-bonding than pure H_2S as the delay between the phases is far greater. The weakening of H-bonds is also amplified at higher pressures in the mixture, which results in the enhanced deviation of S-H stretching frequencies for H_2S, and increased difference between phase transition pressures for $(H_2S)_2H_2$ (i.e. phase I was delayed by 1.4 GPa, but phase II was delayed by 4.9 GPa). Weaker H-bonding in H_2S also reduced the rate at which the phase IV H_2S lattice modes hardened. The ν_2 frequency is unaffected as it lies perpendicular to the direction of H-bonding [81, 89]. It is interesting that the frequency of the H_2 vibrons contained within the $(H_2S)_2H_2$ lattice are not noticeably affected, even though the phase transition pressures are shifted. It is also apparent that the normal H_2 environments

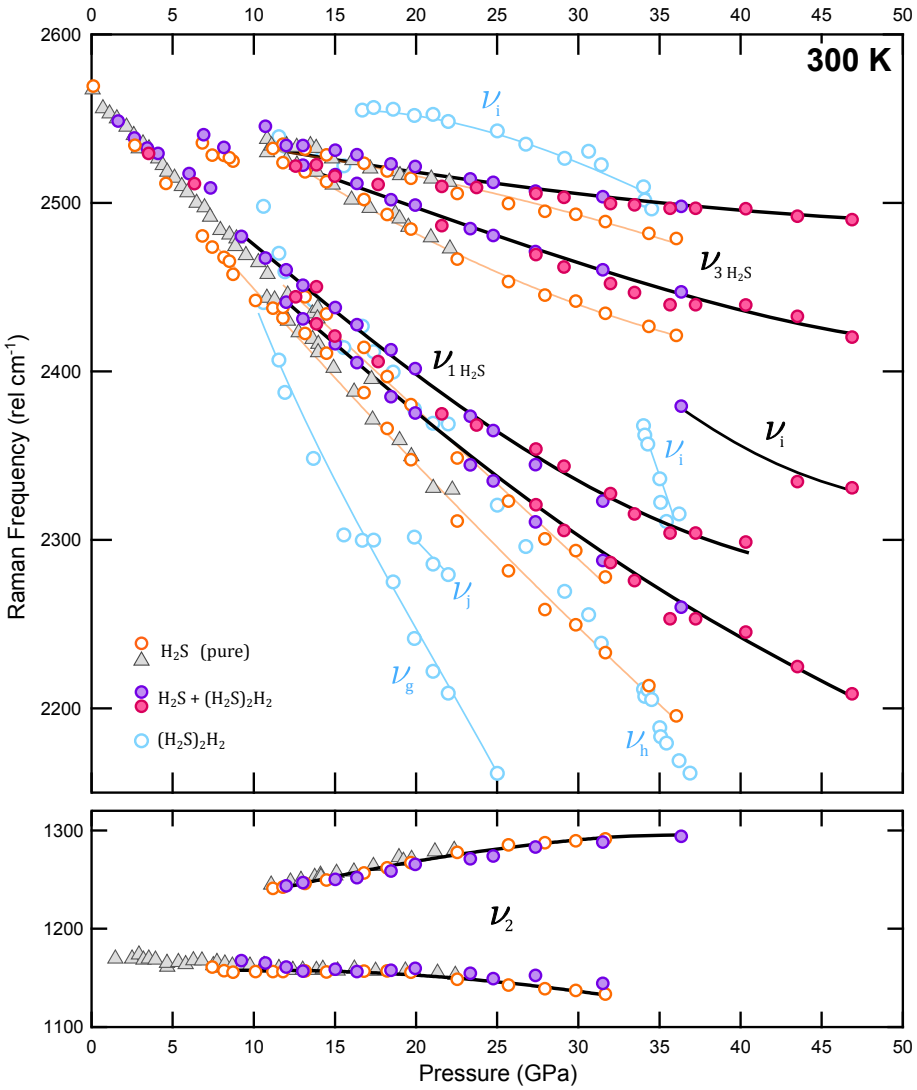

Figure 7.5 Observed Raman excitation frequencies between 1100 - 2600 rel cm^{-1} of $(H_2S)_2H_2$:H_2S mixtures plotted as a function of pressure, at 300 K, alongside data from the respective pure species for comparison. Filled circles are data from the $(H_2S)_2H_2$:H_2S mixture, pink and purple refer to different experimental runs; Open orange circles (Chapter 4) and filled grey triangles (Reference [81]) refer to pure H_2S; Open blue circles refer to pure $(H_2S)_2H_2$ (Chapter 6). Lines are intended as guides for the eye.

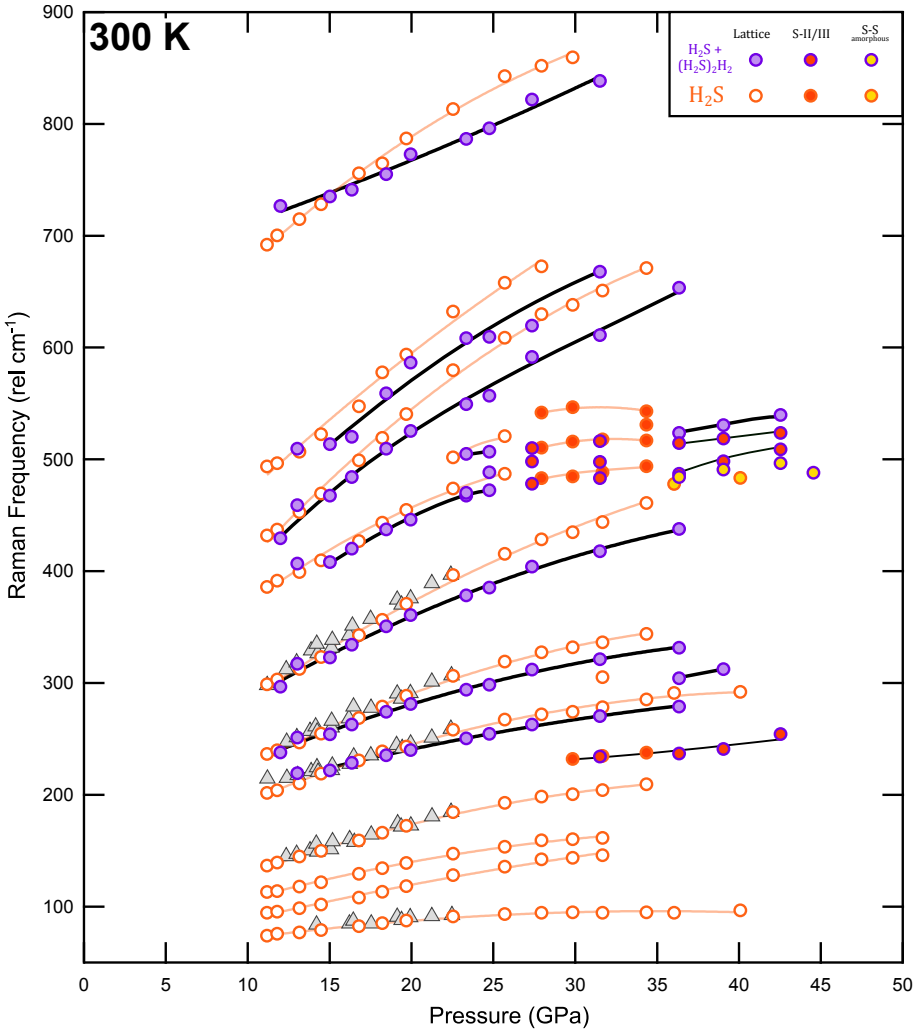

Figure 7.6 Observed Raman excitation frequencies between 0 - 900 rel cm^{-1} of $(H_2S)_2H_2$:H_2S mixtures plotted as a function of pressure, at 300 K, alongside data from pure H_2S for comparison. Purple outlined circles are data from the $(H_2S)_2H_2$:H_2S mixture; Orange outlined circles (Chapter 4) and filled grey triangles (Reference [81]) refer to pure H_2S; Circles filled in red matched frequencies corresponding to elemental sulfur-II or III; circles filled in yellow are assigned to amorphous sulfur. Lines are intended as guides for the eye.

expected from phase I – II for $(H_2S)_2H_2$ remain unaffected; the surrounding (cocrystal) H_2S molecules likely shield the H_2 molecules from the effects of the (pure) H_2S crystallites. This implies that the frequency attenuation of guest H_2 molecules of $(H_2S)_2H_2$ is influenced more by sterics than electrostatic effects.

The H-bonding in $(H_2S)_2H_2$ is affected by the mixture such that the transition to phase III cannot properly occur. This is congruent with a *Cccm* structure for phase III (See section 6.2.2). This would also explain why different phase III H_2 environments are observed around 36 GPa in the two experimental runs. The *Cccm* structure is mainly characterised by H-bonds which have strengthened to the point where the 'H' atom essentially resides equidistant to both S atoms involved in the bond, such that a dynamically alternating H bond is established (i.e. S-H --- :S $\leftrightarrow$ S: --- H-S). If H-bonding never strengthens to this point then these chains are not established in the same manner. The lower dissociation pressure of $(H_2S)_2H_2$ appears to be linked to the dissociation of the H_2S component. This suggests that the enhanced dissociation pressure of pure $(H_2S)_2H_2$ versus pure H_2S arises from the maximal strengthening of H-bonds resulting in the alternating H-bond chains. This idea is consistent with the observed differences in dissociation pressure of the mixture (39.1 GPa) and pure H_2S (40.1 GPa), compared to pure $(H_2S)_2H_2$ (47.7 GPa).

The shifts in S-H stretching frequencies is consistent in both experimental runs. However, only one run showed H_2c present in phase II $(H_2S)_2H_2$. This run also exhibited H_2c, b in the phase III pressure regime, whereas the other showed H_2 vibrons with frequencies corresponding to H_2a, f. This raises the notion that the stoichiometry could potentially differ among crystallites. Another suggestion is that the two mixed samples had slightly different ratios of H_2S:$(H_2S)_2H_2$; the transition from phase II – III in pure $(H_2S)_2H_2$ was shown to be sluggish due to the strength of H-bonding in phase II preventing the phase III conformation from being immediately adopted at the transition pressure. H_2S crystallites somehow weaken the H-bonding in $(H_2S)_2H_2$ then this transition would be expected to be affected. It appears that different H_2 environments are temporarily stabilised (around 36 GPa) despite the lack of the phase III axial H-bond chains. It is worth considering that ionic inclusions prevent symmetrisation of H-bonds within salty ices at high pressures [135]; in the case of the S-H mixtures it seems that the H-bonding is weakened from $\sim$10 GPa (Figure 7.5), although it could be postulated that H_2 molecules partially disrupt the already weakened H-bond

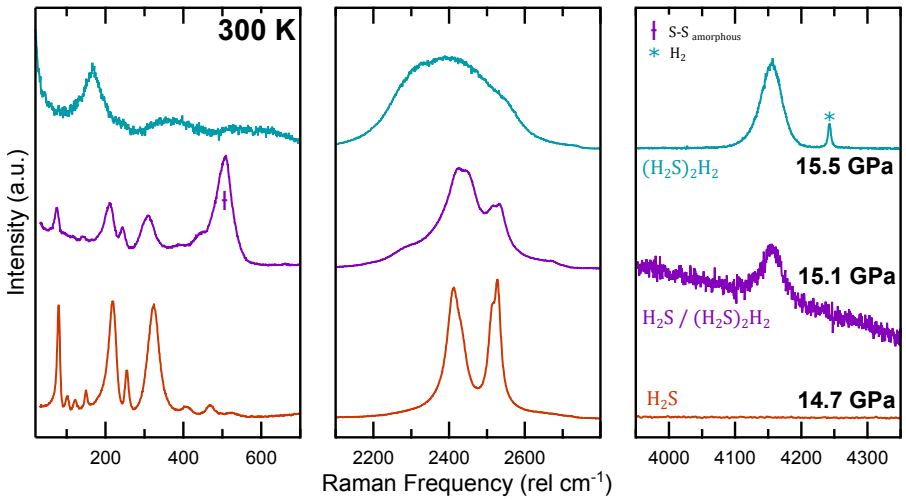

Figure 7.7 Representative Raman spectra of different samples at comparable pressures, at 300 K: pure H_2S on compression (orange); $(H_2S)_2H_2$:H_2 mixture created by decomposition of pure H_2S on decompression (purple); and pure $(H_2S)_2H_2$ on compression (turquoise) * indicates the bulk H_2 vibron, † indicates amorphous elemental sulfur.

network at higher pressures and perhaps prevent the establishment of the axial H-bond chains.

7.5 Mixtures from Decomposition

A mixture of H_2S and $(H_2S)_2H_2$ was also produced from the decomposition of pure H_2S at high pressures. Compression data for the experiment is shown and discussed in Chapter 4. The decomposition mechanism was probed by prolonged exposure to high laser power (532nm, 200 mW). Where exposed, the sample turned black and was found to consist of amorphous sulfur. However, upon decompression to 27 GPa, a weak and broad H_2 vibron was detected at high frequencies in the area surrounding the amorphous sulfur, with a frequency corresponding to $\nu_1 H_2 c$ from $(H_2S)_2H_2$ (see Figure 6.3). Upon further decompression to 17 GPa the vibron narrowed and shifted to a frequency corresponding to $\nu_1 H_2 a$, in excellent agreement with $(H_2S)_2H_2$ compression data [46]. Figure 7.7 shows representative Raman spectra at ∼15 GPa from pure H_2S and $(H_2S)_2H_2$ (on compression) compared to the mixture generated from decomposition and decompression. The frequencies of H_2S $\nu_{1,3}$ stretches were once again shifted to higher frequency in the mixed region.

This observation demonstrates that the high power laser induces complete decomposition; H_2 has only previously been detected in high pressure H_2S samples after direct laser-heating [97], and never detected upon compression alone [38]. This also proves that the formation of $(H_2S)_2H_2$ is favourable over separate H_2S and H_2 phases at these pressures. It is interesting that $(H_2S)_2H_2$ was only detected from 27 GPa, which is where dissociation begins upon compression of H_2S. This could suggest that H_2 molecules (or H atoms) reside within the amorphous sulfur lattice after dissociation/decomposition of H_2S at higher pressures, which is one of the theories considered in section 4.2.4. The trapped H_2 could be liberated from the amorphous sulfur, once below the dissociation onset pressure, forming $(H_2S)_2H_2$ upon encountering H_2S. The opposing consideration is that H_2 somehow forms *at* 27 GPa upon decompression, which seems unlikely, unless H atoms were 'dissolved' within the amorphous S which then form H_2 on decompression. Although this theory remains speculation for now, it is an important consideration that molecular H_2 could potentially exist within a sample at high pressure without necessarily being detected; the lack of detection of molecular H_2 is used as primary evidence for the formation of H_3S in the superconducting phase [28, 32].

7.6 Conclusions

H_2S has been shown to form a clathrate with H_2 stable from 0.2 – 0.47 GPa, resembling $(H_2S)_2H_2$. The clathrate formation only occurs in the fluid phase of H_2S, and is the lowest pressure which $(H_2S)_2H_2$ has been recorded at. Somewhat contrarily, H_2S dissolved in low concentrations within fluid H_2, maintains a fluid state $\sim$4.5 GPa higher than the usual solidification pressure. The S-H stretching frequencies harden upon compression indicating the molecules are isolated within the fluid H_2 matrix, and do not participate in H-bonding, which is an interesting opposition to the low pressure H-bonding observed in clathrates. When considering the behaviour of similar systems, it may be possible to tune the degree of H-bonding within the mixture by varying the H_2S content.

Specific synthesis techniques were utilised to produce many small segregated clusters of H_2S and $(H_2S)_2H_2$ crystallites within a sample. The two components appear to influence each other, with an overall weakening of H-bonding for both of H_2S and $(H_2S)_2H_2$. The softening of S-H stretching modes is attenuated in H_2S, and the H-bond driven phase transitions of $(H_2S)_2H_2$ are deferred to higher

pressures. The unit cell of phase I H_2S appears slightly expanded compared to the pure system. Although the stretching modes were consistent between the two experimental runs, they exhibit slightly different H_2 environments at higher pressures; this suggests that stoichiometry could differ between crystallites. Weaker H-bonding in $(H_2S)_2H_2$ seems to hinder the formation of phase III, by preventing the formation of alternating H-bond chains (i.e. S-H --- :S $\leftrightarrow$ S: --- H-S) in the context of the accepted *Cccm* structure for phase III. It has been postulated that the H_2 environments disrupt the already weakened H-bonding, in a similar manner that ionic inclusions in salty ices prevent the symmetrisation of H-bonds at high pressure. As the dissociation pressure of $(H_2S)_2H_2$ is greatly lowered in the mixture, the implication is that the alternating H-bond chains in the *Cccm* structure are responsible for the enhanced stability with respect to dissociation of pure $(H_2S)_2H_2$, compared to pure H_2S where S-S chains form instead. $(H_2S)_2H_2$ and H_2S mixtures have also been shown to form from laser-induced decomposition of H_2S. However, H_2 was only detected upon decompression to 27 GPa, whereas the decomposition was instigated above 40 GPa. This implies that H_2 (or H atoms) can become trapped or 'dissolved' within an amorphous S lattice at higher pressures without detection. This is an important consideration when regarding the formation of the superconducting phase, as lack of detection of molecular H_2 is used as evidence for the formation of H_3S. The preferential formation of $(H_2S)_2H_2$ at these pressures suggests that the cocrystal is more thermodynamically favourable over separate H_2S and H_2 phases at these pressures. The behaviour of $(H_2S)_2H_2$ and H_2S mixtures has proved insightful to the behaviour of the respective individual pure systems at high pressures.

Chapter 8

Hydrogen Selenide Systems

8.1 Introduction

Selenium is electronically analogous to sulfur; hydrogen selenide is thus very similar to hydrogen sulfide, but with weaker covalent bonds and intermolecular H-bonding. Under ambient conditions, the average Se-H bond length is 1.46 Å and the H-Se-H bond angle 90.9° (S-H = 1.34 Å, H-S-H = 92.1°), reflective of the reduced electronegativity and larger atomic radius [137]. Like H_2S, H_2Se exhibits three low temperature phases at ambient pressure: phase I (172 – 207 K) is cubic ($Fm\bar{3}m$) and orientationally disordered [100, 103]; phase II (82 – 172 K) is also cubic and partially orientationally disordered [138–141]; phase III (< 82 K) is completely ordered, and though the crystal structure has never been determined it is thought to have a lower symmetry than the tetragonal structure of phase III H_2S [83, 87, 138–141]. Similarities between H_2Se and H_2S have also been predicted at high pressures; H_3Se is potentially a high temperature superconductor [42, 43], with a maximum T_c of 110 K at 120 GPa, lower than the 200 K at 155 GPa respectively in the sulfur-hydrogen system [28].

However, H_2Se is appreciably more toxic, corrosive and flammable than H_2S which makes it difficult and dangerous to study experimentally. Practical studies at low temperature often prepare H_2Se *in situ* by reacting Al_2Se_2 and H_2O [138]. The methodology for direct *in situ* synthesis of H_2S (Chapter 5) was applied to H_2Se, to avoid direct handling (Figure 8.1). The results presented in this chapter were the first experimental studies reported on H_2Se at high pressures (published

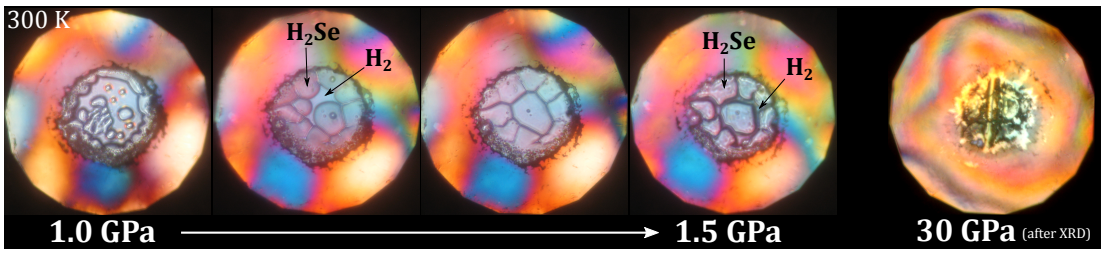

Figure 8.1 Photomicrographs of the formation of phase I H_2Se. The first four images show the successive coalescence of H_2Se from 1.0 GPa and complete solidification at 1.5 GPa; here H_2 can be seen in the thin crack between H_2Se crystallites. This sample transformed entirely to $(H_2Se)_2H_2$ (and H_2). The final image shows the same sample at 30 GPa after the XRD experiment, containing only amorphous Se, Se-IV, and H_2.

in [1]); Zhang *et al.* have since published the only other experimental study of high pressure H_2Se [116].

This chapter presents experiments performed on the H_2Se:$(H_2Se)_2H_2$ mixed system and pure $(H_2Se)_2H_2$. The data published in [1] concerns "pure" H_2Se, although the sample was actually a mixture of H_2Se:$(H_2Se)_2H_2$; however, the effects of mixing discovered in the H_2S:$(H_2S)_2H_2$ system (see section 7.4) was unknown at the time of publication. In hindsight, the accurate phase boundaries for pure H_2Se may be slightly lower than quoted. Nonetheless, the first section of this chapter aims to characterise pure H_2Se at high pressures, utilising the data obtained from H_2Se:$(H_2Se)_2H_2$ mixtures. The approximate phase boundaries for phases I, I′ and IV, and dissociation pressures are established. The second half of the chapter focusses on $(H_2Se)_2H_2$, which is directly compared to the near analogous $(H_2S)_2H_2$ system. Only phase I $(H_2Se)_2H_2$ exists at room temperature as H-bonding does not establish sufficiently to induce further structural changes. The discussion on the dissociation of both systems is condensed into section 8.3.

All samples were synthesised using the methods described in Chapter 5. H_2Se was found to be very sensitive to both intense laser light and x-ray synchrotron radiation, which cause H_2Se to decompose into H_2 and Se. Both 514 nm Ar^+ and 647 nm Kr^+ ion Raman excitation wavelengths were used; 647 nm with laser power < 10 mW was found favourable to limit sample degradation. Exposure times were also kept short, hence coarse diffraction gratings were employed which significantly limited the quality and resolution of the Raman data presented in this chapter. XRD data were collected at beamline 16-IDB at the Advanced Photon Source (APS) using a diffraction wavelength 0.4066 Å. Because decomposition occurred upon any exposure to the high flux beam, all exposure times were kept short and the rocking angles were restricted.

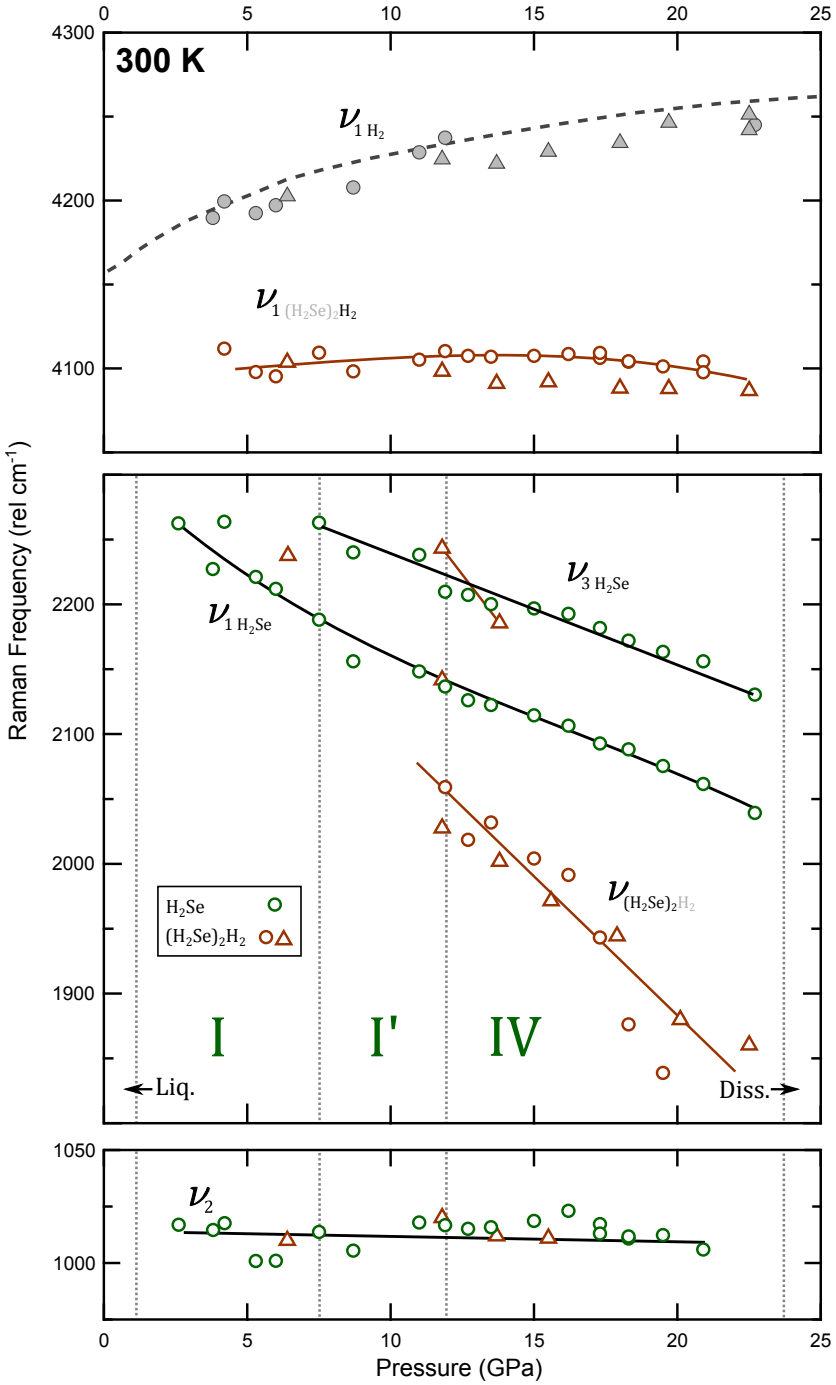

Figure 8.2 Observed Raman excitation frequencies between 950 - 4300 rel cm^{-1} of $(H_2Se)_2H_2$ (brown) and H_2Se (green) plotted as a function of pressure, at 300 K. Different shapes represent different experimental runs. Grey filled shapes refer to bulk H_2. Lines are intended as guides for the eye. Green numerals indicate the different phases of H_2Se (within the mixture). Note the first three points of ν_1 H_2Se; the frequency increases at the third point when $(H_2Se)_2H_2$ is formed.

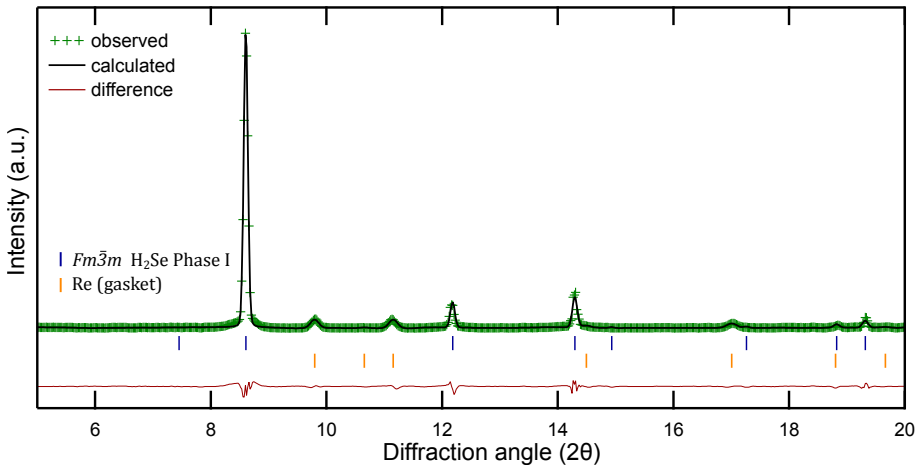

Figure 8.3 Observed diffraction pattern (green +), Le Bail fit (black) and difference plot (red) for phase I H_2Se (4.1 GPa, 300 K) fitted with $Fm\bar{3}m$ symmetry, $a = 5.424(3)$ Å. ($\chi^2 = 1.85$)

8.2 Hydrogen Selenide

8.2.1 Fluid - Phase I

Fluid H_2Se formed from at least 0.4 GPa at 300 K. The samples were loaded at 0.2 GPa, but pressure was raised before heating, to prevent the leakage of H_2 at high temperatures (473 K). The fluid phase boundaries between H_2Se and H_2 were visually well established, with a bubble of H_2 surrounded by H_2Se (Figure 5.4c); crossover between the fluid phases is expected, as in H_2S:H_2, but could not be confirmed due to limited exposure times. Phase I H_2Se began to crystallise above 1.0 GPa and fully solidified at 1.5 GPa (Figure 8.1), reflecting the weaker H-bonding in H_2Se compared to H_2S which solidifies immediately at 0.47 GPa, 300 K.

Phase I was characterised by Raman spectroscopy from a single intense broad band at 2262 rel cm^{-1} (2.6 GPa), arising from the convoluted ν_1 and ν_3 Se-H stretches (symmetric and asymmetric respectively); the Se-H band was 300 cm^{-1} lower in frequency than S-H, reflective of the heavier mass of Se, and lengthened bond (Figures 8.2 and 8.4). The ν_2 bending mode was initially very weak, identified from 2.6 GPa at 1032 rel cm^{-1}, only 175 cm^{-1} lower than H_2S. The low frequency region of the spectra exhibited broad and shapeless features indicative of rotational disorder. XRD data confirmed that phase I H_2Se exhibits $Fm\bar{3}m$ symmetry, with a unit cell length of 5.424(3) Å at 4.1 GPa (Figure 8.3).

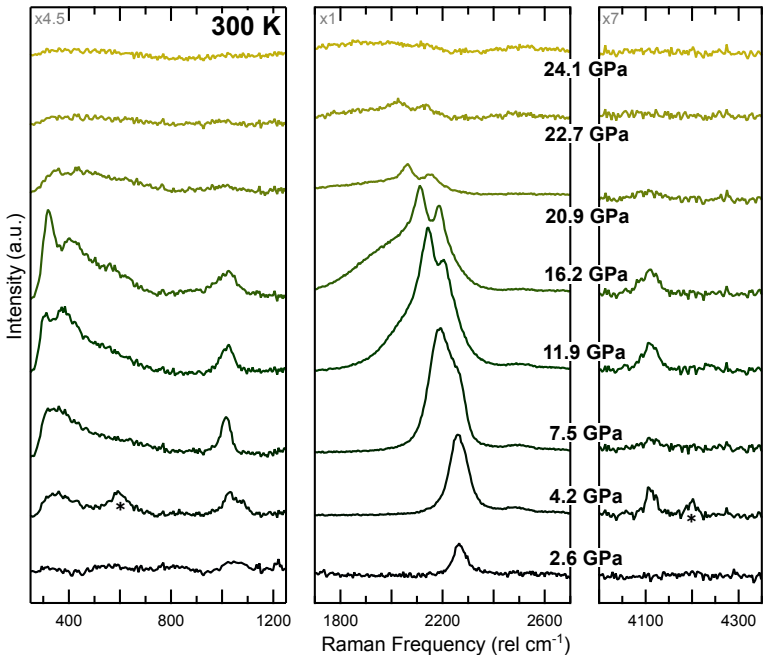

Figure 8.4 Representative Raman spectra of H_2Se and $(H_2Se)_2H_2$ mixture on compression at 300 K. Contributions from bulk molecular H_2 are indicated with *. Relative scales for each panel are indicated top left.

No further XRD data was obtained for other phases of "pure" H_2Se because the sample in question completely transformed to $(H_2Se)_2H_2$ above 4.2 GPa for the sample measured with XRD. As this is the first recorded instance of phase I H_2Se from compression there is no EoS for comparison, but the dimensions seem reasonable compared to H_2S (5.5025(6) Å at 1.1 GPa). Thus it is implicit that the first solid phase of H_2Se at ambient temperature is equivalent to phase I H_2S at ambient pressure: an fcc arrangement of Se atoms with 12-fold orientational disorder of the H_2Se molecules.

8.2.2 Phase I′

At 4.2 GPa the second H_2 vibron corresponding to the formation of $(H_2Se)_2H_2$ was identified. Above this pressure, the sample was actually a mixture of H_2Se and $(H_2Se)_2H_2$, and as such the frequencies quoted for pure H_2Se may be slightly elevated from the actual values. It can be seen on Figure 8.2 that the frequency of ν_1 increases from 2227 to 2264 rel cm^{-1} (from 3.8 to 4.2 GPa) on the formation of $(H_2Se)_2H_2$. However, H-bonding is much weaker in H_2Se than H_2S, so the differences imposed on H_2Se by $(H_2Se)_2H_2$ are expected to be minimal (See section 7.4 for further details). Other than a minor reduction in bond softening,

and slightly delayed phase transitions, H_2S in its respective mixture generally behaved the same as in pure form. In lieu of loading pure H_2Se, herein the H_2Se and $(H_2Se)_2H_2$ mixed sample is treated, with a caveat, as if it were pure H_2Se.

Upon compression the convoluted ν_1 and ν_3 band softened indicative of increased contribution to H-bonding. The ν_2 bending mode gained intensity and a broad feature emerged around $\sim$375 rel cm^{-1} at 4.2 GPa, suggestive of librational modes arising from the hindered rotations. The Se-H stretching band adopted an asymmetric profile upon reaching 7.5 GPa, as ν_1 and ν_3 became non-degenerate (Figure 8.4). ν_3 was slightly less intense and higher in frequency than ν_1, consistent with the spectra of phase I′ of pure H_2S (Figure 4.4). The peak profile also concurs with that of low temperature phase II H_2Se [141]. The librational mode at 375 cm^{-1} strengthened indicating a reduction in orientational disorder which concurred with the sharpening of the ν_2 bending mode.

Given the similarities in the rotationally disordered phases (I and II) of both H_2S and H_2Se it is reasonable to assume that phase I′ of H_2Se is the same as in H_2S. The strengthening librations and non-degeneracy of the stretching modes show that phase I′ (H_2Se) likely exhibits a reduction from 12 to 6-fold orientational disorder, as in phase II [138–141]. It should be noted that, for H_2S, the space groups of phases I′ and II are $P2_13$ and $Pa\bar{3}$ respectively, despite having identical Raman spectra. For this reason it cannot be stated absolutely that phase I′ of H_2Se is distinct from phase II until neutron diffraction studies of both phases have been performed. Nonetheless, it is apparent that H-bonding is still a factor in high pressure H_2Se, despite being weaker. Therefore it seems likely that the pressure driven transition from phase I to phase I′ in H_2Se will also exhibit the same shift in unit cell symmetry. In the H_2S:$(H_2S)_2H_2$ mixture, the transition to phase I′ (H_2S) occurred at the expected pressure, so it can be assumed that 7.5 GPa is accurate for the transition to phase I′ H_2Se at ambient temperature.

8.2.3 Phase IV

Further compression saw the distinct splitting and narrowing of ν_1 and ν_3 stretching modes at 11.9 GPa, as H_2Se entered phase IV. The transition was accompanied by the emergence of a lattice mode at 300 cm^{-1} which suggests a reduction in orientational disorder. The ν_2 bending mode broadened but did not split, as is observed in phase IV H_2S (Figure 4.4). The intensity of all vibrational

modes suddenly dropped at 20.9 GPa and nothing could be measured from 24.1 GPa suggesting the sample dissociated; although the metallisation of H_2Se cannot be claimed or ruled out entirely based on the Raman data alone.

As the lowest symmetry phases of H_2S and H_2Se at ambient pressure (phase III) are thought to be different [83, 87, 138–141], it is plausible that their respective lowest symmetry phases at high pressure (IV) are also not equivalent. Although the low resolution of the H_2Se Raman data could mask some finer details, there is sufficient evidence to support this notion. The ν_2 mode splits upon adoption of phase IV H_2S, and on compression the ν_1 and ν_3 modes also split forming two pairs. In H_2Se the splitting of ν_2, ν_1 and ν_3 is not observed, which suggests phase IV H_2Se has higher symmetry than phase IV H_2S. Phase IV H_2S exhibits a plethora of distinct lattice modes, even in the mixed system. Other than a lone lattice mode at $\sim$300 rel cm^{-1}, the low frequency region of H_2Se generally appeared broad and ill-defined suggesting the orientational disorder exhibited by phases I and I′ still remains in phase IV. Frequencies below 200 rel cm^{-1} could be not be probed due to the quality of the notch filter used on the Raman system for this experiment (see section 3.3); hence the establishment of Se-Se chains (as in H_2S) could neither be confirmed nor denied.

Because H-bonding purportedly drives all phase transitions in H_2S, the differences most likely relate to the weaker H-bonding in H_2Se. The rate of softening of Se-H bonds (-8.80 cm^{-1}/GPa) was slightly less than S-H (-9.97 cm^{-1}/GPa) for ν_1 modes in phase IV, reflective of a reduced contribution to H-bonding upon compression. It is interesting that the transition pressures for phases I′ and IV for H_2Se are very close to the equivalent phases of H_2S, because one would expect more pressure would be required to cause an H-bond driven structural shift in the weaker bound H_2Se system. Because the densities of the H_2Se and H_2S solid phases are comparable [138–141], the similar transition pressures could be explained by the larger atomic radius of Se, and longer Se-H bond length. A shorter distance between a given H and Se lone pair (forming the H-bond) could compensate for the reduced electrostatic potential between them. As a result the approximate strength of intermolecular bonding remains comparable in H_2S and H_2Se until reaching the lower symmetry phases (III and IV) where the amplified strength of H-bonding in H_2S plays a more significant role. It can be postulated that the H-bonding in phase IV H_2Se is not strong enough to prevent rotational disorder, which is not observed in phase IV H_2S.

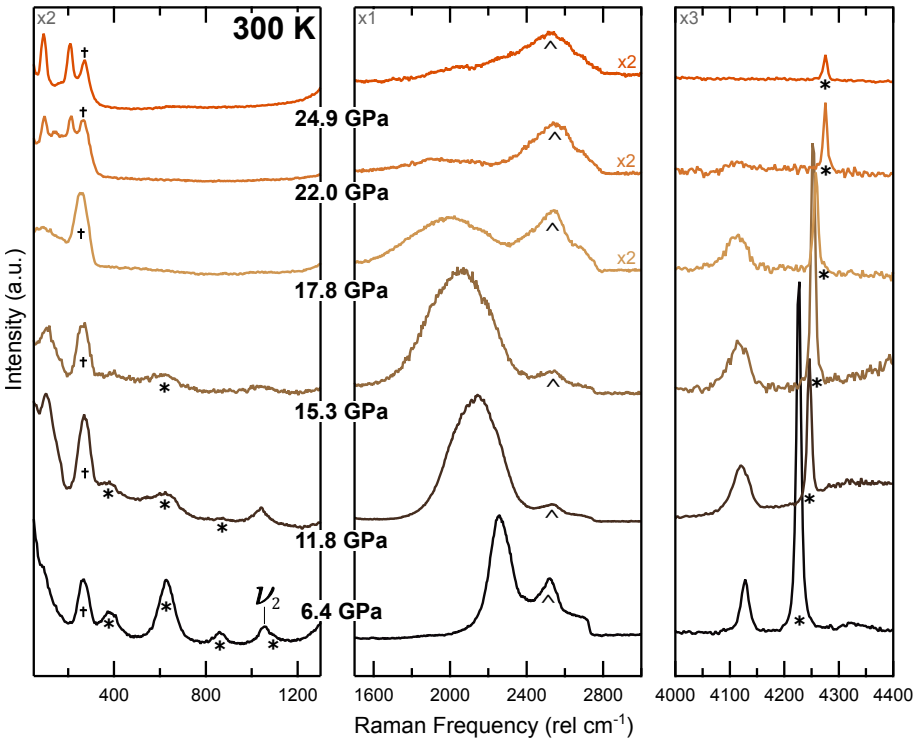

Figure 8.5 Representative Raman spectra of $(H_2Se)_2H_2$ on compression at 300 K. * indicates bulk molecular H_2, ^ indicates 2^{nd} order diamond phonon, † indicates amorphous Se. Relative scales for each panel are indicated top left.

8.3 $(H_2Se)_2H_2$

8.3.1 Results

4.2 GPa was the lowest pressure at which phase I of $(H_2Se)_2H_2$ was observed in both mixed and pure systems. $(H_2Se)_2H_2$ was identified from the ν_1H_2a vibron appearing at 4110 rel cm^{-1}, ~30 cm^{-1} lower than in $(H_2S)_2H_2$. In the pure $(H_2Se)_2H_2$ sample the convoluted Se-H stretching excitation was observed at 2256 rem cm^{-1} at 6.4 GPa. Amorphous Se was detected ~270 rel cm^{-1} for the duration of the experiment with pure $(H_2Se)_2H_2$, which could have been due to the use of higher energy Raman excitation wavelengths (514 nm). Upon increasing pressure the stretching modes broadened and softened as is observed in $(H_2S)_2H_2$. ν_1H_2a broadened but the frequency remained fairly consistent on compression (Figure 8.2). At 11.8 GPa the Se-H stretching excitation became asymmetric concordant with the behaviour of phase I $(H_2S)_2H_2$ on compression; up to three peaks can be fitted from 11.8 – 15.3 GPa, which were consistent with the convoluted νg, νh and νi excitations in phase I $(H_2S)_2H_2$ (section 6.2.1). Above 15.3 GPa only

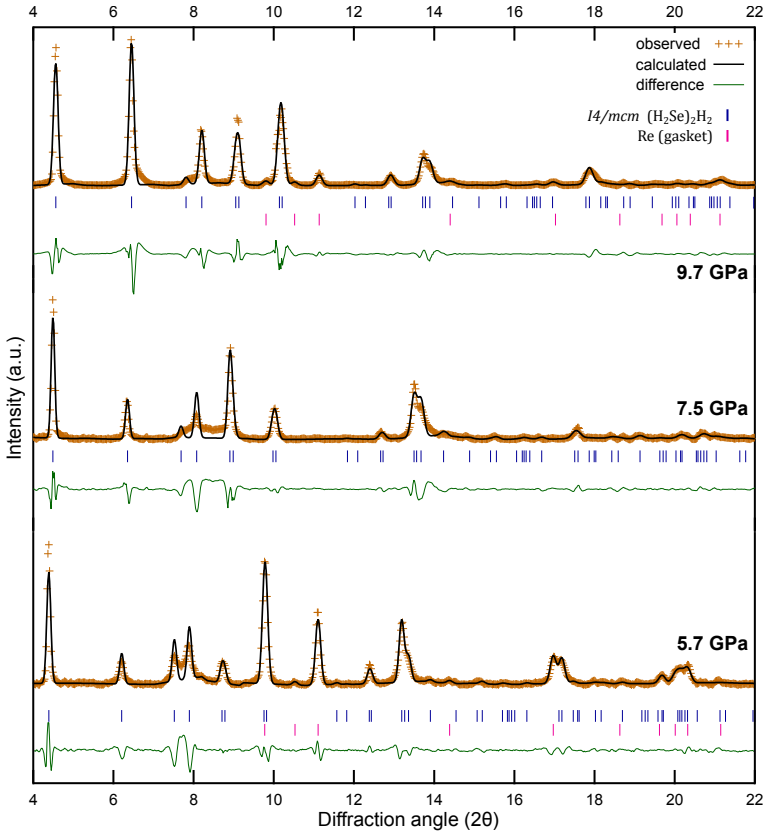

Figure 8.6 Observed diffraction patterns (orange +), Le Bail fits (black) and difference plots (green) for phase I $(H_2Se)_2H_2$ as a function of pressure at 300 K, fitted with $I4/mcm$ symmetry $a = 7.518(4)$ and $c = 6.266(4)$ Å (5.7 GPa).

single excitations were assigned due to the peak broadening and low resolution of the data.

The Se-H stretches did not distinctly split, nor was a second additional H_2 environment observed on compression indicating that H-bonding never developed sufficiently to stabilise phase II. A broad low frequency mode at ∼100 rel cm^{-1} gained intensity up to 17.8 GPa, which may have been the establishment of a weak translational lattice mode. However, above 17.8 GPa the intensity of all Raman excitations began to abate. By 22.0 GPa only a very weak Se-H stretching mode was detected and the sample had completely dissociated upon reaching 24.9 GPa. Low frequency modes corresponding to pure Se-II clearly emerged and developed from 17.8 GPa [144, 145], which may be due to photo-accelerated sample decomposition from the use of higher energy excitation wavelengths.

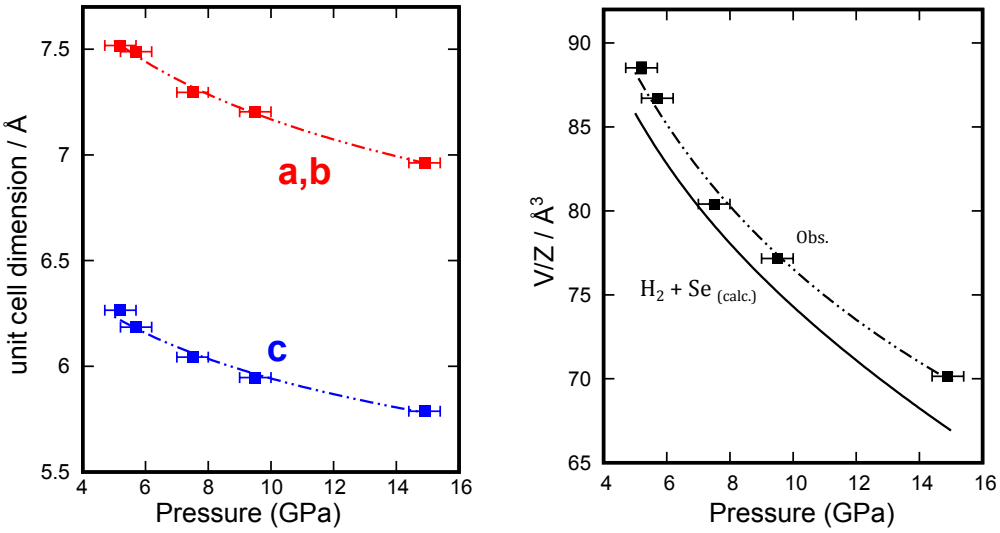

Figure 8.7 left: Changes in unit-cell dimensions for $(H_2Se)_2H_2$ as a function of pressure (a, b = red, c = blue). right: V/Z as a function of pressure for $(H_2Se)_2H_2$. Solid line indicates volume calculated according to the atomic equations of state for H_2[142] and Se.[143]. Functions and associated errors were calculated using the *EosFit7-GUI* software package [77].

XRD measurements showed that phase I $(H_2S)_2H_2$ adopted the $I4/mcm$ structure, with a = 7.518(4) and c = 6.266(4) Å at 5.2 GPa from a Le Bail fit (Figure 8.6). The structure is the same as phase I $(H_2S)_2H_2$ [46], although it should be reiterated that the H positions cannot be determined, and suggested structures of other phases of $(H_2S)_2H_2$ (i.e. $P1$, $I222$ and $Cccm$) all have some reflections in common (see Figure A.9). However given the lack of development of the Se-H stretching region it is clear that only phase I of $(H_2Se)_2H_2$ exists at ambient temperature, and $I4/mcm$ is an appropriate structural assignment. The unit cell dimensions were extracted to 14.9 GPa from the fitted data (Figure 8.7). The change of volume per formula unit (V/Z) on compression showed that $(H_2Se)_2H_2$ is on average 3% greater than the sum of the constituent elements; this indicates the structure is unstable which can be rationalised by the progressive weakening of Se-H bonds on compression.

8.3.2 Discussion

It is interesting that $(H_2Se)_2H_2$ ostensibly forms at lower pressures than $(H_2S)_2H_2$. Although Strobel *et al.* report formation from 3.5 GPa, the studies reported in chapter 6 find that $(H_2S)_2H_2$ does not form until 4.7 GPa, whereas $(H_2Se)_2H_2$ formed from 4.2 GPa. Although all results should be considered, Strobel *et*

al. present no data below 4.5 GPa. Assuming that $(H_2Se)_2H_2$ does form at lower pressures than $(H_2S)_2H_2$, the difference can also be explained in terms of H-bonding potential. For $(H_2X)_2H_2$ to form, (X = S or Se) the phase I H_2X molecular arrangement must be broken in the presence of H_2. The weaker attraction between H_2Se molecules allows molecular rearrangement to occur at slightly lower pressure than H_2S.

The evidence from this study suggests that phase I of $(H_2Se)_2H_2$ is structurally identical to phase I $(H_2S)_2H_2$ with $I4/mcm$ structure [1]. It appears to remain orientationally disordered up to dissociation upon compression at 300 K. The study by Zhang *et al.*, succeeding the publication on which this chapter is based, fits a $Cccm$ structure to "H_3Se" formed at 4.6 GPa [116]. As previously discussed, the atomic arrangement of Se in a $Cccm$ structure is very close to that of $I4/mcm$ and the respective diffraction patterns share common reflections (Figure A.9). Given the studies performed on $(H_2S)_2H_2$, $Cccm$ seems an inappropriate candidate; the Raman data for phase I $(H_2Se)_2H_2$ is not consistent with strong H-bonds, has no lattice modes, appears orientationally disordered with only one H_2 environment. Additionally $Cccm$ produces too many reflections which are unaccounted for in the XRD pattern. For this reson, and several others, a comment was written on the work of Zhang *et al.* which was recently published [2].

Nonetheless Zhang *et al.* produced low temperature data reminiscent of the formation of phase II′ of $(H_2S)_2H_2$, where Se-H stretching modes can be individually distinguished; although there is only a single H_2 environment it appears to be several convoluted contributions, which would be consistent with phase II′. Based on the data from this study, and of Zhang *et al.* it is apparent that $(H_2Se)_2H_2$ is far less stable than $(H_2S)_2H_2$ at ambient temperature. Pressure induced dissociation occurs before H-bonding establishes sufficiently to adopt phase II conformation. Only low temperatures potentially stabilise multiple H_2 environments at 133 K [116]. The disparity between calculated and measured volume of $(H_2Se)_2H_2$ is consistent with the observed low stability and lengthening Se-H bonds; in-fact the data of Strobel *et al.* show the measured volume of $I4/mcm$ $(H_2S)_2H_2$ was also marginally greater than the calculated volume in some experimental runs [46]. $(H_2S)_2H_2$ shows enhanced robustness compared to H_2S, whereas $(H_2Se)_2H_2$ dissociates at the same pressure as H_2Se. This is due to a combination of the weaker covalent Se-H bond, and weaker H-bonding, compared

to their S-H counterparts. It is known that hydride stability decreases down a periodic group due to the weaker bonding, such as the halides; HCl is stable to at least 50 GPa whereas HBr and HI decompose at 42 and 10 GPa respectively [146–149]. The already weak Se-H bond softens to participate further in overall weak H-bonding, resulting in an extremely fragile lattice. Although H-bonding seems stronger in $(H_2S)_2H_2$ than H_2S, it seems the Se-H bond is at an undefined limit, which is unsurprising considering that H_2Te cannot be even be stabilised at 300 K. Thus both $(H_2Se)_2H_2$ and H_2Se experience the same fragility and neither exists above 24 GPa.

The differences in the observations of elemental Se in Raman and XRD data should also be considered. No Se was detected when using a lower energy Raman excitation wavelength (red, 647 nm) (Figure 8.4), whereas a peak corresponding to amorphous Se [150] (which can be compared to the amorphous S peak at ∼475 rel cm^{-1}) was present throughout the entire experiment when using a higher energy wavelength (green, 514 nm). Furthermore, Figure 8.5 shows that the peak corresponding to amorphous Se loses intensity, as the Se-II peaks gain intensity [145, 151]. It is thought that the sample was overexposed at the very beginning of the experiment, causing immediate decomposition of some H_2Se and resulting in the ever present amorphous Se; the Se-H peaks appeared relatively stable throughout the course of the experiment up to ∼18 GPa. Then at higher pressures, the laser could melt and recrystallise amorphous Se into Se-II. Additionally, it is likely that the higher energy laser (514 nm) also decomposes the H_2Se molecules into H_2 and Se above 22 GPa, whereas the red laser merely causes dissociation of H_2Se and $(H_2Se)_2H_2$ to the amorphous state. This is consistent with the XRD experiments, where Se was visibly produced, as a black region in the sample, after exposure to synchrotron radiation. Figure 5.4d shows the sample at 30 GPa after XRD measurements, where only incommensurate monoclinic Se-IV was detected [143]. Given these measurements, and those from Chapter 6, it seems unlikely that the selenium-hydrogen system will be capable of structural development such that high temperature superconductivity would be favourable. It is postulated that the formation of alternating H-bond chains in the *Cccm* structure of phase III $(H_2S)_2H_2$ act as a precursor to the formation of H_3S; whereas $(H_2Se)_2H_2$ dissociates before it can even transition to phase II.

8.4 Conclusions

Phases I and I′ for H_2Se are established at 1.0 and 7.5 GPa respectively, at ambient temperature; all evidence suggests they are analogous to the equivalent high pressure phases of H_2S. However, neutron diffraction studies are required to determine the difference between high pressure phase I′ and low temperature phase II, which exhibit the same Raman spectra but are thought to have different cubic symmetries (like H_2S). Phase IV of H_2Se was observed from ∼11 GPa, around the same pressures as phase IV H_2S at ambient temperature. However, only single ν_1, ν_3 and ν_2 vibrational modes, and a single lattice mode were observed. Consequently phase IV H_2Se is thought to have higher symmetry than phase IV H_2S. Furthermore, evidence of hindered rotational disorder in phase IV H_2Se is not present in phase IV H_2S.

Phase I $(H_2Se)_2H_2$ is structurally analogous to phase I $(H_2S)_2H_2$ with $I4/mcm$ symmetry, and is thought to form at a slightly lower pressure. The relationship between $(H_2Se)_2H_2$ and H_2Se differs slightly to that of $(H_2S)_2H_2$ and H_2S: $(H_2Se)_2H_2$ and H_2Se have comparable stability with respect to pressure driven dissociation, whereas $(H_2S)_2H_2$ demonstrates remarkable stability compared to H_2S. The differences ultimately arise from the weaker Se-H covalent bond and weaker H-bonding, which prevents the formation phase II $(H_2Se)_2H_2$. In that regard, the possibility of high temperature superconductivity in the hydrogen-selenium system seems unlikely.

Chapter 9

Conclusion

This thesis aimed to characterise unexplored high pressure hydrogen-chalcogen compounds, and expand on chartered areas of the dense hydrogen-sulfur system. In this endeavour, three novel low-temperature phases of $(H_2S)_2H_2$ have been discovered at high pressures, and H_2Se and $(H_2Se)_2H_2$ have been synthesised and studied on compression for the first time. Unknown behaviours of H_2S have been recognised and investigated, such as the influence of mixing H_2S and $(H_2S)_2H_2$ crystallites on intermolecular H-bonding, and the formation $(H_2S)_2H_2$ from decomposition of H_2S at high pressures. Herein the main conclusions from each chapter are summarised, and potential future experiments outlined, before setting the results in the wider context of the field.

9.1 Conclusions and Future Work

9.1.1 H_2S

The incentive of studying pure H_2S was to obtain high quality data of known phases for comparison with the novel systems, and to investigate the disputed phase IV structure and dissociation mechanism at high pressures. Although the true nature of H_2S dissociation largely remains speculation, collective high resolution Raman measurements endorse the $I4_1/acd$ model for phase IV H_2 [86], over a number of alternative structures [41, 91–93]. In particular, the use of modern holographic notch filters facilitated measurements below $\sim$100 cm^{-1},

allowing the assignment of a low frequency translational mode to the formation of axial S-S chains in phase IV. Additionally, the absence of this mode in low temperature phases III′ and IV′ led to the conclusion that such S-S chains are not established for these phases as has been previously suggested [38].

Proceeding studies of pure H_2S will likely also rely on contemporary techniques. Neutron studies in large volume DACs are approaching the Mbar regime [152], which would easily enable precise confirmation of the phase IV and V structures of D_2S and perhaps allow the dissociation mechanism to be probed without accelerating decomposition.

9.1.2 Direct Synthesis

Synthesis techniques were developed enabling facile production of H_2X, $(H_2X)_2H_2$ and reproducible mixed systems of H_2X:$(H_2X)_2H_2$ (X = S, Se). H_2 and S were found to react spontaneously at 300 K between 0.2 - 0.4 GPa, but very slowly, whereas H_2 and Se required heating. The most efficient syntheses of H_2S and H_2Se (< 0.5 GPa) requires heating the constituent elements at 373 and 473 K respectively. Less efficient photoreactions were induced in both systems upon exposure to intense laser light with a minimum wavelength of 514 nm. Considering the initial objective was to avoid directly handling H_2S, *in-situ* synthesis was found to offer unprecedented ease for preparing $(H_2X)_2H_2$, and will hence be utilised for further investigation of these high pressure systems. These relatively simple methods have also provided additional relevant and interesting information, from which Chapter 7 is constituted.

Although H_2Te was not attained, the synthesis should be possible via low-temperature photoreaction to avoid immediate decomposition. These experiments will be performed promptly, with the aim of characterising high pressure H_2Te (and potentially $(H_2Te)_2H_2$) for the first time.

9.1.3 $(H_2S)_2H_2$

Proficiency in the preparation of $(H_2S)_2H_2$ generated a number of beneficial studies and results. At ambient temperature, phase I was found stable between 4.7 – 16.7 GPa and confirmed to possess $I4/mcm$ symmetry [46]. High resolution

data provided significant insight into the nature of bonding and structural characteristics; $I222$ presents the best structural candidate of the two existing models of phase II, although both structures fail to account for the expected 2:1 ratio of a:b H_2 environments, setting up potential neutron diffraction studies of $(D_2S)_2H_2$. The transition from phase II to III was predicted at 40 GPa, but was identified as a slow shift from 33 – 40 GPa, reflecting the strength of H-bonding in phase II and the marked differences in bonding arrangements of phases II and III. Consequently, the predicted $Cccm$ model describes phase III well [23]. $(H_2S)_2H_2$ exhibits enhanced stability with respect to pressure induced dissociation (48 GPa) compared to pure H_2S (40 GPa) under the same conditions. Studies of the mixed $(H_2S)_2H_2$:H_2S system (Chapter 7) and $(H_2Se)_2H_2$ (Chapter 8) led to the notion that this amplified stability relies on the adoption of a $Cccm$ structure.

The first novel low temperature phase (II′) of was identified below 173 K at 10 GPa. Phase II′ ostensibly exhibits lower symmetry than $I4/mcm$ phase I, with four individual H_2 environments. This, and the similarities in Raman spectra of phases II′ and II leads to the unfavoured $P1$ DFT model of phase II as a potential structural candidate of phase II′. Upon compression at 80 K, a transition to another novel phase (III′) was identified at 38.5 GPa. Phase III′ would be well described by a lower symmetry version of the ambient temperature phase III $Cccm$ model. A third novel phase (IV′) was found stable from 53 – 120 GPa (80 K), associated with a significant increase in symmetry with respect to phases II′ and III′. Future work is clearly laid out in full structural characterisation of these novel phases via diffraction experiments.

Potential spectral evidence of a phase V′ was identified ∼160 GPa, where bulk H_2 transitions from phase II – III at 80 K. The proximity of these conditions to where maximal T_c measurements were made in the H_2S system suggest phase V′ could be related to the high T_c phase [28]. Moreover, a shifted low frequency H_2 vibron was measured in the bulk H_2 phases of another sample and dubbed as phase X′. The H_2 vibron somewhat mimicked the behaviour of pure H_2 and gained intensity on compression up to 155 GPa, apparently exhibiting extraordinary stability compared to $(H_2S)_2H_2$ and H_2S. Additionally the expanded unit cell compared to H_3S at similar pressures suggests the H:S stoichiometry could be much higher than 3:1. It is suggested that the significant excess of H_2 could be responsible for the drastically different behaviour of this unidentified sulfur-hydrogen compound. Regardless, the stability of sulfur-hydrogen compounds containing molecular H_2

in the setting where the high T_c superconductivity was measured could impact the theory of molecular H_3S. Although tenuous, these results present the most promise for elucidating the nature of high T_c superconductivity. They must be repeated for confirmation and thoroughly investigated, first with Raman spectroscopy before considering experiments measuring conductivity and the Meissner effect.

9.1.4 Mixed hydrogen-sulfur systems

Mixed systems of various sulfur-hydrogen compounds were studied. Following direct synthesis via slow-cooling, evidence of $(H_2S)_2H_2$ was observed at 0.2 GPa within the H_2S fluid phase, consistent with the formation of an H-bonded clathrate. Although a peripheral finding, this is the lowest pressure at which $(H_2S)_2H_2$ and H-bonding has been observed at in the high pressure H_2S system at ambient temperature. A neutron diffraction study would be beneficial for confirming the structure. Contrarily, H_2S was identified in low concentrations in the fluid H_2 phase, exhibiting a distinct absence of H-bonding. The behaviour was congruous with that of gaseous H_2S up to H_2 solidification around 5 GPa, well above the solidification pressure of H_2S. These results suggest that the degree of H-bonding could be tuned by varying the ratio of H_2:H_2S fluid phases at low pressures. This perhaps compliments the observation of phase X′, where existing in an H_2 matrix may influence the behaviour of the sulfur-hydrogen compound.

Synthesis also produced solid mixtures of $(H_2S)_2H_2$ and H_2S. The coexistence of many small crystallites appears to impair the effectiveness of H-bonding in both systems. H-bond driven phase transitions are delayed, the softening of stretching frequencies on compression is reduced, and the unit cell of H_2S in the mixture appears expanded in comparison to the pure species. All these observations are consistent with a reduction in the strength of intermolecular H-bonding between H_2S molecules. Phase III of the $(H_2S)_2H_2$ did not seem to form at all, and the dissociation pressure of $(H_2S)_2H_2$ (48 GPa) was significantly lowered in the mixture (39 GPa). These observations are thought to be linked, and suggest that the formation of alternating axial H-bond chains in phase III are responsible for the enhanced structural stability of $(H_2S)_2H_2$. This is reinforced by experiments detailed in chapter 8: H-bonding in $(H_2Se)_2H_2$ does not establish sufficiently to adopt the equivalent of phase III, and consequently $(H_2Se)_2H_2$ dissociates at the same pressure as H_2Se.

$(H_2S)_2H_2$ was also produced from a sample of pure H_2S following partial decomposition above 40 GPa. However, the characteristic H_2 vibron was only observed upon decomposition to 27 GPa. This observation is important as it advocates that molecular H_2 could potentially be present in a sample at high pressures without necessarily being detected. In this case, it is thought that S-H bonds are broken when the sample is irradiated with a high energy laser, which forms an amorphous S lattice and traps H_2 inside.

It would be interesting to recreate these experiments with the mixed $(H_2Se)_2H_2$:H_2Se system via the quenching method. This would require direct loading of H_2Se to confirm if bonding is different in the mixture, and also to try and recreate the formation of $(H_2S)_2H_2$ from pure H_2S.

9.1.5 Hydrogen-selenium systems

Studies of H_2Se and $(H_2Se)_2H_2$ at high pressures and ambient temperature were reported for the first time, with results published in [1]. H_2Se phases I and I′ are established at 1.0 and 7.5 GPa respectively and appear analogous to the equivalent phases of H_2S. Phase IV H_2Se was observed from 11 GPa around the same pressure but apparently exhibits higher symmetry than the structure of phase IV H_2S: the ν_1, ν_3 and ν_2 vibrational modes do not split, and only a single lattice mode is observed. Additionally the low frequency regions of the Raman spectra indicate phase IV H_2Se exhibits some orientational disorder, which suggests all the differences arise as consequence of impaired H-bonding in the selenium-hydrogen system compared to the equivalent sulfur-hydrogen compounds. Phase I $(H_2Se)_2H_2$ was found structurally analogous to phase I $(H_2S)_2H_2$, however weaker H-bonding also prevents the adoption of phase II; consequently the axial H-bonding chains of phase III are never established, and $(H_2Se)_2H_2$ and H_2Se both dissociate at 24 GPa. *Cccm* may be a precursor to the formation of molecular H_3S; in this regard it seems unlikely that high T_c superconductivity would be experimentally established in the hydrogen-selenium system if an H_3X stoichiometry is responsible for superconductivity.

The natural step for future research in the selenium-hydrogen system is to first load pure H_2Se. This would enable the previous results to be confirmed and the nature of the mixed $(H_2Se)_2H_2$:H_2Se system to be investigated. The high

pressure phases of both H_2Se and $(H_2Se)_2H_2$ at low temperatures then require characterisation.

9.1.6 Closing Remarks

Of the compounds studied, sulfur forms the strongest covalent bond with hydrogen and the strongest intermolecular H-bonds. In this regard, the sulfur-hydrogen system exhibits the most complex behaviour prior to dissociation. The experimental studies of high T_c superconductivity are no exception; complex P/T paths are required to generate a superconducting state from pure H_2S, and the reported maximal T_c values and pressures are not entirely consistent across publications, despite all being remarkably high [28, 33, 35, 153]. Moreover, the results of the few peer-reviewed publications investigating the structure are also somewhat polarised [32, 48, 49]. An important conclusion drawn from these studies is that the properties of mixed sulfur-hydrogen systems can differ wildly from the pure species. The generation of a mixed sulfur-hydrogen system in the high T_c studies is implicit from producing stoichiometric H_3S from H_2S [32], regardless of whether H_3S is molecular or not. Given only partial decomposition has ever been verified, even in studies of laser-heated H_2S [49], and samples subjected to harsh radiation (section 7.5), the high T_c measurements must have been made on a mixed system. Unfortunately this raises more questions than it answers, but is an important consideration nonetheless. What we do know is that high T_c measurements have been made on a sample which produces an XRD pattern consistent with a bcc arrangement of S atoms with a unit cell volume close to a 3:1 stoichiometry of H:S [32]. Returning to the overarching theory that the formation of certain hydrides is thought to lower the pressure at which the predicted superconducting properties of pure H_2 emerge, a high H_2 content should be favourable. Given that the high T_c measurements theoretically always have an excess of pure S in the sample chamber, it seems obvious that $(H_2S)_2H_2$, with excess H_2, is far more suitable precursor.

Another significant conclusion to extract from these studies is the clear enhanced stability to dissociation of $(H_2S)_2H_2$ versus H_2S: using the same excitation energies at 300 K, $(H_2S)_2H_2$ dissociated at 48 GPa versus H_2S at 40 GPa; at 80 K $(H_2S)_2H_2$ was measured up to 120 GPa versus 50 GPa. Although the exact nature of dissociation remains unclear, it appears that the adoption of phase III in $(H_2S)_2H_2$ is significant to the enhanced stability; it is the authors theory that the

establishment of alternating axial H-bond chains is key to this amplified stability. Alternating H-bonding also marries nicely to the theory of symmetrisation in H-bonds in the high T_c phase [30]. This postulation is made in the context of the predicted *Cccm* structure which still requires precise verification, but is within an accessible regime of modern neutron DAC experiments. Nevertheless, the substantial broadening S-H stretching modes peaks is consistent with the establishment of such chains, where the lifetime of an S-H molecular vibration would be incredibly short, and is observed at both ambient and low temperatures. In this context, along with the sharp drop in frequency of the H-H vibrational mode of the phase IV′ H_2 environment which vanishes around the pressures where H_3S is predicted to form [23], the establishment of a molecular H_3S compound seems very plausible. If this were true, it leads to the conclusion that selenium and tellurium hydrogen systems would not exhibit any superconducting phases at all.

The counter-argument to a molecular H_3S mechanism arises from the direct observation of molecular H_2 containing sulfur-hydrogen compounds around the high T_c conditions. This is compounded by the formation of $(H_2S)_2H_2$ from H_2S, which seems to suggest that a sample can contain molecular H_2 without detecting it. The absence of molecular H_2 from high pressure spectra is a key argument presented for the formation of a molecular H_3S compound [28, 32]. This alternate theory would imply a $(H_2S)_{2n}(H_2)_n$ compound, which is not implausible. Indeed, the idea of pre-compressing H_2 as an alloy has been suggested as a possible route to achieving room temperature superconductivity [17, 21, 154]. Until the positions of H atoms can be definitively characterised, this notion cannot be discounted.

Very recently (within two weeks of submitting this thesis) two arXiv publications have emerged with experimental measurements of high T_c superconducting lanthanum hydrides [26, 27]. Drozdov *et al.* claim a T_c of 209 K upon laser heating LaH_x at 170 GPa, which increased to 215 K upon releasing the pressure to 150 GPa. Somayazulu *et al.* report synthesis of a "superhydride", LaH_{10} and an astonishing T_c of 260 K at 190 GPa, with measurements "as high as 280 K in other experiments". Both publications require scrutiny and peer review, and do not deviate from the erratic and complicated nature of high T_c measurements in the sulfur-hydride system. Despite this, these results potentially represent the next breakthrough towards ambient temperature superconductivity.

Although the excitement surrounding sulfur-hydrogen may have had its day, there is still a lot left unanswered. The hydrogen-chalcogens are far more complex than was initially anticipated, and the studies conducted for this thesis have necessitated a near equal volume of future work. Doubtless the high pressure hydrogen-chalcogens will remain an important set of molecular systems for eventually elucidating the nature of high T_c superconductivity at high pressures. The role of theoretical methods is clearly becoming prevalent in such endeavours, whilst technology catches up; yet conducting challenging experimental research is important for pushing the boundaries of what we know is possible, even if each increment is small.

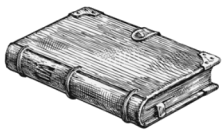

"It was such a relief to be right, even though you knew
you'd only got there by trying every possible way to be wrong."

Terry Pratchett
Feet of Clay

Appendix A

Supplementary Material

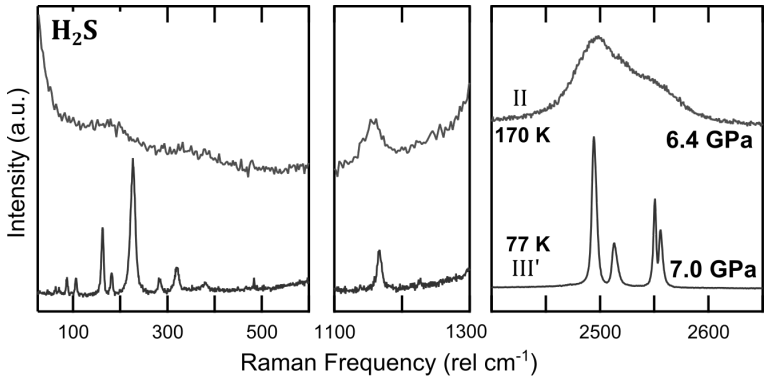

Figure A.1 Chapter 4: Representative Raman spectra of phases II and III′ of pure H_2S, obtained on cooling from 6-7 GPa.

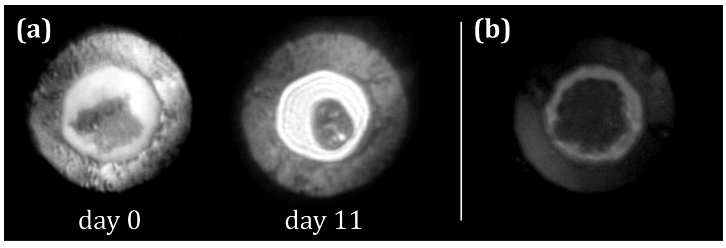

Figure A.2 Chapter 5: (a) Photomicrographs of solid S suspended in fluid H_2 at 0.2 GPa at before and after 11 days at 300 K; exhibiting signs of reaction. (b) An example of a large piece of solid S required to attain an H_2:S ratio between 1 - 1.5.

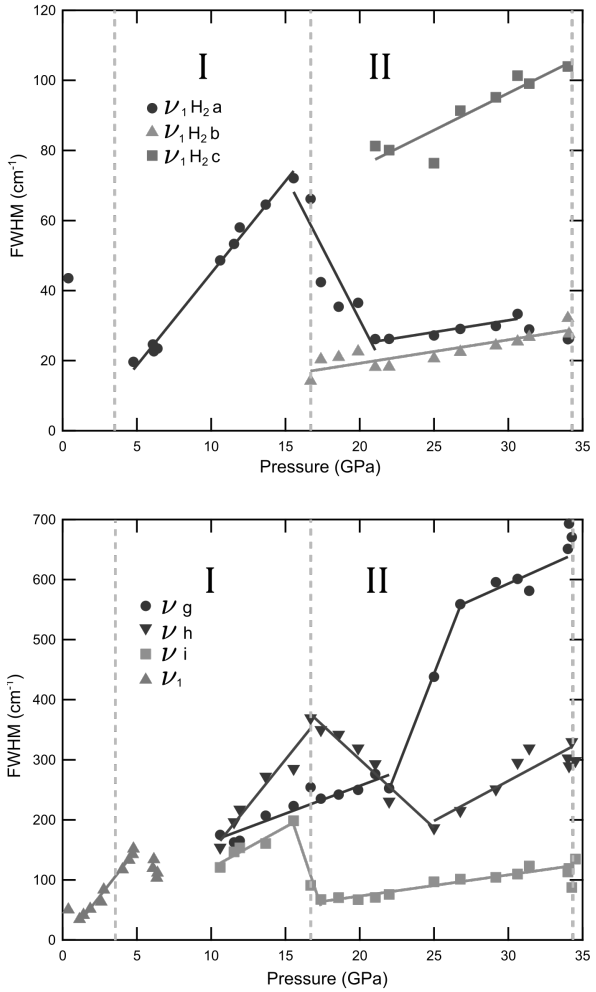

Figure A.3 Chapter 6: Plots of full-width-half-maximum (FWHM) (cm^{-1}) as a function of pressure (GPa) for key vibrational modes from $(H_2S)_2H_2$ at 300 K. FWHM for peaks from H_2 are shown on top and FWHM for peaks from S-H stretches are shown below. Phase boundaries are indicated with dashed lines. Pseudo-Voigt peak fitted using *Fityk*[73] are displayed below in Figures A.4 and A.5

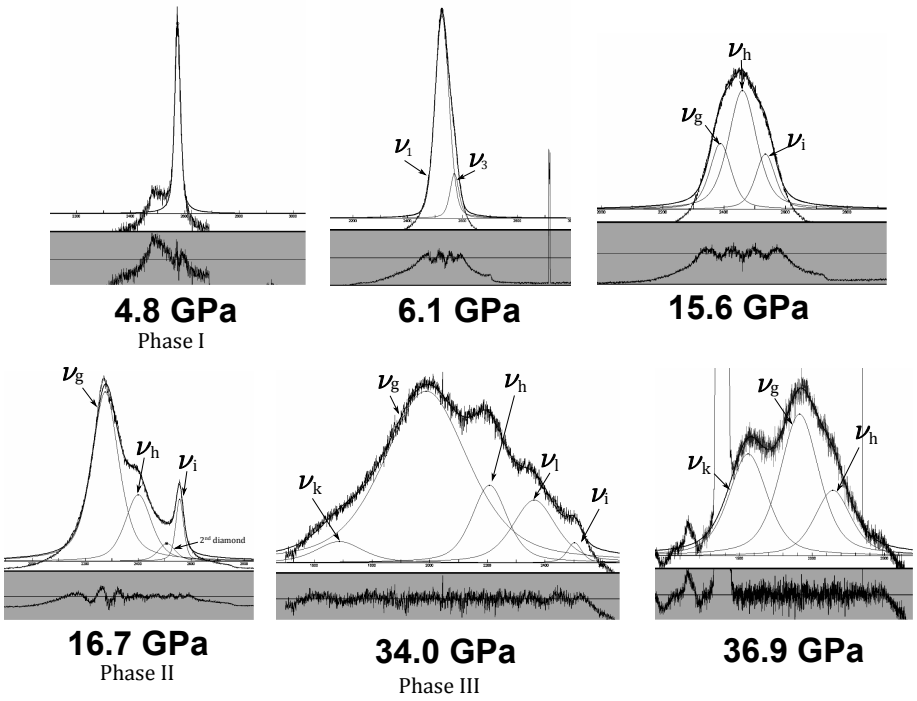

Figure A.4 Chapter 6: Pseudo-Voigt peak fits performed using using *Fityk*[73] for S-H stretches of different phases of $(H_2S)_2H_2$ at 300 K.

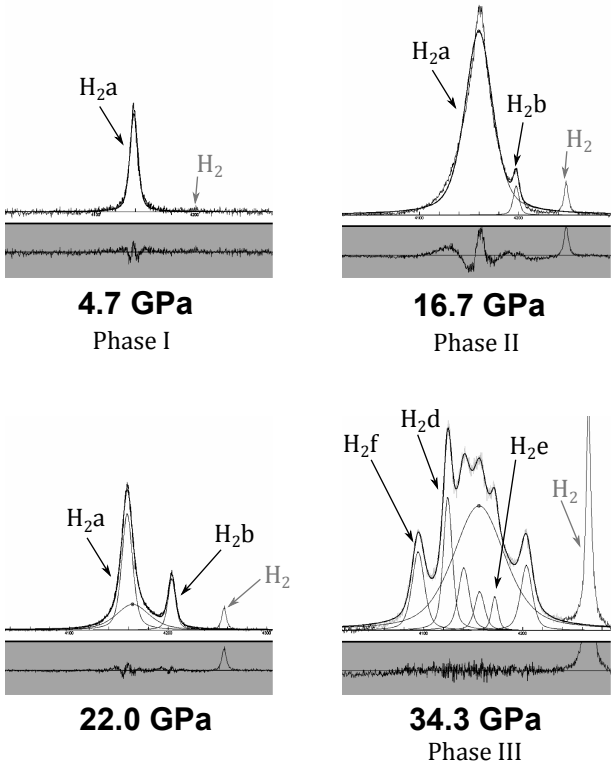

Figure A.5 Chapter 6: Pseudo-Voigt peak fits performed using using *Fityk*[73] for H-H stretches of different phases of $(H_2S)_2H_2$ at 300 K.

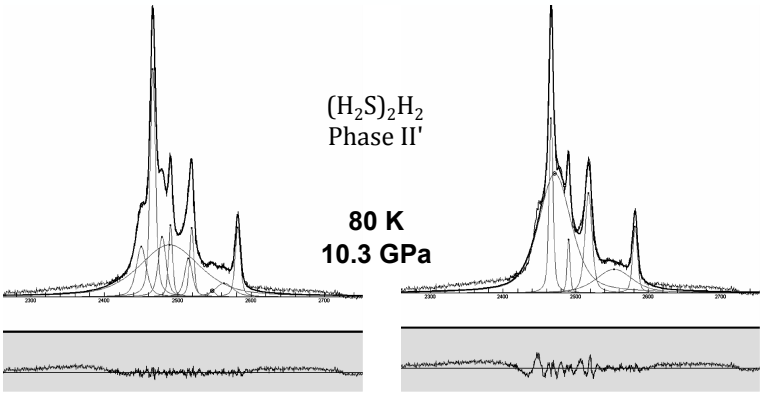

Figure A.6 Chapter 6: Two different Pseudo-Voigt peak fits performed using using *Fityk*[73] for S-H stretching region of phase II′ of $(H_2S)_2H_2$ at 10.3 GPa, 80 K. Left uses 8 peaks to completely describe the excitation, right uses 6 peaks to conservatively describe the excitation, but less accurately

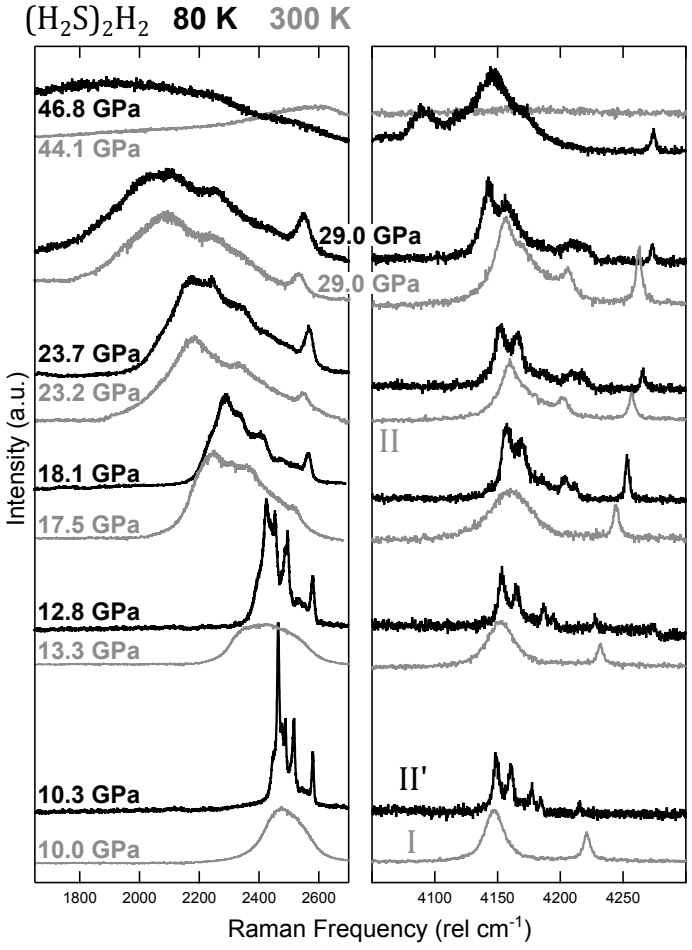

Figure A.7 Chapter 6: Representative Raman spectra of $(H_2S)_2H_2$ as functions of pressure at 80 K and 300 K. This figure exemplifies the similarities between phase II and phase II′, whose S-H stretching regions converge at 29 GPa.

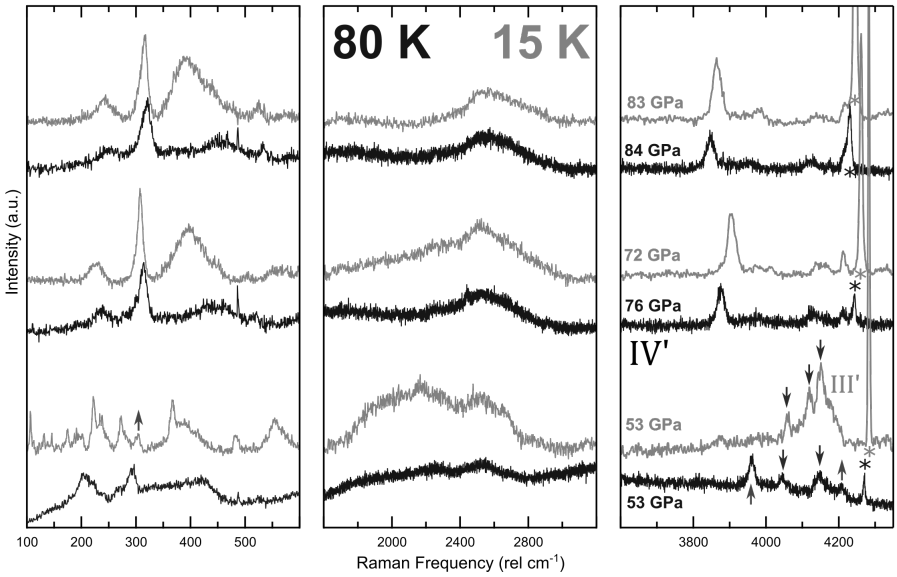

Figure A.8 Chapter 6: Representative Raman spectra of $(H_2S)_2H_2$ as functions of pressure, comparing the transition from phase III′ to IV′ at 80 and 15 K.

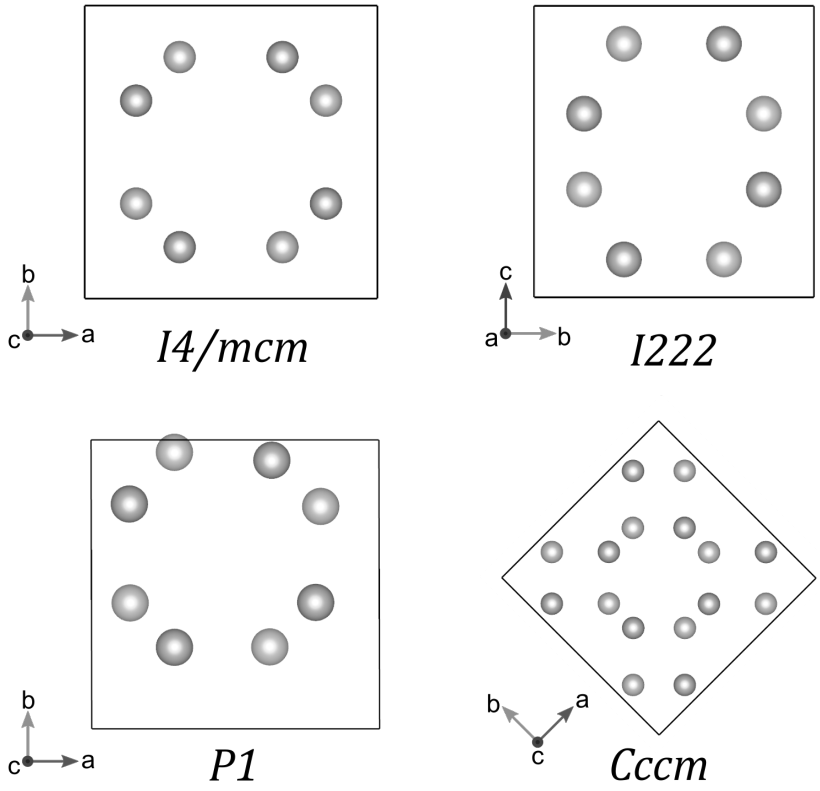

Figure A.9 Chapter 6: Structural models of the phases of $(H_2S)_2H_2$, ommiting H atoms, prepared using *VESTA*[90], showing the comparable arrangement of sulfur atoms and hence similarities in XRD spectra. phase I - $I4/mcm$, phase II - $I222$ and $P1$, phase III - $Cccm$.

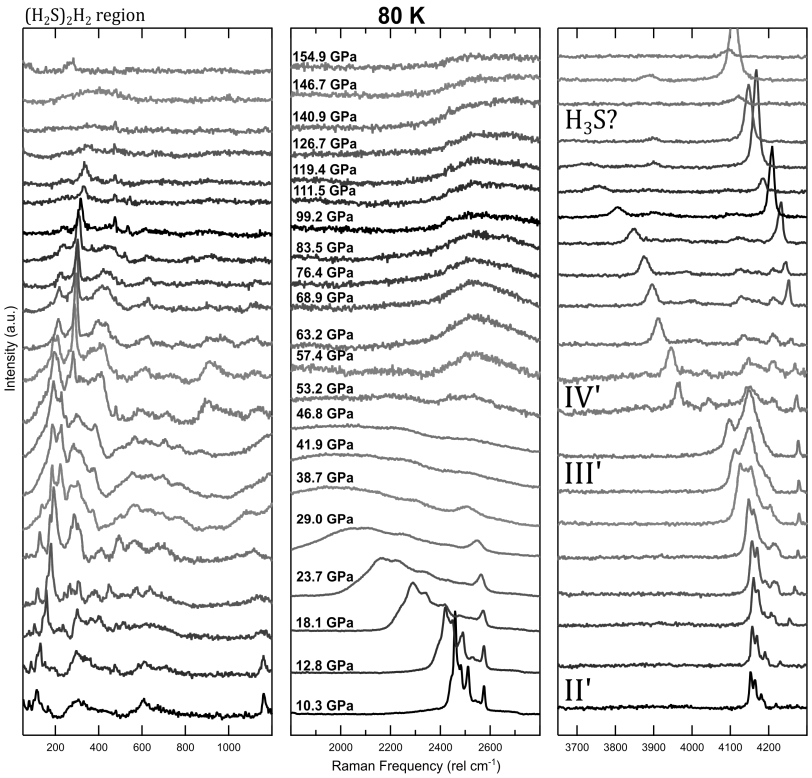

Figure A.10 Chapter 6: Coarse Raman spectra as functions of pressure for $(H_2S)_2H_2$ region of sample at 80 K.

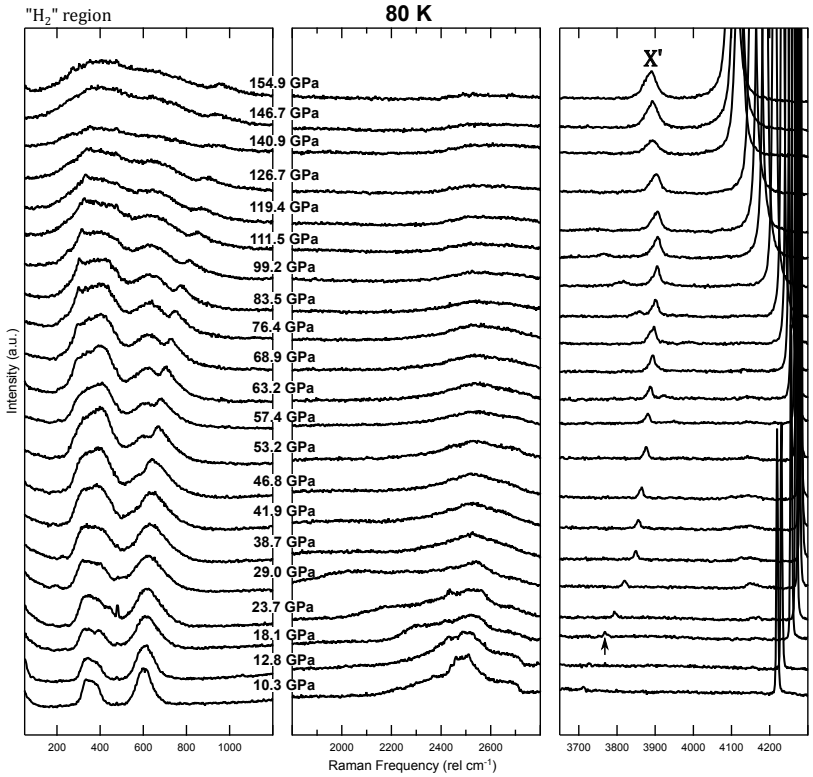

Figure A.11 Chapter 6: Coarse Raman spectra as functions of pressure for H_2 region of the same sample at 80 K, showing development of H_2 vibron from phase X′.

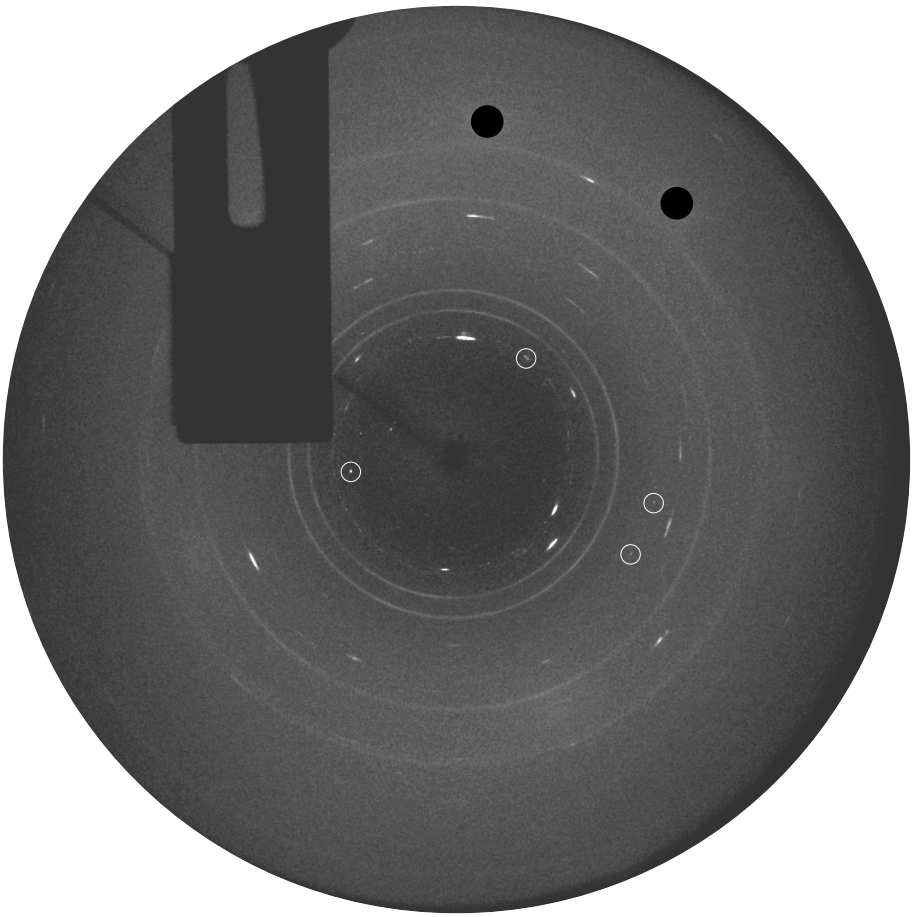

Figure A.12 Chapter 7: Image plate showing raw diffraction data from mixed sample of H_2S (reflections circled in white) and $(H_2S)_2H_2$ (streaky reflections), demonstrating both substances were separate numerous single crystals. Rings are from Re gasket, black circles mask reflections from diamond.

Bibliography

[1] E. J. Pace, J. Binns, M. Peña Alvarez, P. Dalladay-Simpson, E. Gregoryanz, and R. T. Howie, "Synthesis and stability of hydrogen selenide compounds at high pressure," *J. Chem. Phys.* **147**, 184303 (2017).

[2] E. J. Pace, J. Binns, P. Dalladay-Simpson, M. Peña Alvarez, and R. T. Howie, "Comment on "Synthesis and properties of selenium trihydride at high pressures"," *Phys. Rev. B* **98**, 106101 (2018).

[3] P. W. Bridgman, *The Physics of High Pressure* (G. Bell and Sons, London, UK, 1931).

[4] P. W. Bridgman, "Measurements of the deviation from Ohm's law in metals at high current densities," *Proc. Natl. Acad. Sci. USA* **7**, 299–303 (1921).

[5] S. M. Stishov and S. V. Popova, "A new modification of silica," *Geochem.* **10**, 923–926 (1961).

[6] T. Takahashi and W. A. Bassett, "High-pressure polymorph of iron," *Science* **145**, 483–6 (1964).

[7] H. K. Mao and P. M. Bell, "Observations of hydrogen at room temperature (25 °C) and high pressure (to 500 Kilobars)." *Science* **203**, 1004–6 (1979).

[8] H. K. Mao and R. J. Hemley, "Optical studies of hydrogen above 200 gigapascals: Evidence for metallization by band overlap," *Science* **244**, 1462–1465 (1989).

[9] W. A. Bassett, "Diamond anvil cell, 50^{th} birthday," *High Press. Res.* **29**, 163–186 (2009).

[10] C. E. Weir, E. R. Lippincott, A. Van Valkenburg, and E. N. Bunting, "Infrared studies in the 1 to 15-micron region to 30,000 atmospheres," *J. Res. Natl. Stand.* **63A**, 55 (1959).

[11] A. Van Valkenburg, "Visual observations of high pressure phase transitions," *Rev. Sci. Instr.* **33**, 1462 (1962).

[12] R. A. Forman, G. J. Piermarini, J. D. Barnett, and S. Block, "Pressure measurement made by the utilization of ruby sharp-line luminescence," *Science* **176**, 284–285 (1972).

[13] H. K. Mao and P. M. Bell, "High-pressure physics: The 1-megabar mark on the ruby R1 static pressure scale," *Science* **191**, 851–852 (1976).

[14] E. Wigner and H. B. Huntington, "On the possibility of a metallic modification of hydrogen," *J. Chem. Phys.* **3**, 764–770 (1935).

[15] N. W. Ashcroft, "Metallic hydrogen: a high-temperature superconductor?" *Phys. Rev. Lett.* **21**, 1748–1749 (1968).

[16] J. M. McMahon and D. M. Ceperley, "Ground-State Structures of Atomic Metallic Hydrogen," *Phys. Rev. Lett.* **106**, 165302 (2011).

[17] N. W. Ashcroft, "Hydrogen dominant metallic alloys: high temperature superconductors?" *Phys. Rev. Lett.* **92**, 187002 (2004).

[18] V. L. Ginzburg, "Once again about high-temperature superconductivity," *Contemp. Phys.* **33**, 15–23 (1992).

[19] J. Feng, W. Grochala, T. Jaroń, R. Hoffmann, A. Bergara, and N. W. Ashcroft, "Structures and potential superconductivity in SiH_4 at high pressure: En route to "metallic hydrogen"," *Phys. Rev. Lett.* **96**, 017006 (2006).

[20] E. Zurek, R. Hoffmann, N. W. Ashcroft, A. R. Oganov, and A. O. Lyakhov, "A little bit of lithium does a lot for hydrogen," *PNAS* **106**, 17640–3 (2009).

[21] H. Wang, J. S. Tse, K. Tanaka, T. Iitaka, and Y. Ma, "Superconductive sodalite-like clathrate calcium hydride at high pressures." *Proc. Natl. Acad. Sci. USA* **109**, 6463–6 (2012).

[22] Y. Li, J. Hao, H. Liu, Y. Li, and Y. Ma, "The metallization and superconductivity of dense hydrogen sulfide," *J. Chem. Phys.* **140**, 174712 (2014).

[23] D. Duan, Y. Liu, F. Tian, D. Li, X. Huang, Z. Zhao, H. Yu, B. Liu, W. Tian, and T. Cui, "Pressure-induced metallization of dense $(H_2S)_2H_2$ with high-T_c superconductivity," *Sci. Rep.* **4**, 6968 (2014).

[24] X. Feng, J. Zhang, G. Gao, H. Liu, and H. Wang, "Compressed sodalite-like MgH_6 as a potential high-temperature superconductor," *RSC Adv.* **5**, 59292–59296 (2015).

[25] H. Liu, I. I. Naumov, R. Hoffmann, N. W. Ashcroft, and R. J. Hemley, "Potential high-T_c superconducting lanthanum and yttrium hydrides at high pressure." *PNAS* **114**, 6990–6995 (2017).

[26] A. P. Drozdov, V. S. Minkov, S. P. Besedin, P. P. Kong, M. A. Kuzovnikov, D. A. Knyazev, and M. I. Eremets, "Superconductivity at 215 K in lanthanum hydride at high pressures," (2018), arXiv:1808.07039 .

[27] M. Somayazulu, M. Ahart, A. K. Mishra, Z. M. Geballe, M. Baldini, Y. Meng, V. V. Struzhkin, and R. J. Hemley, "Evidence for superconductivity above 260 K in lanthanum superhydride at megabar pressures," (2018), arXiv:1808.07695 .

[28] A. P. Drozdov, M. I. Eremets, I. A. Troyan, V. Ksenofontov, and S. I. Shylin, "Conventional superconductivity at 203 kelvin at high pressures in the sulfur hydride system," *Nature* **525**, 73–76 (2015).

[29] E. E. Gordon, K. Xu, H. Xiang, A. Bussmann-Holder, R. K. Kremer, A. Simon, J. K uhler, and M. H. Whangbo, "Structure and composition of the 200K-superconducting phase of H_2S at ultrahigh pressure: the Perovskite $(SH^-)(H_3S^+)$," *Angew. Chem. Int. Ed.* **55**, 3682–3684 (2016).

[30] I. Errea, M. Calandra, C. J. Pickard, J. R. Nelson, R. J. Needs, Y. Li, H. Liu, Y. Zhang, Y. Ma, and F. Mauri, "Quantum hydrogen-bond symmetrization in the superconducting hydrogen sulfide system," *Nature* **532**, 81–84 (2016).

[31] R. Akashi, W. Sano, R. Arita, and S. Tsuneyuki, "Possible magnéli phases and self-alloying in the superconducting sulfur hydride," *Phys. Rev. Lett.* **117**, 075503–075506 (2016).

[32] M. Einaga, M. Sakata, T. Ishikawa, K. Shimizu, M. I. Eremets, A. P. Drozdov, I. A. Troyan, N. Hirao, and Y. Ohishi, "Crystal structure of the superconducting phase of sulfur hydride," *Nat. Phys.* **12**, 835–839 (2016).

[33] I. A. Troyan, A. Gavriliuk, R. Rüffer, A. Chumakov, A. Mironovich, I. Lyubutin, D. Perekalin, A. P. Drozdov, and M. I. Eremets, "Observation of superconductivity in hydrogen sulfide from nuclear resonant scattering," *Science* **351**, 1303–1306 (2016).

[34] F. Capitani, B. Langerome, J.-B. Brubach, P. Roy, A. Drozdov, M. I. Eremets, E. J. Nicol, J. P. Carbotte, and T. Timusk, "Spectroscopic evidence of a new energy scale for superconductivity in H_3S," *Nat. Phys.* **13**, 859–863 (2017).

[35] K. Shimizu, M. Einaga, M. Sakata, A. Masuda, H. Nakao, M. I. Eremets, A. P. Drozdov, I. A. Troyan, N. Hirao, S. Kawaguchi, and Y. Ohishi, "Superconductivity and structural studies of highly compressed hydrogen sulfide," *Physica. C, Superconductivity.* **552**, 27–29 (2018).

[36] M. Sakashita, H. Yamawaki, H. Fujihisa, K. Aoki, S. Sasaki, and H. Shimizu, "Pressure-induced molecular dissociation and metallization in hydrogen-bonded H_2S Solid," *Phys. Rev. Lett.* **79**, 1082–1085 (1997).

[37] M. Sakashita, H. Fujihisa, H. Yamawaki, and K. Aoki, "Molecular dissociation in deuterium sulfide under high pressure: Infrared and Raman study," *J. Phys. Chem. A* **104**, 8838–8842 (2000).

[38] H. Fujihisa, H. Yamawaki, M. Sakashita, A. Nakayama, T. Yamada, and K. Aoki, "Molecular dissociation and two low-temperature high-pressure phases of H_2S," *Phys. Rev. B* **69**, 214102 (2004).

[39] S. Duwal and C.-S. Yoo, "Phase diagram and symmetrization of dense D_2S," *J. Phys. Chem. C* **120**, 21770–21777 (2016).

[40] R. Rousseau, M. Boero, M. Bernasconi, M. Parrinello, and K. Terakura, "*Ab initio* simulation of phase transitions and dissociation of H_2S at high pressure," *Phys. Rev. Lett.* **85**, 1254–1257 (2000).

[41] L. Wang, F. Tian, W. Feng, C. Chen, Z. He, Y. Ma, T. Cui, B. Liu, and G. Zou, "Order-disorder phase transition and dissociation of hydrogen sulfide under high pressure: *Ab initio* molecular dynamics study," *J. Chem. Phys.* **132**, 164506 (2010).

[42] J. A. Flores-Livas, A. Sanna, and E. K. U. Gross, "High temperature superconductivity in sulfur and selenium hydrides at high pressure," *Eur. Phys. J. B* **89**, 63 (2015).

[43] S. Zhang, Y. Wang, J. Zhang, H. Liu, X. Zhong, H.-F. Song, G. Yang, L. Zhang, and Y. Ma, "Phase diagram and high-temperature superconductivity of compressed selenium hydrides," *Sci. Rep.* **5**, 15433 (2015).

[44] X. Zhong, H. Wang, J. Zhang, H. Liu, S. Zhang, H.-F. Song, G. Yang, L. Zhang, and Y. Ma, "Tellurium hydrides at high pressures: High-temperature superconductors," *Phys. Rev. Lett.* **116**, 057002 (2016).

[45] D. Szczęśniak, I. A. Wrona, E. A. Drzazga, A. Z. Kaczmarek, and K. A. Szewczyk, "On the critical temperature discontinuity at the theoretical bcc-fcc phase transition in compressed selenium and tellurium superconductors," *J. Phys. Condens. Matter* **29**, 445602 (2017).

[46] T. A. Strobel, P. Ganesh, M. Somayazulu, P. R. C. Kent, and R. J. Hemley, "Novel cooperative interactions and structural ordering in $H2_S$-H_2," *Phys. Rev. Lett.* **107**, 255503 (2011).

[47] S. Duwal and C.-S. Yoo, "Reversible photochemical transformation of S and H_2 mixture to $(H_2S)_2H_2$ at high pressures," *J. Phys. Chem. C* **121**, 12863–12870 (2017).

[48] B. Guigue, A. Marizy, and P. Loubeyre, "Direct synthesis of pure H_3S from S and H elements: No evidence of the cubic superconducting phase up to 160 GPa," *Phys. Rev. B* **95**, 020104(R) (2017).

[49] A. F. Goncharov, S. S. Lobanov, V. B. Prakapenka, and E. Greenberg, "Stable high-pressure phases in the H-S system determined by chemically reacting hydrogen and sulfur," *Phys. Rev. B* **95**, 140101 (2017).

[50] A. Smekal, "Zur quantentheorie der dispersion," *Naturwissenschaften* **11**, 873–875 (1923).

[51] G. Landsberg and L. Mandelstam, "Über die lichtzerstreuung in kristallen," *Z. Phys.* **50**, 769–780 (1928).

[52] C. V. Raman and K. S. Krishnan, "A new type of secondary radiation," *Nature* **121**, 501–502 (1928).

[53] D. A. Long, *Raman Spectroscopy* (McGraw-Hill, Columbus, OH, US, 1977).

[54] P. W. Atkins and R. Friedman, *Molecular Quantum Mechanics* (Oxford University Press, Oxford, UK, 2011).

[55] W. Friedrich, P. Knipping, and M. Laue, "Interferenzerscheinungen bei röntgenstrahlen," *Ann. Phys.* **346**, 971–988 (1913).

[56] W. H. Bragg and W. L. Bragg, "The reflection of x-rays by crystals," *Proc. Royal Soc. A* **88**, 428–438 (1913).

[57] N. W. Ashcroft and N. D. Mermin, *Solid State Physics* (Holt, Rinehart & Winston, London, UK, 1976).

[58] M. I. Aroyo, ed., *International Tables for Crystallography*, Vol. A (International Union of Crystallography, Chester, UK, 2016).

[59] R. E. Dinnebier and S. J. L. Billinge, "Principles of Powder Diffraction," in *Powder Diffraction: Theory and Practice* (Royal Society of Chemistry, Cambridge, UK, 2008).

[60] M. Riteveld, H., *The Rietveld Method*, edited by R. A. Young (Oxford Science Publications, Oxford, UK, 1993).

[61] A. Le Bail, "Whole powder pattern decomposition methods and applications: A retrospection," *Powder Diffr.* **20**, 316–326 (2005).

[62] A. Jayaraman, "Diamond anvil cell and high-pressure physical investigations," *Rev. Mod. Phys.* **55**, 65–108 (1983).

[63] R. Boehler and K. De Hantsetters, "New anvil designs in diamond-cells," *High Press. Res.* **24**, 391–396 (2004).

[64] G. Hernandez, *Fabry-Perot Interferometers* (Cambridge University Press, Cambridge, UK, 1986).

[65] G. J. Piermarini, S. Block, J. D. Barnett, and R. A. Forman, "Calibration of the pressure dependence of the R1 ruby fluorescence line to 195 kbar," *J. Appl. Phys.* **46**, 2774 (1975).

[66] H. K. Mao, J. Xu, and P. M. Bell, "Calibration of the ruby pressure gauge to 800 kbar under quasi-hydrostatic conditions," *J. Geophys. Res.* **91**, 4673 (1986).

[67] M. Hanfland, K. Syassen, S. Fahy, Steven G. Louie, and Marvin L. Cohen, "Pressure dependence of the first-order Raman mode in diamond," *Phys. Rev. B* **31**, 6896–6899 (1985).

[68] Y. Akahama and H. Kawamura, "High-pressure Raman spectroscopy of diamond anvils to 250 GPa: Method for pressure determination in the multimegabar pressure range," *J. Appl. Phys.* **96**, 3748–3751 (2004).

[69] Y. Akahama and H. Kawamura, "Pressure calibration of diamond anvil Raman gauge to 310 GPa," *J. Appl. Phys.* **100**, 043516 (2006).

[70] Y. Akahama and H. Kawamura, "Pressure calibration of diamond anvil Raman gauge to 410 GPa," *J. Phys. Conf. Ser.* **215**, 012195 (2010).

[71] M. S. Liu, L. A. Bursill, S. Prawer, and R. Beserman, "Temperature dependence of the first-order Raman phonon line of diamond," *Phys. Rev. B* **61**, 3391–3395 (2000).

[72] A. F. Goncharov, "Raman spectroscopy at high pressures," *Int. J. Spectrosc.* **2012**, 1–16 (2012).

[73] M. Wojdyr, "*Fityk*: a general-purpose peak fitting program," *J. Appl. Crystallogr.* **43**, 1126–1128 (2010).

[74] C. Prescher and V. B. Prakapenka, "*DIOPTAS*: a program for reduction of two-dimensional X-ray diffraction data and data exploration," *High Press. Res.* **35**, 223–230 (2015).

[75] J. Rodríguez-Carvajal, "Recent advances in magnetic structure determination by neutron powder diffraction," *Physica B Condens. Matter* **192**, 55–69 (1993).

[76] V. Petříček, M. Dušek, and L. Palatinus, "Crystallographic computing system *JANA* 2006: General features," *Z. Kristallogr. Cryst.* **229**, 345–352 (2014).

[77] J. Gonzalez-Platas, M. Alvaro, F. Nestola, and R. Angel, "*EosFit7-GUI*: A new graphical user interface for equation of state calculations, analyses and teaching," *J. Appl. Crystallogr.* **49**, 1377–1382 (2016).

[78] A. Dewaele, M. Torrent, P. Loubeyre, and M. Mezouar, "Compression curves of transition metals in the Mbar range: Experiments and projector augmented-wave calculations," *Phys. Rev. B* **78**, 104102 (2008).

[79] H. Shimizu, H. Yamaguchi, S. Sasaki, A. Honda, S. Endo, and M. Kobayashi, "Pressure-temperature phase diagram of solid hydrogen sulfide determined by Raman spectroscopy," *Phys. Rev. B* **51**, 9391–9394 (1995).

[80] J. W. Stewart, "Compression and phase transitions of solid NH_3, SiF_4, H_2S, and CF_4," *J. Chem. Phys.* **33**, 128 (1960).

[81] H. Shimizu, Y. Nakamichi, and S. Sasaki, "Pressure-induced phase transition in solid hydrogen sulfide at 11 GPa," *J. Chem. Phys.* **95**, 2036 (1991).

[82] A. Anderson, O. S. Binbrek, and H. C. Tang, "Raman and infrared study of the low temperature phase of solid H_2S and D_2S," *J. Raman Spectrosc.* **6**, 213–220 (1977).

[83] J. K. Cockcroft and A. N. Fitch, "The solid-phases of deuterium sulfide by powder neutron diffraction," *Z. Kristallogr. Cryst.* **193**, 1–19 (1990).

[84] S. Endo, N. Ichimiya, K. Koto, S. Sasaki, and H. Shimizu, "X-ray-diffraction study of solid hydrogen sulfide under high pressure," *Phys. Rev. B* **50**, 5865–5867 (1994).

[85] S. Sasaki and H. Shimizu, "High-pressure Brillouin study on orientationally disordered solid phase I of H_2S and D_2S," *J. Phys. Soc. Jpn.* **64**, 3309–3314 (1995).

[86] H. Fujihisa, H. Yamawaki, M. Sakashita, K. Aoki, S. Sasaki, and H. Shimizu, "Structures of H_2S: Phases I′ and IV under high pressure," *Phys. Rev. B* **57**, 2651–2654 (1998).

[87] E. Sándor and S. O. Ogunade, "Structure and phase transition in solid hydrogen and deuterium sulphides," *Nature* **224**, 905–907 (1969).

[88] J. S. Loveday, R. J. Nelmes, S. Klotz, J. M. Besson, and G. Hamel, "Pressure-induced hydrogen bonding: Structure of D_2S phase I′," *Phys. Rev. Lett.* **85**, 1024–1027 (2000).

[89] A. I. Anderson, S. Demoor, and R. C. Hanson, "Raman Study of a new high pressure phase of hydrogen sulfide," *Chem. Phys. Lett.* **140**, 471–475 (1987).

[90] K. Momma and F. Izumi, "*VESTA*: a three-dimensional visualization system for electronic and structural analysis," *J. Appl. Crystallogr.* **41**, 653–658 (2008).

[91] S. Endo, A. Honda, K. Koto, O. Shimomura, T. Kikegawa, and N. Hamaya, "Crystal structure of high-pressure phase-IV solid hydrogen sulfide," *Phys. Rev. B* **57**, 5699–5703 (1998).

[92] T. Ikeda, "Pressure-induced phase transition of hydrogen sulfide at low temperature: Role of the hydrogen bond and short S-S contacts," *Phys. Rev. B* **64**, 104103 (2001).

[93] R. Rousseau, M. Boero, M. Bernasconi, M. Parrinello, and K. Terakura, "Static structure and dynamical correlations in high pressure H_2S," *Phys. Rev. Lett.* **83**, 2218–2221 (1999).

[94] L. Wang, Z. He, Y. Ma, T. Cui, B. Liu, and G. Zou, "Structural and dynamical properties of H_2S under high pressure: *Ab initio* molecular dynamics studies," *J. Phys. Condens. Matter* **19**, 425232 (2007).

[95] S. Endo, A. Honda, S. Sasaki, H. Shimizu, O. Shimomura, and T. Kikegawa, "High-pressure phase of solid hydrogen sulfide," *Phys. Rev. B* **54**, R717–R719 (1996).

[96] H. Shimizu, T. Ushida, S. Sasaki, M. Sakashita, H. Yamawaki, and K. Aoki, "High-pressure phase transitions of solid H_2S probed by Fourier-transform infrared spectroscopy," *Phys. Rev. B* **55**, 5538–5541 (1997).

[97] A. F. Goncharov, S. S. Lobanov, I. Kruglov, X.-M. Zhao, X.-J. Chen, A. R. Oganov, Z. Konôpková, and V. B. Prakapenka, "Hydrogen sulfide at high pressure: Change in stoichiometry," *Phys. Rev. B* **93**, 174105 (2016).

[98] D. Duan, X. Huang, F. Tian, D. Li, H. Yu, Y. Liu, Y. Ma, B. Liu, and T. Cui, "Pressure-induced decomposition of solid hydrogen sulfide," *Phys. Rev. B* **91**, 180502 (2015).

[99] Y. Li, L. Wang, H. Liu, Y. Zhang, J. Hao, C. J. Pickard, J. R. Nelson, R. J. Needs, W. Li, Y. Huang, I. Errea, M. Calandra, F. Mauri, and Y. Ma, "Dissociation products and structures of solid H_2S at strong compression," *Phys. Rev. B* **93**, 020103 (2016).

[100] A. Kruis and K. Clusius, "Über die Molwärmen und umwandlungen der kondensierten hydride und deuteride des schwefels und selens," *Z. Phys. Chem.* **38B**, 156–176 (1938).

[101] N. Kitamura, Y. Kashiwase, J. Harada, and G. Honjo, "Electron diffraction study of the phase transition of hydrogen sulfide at -170 °C," *Acta Crystallogr.* **14**, 687–688 (1961).

[102] J. Harada and N. Kitamura, "Structure and phase transition of solid hydrogen sulphide," *J. Phys. Soc. Jpn.* **19**, 328–343 (1964).

[103] G. Natta, "Structure of hydrogen sulphide and hydrogen selenide," *Nature* **127**, 129–129 (1931).

[104] C. P. Smyth and C. S. Hitchcock, "The dielectric constants and transitions of solid ammonia, hydrogen sulfide and methyl alcohol," *J. Am. Chem. Soc.* **56**, 1084–1087 (1934).

[105] M. L. Huggins, "Bond energies and polarities," *J. Am. Chem. Soc.* **75**, 4123–4126 (1953).

[106] H. Luo, S. Desgreniers, Y. K. Vohra, and A. L. Ruoff, "High-pressure optical studies on sulfur to 121 GPa: Optical evidence for metallization," *Phys. Rev. Lett.* **67**, 2998–3001 (1991).

[107] S. Kometani, M. I. Eremets, K. Shimizu, M. Kobayashi, and K. Amaya, "Observation of pressure-induced superconductivity of sulfur," *J. Phys. Soc. Jpn.* **66**, 2564–2565 (1997).

[108] M. Becucci, R. Bini, E. Castellucci, B. Eckert, and H. J. Jodl, "Mode assignment of sulfur $\alpha - S_8$ by polarized raman and FTIR studies at low temperatures," *J. Phys. Chem. B* **101**, 2132–2137 (1997).

[109] B. E. Langner, "Selenium and Selenium Compounds," in *Ullmann's Encyclopedia of Industrial Chemistry* (Wiley-VCH Verlag GmbH & Co. KGaA, Weinheim, DE, 2000).

[110] F. Pouliquen, C. Blanc, E. Arretz, I. Labat, J. Tournier-Lasserve, A. Ladousse, J. Nougayrede, G. Savin, R. Ivaldi, M. Nicolas, J. Fialaire, R. Millischer, C. Azema, L. Espagno, H. Hemmer, and J. Perrot, "Hydrogen Sulfide," in *Ullmann's Encyclopedia of Industrial Chemistry* (Wiley-VCH Verlag GmbH & Co. KGaA, Weinheim, DE, 2000).

[111] K. S. Andrikopoulos, F. A. Gorelli, M. Santoro, and S. N. Yannopoulos, "Elemental sulfur under high hydrostatic pressure: an up-to-date Raman study," *High Press. Res.* **33**, 134–140 (2013).

[112] G. C. Vezzoli, F. Dachille, and R. Roy, "Melting curve of sulfur to 31 kilobars," *Inorg. Chem.* **8**, 2658–2661 (1969).

[113] V. Diatschenko, C. W. Chu, D. H. Liebenberg, D. A. Young, M. Ross, and R. L. Mills, "Melting curves of molecular hydrogen and molecular deuterium under high pressures between 20 and 373 K," *Phys. Rev. B* **32**, 381–389 (1985).

[114] B. Eckert, R. Schumacher, H. J. Jodl, and P. Foggi, "Pressure and photo-induced phase transitions in sulphur investigated by Raman spectroscopy," *High Press. Res.* **17**, 113–146 (2000).

[115] W. M. Haynes, *CRC Handbook of Chemistry and Physics*, 95th ed. (CRC Press and Taylor & Francis, Boca Raton, FL, US, 2014).

[116] X. Zhang, W. Xu, Y. Wang, S. Jiang, F. A. Gorelli, E. Greenberg, V. B. Prakapenka, and A. F. Goncharov, "Synthesis and properties of selenium trihydride at high pressures," *Phys. Rev. B* **97**, 064107 (2018).

[117] N. N. Greenwood and A. Earnshaw, *Chemistry of the Elements*, 2nd ed. (Butterworth-Heinemann, Oxford, UK, 1997).

[118] F. Fehér, *Handbook of Preparative Inorganic Chemistry*, edited by G. Brauer, Vol. 1 (Academic Press, New York, US, 1963) page 438.

[119] S. Atkins, *Inorganic Chemistry*, 5th ed., edited by W. H. Freedman (W. H. Freeman and Co., New York, US, 2010).

[120] H. Shimizu, Y. Nakamichi, and S. Sasaki, "High-pressure Raman study of liquid and solid ethanol at pressures up to 17 GPa," *J. Raman Spectrosc.* **21**, 703–704 (1990).

[121] S. H. Moon and H. G. Drickamer, "Effect of pressure on hydrogen bonds on organic solids," *J. Chem. Phys.* **61**, 48–54 (1974).

[122] M. B. Kruger, Q. Williams, and R. Jeanloz, "Vibrational spectra of $Mg(OH)_2$ and $Ca(OH)_2$ under pressure," *J. Chem. Phys.* **91**, 5910–5915 (1989).

[123] X.-D. Liu, R. T. Howie, H.-C. Zhang, X.-J. Chen, and E. Gregoryanz, "High-Pressure behavior of hydrogen and deuterium at low temperatures," *Phys. Rev. Lett.* **119**, 065301 (2017).

[124] H. Davy, "The Bakerian Lecture: On some of the combinations of oxymuriatic gas and oxygene, and on the chemical relations of these principles, to inflammable bodies," *Philos. Trans. Royal Soc. Lon.* **101**, 1–35 (1811).

[125] P. Buchanan, A. K. Soper, H. Thompson, R. E. Westacott, J. L. Creek, G. Hobson, and C. A. Koh, "Search for memory effects in methane hydrate: Structure of water before hydrate formation and after hydrate decomposition," *J. Chem. Phys.* **123**, 164507 (2005).

[126] H. Hirai, T. Kondo, M. Hasegawa, T. Yagi, Y. Yamamoto, T. Komai, K. Nagashima, M. Sakashita, H. Fujihisa, and K. Aoki, "Methane hydrate behavior under high pressure," *J. Phys. Chem. B* **104**, 1429–1433 (2000).

[127] V. R. Belosludov, T. M. Inerbaev, R. V. Belosludov, J. Kudoh, and Y. Kawazoe, "Absolute stability boundaries of clathrate hydrates of cubic structure II," *J. Supramol. Chem.* **2**, 377–383 (2002).

[128] A. Braeuer, S. Dowy, A. Leipertz, R. Schatz, and E. Schluecker, "Injection of ethanol into supercritical CO_2: Determination of mole fraction and phase state using linear Raman scattering," *Opt. Express* **15**, 8377 (2007).

[129] O. H. Scalise and A. E. Rodriguez, "High-pressure phase equilibria study of the hydrogen-water fluid mixture," *Fluid Ph. Equilibria* **99**, 49–62 (1994).

[130] W.-P. Hsieh and Y.-H. Chien, "High pressure Raman spectroscopy of H_2O-CH_3OH mixtures," *Sci. Rep.* **5**, 8532 (2015).

[131] T. A. Dolenko, S. A. Burikov, S. A. Dolenko, A. O. Efitorov, I. V. Plastinin, V. I. Yuzhakov, and S. V. Patsaeva, "Raman spectroscopy of water–ethanol solutions: The estimation of hydrogen bonding energy and the appearance of clathrate-like structures in solutions," *J. Phys. Chem. A* **119**, 10806–10815 (2015).

[132] K. Kosugi, T. Nakabayashi, and N. Nishi, "Low-frequency Raman spectra of crystalline and liquid acetic acid and its mixtures with water. Is the liquid dominated by hydrogen-bonded cyclic dimers?" *Chem. Phys. Lett.* **291**, 253–261 (1998).

[133] J.-H. Guo, Y. Luo, A. Augustsson, S. Kashtanov, J.-E. Rubensson, D. K. Shuh, H. Ågren, and J. Nordgren, "Molecular structure of alcohol-water mixtures," *Phys. Rev. Lett.* **91**, 157401 (2003).

[134] S. Dixit, J. Crain, W. C. K. Poon, J. L. Finney, and A. K. Soper, "Molecular segregation observed in a concentrated alcohol–water solution," *Nature* **416**, 829–832 (2002).

[135] L. E. Bove, R. Gaal, Z. Raza, A. A. Ludl, S. Klotz, A. M. Saitta, A. F. Goncharov, and P. Gillet, "Effect of salt on the H-bond symmetrization in ice," *Proc. Natl. Acad. Sci. USA* **112**, 8216–8220 (2015).

[136] R. T. Howie, R. Turnbull, J. Binns, M. Frost, P. Dalladay-Simpson, and E. Gregoryanz, "Formation of xenon-nitrogen compounds at high pressure," *Sci. Rep.* **6**, 34896 (2016).

[137] R. D. Johnson, "NIST Computational Chemistry Comparison and Benchmark Database 101," National Institute of Standards and Technology, Gaithersburg MD, US (2018).

[138] J. H. Loehlin, P. G. Mennitt, and J. S. Waugh, "Proton resonance study of molecular motion and phase behavior of solid H_2S and H_2Se," *J. Chem. Phys.* **44**, 3912–3917 (1966).

[139] Z. M. E. Saffar and P. Schultz, "On a proton magnetic resonance study of H_2S and H_2Se," *J. Chem. Phys.* **56**, 2524–2526 (1972).

[140] G. Facey, R. E. Wasylishen, M. J. Collins, C. I. Ratcliffe, and J. A. Ripmeester, "A deuterium and selenium-77 NMR study of the condensed phases of hydrogen selenide," *J. Phys. Chem.* **90**, 2047–2052 (1986).

[141] B. A. Paldus, S. A. Schlueter, and A. Anderson, "Raman and infrared spectra of solid hydrogen selenide," *J. Raman Spectrosc.* **23**, 87–92 (1992).

[142] P. Loubeyre, R. LeToullec, D. Hausermann, M. Hanfland, R. J. Hemley, H. K. Mao, and L. W. Finger, "X-ray diffraction and equation of state of hydrogen at megabar pressures," *Nature* **383**, 702–704 (1996).

[143] M. I. McMahon, C. Hejny, J. S. Loveday, L. F. Lundegaard, and M. Hanfland, "Confirmation of the incommensurate nature of Se-IV at pressures below 70 GPa," *Phys. Rev. B* **70**, 054101 (2004).

[144] Y. Akahama, M. Kobayashi, and H. Kawamura, "Pressure-induced superconductivity and phase transition in selenium and tellurium," *Solid State Commun.* **84**, 803–806 (1992).

[145] L. Properzi, A. Polian, P. Munsch, and A. Di Cicco, "Investigation of the phase diagram of selenium by means of Raman spectroscopy," *High Press. Res.* **33**, 35–39 (2013).

[146] E. Katoh, H. Yamawaki, H. Fujihisa, M. Sakashita, and K. Aoki, "Raman and infrared study of phase transitions in solid HBr under pressure," *Phys. Rev. B* **59**, 11244–11250 (1999).

[147] T. Kume, T. Tsuji, S. Sasaki, and H. Shimizu, "Phase study on solid hydrogen bromide by high-pressure and low-temperature Raman spectroscopy," *Phys. Rev. B* **58**, 8149–8151 (1998).

[148] J. Binns, X.-D. Liu, P. Dalladay-Simpson, V. Afonina, E. Gregoryanz, and R. T. Howie, "Synthesis and stability of hydrogen iodide at high pressures," *Phys. Rev. B* **96**, 144105 (2017).

[149] J. Binns, P. Dalladay-Simpson, M. Wang, G. J. Ackland, E. Gregoryanz, and R. T. Howie, "Formation of H_2-rich iodine-hydrogen compounds at high pressure," *Phys. Rev. B* **97**, 024111 (2018).

[150] Z. He, Z. G. Wang, H. Y. Zhu, X. R. Liu, J. P. Peng, and S. M. Hong, "High-pressure behavior of amorphous selenium from ultrasonic measurements and Raman spectroscopy," *Appl. Phys. Lett.* **105**, 011901 (2014).

[151] Y. Akahama, M. Kobayashi, and H. Kawamura, "Structural studies of pressure-induced phase transitions in selenium up to 150 GPa," *Phys. Rev. B* **47**, 20–26 (1993).

[152] R. Boehler, M. Guthrie, J. J. Molaison, A. M. dos Santos, S. Sinogeikin, S. Machida, N. Pradhan, and C. A. Tulk, "Large-volume diamond cells for neutron diffraction above 90 GPa," *High Press. Res.* **33**, 546–554 (2013).

[153] A. P. Drozdov, M. I. Eremets, and I. A. Troyan, "Conventional superconductivity at 190 K at high pressures," (2014), arXiv:1412.0460 .

[154] G. Gao, A. R. Oganov, A. Bergara, M. Martinez-Canales, T. Cui, T. Iitaka, Y. Ma, and G. Zou, "Superconducting high pressure phase of germane," *Phys. Rev. Lett.* **101**, 107002 (2008).

Publications

THE JOURNAL OF CHEMICAL PHYSICS **147**, 184303 (2017)

Synthesis and stability of hydrogen selenide compounds at high pressure

Edward J. Pace,[1] Jack Binns,[2] Miriam Peña Alvarez,[3] Philip Dalladay-Simpson,[2] Eugene Gregoryanz,[2,3] and Ross T. Howie[2,a)]

[1]*School of Chemistry and Centre for Science at Extreme Conditions, University of Edinburgh, Edinburgh EH9 3FD, United Kingdom*

[2]*Center for High Pressure Science and Technology Advanced Research, 1690 Cailun Rd., Building 6, Pudong, Shanghai 201203, People's Republic of China*

[3]*School of Physics and Astronomy and Centre for Science at Extreme Conditions, University of Edinburgh, Edinburgh EH9 3FD, United Kingdom*

(Received 12 September 2017; accepted 24 October 2017; published online 13 November 2017)

The observation of high-temperature superconductivity in hydride sulfide (H_2S) at high pressures has generated considerable interest in compressed hydrogen-rich compounds. High-pressure hydrogen selenide (H_2Se) has also been predicted to be superconducting at high temperatures; however, its behaviour and stability upon compression remains unknown. In this study, we synthesize H_2Se *in situ* from elemental Se and molecular H_2 at pressures of 0.4 GPa and temperatures of 473 K. On compression at 300 K, we observe the high-pressure solid phase sequence (I-I′-IV) of H_2Se through Raman spectroscopy and x-ray diffraction measurements, before dissociation into its constituent elements. Through the compression of H_2Se in H_2 media, we also observe the formation of a host-guest structure, $(H_2Se)_2H_2$, which is stable at the same conditions as H_2Se, with respect to decomposition. These measurements show that the behaviour of H_2Se is remarkably similar to that of H_2S and provides further understanding of the hydrogen chalcogenides under pressure. *Published by AIP Publishing.*
https://doi.org/10.1063/1.5004242

I. INTRODUCTION

The recent claim of high-temperature superconductivity in hydrogen sulfide at megabar pressures has drawn attention back to the formation of hydrides with exotic properties.[1] The superconductive mechanism, composition, structure, and stability field of sulfur hydride at high pressures have been extensively investigated, although decisive conclusions have yet to be reached.[2–10] Despite this interest and predictions of high T_c superconductivity, the heavier hydrogen chalcogenides (i.e., H_2Se and H_2Te) remain experimentally unexplored.[11,12]

H_2Se is known to form from the direct reaction between Se and H_2 at high temperature. However, experimental studies of the solid state are limited to ambient pressure, low temperature investigations.[13–16] As the heavier sister molecule to hydrogen sulfide, hydrogen selenide is likely to exhibit similar behaviour at high pressure; indeed, theoretical studies at the megabar regime find similarities in the solid phases.[11,17]

H_2S exhibits three solid phases between pressures of 0.5 GPa and 27 GPa at 300 K: transitioning from a rotationally disordered solid (I-I′) to an ordered hydrogen-bonded structure (IV), before dissociating.[18–26] To date, there have been no experimental high-pressure investigations of H_2Se, but low temperature studies at ambient pressure find strong similarities in the crystal structures and Raman characteristics of phases I–III, with their corresponding phases in H_2S.[14,16] Mixtures of H_2S and H_2 are known to form $(H_2S)_2H_2$, a host-guest compound at pressures as low as 3.5 GPa.[27] High T_c superconductivity has been predicted in high-pressure simulations of both H_2S and $(H_2S)_2H_2$ compounds.[28,29] Combined experimental and theoretical efforts have suggested the high-T_c phase as an H_3S compound, with a maximum T_c of 203 K at 155 GPa.[1,8,29] With Se being larger and slightly less electronegative, computational studies predict lower stability with respect to pressure but propose the formation of superconducting phases H_3Se and HSe above ~120 GPa, with maximum T_c estimated between 110 and 130 K.[11,17] To further understand the predicted exotic phenomena, it is important to first investigate the formation and high-pressure stability of H_2Se and to compare the behaviour with that of the extensively studied H_2S.

In this study, we report the direct synthesis of H_2Se from its constituent elements at conditions of 0.4 GPa and ~473 K. We find that phase I of H_2Se undergoes a phase transition at 12 GPa, similar to the transition to phase IV in H_2S. In H_2-rich mixtures, we observe the formation of a host-guest $(H_2Se)_2H_2$ structure above 4.2 GPa. This compound is identified by characteristic vibrational Raman spectra differing from pure H_2Se. The structure and stoichiometry of this compound were confirmed through x-ray diffraction measurements whereby we find $(H_2Se)_2H_2$ to crystallize in a body-centered tetragonal structure, space group *I*4/*mcm*, analogous to that observed in $(H_2S)_2H_2$. Both H_2Se and $(H_2Se)_2H_2$ are stable to 24 GPa at 300 K, after which both decompose into their constituent elements.

a)Email: ross.howie@hpstar.ac.cn

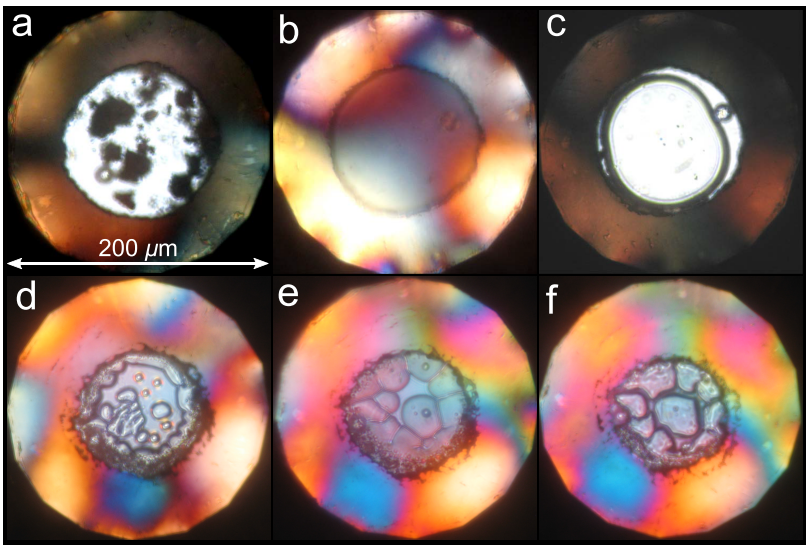

FIG. 1. Photomicrographs of the synthesis of H_2Se in a diamond-anvil cell sample chamber. The sample chamber is formed by a rhenium gasket. (a) H_2 and solid Se at 0.4 GPa and room temperature, (b) H_2Se–H_2 mixture at 0.4 GPa and 473 K, (c) liquid phase separation of H_2Se (central bubble) and H_2 (surrounding area) at 0.4 GPa and room temperature after heating, (d) H_2Se beginning to solidify, (e) slow coalescence of H_2Se regions, (f) completely solidified H_2Se at 1.5 GPa.

II. EXPERIMENTAL DETAILS

At ambient condition, H_2Se is a highly toxic and flammable gas. Such hazards can be avoided by the direct synthesis of H_2Se from Se and fluid H_2 in a diamond-anvil cell. Moreover, this technique also allows precise control of the ratio of H_2Se to H_2. High purity selenium (99.999%) was loaded into a diamond-anvil cell with a small chip of ruby and subsequently gas loaded with research grade hydrogen (99.9999%) at 0.2 GPa [Fig. 1(a)].[30] Rhenium gaskets were used to form the sample chamber in all experimental runs. Sample sizes ranged between 100 and 125 μm once in the solid state. Once loaded, Se–H_2 mixtures were then compressed to 0.4 GPa and heated to 473 K for at least 2 h until all the Se had reacted [Fig. 1(b)]. On slowly cooling to room temperature, liquid H_2Se was obtained with clear phase separation from fluid H_2 as a consequence of non-stoichiometry [Fig. 1(c)]. We found that heating was necessary to promote the reaction of Se and H_2. Leaving Se–H_2 mixtures at pressures between 0.2 GPa and 3 GPa for one month did not promote synthesis at room temperature.

H_2Se is very sensitive to both laser light and x-ray synchrotron radiation, which causes the sample to decompose, therefore precautions were required during data acquisition. Raman spectroscopy measurements were made using a custom-built micro-focused Raman system.[31,32] The laser power of the system was kept below 10 mW to prevent decomposition of the sample to Se and H_2. We have found that 647 nm laser emission was favorable over shorter wavelengths and did not cause any degradation of the sample during data acquisition. We found that the sample in the liquid state was much more prone to laser damage; thus, measurements were collected above pressures of 3.8 GPa. X-ray diffraction data were collected at beamline 16-IDB at the Advanced Photon Source (USA). Angle-dispersive x-ray diffraction patterns were recorded on a Pilatus 1M-F image-plate detector with a micro-focused synchrotron radiation of 30 keV. Data were integrated with DIOPTAS[33] to yield intensity vs. 2θ plots. Patterns were indexed with GSAS-II,[34] and Le Bail[35] refinements were carried out in JANA2006.[36] Exposure of H_2Se to synchrotron x-ray radiation resulted in the formation of amorphous Se at the point of exposure, requiring the acquisition of data from a different sample position at each pressure point. Powder quality was very poor in all samples excluding the possibility of Rietveld profile refinement.

III. RESULTS AND DISCUSSION

On compression above 1 GPa, H_2Se began to nucleate in fluid H_2 [see Figs. 1(d)–1(f)] with full crystallization occurring at pressures of 1.5 GPa [Fig. 1(g)]. Strong vibrational modes are observed in the Raman spectra, the most intense being the symmetrical ν_1 and asymmetrical ν_3 stretching modes, shown in Fig. 2(a). In phase I, these modes appear as a single broad band (~2250 cm^{-1} at 2.5 GPa). The ν_2 molecular bending mode, observed at frequencies of ~1010 cm^{-1}, is largely unaffected by pressure due to the "bent" molecular geometry. The behaviour of the vibrational Raman spectra of H_2Se is very similar to that of H_2S but shifted to lower frequencies. In phase I, the Raman frequencies of ν_1 and ν_3 of H_2Se differ by 300 cm^{-1} compared with the equivalent modes of H_2S, whilst the bending mode differs by 175 cm^{-1} (see Fig. 3).[26,39] In all our experimental runs, H_2Se tended to form multiple single crystals (see the insets of Fig. 4); however, due to the sensitivity of the sample to synchrotron x-ray exposure, it was difficult to acquire data capable of completely refining a structure. Despite this, we were able to determine the structure of H_2Se at 4.1 GPa, confirming that H_2Se crystallizes into cubic phase-I [$Fm\bar{3}m$, a = 5.424(3) Å], shown in Fig. 4. The structure of phase I of H_2Se is equivalent to that of phase I of H_2S.[18]

At pressures of 7.7 GPa, the unresolved ν_1 and ν_3 modes begin to differ in intensity, with ν_1 being the more intense. This was determined previously for H_2S to indicate transformation to an intermediate phase I′.[39] Above pressures of 12 GPa, there is a further transformation to phase IV, characterised by the splitting of ν_1 and ν_3, and from a reduction in peak width and increase in intensity. The asymmetrical stretching

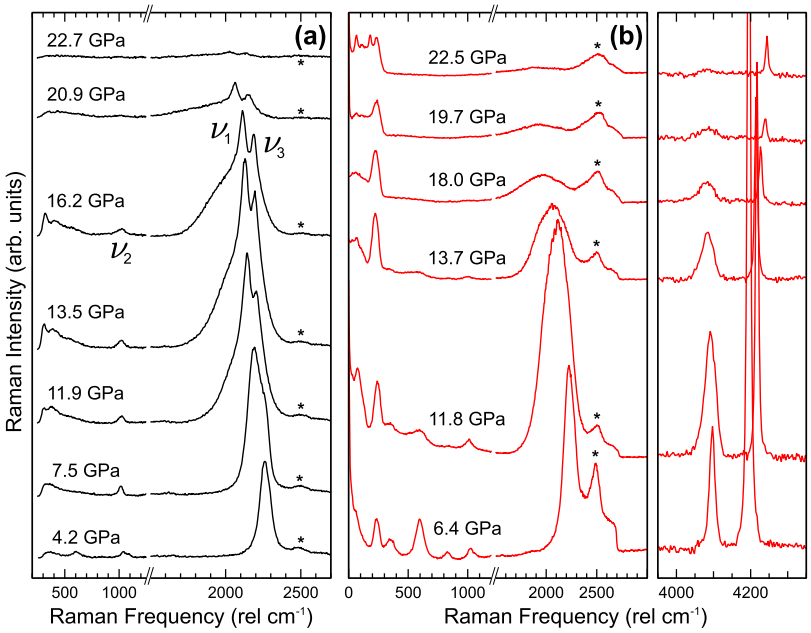

FIG. 2. (a) Representative Raman spectra of H_2Se on compression at 300 K (black). (b) Representative Raman spectra of $(H_2Se)H_2$ formed from a H_2-rich mixture at 300 K (red). The second order diamond is indicated by *.

mode, ν_3, is higher in frequency by 860 cm^{-1} compared with ν_1. Due to the instability of the sample to synchrotron x-ray exposure, we were unable to confirm a structural transition to phase I′ or IV in H_2Se through x-ray diffraction analysis; however, the Raman characteristics of the transitions are identical to those observed in H_2S. On further compression above 20 GPa, we see the reduced intensity of all vibrational modes, and the crystallites visibly darken as H_2Se dissociates into its constituent elements. The decomposition is complete by 24 GPa, and at 30 GPa, the x-ray diffraction measurements showed only incommensurate monoclinic Se-IV, whilst Raman measurements showed only the characteristic Raman spectrum of Se and H_2. In H_2S, the dissociation at 300 K occurs from ~27–50 GPa,[23,24] the onset being slightly higher than that observed here in H_2Se although over a much greater pressure range. Given the reduced X–H bond strength, it is unsurprising that H_2Se decomposes at lower pressure and within a much smaller pressure range than H_2S; hence, one would expect H_2Te to decompose at even lower pressure, if it can be stabilized at all at room temperature. This successive reduction of hydride decomposition pressure throughout group 16 reflects the trend observed in the hydrogen halides, where HCl is stable to at least 50 GPa, with HBr and HI decomposing at 42 GPa and 10 GPa, respectively.[40–42]

In all sample concentrations we studied with excess H_2, we observed partial or full formation of an H_2Se–H_2 compound above pressures of 4.2 GPa, which we identify as $(H_2Se)_2H_2$. Full formation of H_2Se was observed in samples with high H_2 concentration, as demonstrated in our x-ray diffraction measurements [Fig. 2(b)]. The formation was initially identified through the appearance of a second vibrational mode assigned to H_2 within the newly formed compound [see Fig. 2(b)]. This mode is ~100 cm^{-1} lower in frequency compared with pure H_2 and has different frequency pressure dependence. The ν_1 and ν_3 modes of H_2Se also behave very differently in the compound than in H_2Se, whereby we observe no splitting at phase IV conditions, and the modes soften rapidly with pressures above 12 GPa. These observations are very similar to the Raman characteristics for $(H_2S)_2H_2$ above 17 GPa, which was synthesized in H_2S–H_2 mixtures.[27] To confirm that this is an analogous compound formed in H_2Se–H_2 mixtures, we have performed x-ray diffraction measurements (see Figs. 4 and 5). Due to the sample sensitivity to synchrotron x-ray exposure and propensity to form large single-crystal grains, it was difficult to collect high-quality diffraction patterns; however, we were able to obtain a sufficient number of reflections to allow indexing to a body-centered tetragonal structure, space group $I4/mcm$ with a = 7.518(4) and c = 6.266(4) Å at 5.2 GPa, and unit-cell dimensions could be extracted to 14.9 GPa (see Fig. 5). The significant diffuse scattering observed is strongly suggestive of hindered rotational disorder in the H_2Se molecules.[43]

It is interesting that changes in volume per formula unit (V/Z) with pressure shows that $(H_2Se)_2H_2$ adopts a volume marginally greater (3% on average) than the sum of its constituent elements [solid line in Fig. 5(b)]. This is an indication that $(H_2Se)_2H_2$ is highly unstable, which is in agreement with our other observations. It is notable that the volume difference increases with pressure, reflecting the increased instability of $(H_2Se)_2H_2$ relative to decomposition into Se and H_2 with increasing pressure. Similar behaviour is observed in pure H_2Se at pressure; at 4.1 GPa, we observe V/Z = 39.887(4) Å^3, while the volume calculated from the constituent elements is V/Z = 37.321 Å^3. This behaviour, although highly unusual, is not unique; recently we have reported on the equation of state of HI, another highly unstable compound under pressure, which appears to have an experimentally determined V/Z 7.3% greater than that calculated from I and H.[42]

On compression, we do not see any evidence for further phase transitions in $(H_2Se)_2H_2$, such as the ordering transition observed in $(H_2S)_2H_2$. Instead, $(H_2Se)_2H_2$ starts to decompose at exactly the same pressure conditions as H_2Se observing the reduced intensity of the vibrational modes. At pressures

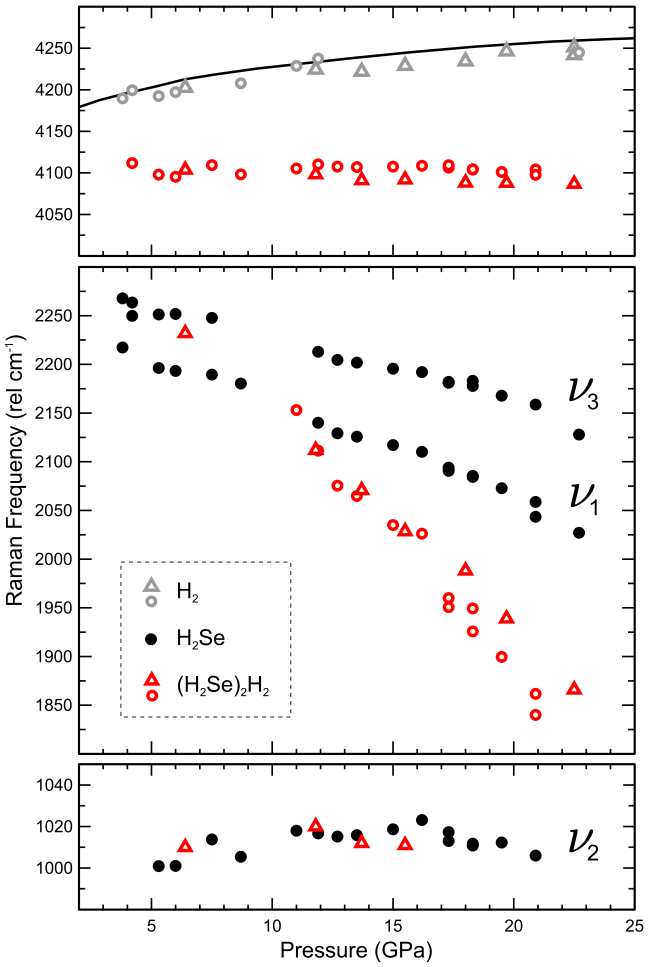

FIG. 3. Vibrational Raman frequencies of H_2Se (black closed circles), $(H_2Se)_2H_2$ (red open circles/triangles), and H_2 (grey open circles/triangles) as functions of pressure. Filled circles, open circles, and open triangles correspond to different experimental runs. Top panel: Vibrational modes of excess hydrogen (grey symbols) and hydrogen molecules within $(H_2Se)_2H_2$ (red). Solid black line corresponds to measurements of pure H_2. Middle panel: Symmetrical, ν_1, and asymmetrical, ν_3, stretching modes of H_2Se (black) and the corresponding modes within $(H_2Se)_2H_2$ (red). Bottom panel: The ν_2 molecular bending mode of H_2Se (black) and the corresponding mode within $(H_2Se)_2H_2$ (red).

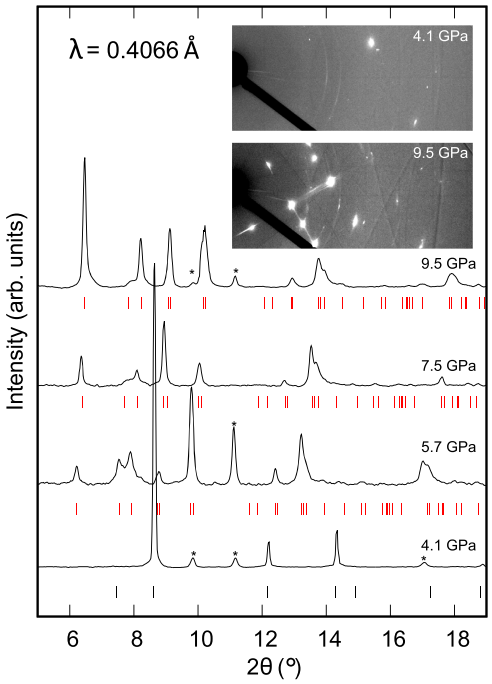

FIG. 4. X-ray diffraction data for H_2Se and $(H_2Se)_2H_2$ at high pressures. Below 4.1 GPa, diffraction spots due to phase-I of H_2Se are observed (black tick marks). Above 4.1 GPa, diffraction spots corresponding to the hydrogen-bonded compound $(H_2Se)_2H_2$ are observed up to pressures of 14.9 GPa (red tick marks). Peaks marked with (*) are due to the Re gasket. Inset: Single crystal-like x-ray diffraction patterns of H_2Se at 4.1 GPa and $(H_2Se)_2H_2$ at 9.5 GPa, the latter of which includes significant streaks of diffuse scattering.

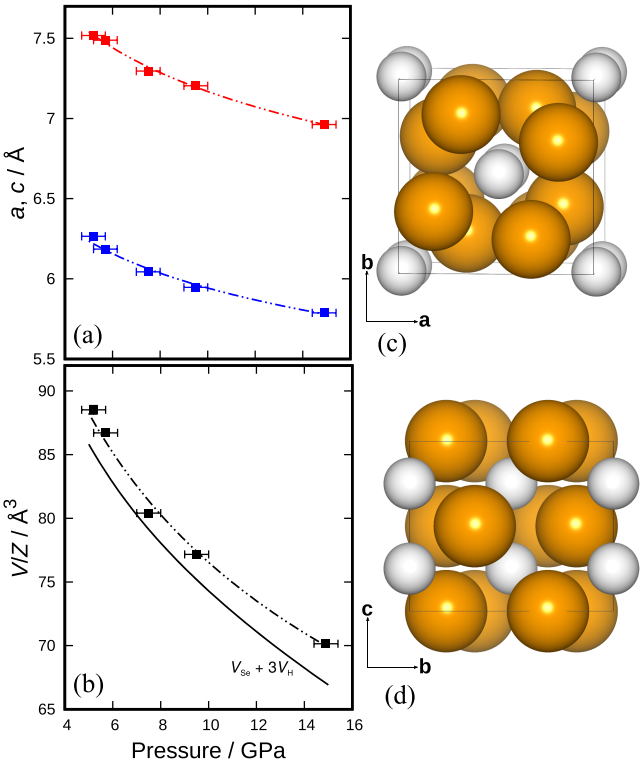

FIG. 5. (a) Changes in unit-cell dimensions for $(H_2Se)_2H_2$ as a function of pressure (a—red and c—blue). (b) V/Z as a function of pressure for $(H_2Se)_2H_2$. The solid line indicates volume calculated according to the atomic equations of state for H_2[37] and Se.[38] [(c) and (d)] Structure of $(H_2Se)_2H_2$ viewed down the c and a axes illustrating the layered nature of the compound.

approaching 22.5 GPa, the sample visibly phase separates and the transparent $(H_2Se)_2H_2$ crystals become dark and metallic, which shows the characteristic low frequency modes of Se [see Fig. 2(b)], with the remaining sample being transparent molecular hydrogen.

Recent x-ray synchrotron measurements have suggested that high-Tc superconducting H_2S could be due to the formation of H_3S, which reforms upon partial decomposition of H_2S at high pressure.[8–10] Our study demonstrates that H_2Se and H_2Se–H_2 mixtures behave very similar to H_2S and H_2S–H_2 at high pressure and 300 K. Assuming the decomposition of H_2Se can be stabilized by low temperatures, it is very plausible that H_3Se is formed at high pressures; if H_3S is indeed the thermodynamically stable high pressure phase of H_2S. Given that the behaviour of H_2S above 100 GPa is not completely understood,[2–10] experiments on H_2Se at the conditions in which superconductivity is predicted could prove very insightful for all the hydrogen chalcogenides.

ACKNOWLEDGMENTS

This work was supported by a research grant from the UK Engineering and Physical Sciences Research Council. Portions of this work were performed at HPCAT (Sector 16), Advanced Photon Source (APS), Argonne National Laboratory. HPCAT operations are supported by DOE-NNSA under Award No. DE-NA0001974, with partial instrumentation funding by NSF. The Advanced Photon Source is a U.S. Department of Energy (DOE) Office of Science User Facility operated for the DOE Office of Science by Argonne National Laboratory under Contract No. DE-AC02-06CH11357. The authors thank Ross Hrubiak for his assistance.

[1] A. P. Drozdov, M. I. Eremets, I. A. Troyan, V. Ksenofontov, and S. I. Shylin, Nature **525**, 73 (2015).
[2] A. F. Goncharov, S. S. Lobanov, V. B. Prakapenka, and E. Greenberg, Phys. Rev. B **95**, 140101 (2017).
[3] B. Guigue, A. Marizy, and P. Loubeyre, Phys. Rev. B **95**, 020104(R) (2017).
[4] I. Troyan, A. Gavriliuk, R. Rüffer, A. Chumakov, A. Mironovich, I. Lyubutin, D. Perekalin, A. P. Drozdov, and M. I. Eremets, Science **351**, 1303 (2016).
[5] E. E. Gordon, K. Xu, H. Xiang, A. Bussmann-Holder, R. K. Kremer, A. Simon, J. Köhler, and M. H. Whangbo, Angew. Chem., Int. Ed. **55**, 3682 (2016).
[6] I. Errea, M. Calandra, C. J. Pickard, J. R. Nelson, R. J. Needs, Y. Li, H. Liu, Y. Zhang, Y. Ma, and F. Mauri, Nature **532**, 81 (2016).
[7] R. Akashi, W. Sano, R. Arita, and S. Tsuneyuki, Phys. Rev. Lett. **117**, 075503 (2016).
[8] M. Einaga, M. Sakata, T. Ishikawa, K. Shimizu, M. I. Eremets, A. P. Drozdov, I. A. Troyan, N. Hirao, and Y. Ohishi, Nat. Phys. **12**, 835 (2016).
[9] A. F. Goncharov, S. S. Lobanov, I. Kruglov, X.-M. Zhao, X.-J. Chen, A. R. Oganov, Z. Konôpková, and V. B. Prakapenka, Phys. Rev. B **93**, 174105 (2016).
[10] Y. Li, L. Wang, H. Liu, Y. Zhang, J. Hao, C. J. Pickard, J. R. Nelson, R. J. Needs, W. Li, Y. Huang, I. Errea, M. Calandra, F. Mauri, and Y. Ma, Phys. Rev. B **93**, 020103 (2016).
[11] S. Zhang, Y. Wang, J. Zhang, H. Liu, X. Zhong, H.-F. Song, G. Yang, L. Zhang, and Y. Ma, Sci. Rep. **5**, 15433 (2015).
[12] X. Zhong, H. Wang, J. Zhang, H. Liu, S. Zhang, H.-F. Song, G. Yang, L. Zhang, and Y. Ma, Phys. Rev. Lett. **116**, 057002 (2016).
[13] G. Natta, Nature **127**, 129 (1931).
[14] J. H. Loehlin, P. G. Mennitt, and J. S. Waugh, J. Chem. Phys. **44**, 3912 (1966).
[15] Z. M. E. Saffar and P. Schultz, J. Chem. Phys. **56**, 2524 (1972).
[16] B. A. Paldus, S. A. Schlueter, and A. Anderson, J. Raman Spectrosc. **23**, 87 (1992).
[17] J. A. Flores-Livas, A. Sanna, and E. K. U. Gross, Eur. Phys. J. B **89**, 63 (2016).
[18] J. K. Cockcroft and A. N. Fitch, Z. Kristallogr. **193**, 1 (1990).
[19] H. Fujihisa, H. Yamawaki, M. Sakashita, K. Aoki, S. Sasaki, and H. Shimizu, Phys. Rev. B **57**, 2651 (1998).
[20] S. Endo, A. Honda, K. Koto, O. Shimomura, T. Kikegawa, and N. Hamaya, Phys. Rev. B **57**, 5699 (1998).
[21] J. S. Loveday, R. J. Nelmes, S. Klotz, J. M. Besson, and G. Hamel, Phys. Rev. Lett. **85**, 1024 (2000).
[22] R. Rousseau, M. Boero, M. Bernasconi, M. Parrinello, and K. Terakura, Phys. Rev. Lett. **85**, 1254 (2000).
[23] H. Fujihisa, H. Yamawaki, M. Sakashita, A. Nakayama, T. Yamada, and K. Aoki, Phys. Rev. B **69**, 214102 (2004).
[24] M. Sakashita, H. Yamawaki, H. Fujihisa, K. Aoki, S. Sasaki, and H. Shimizu, Phys. Rev. Lett. **79**, 1082 (1997).
[25] S. Endo, A. Honda, S. Sasaki, H. Shimizu, O. Shimomura, and T. Kikegawa, Phys. Rev. B **54**, R717 (1996).
[26] H. Shimizu, Y. Nakamichi, and S. Sasaki, J. Chem. Phys. **95**, 2036 (1991).
[27] T. A. Strobel, P. Ganesh, M. Somayazulu, P. R. C. Kent, and R. J. Hemley, Phys. Rev. Lett. **107**, 255503 (2011).
[28] Y. Li, J. Hao, H. Liu, Y. Li, and Y. Ma, J. Chem. Phys. **140**, 174712 (2014).
[29] D. Duan, Y. Liu, F. Tian, D. Li, X. Huang, Z. Zhao, H. Yu, B. Liu, W. Tian, and T. Cui, Sci. Rep. **4**, 6968 (2014).
[30] H. K. Mao, J. Xu, and P. M. Bell, J. Geophys. Res. **91**, 4673, doi: 10.1029/jb091ib05p04673 (1986).
[31] P. Dalladay-Simpson, R. T. Howie, and E. Gregoryanz, Nature **529**, 63 (2016).
[32] R. T. Howie, R. Turnbull, J. Binns, M. Frost, P. Dalladay-Simpson, and E. Gregoryanz, Sci. Rep. **6**, 34896 (2016).
[33] C. Prescher and V. B. Prakapenka, High Pressure Res. **35**, 223 (2015).
[34] B. H. Toby and R. B. Von Dreele, J. Appl. Crystallogr. **46**, 544 (2013).
[35] A. Le Bail, H. Duroy, and J. Fourquet, Mater. Res. Bull. **23**, 447 (1988).
[36] V. Petříček, M. Dušek, and L. Palatinus, Z. Kristallogr. - Cryst. Mater. **229**, 345 (2014).
[37] P. Loubeyre, R. LeToullec, D. Hausermann, M. Hanfland, R. J. Hemley, H. K. Mao, and L. W. Finger, Nature **383**, 702 (1996).
[38] M. I. McMahon, C. Hejny, J. S. Loveday, and L. F. Lundegaard, Phys. Rev. B **70**, 054101 (2004).
[39] H. Shimizu, H. Yamaguchi, S. Sasaki, A. Honda, S. Endo, and M. Kobayashi, Phys. Rev. B **51**, 9391 (1995).
[40] E. Katoh, H. Yamawaki, H. Fujihisa, M. Sakashita, and K. Aoki, Phys. Rev. B **59**, 11244 (1999).
[41] T. Kume, T. Tsuji, S. Sasaki, and H. Shimizu, Phys. Rev. B **58**, 8149 (1998).
[42] J. Binns, X.-D. Liu, P. Dalladay-Simpson, V. Afonina, E. Gregoryanz, and R. T. Howie, Phys. Rev. B **96**, 144105 (2017).
[43] J. Binns, G. J. McIntyre, J. A. Barreda-Argüeso, J. González, F. Aguado, F. Rodríguez, R. Valiente, and S. Parsons, Acta Crystallogr., Sect. B: Struct. Sci., Cryst. Eng. Mater. **73**, 844 (2017).

Comment on "Synthesis and properties of selenium trihydride at high pressures"

Edward J. Pace
School of Chemistry and Centre for Science at Extreme Conditions, University of Edinburgh, Edinburgh EH9 3FD, United Kingdom

Jack Binns, Phillip Dalladay-Simpson, and Ross T. Howie
Center for High Pressure Science & Technology Advanced Research, 1690 Cailun Road, Building 6, Pudong, Shanghai 201203, People's Republic of China

Miriam Peña Alvarez
School of Physics and Astronomy and Centre for Science at Extreme Conditions, University of Edinburgh, Edinburgh EH9 3FD, United Kingdom

(Received 16 April 2018; revised manuscript received 24 April 2018; published 11 September 2018)

A recent article by Zhang *et al.* [Phys. Rev. B **97**, 064107 (2018)] claimed the high-pressure synthesis and metallization of H_3Se, or selenium trihydride, at 23 GPa and 203 K. Here, we demonstrate that the synthesised compound is not H_3Se but the previously reported, and already well characterized, $(H_2Se)_2H_2$. The claim of metallization is unsubstantiated by the experimental evidence and can be explained by the decomposition of $(H_2Se)_2H_2$ into metallic Se and molecular H_2.

DOI: 10.1103/PhysRevB.98.106101

Zhang *et al.* [1] synthesise H_2Se directly from heating elemental Se in H_2 media at pressures of 0.3 GPa. The synthesis process of forming the H_2Se from the constituent elements at high temperature was already reported recently by Pace *et al.* [2]. In both reports, a molecular compound is formed on compression at ∼4.2 GPa and characterized through both synchrotron x-ray diffraction and Raman spectroscopy. Zhang *et al.* claim to form a new compound, "selenium trihydride"; however, here we show that the experimental evidence for this new compound is entirely consistent with the previously reported $(H_2Se)_2H_2$.

Reference [1] presents the room-temperature powder x-ray diffraction pattern of the synthesized compound at 7 GPa (Fig. 4 in Ref. [1]). The authors compare the observed reflection positions with those of a face-centered orthorhombic phase space group *Cccm*, predicted by theory [3]; however, no refinement was performed against the observed data, as evidenced by the lack of unit-cell dimensions reported in the text. Furthermore, the authors have not displayed tick marks for all the expected reflections of the predicted *Cccm* structure. While many of these predicted reflections are weak, they are *not* systematically absent. In total, the authors of Ref. [1] omit 27 reflections in the 2θ range for the data set at 7 GPa. In Fig. 1(a), we show for comparison the tick marks presented in Ref. [1] (shown in red) and include the additional tick marks (shown in gray) that should be present for the predicted *Cccm* structure.

The predicted "H_3Se" structure presented by [3] contains 16 Se atoms bonded to 32 H atoms with the remaining 16 H atoms forming H_2 molecules, giving a formula of $(H_2Se)_2H_2$. This structure differs from that reported by Ref. [2] only in the "freezing out" of hydrogen atom positions as a result of the calculation being performed at 0 K. This reduction in symmetry doubles the volume of the unit cell. The stoichiometry of this structure is identical to that reported in Ref. [2] and does not contain any "H_3Se" molecules as implied by "selenium trihydride."

Distinguishing between these structures requires locating hydrogen atom positions, but hydrogen is an extremely weak scatterer of x rays and cannot typically be located accurately by high-pressure x-ray diffraction. The observed scattering is therefore due entirely to Se atoms. The Se atom positions in the *Cccm* phase and the previously reported $I4/mcm$ structure are indistinguishable. To illustrate the direct relationship between the structures, we present the refinements of both unit cells against the x-ray diffraction data from Ref. [1], (a) at 7 GPa and 300 K and (b) at 39.5 GPa and 170 K. We find that the $I4/mcm$ structure reported in Ref. [2] explains the observed scattering without redundant reflections or enlarged unit cell. The refined unit-cell dimensions are $a = 7.262(1)$ Å, $c = 6.094(4)$ Å at 7 GPa and $a = 6.304(1)$ Å, $c = 5.430(5)$ Å at 39.5 GPa. This analysis, and the fact that the volumes reported in Ref. [1] (see Fig. 6) match that of $(H_2Se)_2H_2$ in Ref. [2], demonstrates the equivalence of "H_3Se" and the previously reported $(H_2Se)_2H_2$.

In Fig. 2 we present a comparison of the Raman data between that of Ref. [1] at 203 K and Ref. [2] at 300 K as a function of pressure. Below 20 GPa, both data sets are in excellent agreement, with slight modifications in frequency due to the temperature difference between the two studies. The appearance of a second hydrogen vibrational mode is not attributed to the formation of H_3Se as described in Ref. [1] but is indicative of the formation of $(H_2Se)_2H_2$, and the behavior is analogous with the formation of $(H_2S)_2H_2$. At ∼20 GPa, we see slight deviation in the appearance of the spectra, but this can be attributed to the ability to resolve the spectra at low temperature, while at 300 K, $(H_2Se)_2H_2$ is close to decomposition pressure.

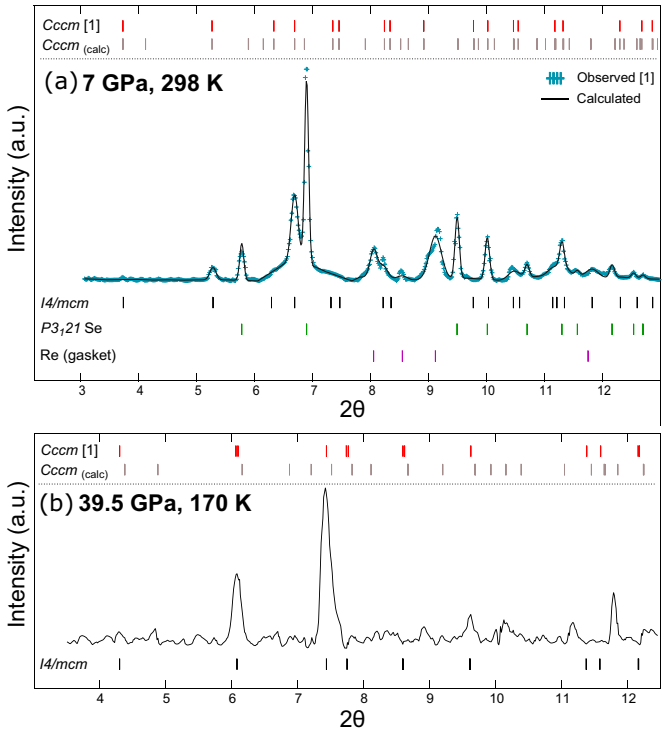

FIG. 1. (a) Le Bail refinement of $I4/mcm$ fitted to the x-ray diffraction data from Ref. [1] (Fig. 4) at 7 GPa and 298 K. Reflections in fit: $(H_2Se)_2H_2$ $I4/mcm$ (black), $P3_121$ Se (green), Re (purple). (b) X-ray diffraction data from Ref. [1] (Fig. 5) at 39.5 GPa and 170 K, showing reflections for $(H_2Se)_2H_2$ $I4/mcm$ (black). Top panels in Figs. 1(a) and 1(b) show the difference between the reflections predicted for *Cccm*-H_3Se and the reflections that were actually presented in Ref. [1].

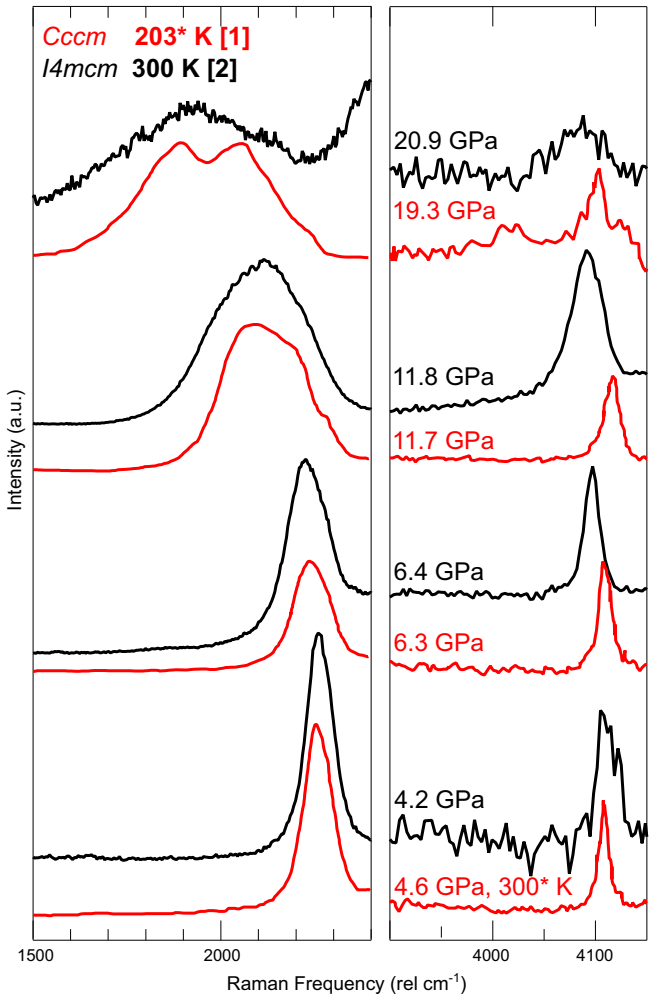

FIG. 2. Comparison of Raman spectra as a function of increasing pressure: Ref. [1] (red) "*Cccm*-H_3Se" at 203 K (300 K at 4.6 GPa), Ref. [2] (black) $I4/mcm$-$(H_2Se)_2H_2$ at 300 K.

At room temperature, both Refs. [1,2] are in agreement that H_2Se [and $(H_2Se)_2H_2$] decomposes due to laser light, synchrotron radiation, and also when compressed to pressures above ∼21 GPa. However, at pressures above 23 GPa and 203 K, Zhang *et al.* claim that "H_3Se" transforms into a metallic state. The evidence for such a transition relies on the sample becoming "visually nontransparent and shiny" together with the significantly weakened Raman spectra. Visual observation evidence is insufficient to claim a transition to a metallic state, with similar results being recently used in support of the widely criticized metallization of hydrogen [4,5]. The limited evidence presented for metallization of "H_3Se" is entirely equivalent to that presented for the decomposition, either light or pressure induced, at 300 K. As the x-ray diffraction data still show the persistence of $I4/mcm$-$(H_2Se)_2H_2$, we conclude that the compound is stabilized at low temperature at this pressure but on x-ray/laser irradiation is partially decomposed, giving *nontransparent and shiny* elemental selenium. Figure 1(c) of Ref. [1] shows that the appearance of the decomposed sample is exactly the same as that of the excess Se precursor in Fig. 1(a).

In conclusion, by applying structural analysis to the data presented by Zhang *et al.*, we find that the claimed compound is not *Cccm*-H_3Se but instead $I4/mcm$-$(H_2Se)_2H_2$, which has already been reported and characterized at room temperature [2]. The nomenclature of either H_3Se or "selenium trihydride" is incorrect, misleading, and should not be applied to a molecular compound containing molecular hydrogen selenide and molecular hydrogen. The claims for metallization are unsupported by the evidence, and to the contrary, indicates the much simpler explanation of sample decomposition.

[1] X. Zhang, W. Xu, Y. Wang, S. Jiang, F. A. Gorelli, E. Greenberg, V. B. Prakapenka, and A. F. Goncharov, Phys. Rev. B **97**, 064107 (2018).

[2] E. J. Pace, J. Binns, M. Peña Alvarez, P. Dalladay-Simpson, E. Gregoryanz, and R. T. Howie, J. Chem. Phys. **147**, 184303 (2017).

[3] J. A. Flores-Livas, A. Sanna, and E. K. U. Gross, Eur. Phys. J. B **89**, 63 (2016).

[4] X.-D. Liu, P. Dalladay-Simpson, R. T. Howie, B. Li, and E. Gregoryanz, Science **357**, eaan2286 (2017).

[5] A. F. Goncharov and V. V. Struzhkin, Science **357**, eaam9736 (2017).